Pasquale Giovine
Paolo Maria Mariano
Giuseppe Mortara
Editors

Views on Microstructures in Granular Materials

Birkhäuser

Advances in Mechanics and Mathematics

Advances in Continuum Mechanics

Volume 44

More information about this subseries at http://www.springer.com/series/16097

Pasquale Giovine • Paolo Maria Mariano
Giuseppe Mortara

Editors

Views on Microstructures in Granular Materials

Birkhäuser

Editors

Pasquale Giovine
Department of Civil, Energy, Environment,
and Materials Engineering (DICEAM)
University 'Mediterranea' of Reggio Calabria
Reggio Calabria, Italy

Paolo Maria Mariano
Department of Civil and Environmental
Engineering
University of Florence
Firenze, Italy

Giuseppe Mortara
Department of Civil, Energy, Environment,
and Materials Engineering (DICEAM)
University of Reggio Calabria
Reggio Calabria, Italy

Views on Microstructures in Granular Materials: Preface

Granular materials are sets of thousands to millions of individual particles—grains with a diameter greater than one micron—each able to move independently of the neighboring particles, unless the environment forces them to a certain degree of compactness or to flow into constrained regions such as channels.

Viewed with the naked eye, grains are simple, at times even described merely by indicating the placement in space of their mass center. However, grain clusters behave as complex media. Their behavior depends on several factors, e.g., the size distribution of the grains, the roughness of the grain boundaries, and their potential chemical activity, determining partial cohesion, history, whether they are dry or embedded in a ground fluid, etc.

Such materials oscillate from fluid-like behavior to solid-like states in which grains are jammed to various degrees. Under the latter conditions, we also recognize groups of grains at equilibrium but additionally rattles, i.e., mechanically unstable grain sub-clusters. Essentially, we meet metastable jammed states: the energy exhibits local minimizers rather than global ones. Variety in the ways in which grains can be jammed does not allow us to identify specific reference representative volume elements from which we may start homogenizing at continuum scale.

Due to such difficulty, statistical approaches may offer appropriate views at least for jammed states. With this aim, in 1989, S.F. Edwards and R.B.S. Oakeshott proposed adopting for mechanically stable configurations of grains in a given domain a microcanonical view, in which volume plays the same role as energy so that configurations occupying the same volume are considered to be equi-probable. The probability P_ς that a granular sub-cluster of volume $\bar{V} < V$ is in a given state ς is $P_\varsigma = \exp(-\frac{\bar{V}}{\chi(V)})$. The scalar factor $\chi(V)$, dubbed the so-called *compactions*, is the inverse of a temperature and behaves as an order parameter, which may characterize non-equilibrium phases.[1]

---

[1] Edwards E.F., Oakeshott R.B.S. (1989), Theory of powders, *Physica A*, **157**, 1080–1090.

A related crucial problem is to decide what kind of continuum is the target of our homogenization procedures.[2] Is it Cauchy type, Cosserat type, or does it refer to more complex media? The simplest models refer to the standard format of continuum mechanics, for which the sole kinematic descriptor is the placement of grains, its variations given just by the point velocity field, and can be considered in short as schemes of frictional plasticity, friction described by Mohr–Coulomb's critical state criterion or related refinements.[3] Such schemes do not include intrinsic length scales, which appear when we refine the representation of kinematic modes, e.g., accounting for independent grain rotations, with the construction of the pertinent Cosserat scheme, possibly coupled with the local grain strain, in a micromorphic-type model (specific examples are some independent works by J.D. Goddard and P. Giovine, but not only these).[4]

Granular flows display even more intricate behavior and present a number of delicate problems in modeling. First, a reference configuration from which we may start homogenizing is hard (if not impossible) to find; thus, the description at continuum scale is naturally Eulerian. In 1998, M.-L. Tan and I. Goldhirsch have even questioned whether hydrodynamic representation of granular flow is appropriate.[5] Their argument rests on the consideration that hydrodynamic-like equations are "intimately related to the notion of scale separation" and they found "that such a scale separation is nonexistent" in granular systems "except when the system is very nearly elastic." Such a viewpoint emerges from the analysis of a simply sheared stationary monodisperse granular system composed of disks (spheres) in two (three) dimensions, with a fixed normal restitution coefficient. Two key aspects characterize it: the product of mean free time τ_0 by shear rate γ (the inverse of which is the macroscopic time scale, whereas the other is a microscopic time scale) is not small unless the system is nearly elastic. The mean path shows spatial variations. The pertinent conclusion already mentioned was criticized 1 year later by J.W. Dufty and J.J. Brey.[6] First, they analyze an elastically colliding flow of grains undergoing uniform shear with nonsmall $\gamma\tau_0$ and show that the hydrodynamic description applies for $t \gg \tau_0$. Then, they find that the spatial variations of mean path, used by Tan and Goldhirsch, are the same for both elastic and inelastic collisions; they conclude that spatial variations are "due

---

[2]See remarks in Kamrin K. (2017), A hierarchy of granular continuum models: Why flowing grains are both simple and complex, *EPJ Web of Conferences*, **140**, art. 01007.

[3]See, e.g., Mortara G. (2015), A constitutive framework for the elastoplastic modelling of geomaterials, *Int. J. Solids Struct.*, **63**, 139–152, and (2019), A new yield criterion for soils with embedded tension cut-off, *Meccanica*, **54**, 683–696.

[4]Examples are Goddard J.D. (2014), Continuum modeling of granular media, *Appl. Mech. Rev.*, **66**, art. 050801; Giovine P. (2017), "Extended granular micromechanics", *EPJ Web of Conferences*, **140**, art. 11009.

[5]Tan M.-L., Goldhirsch I. (1998), Rapid granular flows as mesoscopic systems, *Phys. Rev. Lett.*, **81**, 3022–3025.

[6]Dufty J.W., Brey J.J. (1999), Comment on "Rapid granular flows as mesoscopic systems", *Phys. Rev. Lett.*, **82**, 4566.

to the hydrodynamics itself, not the underlying kinetics." In any case, one problem remains: what kind of hydrodynamic description and how to get it?

If we refer to flow with low grain density, we could think of starting from the Boltzmann equation, possibly accounting for inelastic collisions, and we would find the problem of rigorously obtaining the continuum limit. We could also consider expansion of the distribution function, taking 13 moments as in Grad's proposal or enlarging the view in the spirit of I. Müller's and T. Ruggeri's extended thermodynamics.[7] In this setting, when we account for the widespread inelastic collisions, Boltzmann's distribution—the probability of a state is proportional to the exponential of its energy—does not apply. At variance, in the presence of elastic collisions and increasing grain density, we could directly approach the description at continuum scale through Hamiltonian terms, but reality introduces friction or other non-Hamiltonian effects, although we could think of mimicking them by using Hamiltonian structures involving pseudo-potentials, at the cost of losing the possibility of describing oscillatory instabilities, which fall outside the Hamiltonian realm.

In statics, such instabilities play a nontrivial role as sources of large-scale shear-banding and collapse mechanisms.[8] In any case, even if we did feel satisfied by Hamiltonian or pseudo-Hamiltonian structures, we should construct explicitly their elements in terms of average, at least in a portion of space. If so, the procedure would also open the path toward continuum schemes that are not necessarily Hamiltonian. Also, in analyzing a window in space with the aim of making appropriate averages, we realize that the microcanonical assumption mentioned above does not apply. That window has to be considered as a grand canonical ensemble: the grain cluster it contains at a certain instant may lose elements and receives energy from (or transfers it to) the environment through its boundary, owing to collisions. A question is how to consider fluctuations beyond the average velocity v, which we can define presuming to know the pertinent distribution function.

Actually, to compute the average velocity explicitly, we need a specific form of that distribution. In a rather traditional approach the fluctuation $\bar{v} := w - v$ is considered, with w the velocity of a grain at a point in the window and a certain instant as the ingredient for defining a Reynolds tensor $\bar{H}$ by averaging $\bar{v} \otimes \bar{v}$ over the window considered in terms of the same distribution function used to define v. Such a tensor essentially plays the role that we can call a (tensor) granular temperature. Starting from 2003, G. Capriz proposed changing this

[7]Müller I., Ruggeri T. (1998), Rational extended thermodynamics (2nd ed.), *Springer Verlag*, New York.

[8]Chattoraj J., Gendelman O., Pica Ciamarra M., Procaccia I. (2019), Oscillatory instabilities in frictional granular matter, *Phys. Rev. Lett.*, **123**, art. 098003 (1–5); di Prisco C., Matiotti R., Nova R. (1995), Theoretical investigation of the undrained stability of shallow submerged slopes, *Geotechnique*, **45**, 479–496; Muir Wood D. (2002), Some observations of volumetric instabilities in soils, *Int. J. Solids Struct.*, **39**, 3429–3449.

view,[9] a proposal further refined in independent collaborations with M. Brocato, P. Giovine, and P.M. Mariano.[10] The new approach foresees a decomposition of $\bar{v}$ into a homogeneous component and spurious fluctuations. The former accounts for fluctuating expansion and contraction of the grain cluster within the window (indeed, a *loculus* in space) at a given instant. Through it we can evaluate mass gain or loss beyond the averaged motion. Also, we can associate with such a (low-spatial-scale) mechanism true interactions power-conjugated with it, which satisfy an appropriate balance. In this way, we set the description of (above all fast) granular flows within the mechanics of complex materials, enriched by an energy balance associated with the spurious fluctuations. When we consider a grain cluster moving with and into a ground fluid, the previous view allows us to capture a refined description of anisotropies that we may recognize in nature—falling hail is an obvious example.[11]

The size of grains larger than one micron, defining granular materials, avoids thermal fluctuations. However, even in jammed states we may induce thermal-like agitations by applying tapping or sharing protocols repeatedly.[12] After the time interval pertinent to the external excitation, they decay. A question is then how to interpret thermodynamics for granular materials.[13] If we think of jammed states and the possible externally induced dynamics by repeated shaking, we can create, at least in principle, different jammed states, and may factorize the state space by the total stress pertaining to the cluster in a given window considered now as a canonical ensemble for it exchanging energy with the environment. Frequency by which a given state is accessible allows us to define a density of states, depending on the total stress (leaving a part fluctuation components due to shaking), so that we can obtain a temperature-like tensor as the derivative of a state density logarithm with respect to the stress. For granular flow such a structure requires refinements, even to be abandoned, owing to the nontrivial role of stress fluctuations and (above all) the lack of validity for the canonical ensemble assumption. In the way of considering fluctuations as sketched above, the spurious ones, or at least some of them, play a thermal-like role here. The pertinent Reynolds-type tensor could itself be considered a (tensor) granular temperature, as its evolution equation is a

[9]Capriz G. (2003), Elementary preamble to a theory of granular gases, *Rend. Mat. Univ. Padova*, **110**, 179–198.

[10]The list includes Brocato M., Capriz G. (2011), Clockwork, ephemeral and hybrid continua, *Phys. Mesomech.*, **14**, 124–144; Capriz G., Giovine P. (2017), Classes of ephemeral continua, *Math. Meth. Appl. Sci.*, **43**, 1175–1196; Capriz G., Mariano P.M. (2014), Objective fluxes in a multiscale continuum description of sparse medium dynamics, *Phys. A*, **415**, 354–365.

[11]Mariano P.M. (2020), Flows of suspended grains: mixing a sparse phase with simple and complex continua, *Int. J. Solids Struct.*, **187**, 141–161.

[12]See, for example, Becker V., Kassner K. (2015), Protocol-independent granular temperature supported by numerical simulations, *Phys. Rev. E. Stat. Nonlin. Soft Matter Phys.*, **92**, art. 052201 (1–15).

[13]See, for example, Goldhirsch I. (2008), Introduction to granular temperature, *Powder Tech.*, **182**, 130–136.

low-scale energy balance. But we can also define a scalar granular temperature by using the distribution of spurious fluctuation (scalar) kinetic energy.[14]

Clearly, the description of granular matter behavior offers a number of nontrivial challenges, which can be tackled from different viewpoints, using refined mathematical theories as well as advanced numerical and experimental methods. In particular, experiments in soil mechanics have been enriched in last decades by the introduction of new techniques, which enable the observation of granules at the contact scale. Also, the introduction of numerical tools such as the Discrete Element Method revealed the role of the microstructure in characterizing the behavior of soils. These new tools help in understanding the complex behavior of granular materials at the macroscale. To take into account all the complex phenomena that occur at the microscale, interaction among different areas of expertise, engineering, physics, and mathematics, as well as chemistry, is thus of fundamental importance for a complete and rational description of a granular material, even if it is concretely arduous to account critically in a unique volume for the variety of existing approaches and related results.

For this reason, in the present book we focus attention only on specific issues and viewpoints, trying at least to present a wide range of scenarios on the matter. Our choices of the material presented here include experimental questions connected with X-ray tomography techniques for analyzing sand, the theoretical analysis of dense inhomogeneous granular shearing, the evaluation of effective stress in unsaturated soils, the modeling of solids with nanopores as a scheme for compacted soils, hyper-plasticity, wave propagation in granular systems, yield criteria, the scheme of partly saturated porous media, some of the computational problems emerging in the analysis of granular matter, multi-scale phenomena in flows of grains with internal structure, and related continuum modeling. All the chapters that constitute the present book offer an overview intended for addressing further research work.

Reggio Calabria, Italy	Pasquale Giovine
Firenze, Italy	Paolo Maria Mariano
Reggio Calabria, Italy	Giuseppe Mortara

---

[14]Capriz G., Mariano (2019) P. M., Interactions in a multi-scale representation of sparse media: from mechanics to thermodynamics, *J. Elast.*, **135**, 91–115.

Contents

X-Ray Tomography Experiments on Sand at Different Scales

Edward Andò, Gioacchino Viggiani, and Jacques Desrues

Abstract This paper presents a brief introduction to some tools used for quantitative analysis of 3D fields coming from X-ray tomography with a view to elucidate micro-mechanisms of deformation in granular materials. A long-standing research objective in Laboratoire 3SR is to fully describe strain localisation in sand—results at different scales of analysis are presented and discussed alongside recent numerical advances which to our mind are the quintessential example of successful upscaling from micro to macro.

Keywords Micro-to-macro · Experimental micro-mechanics · Sand · X-ray tomography · Image correlation

1 Introduction

This paper is based on numerous decades of experimental research on strain localisation in sand carried out in Laboratoire 3SR, Grenoble. This project has had a recent increase in momentum thanks to the acquisition of a first laboratory X-ray scanner nearly 10 years ago, followed recently by a second. Despite sand's relative simplicity as a material, its shape is not, and neither is its mechanical response—X-ray tomography is ideally suited to studying both of these aspects when coupled with mechanical experiments and analysis of the acquired 3D fields.

The paper is divided into two sections: the first recalls the key aspects of the tools used—this part is largely based on previously published material [5, 38]. The second presents recent and very recent work, and discusses some aspects of our vision for the future.

E. Andò · G. Viggiani (✉) · J. Desrues
Univ. Grenoble Alpes, CNRS, Grenoble INP, 3SR, Grenoble, France
e-mail: cino.viggiani@3sr-grenoble.fr

2 3D Field Measurements

Most laboratory soil characterisation is based on observations of specimen boundaries, where forces, deformations, energy potential, and flow are either imposed or measured. Measurements are then interpreted to determine material behaviour using constitutive equations in terms of stress, strain, flow rate, and gradients. This approach assumes homogeneity within the specimen and is therefore inadequate for the study of non-homogeneous processes; the study of such processes requires field measurements. Full-field methods have been extensively used in experimental geomechanics—see [39] for a relatively complete review. The use of X-ray imaging in experimental geomechanics dates back to the 1960s e.g. [29]. X-rays were used to obtain two-dimensional (2D) radiographs on photographic plates. Radiographs represent maps of attenuation accumulated along the ray path through the soil mass. These early studies lacked quantitative measurements of the observed attenuation/density changes and were limited to 2D observations. Both limitations are overcome by X-ray computed tomography (CT), in which radiographs obtained at many different angular positions are used to reconstruct a three-dimensional (3D) field of X-ray attenuation (closely related to mass density). First developed for medical imaging, X-ray CT is now widely used in material sciences, geosciences, and geomechanics—as attested by the GeoX series of International Workshops [2, 19, 28], now merged with the International Conference on Tomography of Materials and Structures (ICTMS—last held in Lund in 2017). The 3D images or fields coming from X-ray CT are composed of voxels (3D pixels) whose values can be interpreted as a mean local X-ray attenuation coefficient when the voxels are significantly larger than the grain size; alternatively, one can delineate individual grains when the voxels are significantly smaller than the grains. The 3D tomographic images provide unprecedented insight into the nature and complexity of bio-, hydro-, thermo-, chemo-, and mechanical processes taking place within a soil mass. Consequently, many laboratories around the world have been deploying this technology, either adapted from medical systems or specifically designed to address materials research, to learn about soils and soil processes. It is worth noting that besides laboratory scanners, there is also the possibility of using synchrotron facilities for X-ray imaging. These facilities provide a much more powerful source of X-rays allowing both fast scanning and high spatial resolution, as well as more advanced imaging techniques such as phase contrast tomography. Although synchrotron facilities are used in geomechanics applications, they are limited in number (about 40 worldwide), and access is also limited. The work discussed in this paper has all been performed on laboratory X-ray scanners—in particular two machines situated in Grenoble. The lower resolution *micro-focus* machine—soon to be 10 years old—is situated in Laboratoire 3SR. Technical details of this machine can be found in [4, 38]. Figure 1 presents a picture of a small-scale triaxial apparatus for sand installed in the scanner.
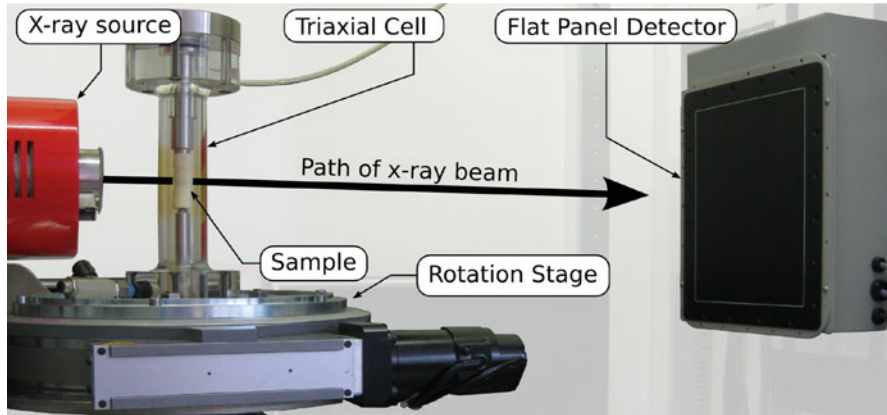
Fig. 1 Picture of the inside of the micro-focus X-ray tomograph in Laboratoire 3SR with a triaxial cell installed

2.1 X-Ray Tomography for Sand

For three-dimensional experimental micro-mechanics, X-ray tomography is perfect for sand, and sand is perfect for X-ray tomography for a number of reasons:

– standard lab X-ray sources generally produce an X-ray beam of an energy sufficient to penetrate silica particles without attenuation artefacts;
– standard micro-focus X-ray sources permit an effective spatial resolution sufficient to identify sand particles uniquely;
– the size of standard X-ray detectors is sufficient to image a mechanically representative collection of particles at this resolution;
– sand can be reasonably held in different quasi-static states allowing time to perform an X-ray scan.

X-ray tomography, first used to study a triaxial test on sand by Desrues et al. [17], is now routinely of sufficient spatial resolution to identify individual sand particles, and—when repeated during a test carried out *in-situ* within an imaging system— to follow them throughout a test see: [7, 22, 24]. The types of images that will be discussed in this paper are those of samples containing a sufficient number of grains to represent the mechanical behaviour at the macro-scale (which sets a lower bound on the field of view), but with identifiable grains (which sets an upper bound on the spatial resolution). Practically speaking, an intermediate scale with around 20 particles across the diameter of the specimen represents a reasonable trade-off between the very high resolution image of few particles (of an insufficient number to allow emergent phenomena to be studied) and the large field-of-view image of many more particles (but where grains cannot be identified).

2.2   Quantitative Analysis of Field Measurements

Analysing a Single Field

The result of an X-ray tomography scan is the reconstruction of a discretised 3D field of the lumped X-ray attenuation within the volume (hereafter referred to as "greyvalue"). The discretisation basis is small volume-elements—voxels—which have a given physical size (the misleadingly named 1D "pixel size" and often erroneously referred to as the resolution, which is a more slippery metrological concept). This physical size of the voxels with respect to the physical size of the grains defines the ambition that one can have when analysing X-ray tomographies of granular assemblies: with a few pixels across a grain diameter a mean density can be measured; tens of pixels across a grain diameter allow individual grains to be identified and measured, with hundreds of pixels across a diameter details of grain shape and composition can be obtained. Regardless of the pixel size, the 3D fields coming from each scan contain typically a more than 1000^3 voxels.

When there is sufficient resolution to identify individual grains, at the very first order, the solid phase can be separated from voids by establishing a threshold greyvalue, either set by modelling the greyvalue distribution in the reconstructed images or set in such a way to obtain the total solid volume measured, for example, at the end of a test. The discretised solid phase is then typically separated into individual particles based on geometrical arguments implemented, for example, in a morphology watershed, resulting in individually labelled 3D grains.

A labelled 3D image is the ideal starting point for all grain-based measurements: for example, each grain can be individually interrogated as a discrete and contiguous cloud of voxels, allowing, for example, for a grain-size distribution to be reconstructed, on the condition of having a well-defined "size" to measure, with a relative error in the order of the pixel size.

Comparing Fields

The non-destructive nature of X-ray tomography measurements means that repeated scans can be easily performed throughout a process (e.g., during mechanical loading). A sequence of scans calls for analysis taking advantage of the time dimension (loading) which complements the three dimensions of space. In the study of the mechanics of sand, the most desirable quantity is the local rearrangement of the material, for which Digital Image Correlation (DIC) can be used. DIC is a technique for measuring displacements between images which has its roots in stereophotogrammetry e.g., [12, 18]. Simply put, the principle of DIC is the matching of patterns in the measured field (in 2 or 3D). In carefully designed experimental conditions it is possible to reach accuracies well below the pixel size when appropriate image interpolation is used. It is out of the scope of this

paper to offer a through description of DIC—some outstanding contributions follow: [11, 33, 34], a recent summary paper of the application of DIC to geomechanics can be found in [23].

In 2D photographies—from which DIC is born—is generally possible to apply an optimal texture to the surface being studied, facilitating and improving the pattern matching. In 3D volumes this is not possible, and the natural texture of the material is necessarily used as the texture for correlation.

Given that sand—at the "meso" scale—is a material with a large natural density contrast (i.e., between pores and grains), digital image correlation is a perfectly suited tool for following "meso" scale rearrangements in X-ray tomography images. A Digital Image Analysis code has been developed in Grenoble [37] which is used for the "meso" scale analysis presented in the second part of this paper.

Grain Tracking

When the pixel size is sufficiently small that individual grains can be identified, two families of techniques exist for making measurements of kinematics on images of deforming granular materials. Either grain tracking can be implemented by labelling all images in a series and following grains thus yielding displacement or image correlation can be used at the grain level. It may seem that image correlation has few chances of working, since there is little texture *within* individual grains. However, grains have unique shapes, which can be leveraged to perform grain-based image correlation—see [22] for the first use of *discrete* image correlation on sand.

In the context of grain tracking, the splitting and labelling procedure is repeated for each imaged state, and since grains will not have the same unique number, labels are reconciled by tracking grains from increment to increment using a specifically developed technique called ID-Track [7]—this is essentially the grain tracking step. Following the displacements of the centre-of-mass of each grain over an increment yields a very precise evaluation of the displacement of the particle (with an error less than 0.1 pixels).

The measurement of rotations is more challenging: at this resolution grain shapes are not detailed enough for the long and short axes of the moment of inertia tensor to be stable. To overcome this, grain tracking has been hybridised with discrete DIC [6], where tracked grains are matched based on their images. An example of the complex steps of image manipulation required is illustrated in Fig. 2, where starting from an existing grain tracking, a discrete image correlation is performed for a pair of grains. Details can be found in [4].

This sort of grain-scale measurement can yield fine results—Fig. 3 presents an example illustrating that relatively small rotations can be detected, revealing patterns of rotating grains at different steps during a triaxial compression test. Please note that the results presented in this figure have not been obtained on Hostun sand (such results exist on Hostun sand of course), but rather on Caicos Ooids which is very rounded and often close to spherical and thus far more challenging for the accurate measurement of rotations—in the order of 2° accuracy.

Reference Configuration   Deformed Configuration
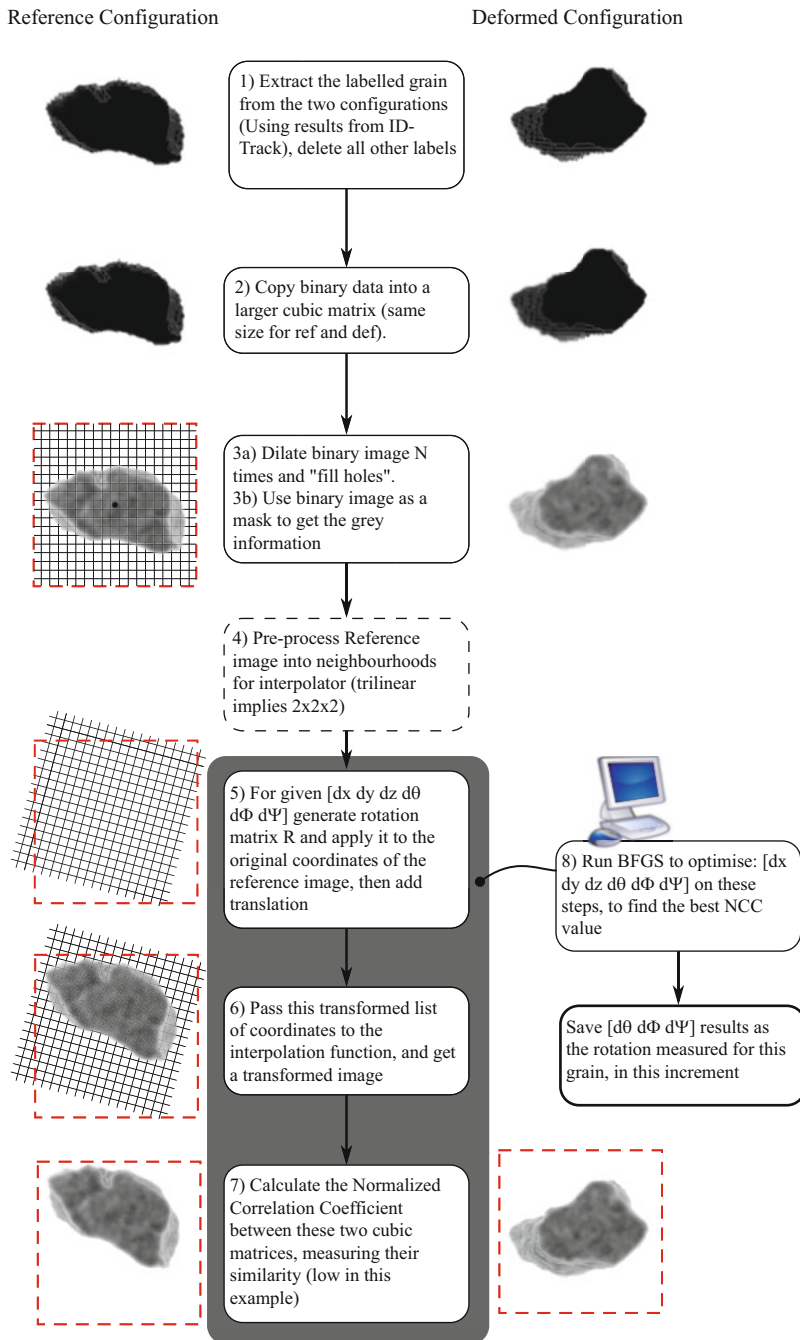
Fig. 2 Flow chart of the grain rotation measurement proposed in [6]
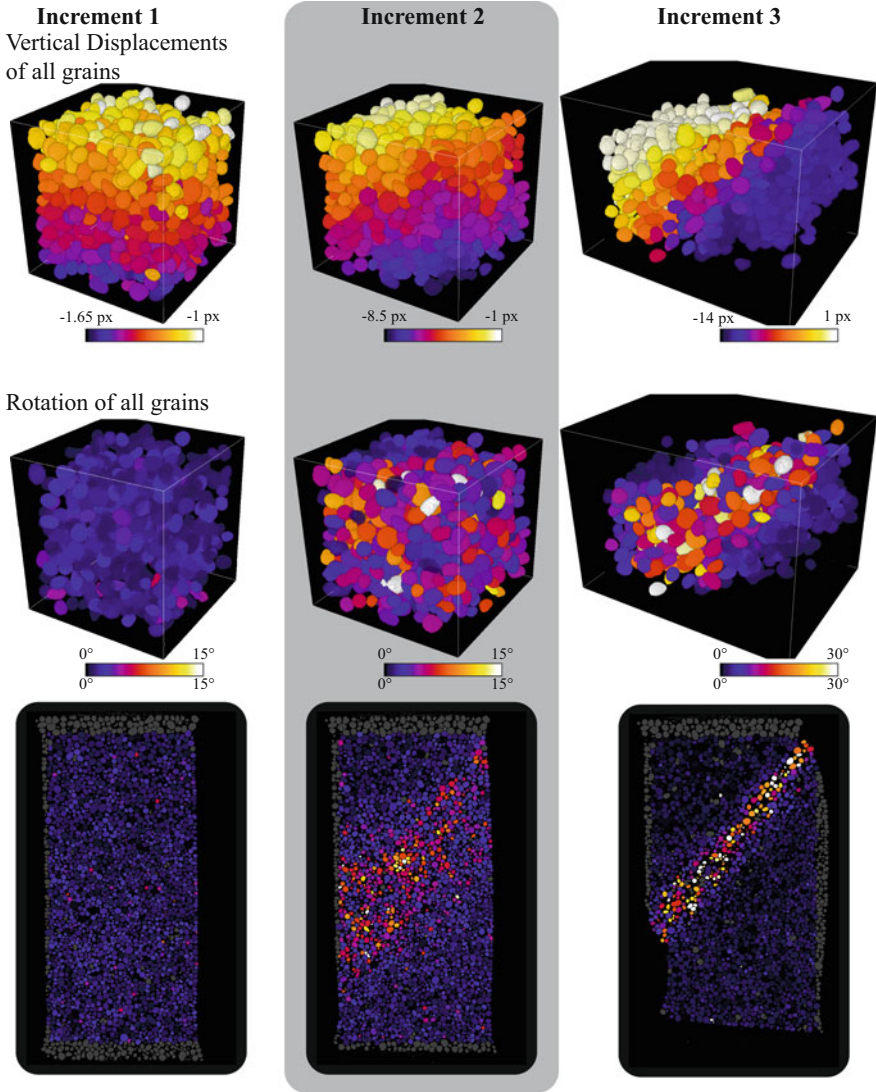
Fig. 3 3D kinematics (displacements and rotations) of individual grains in different increments (1: pre-preak, 2: around peak, 3: post-peak) of a triaxial compression test on Caicos Ooids (from [6])

3 What Do Micro-Mechanics Experiments Mean on Sand?

This section presents some very recent results and perspectives in the context of micro-to-macro—in short our take on what micro-mechanics experiments mean on sand.

The mechanical behaviour of sand is complex, despite it being a collection of relatively simple constituents—familiar sand grains. It is of obvious engineering interest to capture the mechanical response of sand to applied stresses and strains in continuum models that can be implemented in finite element simulations of geotechnical engineering problems. The averaging that is at the heart of developing a continuum model can at times be difficult to justify—the strain localisation that accompanies large strains is a perfect example of this. It is well known that localised shearing in bands depends strongly on the grain size, and thus is a clear manifestation of the micro-scale under macro-loading. Furthermore, and very importantly, the macro response of the so-called "unit" or "element" tests performed in soil mechanics laboratories (e.g., axisymmetric triaxial tests) is controlled by the emergence and evolution of this type of localised phenomenon.

The obvious manifestation of the grain scale motivates an ongoing experimental campaign using full-field measurements, to directly access processes at the grain scale. Specifically, X-ray tomography is perfectly suited to non-destructively accessing the grain scale in three dimensions in relatively small specimens of sand. Inherent in this type of imaging technique is a trade-off between the scanned volume (known as the field of view) and the size of the smallest object that can be detected. This means that depending on the scale at which the question is posed, different sample sizes will be necessary.

Figure 4 shows an example, over around two orders of magnitude of spatial resolution and field of view of how sand can be accessed using X-ray tomography. At the heart of the experiments that are discussed here, is the precious ability to be able to repeat X-ray scans at different stages of deformation. This in turn opens the possibility of finely assessing local displacements due to applied loads.

Experimentation at the different scales presented in Fig. 4 clearly allows different questions to be asked: from the details of grain shape, through the grain-scale
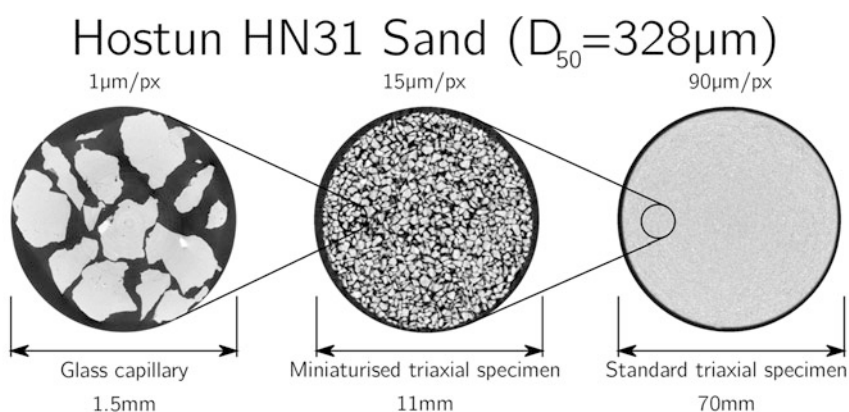
Fig. 4 Illustration of three scales of analysis on Hostun sand discussed in this paper—from [5]

kinematics of shear banding, to the structural effects of strain localisation in regular-sized triaxial tests ($\varphi = 70\,mm$) in sand.

Recent results from a long-term micro-scale investigation into the mechanical behaviour of sand using X-ray tomography will be presented at the different scales shown above. The section opens with very recent results on standard-sized specimens that are still sometimes naively taken as a constitutive response, i.e., the response of a material point. Investigation of localised strain in these standard conditions reveals an enormous extent of strain localisation occurring gradually from the early stages of the test.

The presence of these deformation structures motivates a mechanical study on smaller specimens where the reduced number of particles encourages the emergence of a single, simple localised failure mechanism in the specimen, and the reduced size allow individual grains to be observed in the experiment.

This "unit test" for a shear band appears to be a good candidate for micro-to-macro simulations, i.e., grain-scale simulations whose final objective is to recover a stress–strain (macro) response. In this sense, recent DEM simulations of our experiments, lead by Jose Andrade and his group in CalTech see: [26], are in our mind the first fully convincing micro-to-macro simulations on real sand. A few illustrative results from this study are commented, and some future paths are discussed.

Such a powerful tool that almost allows X-ray tomographies to directly yield mechanical responses requires initial states of granular assemblies to be described finely. To this end, recent work has also been focussing on the challenging measurement of *granular fabric*, which motivates an even closer look at the grains we study. Again, a few illustrative examples from collaborative work with Ivo Herle and Max Wiebicke in Dresden [40] are presented and discussed.

We conclude with a general discussion about current and future research directions at these different scales of interest for this apparently simple geomaterial, including a discussion on FEM × DEM double scale or "hierarchical" numerical approach.

3.1 Standard Scale Triaxial Tests

A campaign of standard-sized triaxial tests (70 mm diameter) with *in-situ* X-ray tomography has recently been performed in Grenoble on Hostun HN31 sand. In this work, presented in [14, 15], X-ray observations of the sample can detect the granular texture (without the ability—or the intention—to usefully identify individual grains). These X-ray images, when coupled with (3D) image correlation, allow incremental strain fields to be measured. Figure 5 shows views from different angles of an incremental deviatoric strain field measured far after the peak of the stress–strain response.

What is remarkable about such an *incremental* strain field is the fact that there is massive strain localisation arranged into a structure of intersecting bands, all

Incremental deviatoric strain
from scan 26 to scan 27

0 ▮▮▮▮▮▮▮▮ 20%

Zones with too much strain
to correlate successfully
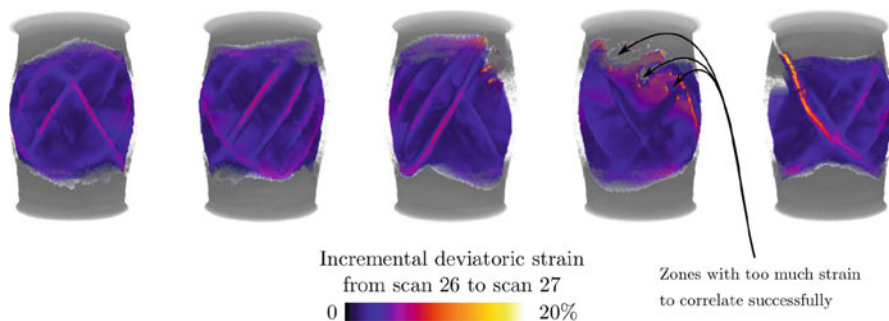
Fig. 5 Different angles from the 3D rendering of the incremental deviatoric strain field over a 1.5% axial shortening of the specimen (starting from 18% shortening (i.e., far after the stress peak). This field is overlaid onto the X-ray field of the sample. Sample initial diameter = 70 mm, initial height = 140 mm. Adapted from [15]

of which are still concurrently active so late in the test. This observation in itself is not that surprising—since after the failure of the specimen, localised strains are expected. However, our measurement tools allow the investigation of the development of this structure of bands, which has its roots well before the stress peak. A video accompanying the paper[1] illustrates fields of early strain increments indicating an early emergence of the structure visible in Fig. 5. This early emergence in turn indicates that this sort of experiment is not a unit-test—meaning that in the context of sand-grain-scale micro-to-macro, this scale of analysis will be abandoned in favour of a smaller granular system.

4   Micro-Scale Triaxial Tests

Due to spatial resolution and field-of-view trade offs inherent in X-ray tomography, the choice of a smaller granular system means that grain-scale deformation phenomena can be studied at higher resolution, meaning that individual grains can be identified and followed through space and time. Based on the size of the shear bands seen at the large scale, the reduced sample size is chosen as 11 mm diameter and 22 mm height. The fewer degrees of freedom in the granular system means that the emergence of a single shear band—what appears to be a unit deformation mechanism in this material—can be studied in detail. Figure 6 shows the sort of grain-scale measurements that are now routine, as discussed in [6, 7, 16]. What is immediately striking is how well the measured incremental grain rotations pick up the shear band once the sample has failed. This zone corresponds, in space, with the local deviatoric strain field (which is itself calculated from measured grain

---

[1] https://doi.org/10.13140/RG.2.2.15390.02880.
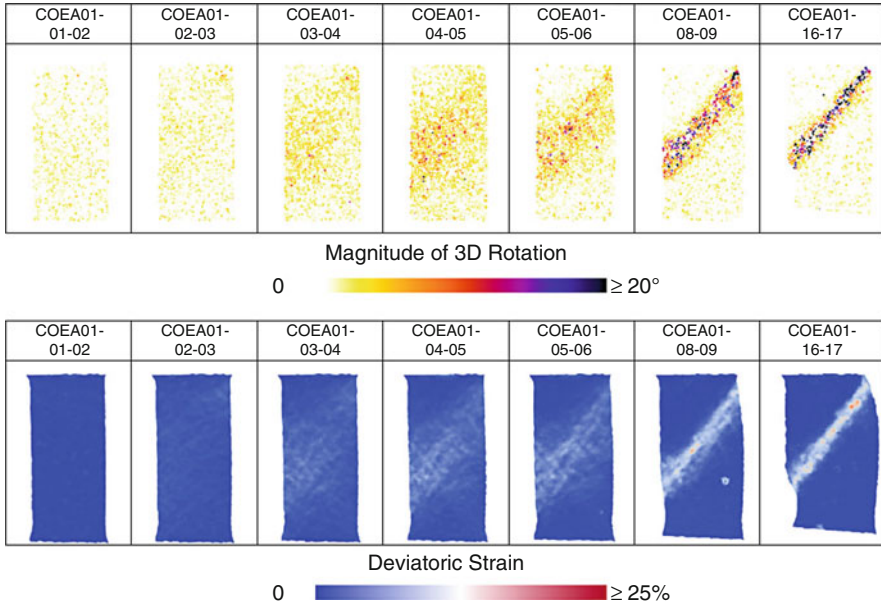
Fig. 6 Incremental grain rotations and incremental deviatoric strain illustrated in vertical slices for a triaxial test on Caicos Ooids—similar results exist on Hostun sand

displacements). Again at this scale, a progressive emergence of the band is visible, without the complications of the emergence of multiple bands. As the sample is sheared, strains become increasingly concentrated into the mature shear band that is visible by the end of the test.

Experiments at this scale appear to be ideal to attempt a particularly radical version of the "micro-to-macro" modelling approach—the explicit simulation of the experiment, with each grain individually described starting from the X-ray tomography of the initial state of the experiment—because of the ability to describe individual grains as well as the "simplicity" of the failure mechanism. This sort of micro-to-macro approach is radical in the sense that is takes practically no shortcuts—a sufficiently good description of the micro-scale with sufficient degrees of freedom is expected exhibit all the complexity we know well when considering sand as a continuous medium. The ambitious modelling work lead by Jose Andrade and his group in CalTech [26] is in our opinion one of the most successful examples of micro-to-macro in the sense of pure micro-scale simulation to predict macro- (and meso-) scale mechanical responses. Figure 7a illustrates the micro-scale input into the Level Set Discrete Element Model (LS-DEM) described above—which is built *directly* from the initial X-ray tomography image of the experiment shown in Fig. 6.

By exactly reproducing the actual experimental conditions *in-silico* such as the behaviour of the membrane and the details of load application (e.g., the initial
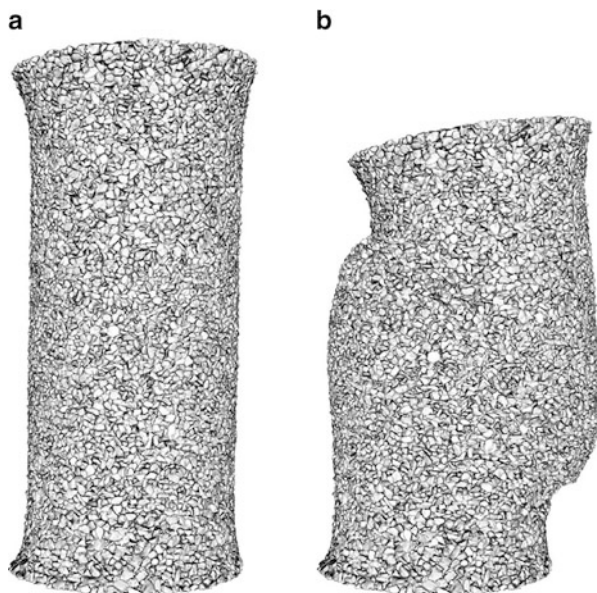
Fig. 7 3D rendering of LS-DEM samples from [26]. On the left sample inter isotropic stress of 100 kPa, on the right after 15% axial shortening

state and degrees of freedom of the mobile loading platen) a DEM simulation is performed on a digital "avatar" of the sample HNEA01 tested in Grenoble. Figure 7b is the *numerically* deformed specimen, after 15% axial shortening, where a single shear band is visible, which essentially coincides with the one emerging during in the experiment.

More importantly, not only is the final state remarkably similar to the one obtained in the experiment, but also the mechanism of emergence of the single shear band appears to be the same: Fig. 8 shows incremental grain rotations in a vertical slice from both the experiment and the simulation gradually concentrating with excellent correspondence. Not less importantly, the "macro" (stress–strain) response of the experiment and the simulation are also very similar: Fig. 9 presents the axial stress normalised by the confinement and the volumetric strain both plotted against the axial strain.

This numerical simulation appears to have captured a number of important features of granular plasticity in a real sand with thanks to the explicit description of grain shapes. Taken as a strong—if not perfect—numerical reference for this material, three clear paths emerge for the future use and development of such numerical tools:

1. **Validating the granular model on new stress paths that can be accessed experimentally** with X-ray tomography in order to further improve confidence in the use of this numerical model as a proxy for the mechanical behaviour of Hostun sand.
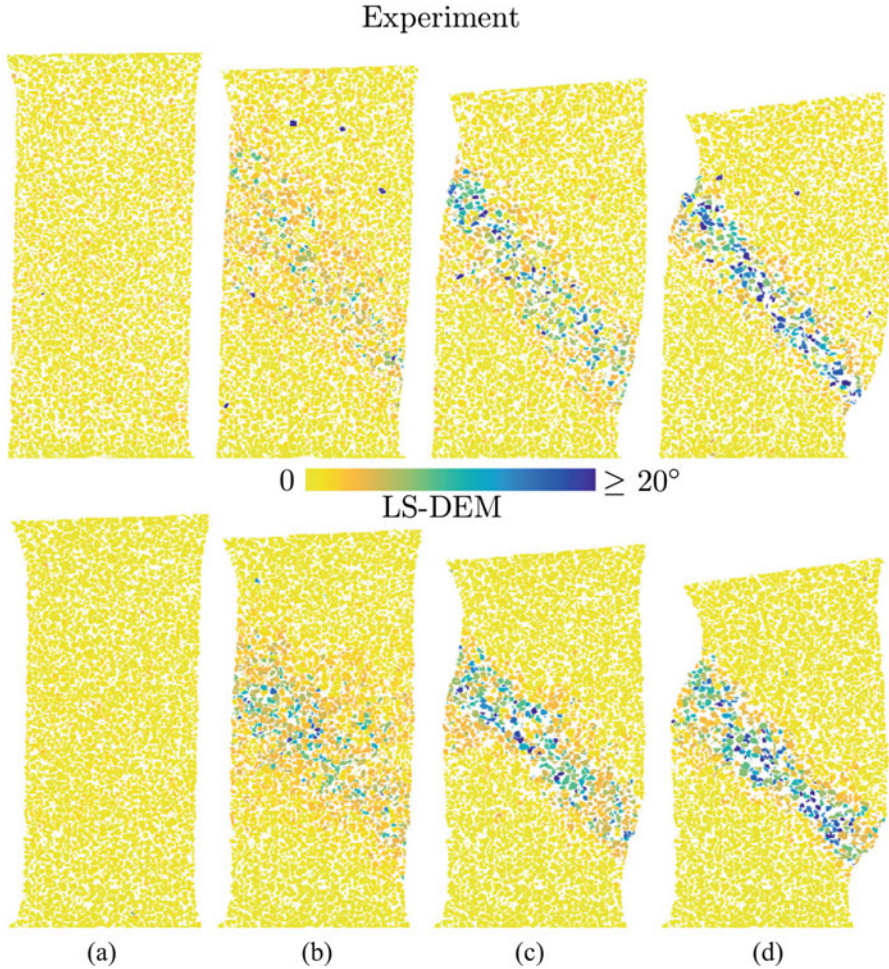
Fig. 8 Vertical slices showing the angle of grain rotation (rotation axis not shown) for both experiments (top) where measurements are made with digital image correlation and (bottom) for LS-DEM simulation. Figure from [26]

An immediate candidate for this is the work of Erminio Salvatore—see [31] for example—where a small sand sample is yielded progressively, alternating triaxial extension and compression. Figure 10 shows a number of incremental full-field results at the end of such a test, at the fourth load reversal—the stress state is initially triaxial compression (state 14) and then becomes triaxial extension (15 onwards). The top row of images shows vertical slices through the incremental deviatoric strain field between states, whereas the bottom row shows incremental grain rotations projected onto this plane with clockwise and anticlockwise (positive and negative) components. The increment marked
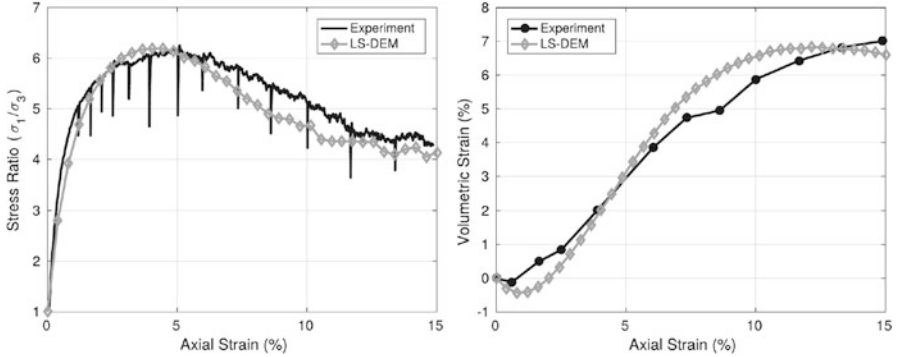
Fig. 9 Axial strain vs. (left) stress ratio and (right) volumetric strain for experiment and LS-DEM simulation from [26]
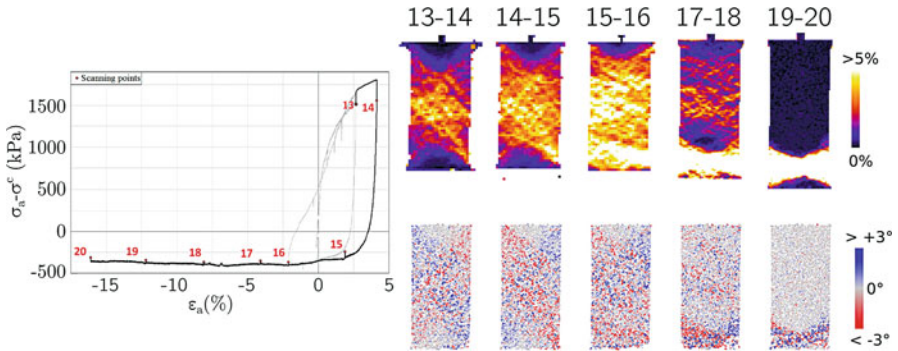
Fig. 10 Left: stress deviator vs. axial strain. Right: vertical slices through incremental deviatoric strain field (top) and incremental grain rotations projected onto the slice (bottom). Adapted from [9]

13–14 shows an increment in triaxial compression, where compression-like deformation mechanisms around the friction cones are visible at the top of the specimen with positive rotations to the left and negative rotations to the right. In unloading towards extension (14–15) this mechanism reverses in sign, but what is remarkable is that this reversed mechanism persists, for two "unloading" steps (i.e., 6% axial extension)—which is naively unexpected given the stress state is not on the yield surface. The necking extension-like mechanism then starts to emerge and eventually causes the specimen to fail. The prediction of this sort of behaviour—even simply at the macro stress–strain level—remains a challenge for many phenomenological models.

2. **Exploring stress paths** with this granular model that are difficult or challenging in reality.

   More specifically, of particular interest is stress-probing where the response of the material is measured (starting from the same state) on a number of

different stress increments in different directions in the stress space. Very few experimental investigations of this type have been carried out (see: [3, 30]—the latter being on Hostun sand) no doubt due to the significant experimental complexity of stress control, small strain measurements as well as the production of extremely repeatable (nominally identical) samples.

In the spirit of [13, 35] stress-probing can be conducted numerically with DEM, allowing a number of valuable insights into the mechanical behaviour of a simulated Hostun sand—both at the micro- and macro-scale. Given the significantly better representation of Hostun sand now available with LS-DEM, this is a path to be probed.

3. **Generalising the tool: from a specimen to the material.** This final, but crucial point refers to the fact that so far with LS-DEM, existing granular systems have been simulated directly starting from one given scanned assembly.

Since it is difficult to recover *undisturbed* specimens of sand from a site, an elegant use of LS-DEM is to study the mechanical responses of different possible granular configurations for recovered material—directly exploring the effects of microstructural variability such as the depositional anisotropy. In order to validate such a tool, carefully controlled initial states must be described experimentally, and compared to predictions from LS-DEM. Preparing different numerical specimens given some known grain shapes is not expected to be a major hurdle, the key point will be in choosing the salient descriptors for different granular configurations, what is commonly referred to as granular fabric, which will be discussed in the next section.

4.1 Zooming Further into Granular Fabric

In X-ray tomography, the identification of individual sand particles—given sufficient resolution—is relatively easy. This means that the measurement of properties attached to sand grains is possible. However, the mechanical behaviour of a granular assembly depends not only on the size and shape of grains, but also crucially on their arrangement—the combination of which is generally known as micro-structure. From a measurement point of view, the direct measurement of the most crucial details of the granular arrangement, i.e., interparticle contact positions and orientations is extremely difficult for the simple reason that an interparticle contact is not a separate measurable entity. Recent work with Ivo Herle and Max Wiebicke in TU Dresden and Yannis Dafalias' group in NTUA on the experimental measurement of granular fabric has highlighted a number of challenges—as discussed in [5]—in making this measurement at this scale.

Andò et al. [8], Wiebicke et al. [40] offers a recent example of the sort of metrological work required to understand and improve measurements of fabric on images from X-ray tomography, the upshot of which is that even given considerable effort, the measurement remains challenging. Given the fundamental importance of this measurement, it is essential to have an appreciation of the error being
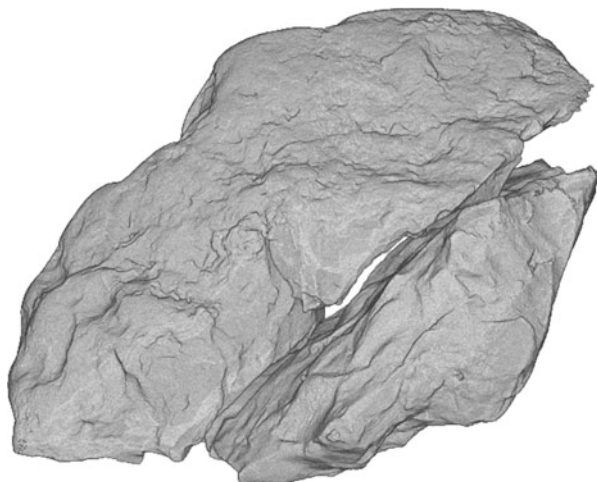
Fig. 11 3D rendering of two Hostun HN31 sand grains in contact from X-ray tomographies at 1 μm pixel size (to be compared to the 15 μm of the experiments discussed above). Figure from [40]

made, and in what cases the error is tolerable. When making measurement on spherical particles, a relatively clear assessment of the errors can be made using the tool developed in [36] to generate artificial images used as ground truths. The classification of these errors is possible due to the fact that only one type of contact topology exists between spherical particles.

When studying a natural sand like Hostun HN31, every particle is unique and no ground truth can be established to study measurement error at the scale of the experiments discussed in the previous section. Some inroads can be made into this problem by getting "golden standards", i.e., much higher resolution images of the same particles, which can be used to gain insight into the errors made at the scale of the experiments—see Fig. 11, which presents a clear example of the sort of complex contact topology routinely encountered in this material. The study of errors in the measurement of contacts between natural sand grains shows that the errors made depends strongly on contact topology [40], however, taking this information into account allows measurements to be improved to the point where they can be used to track fabric evolution with confidence. A striking example of this is the ability to distinguish granular fabric evolution in and out of a shear band—see the contribution by Wiebicke et al. in this volume, building on results presented in [41].

Ongoing work aims to continue to improve the quality of measurements made to the point of being able to explain the drastic changes in stiffness associated to load reversal, where strains are negligible.

5 Conclusion

This paper has presented the results from a long-standing (and ongoing) micro-mechanical study of Hostun HN31 sand. In this study, X-ray tomography has been used extensively to make measurements in the spatial domain—taking advantage of the different spatial scales that can be accessed with such a tool. Given such freedom, choosing the scale of analysis is key—the study of the micro-mechanics of sand therefore requires *representative* granular mechanisms to be identified and investigated.

The analysis of the evolving strain field in triaxial compression on standard-sized samples reveals complex, localised deformation mechanisms starting early in the test. This means that to isolate elementary deformation mechanisms, the size of the granular system to be studied must be smaller—taking inspiration from the mechanisms seen at the large(r) scale. This gives the added advantage of higher spatial resolution with the use of standard X-ray tomography techniques, allowing for true grain-scale measurements.

Results from a mature investigation on smaller samples clearly show that grain-scale measurements are indeed possible, and that elementary deformation mechanisms can indeed be isolated and studied at the grain level. A major limitation in the measurements possible at this scale remains that they are restricted to kinematics only, i.e., no intergranular forces are measured, which are required for a complete understanding of the micro-mechanics of sand. This is one key motivation for a recent, straightforward micro-to-macro approach: a DEM simulation that explicitly represents tens of thousands of irregular sand grains starting from an X-ray tomography image of a tested sample. The careful application of the loading experienced by the real specimen results in the development of a remarkably similar deformation mechanism in the numerical sample—allowing intergranular forces to be studied by proxy. Taken as a strong—if not perfect—numerical "avatar" for this Hostun sand, LS-DEM can be developed in different directions as discussed in the paper, including validation on stress reversal and the study of the directional response of sand (stress-probing).

A further key micro-to-macro perspective is to adapt such powerfully predictive (but computationally expensive) discrete models for direct use as a replacement for a constitutive law in FEM × DEM approaches (e.g., [20, 21, 27, 32]), by simplifying the assembly studied to its most salient details.

The future for micro-to-macro on sand is to pursue other key grain-scale deformation mechanisms in sand, such as breakage [1, 25] and creep [10] to name just two.

References

1. Alikarami, R., Andò, E., Gkiousas-Kapnisis, M., Torabi, A., and Viggiani, G. (2015), "Strain localisation and grain breakage in sand under shearing at high mean stress: insights from in situ X-ray tomography", in: *Acta Geotechnica*, Vol. 10, No. 1, pp. 15–30.

2. Alshibli, K. A. and Reed, A. H. (2012), *Advances in computed tomography for geomaterials: GeoX 2010*, John Wiley & Sons.

3. Anandarajah, A., Sobhan, K., and Kuganenthira, N. (1995), "Incremental stress-strain behavior of granular soil", in: *Journal of geotechnical engineering*, Vol. 121, No. 1, pp. 57–68.

4. Andò, E. (2013), "Experimental investigation of micro-structural changes in deforming granular media using x-ray tomography", PhD thesis, Université de Grenoble.

5. Andò, E., Dijkstra, J., Roubin, E., Dano, C., and Boller, E. (2018), "A peek into the origins of creep in sand", in: *Granular Matter*. Vol. 21, p. 11.

6. Andò, E., Hall, S. A., Viggiani, G., Desrues, J., and Bésuelle, P. (2012a), "Experimental micromechanics: grain-scale observation of sand deformation", in: *Géotechnique Letters*, Vol. 2, No. 3, pp. 107–112.

7. Andò, E., Hall, S. A., Viggiani, G., Desrues, J., and Bésuelle, P. (2012b), "Grain-scale experimental investigation of localised deformation in sand: a discrete particle tracking approach", in: *Acta Geotechnica*, Vol. 7, No. 1, pp. 1–13.

8. Andò, E., Hall, S., Viggiani, G., and Desrues, J. (2013), "Experimental micro-mechanics of granular media studied by x-ray tomography: recent results and challenges", in: *Géotechnique Letters*, Vol. 3, pp. 142–146.

9. Andò, E., Salvatore, E., Desrues, J., Charrier, P., Toni, J.-B., Modoni, G., and Viggiani, G. (2017), "Strain Localisation in Sand in Cycles of Triaxial Compression and Extension: Continuum and Grain-Scale Analysis", in: *International Workshop on Bifurcation and Degradation in Geomaterials*, Springer, pp. 489–497.

10. Tengattini, Alessandro, Andò, E., and Viggiani, C. 3D Metrology in Geomaterials. Presented at the 19th Hercules Specialized Course in Quantitative Imaging using X-rays and Neutrons, University of Grenoble, Grenoble, France, 15–19 May 2017.

11. Bay, B. K. (2008), "Methods and applications of digital volume correlation", in: *The Journal of Strain Analysis for Engineering Design*, Vol. 43, No. 8, pp. 745–760.

12. Butterfield, R., Harkness, R. M., and Andrews, K. Z. (1970), "A stereo-photogrammetric technique for measuring displacement fields", in: *Géotechnique*, Vol. 20, No. 3, pp. 308–314.

13. Calvetti, F., Viggiani, G., and Tamagnini, C. (2002), "A numerical investigation of the incremental behavior of granular soils", in: *Rivista Italiana di Geotecnica*, Vol. 3/03, pp. 1–29.

14. Desrues, J., Andò, E., Bèsuelle, P., Viggiani, G., Debove, L., Charrier, P., and Toni, J. (2017), "Localisation Precursors in Geomaterials?", in: *International Workshop on Bifurcation and Degradation in Geomaterials*, Springer, pp. 3–10.

15. Desrues, J., Mevoli, F., Viggiani, G., Andò, E., and Debove, L. (2018), "How does strain localise in standard triaxial tests on sand: revisiting the mechanism 20 years later", in: *Mechanics Research Communications*, Vol. 92, pp. 142–146.

16. Desrues, J. and Andò, E. (2015), "Strain localisation in granular media", in: Comptes Rendus Physique, Vol. 16, No. 1, pp. 26–36.

17. Desrues, J., Chambon, R., Mokni, M., and Mazerolle, F. (1996), "Void ratio evolution inside shear bands in triaxial sand specimens studied by computed tomography", in: *Géotechnique*, Vol. 46, No. 3, pp. 529–546.

18. Desrues, J. and Viggiani, G. (2004), "Strain localization in sand: an overview of the experimental results obtained in Grenoble using stereophotogrammetry", in: *International Journal for Numerical and Analytical Methods in Geomechanics*, Vol. 28, pp. 279–321.

19. Desrues, J., Viggiani, G., and Besuelle, P. (2010), *Advances in X-ray Tomography for Geomaterials*, vol. 118, John Wiley & Sons.

20. Guo, N. and Zhao, J. (2014), "A coupled FEM/DEM approach for hierarchical multiscale modelling of granular media", in: *International Journal for Numerical Methods in Engineering*, Vol. 99, No. 11, pp. 789–818.

21. Guo, N. and Zhao, J. (2016), "Multiscale insights into classical geomechanics problems", in: *International Journal for Numerical and Analytical Methods in Geomechanics*, Vol. 40, No. 3, pp. 367–390.

22. Hall, S., Bornert, M., Desrues, J., Pannier, Y., Lenoir, N., Viggiani, G., and Besuelle, P. (2010), Ą"Discrete and continuum experimental study of localised deformation in Hostun sand under triaxial compression using X-ray μCT and 3D digital image correlation", in: Géotechnique, Vol. 60, No. 5, pp. 315–322.

23. Hall, S. A. (2012), "Digital image correlation in experimental geomechanics", in: *ALERT Geomaterials Doctoral Summer School*, pp. 69–102.

24. Hasan, A. and Alshibli, K. (2012), "Three dimensional fabric evolution of sheared sand", in: *Granular Matter*, Vol. 14, No. 4, pp. 469–482.

25. Karatza, Z., Andò, E., Papanicolopulos, S.-A., Ooi, J., and Viggiani, G. (2017), "Evolution of deformation and breakage in sand studied using X-ray tomography", in: *Géotechnique*, pp. 1–11.

26. Kawamoto, R., Andò, E., Viggiani, G., and Andrade, J. E. (2018), "All you need is shape: predicting shear banding in sand with LS-DEM", in: *Journal of the Mechanics and Physics of Solids*, Vol. 111, pp. 375–392.

27. Nitka, M., Combe, G., Dascalu, C., and Desrues, J. (2011), "Two-scale modeling of granular materials: a DEM-FEM approach", in: *Granular Matter*, Vol. 13, No. 3, pp. 277–281.

28. Otani, J. and Obara, Y. (2004), "X-Ray CT for geomaterials: Soils, concrete, rocks", in: *Proceedings of the International Workshop on X-Ray CT for Geomaterials: GEOX2003, Kimamoto, Japan, Royal Swets and Zeitlinger: Lisse*.

29. Roscoe, K. H. (1970), "The influence of strains in soil mechanics", in: *Geotechnique*, Vol. 20, No. 2, pp. 129–170.

30. Royis, P. and Doanh, T. (1998), "Theoretical analysis of strain response envelopes using incrementally non-linear constitutive equations", in: *International journal for numerical and analytical methods in geomechanics*, Vol. 22, No. 2, pp. 97–132.

31. Salvatore, E., Andò, E., Modoni, G., and Viggiani, G. (2016), "Micromechanical Study of Cyclically Loaded Sands with x-ray Microtomography and Digital Image Correlation", in: *Procedia Engineering*, Vol. 158, pp. 92–97.

32. Shahin, G., Desrues, J., Dal Pont, S., Combe, G., and Argilaga, A. (2016), "A study of the influence of REV variability in double-scale FEM× DEM analysis", in: *International Journal for Numerical Methods in Engineering*, Vol. 107, No. 10, pp. 882–900.

33. Smith, T., Bay, B., and Rashid, M. (2002), "Digital Volume Correlation Including Rotational Degrees of Freedom during Minimization", in: *Experimental Mechanics*, Vol. 42, No. 3, pp. 272–278.

34. Sutton, M. A., Orteu, J. J., and Schreier, H. (2009), *Image correlation for shape, motion and deformation measurements: basic concepts, theory and applications*, Springer Science & Business Media.

35. Tamagnini, C., Calvetti, F., and Viggiani, G. (2005), "An assessment of plasticity theories for modeling the incrementally nonlinear behavior of granular soils", in: *Journal of Engineering Mathematics*, Vol. 52, No. 1, pp. 265–291.

36. Tengattini, A. and Andò, E. (2015), "Kalisphera: an analytical tool to reproduce the partial volume effect of spheres imaged in 3D", in: *Measurement Science and Technology*, Vol. 26, No. 9, p. 095606.

37. Tudisco, E., Andò, E., Cailletaud, R., and Hall, S. A. (2017), "TomoWarp2: a local digital volume correlation code", in: *SoftwareX*, Vol. 6, pp. 267–270.

38. Viggiani, G., Andò, E., Takano, D., and Santamarina, J. (2015), "Laboratory X-ray tomography: A valuable experimental tool for revealing processes in soils", in: *Geotechnical Testing Journal*, Vol. 38, No. 1, pp. 61–71.

39. Viggiani, G. and Hall, S. A. (2012), "Full-field measurements in experimental geomechanics: historical perspective, current trends and recent results", in: *ALERT Doctoral School*, pp. 3–68.

40. Wiebicke, M., Andò, E., Herle, I., and Viggiani, C. (2017a), "On the metrology of interparticle contacts in sand from x-ray tomography images", in: *Measurement Science and Technology*.

41. Wiebicke, M., Andò, E., Salvatore, E., Viggiani, G., and Herle, I. (2017b), "Experimental measurement of granular fabric and its evolution under shearing", in: *EPJ Web of Conferences*, vol. 140, EDP Sciences, p. 02020.

Dense, Inhomogeneous, Granular Shearing

Diego Berzi and James T. Jenkins

Abstract We make use of recent extensions of kinetic theory for dense, dissipative shearing flows to phrase and solve boundary-value problems for steady flows of a dense aggregate of identical frictional spheres sheared in a gravitational field between horizontal, rigid, bumpy boundaries by the upper boundary or in the absence of gravity between two coaxial, bumpy cylinders by the inner cylinder. In both scenarios, the resulting flow consists of a region of rapid, collisional flow and a denser region of slower flow in which more enduring particle contacts play a role. In the denser region, or bed, we assume that the collisional production of energy is negligible and the anisotropy of the contact forces influences the shear stress and the pressure in the same way. We show profiles of average velocity and provide relationships between the thickness of the fast flow, the gravitational acceleration (if present), the velocity of the moving boundary, the shear stress and the confining pressure.

Keywords Granular flow · Kinetic theory

1 Introduction

It is widely believed that kinetic theory of granular gases [1, 2] is the correct framework to model dilute granular flows, but fails in dealing with dense situations. This belief rests on the assumptions that, in dense granular flows, the particle interactions are no longer uncorrelated, binary and nearly instantaneous, the particle surface friction plays a dominant role and the particle velocity fluctuations—measured by the granular temperature [3], one-third of the mean square of the

D. Berzi (✉)
Politecnico di Milano, Milano, Italy
e-mail: diego.berzi@polimi.it
http://intranet.dica.polimi.it/people/berzi-diego/

J. T. Jenkins
Cornell University, Ithaca, NY, USA

fluctuation velocity of the particles, a key ingredient of kinetic theory—are no longer meaningful.

Over the last 15 years, a phenomenological approach to dense granular flows [4] acquired vast popularity. It is based on an empirical, local relation (the so-called μ-I rheology) between the particle shear stress, pressure and shear rate which depends upon dimensional arguments and ignores the role of velocity fluctuations. It has been shown to work in many flow configurations (e.g., simple shearing [5], inclined heap flows [6]), although, more recently, it has become apparent that it fails in situations dominated by the boundaries (thin flows over rigid beds [7]) and in regions where the ratio of the particle shear stress to the particle pressure is less than a yield [8] (granular beds). To repair this, Kamrin and coworkers [9] have proposed the introduction of a new state variable, the granular fluidity, and an evolution equation for it that contains a diffusive-like term, which permits nonlocal effects to be treated. A recently revealed relation between the fluidity and the velocity fluctuations [10] suggests that Kamrin's nonlocal rheology and the kinetic theory of granular gases can be reconciled.

Kinetic theory of granular gases has been extended in significant ways over the last 20 years to make it applicable to dense granular flows. A length scale has been introduced in the constitutive relation for the rate at which fluctuation kinetic energy is dissipated in collisions [11–13]; this accounts for the velocity correlation that develops at solid volume fraction larger than the freezing point [14–16]. The transformation of translational kinetic energy into rotational kinetic energy associated with particle surface friction has been modelled by introducing an effective coefficient of collisional restitution [17, 18]. Moreover, the role of friction in determining the maximum volume fraction at which a random assembly of rigid spheres can be sheared is now understood [19]. Finally, the possibility of non-instantaneous collisions and the development of rate-independent components of the stresses associated with finite particle stiffness have been incorporated in the theory [20].

Experiments [21] and numerical simulations [8, 22] have shown that velocity decays exponentially inside granular beds at the bottom of shearing flows. In the search for boundary conditions for the differential equations of kinetic theory that govern granular shearing, Jenkins and Askari [23] have suggested that in the bed, the working of the shear stress can be ignored; so that in steady, fully developed flows, the diffusion of fluctuation energy of the particles exactly balances its rate of collisional dissipation. This balance results in exponentially decaying profiles of the granular temperature.

Recently, we have employed an extended kinetic theory for dense granular gases to determine profiles of average velocity, solid volume fraction and temperature for granular flows in a Couette cell [20, 24]. In that case, the granular material was sheared by the motion of a bumpy, rigid boundary in the absence of gravity. We assumed that a granular bed was present at a distance from the moving boundary, and showed how the exponential decay of the granular temperature predicted by Jenkins and Askari [23] determined the exponential decay of the average particle velocity.

Here, we use extended kinetic theory to determine features of the inhomogeneous flow of identical spheres sheared between two parallel, bumpy planes, one moving at constant velocity and one at rest, when gravity acts perpendicular to the planes. We first determine the influence of the velocity of the moving plane and gravity on the flow and show that our results are in agreement with experiments [25] in which a slider was pulled at constant velocity on the top of a granular layer composed of glass spheres. We then apply the theory to the annular shearing between two coaxial cylinders in the absence of gravity, with the inner cylinder rotating at constant angular velocity, while the outer cylinder is at rest. In this case, it is the centrifugal force which breaks the symmetry of the problem and induces inhomogeneity. We show that our predictions are in qualitative agreement with numerical simulations on disks [8].

2 Planar Granular Shearing with Gravity

Identical spheres of mass density ρ_p and diameter d are sheared between two parallel planes, with the upper plane moving at constant velocity, in the presence of gravity. The two planes are made bumpy by gluing a layer of spheres, identical to those of the flow, in a regular, hexagonal fashion. The bumpiness ψ of the planes is determined by the mean interparticle distance between the glued grains [26]. We take x and y to be the directions parallel and perpendicular to the planes, respectively, with the y-axis pointing upward. The only non-zero component of the average particle velocity is the x-component, u; while ν is the solid volume fraction. The distance, h, between the planes, the velocity, V, of the upper plane and the gravity, g, are the control variables of the system. The flow configuration is depicted in Fig. 1.

Fig. 1 Sketch of the planar shearing in the presence of gravity with the frame of reference
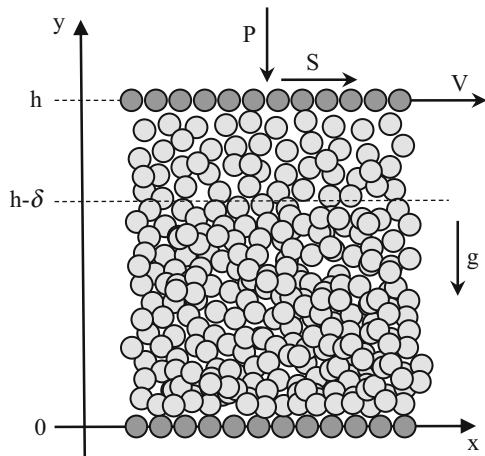
We focus on dense situations, in which the dependence of the solid volume fraction on the y-coordinate can be neglected and the y-momentum balance integrated to provide the following distribution of particle pressure:

$$p = P + 0.6\rho_p g(h - y), \tag{1}$$

where P is the pressure at the moving plane and 0.6 is, roughly, the depth-averaged solid volume fraction. When the pressure gradient along the x-direction is negligible, the x-momentum balance indicates that the particle shear stress s is uniform and equal to its value, S, at the moving plane. As observed in the simulations, the flow domain can, in general, be divided into two sub-regions: a region of fast flow, adjacent to the moving boundary of thickness δ and a region of slow flow, of thickness $h - \delta$ (Fig. 1). Koval et al. [8] distinguished between the two regions by whether the local value of the stress ratio s/p was greater or less than its minimum (yield) value in simple shearing. Here, we identify the fast and slow flows as those in which the solid volume fractions are, respectively, less than and greater than the largest value, ν_E, for which the aggregate can be sheared without expanding.

2.1 Fast Flow

In the fast flow, we use the constitutive relations for the pressure and the shear stress of kinetic theory [2] in the dense limit [19],

$$p = \rho_p 2(1 + e)\nu^2 g_0 T; \tag{2}$$

and

$$S = \rho_p d \frac{8J\nu^2 g_0}{5\pi^{1/2}} T^{1/2} u', \tag{3}$$

where e is the coefficient of normal restitution (the negative of the ratio of pre- to post-collisional relative velocity along the line of centres of two colliding grains); g_0 is the radial distribution function at contact, here taken to be the dense limit of a fit to the results of numerical simulations of simple shearing [19], $g_0 = 2/(\nu_c - \nu)$, for e less than 0.95, where ν_c is critical volume fraction whose value depends on particle friction [27]; T is the granular temperature; and $J = (1 + e)/2 + \pi(1 + e)^2(3e - 1)/[96 - 24(1 - e)^2 - 20(1 - e^2)]$. Here, and in what follows, a prime indicates a derivative with respect to y.

The fluctuation energy balance is

$$Q' = su' - \Gamma, \tag{4}$$

where Q is the flux of fluctuation energy:

$$Q = -\rho_p d \frac{4M v^2 g_0}{\pi^{1/2}} T^{1/2} T', \tag{5}$$

with $M = (1+e)/2 + 9\pi(1+e)^2(2e-1)/[128 - 56(1-e)]$; and Γ is the collisional rate of dissipation:

$$\Gamma = \rho_p \frac{12\left(1 - \epsilon^2\right) v^2 g_0}{\pi^{1/2} L} T^{3/2}, \tag{6}$$

where ϵ is an effective coefficient of restitution that incorporates rolling and sliding [18]. The quantity L in (6) is the correlation length of extended kinetic theory [12, 28] that accounts for the failure of molecular chaos at volume fractions larger than 0.49. Here, as in [13], we employ

$$L = \left[\frac{4J}{15\left(1 - \epsilon^2\right)}\right]^{1/2} \left[1 + \frac{26\left(1 - \epsilon\right)}{15} \frac{v - 0.49}{0.64 - v}\right]^{3/2} \frac{d^2 u'}{T^{1/2}}. \tag{7}$$

We now make lengths dimensionless by d, velocities by $(P/\rho_p)^{1/2}$, stresses by P, and energy flux by $(P^3/\rho_p)^{1/2}$. Then, the dimensionless forms of the upper plate velocity and gravity are $V\rho_p^{1/2}/P^{1/2}$ and $g\rho_p d/P$, respectively. For simplicity, in what follows, we employ the same notation, even if we refer to dimensionless quantities.

We take the derivative of (2) with respect to y, and use (1) and (5) to obtain a differential equation for the solid volume fraction [28]:

$$v' = \frac{\pi^{1/2} Q}{4M \left(v^2 g_0\right)_v T^{3/2}} - \frac{0.6g}{2(1 + e)\left(v^2 g_0\right)_v T}; \tag{8}$$

where the subscript indicates the derivative with respect to v and, from (1) and (2), $T = [1 + 0.6g(h - y)]\left[2(1 + e)v^2 g_0\right]^{-1}$. A differential equation for the particle velocity is obtained by inverting (3),

$$u' = \frac{5\pi^{1/2} S}{8J v^2 g_0 T^{1/2}}. \tag{9}$$

Finally, the differential equation for the energy flux is, from (4) with (6) and (9),

$$Q' = \frac{5\pi^{1/2} S^2}{8J v^2 g_0 T^{1/2}} - \frac{12\left(1 - \epsilon^2\right) v^2 g_0 T^{3/2}}{\pi^{1/2} L}, \tag{10}$$

where L is calculated from (7) and (9). The system of three differential equations (8) through (10) permits the determination of the distribution of ν, u and Q in the fast flow, once appropriate boundary conditions are provided.

At $y = h$, we use the boundary conditions derived by Richman [26] for the flows of spheres over bumpy planes: a slip velocity given by

$$u_B = \left(\frac{\pi}{2}\right)^{1/2} S \left\{ \frac{1 - 5(1+e)(1+B)\sin^2\psi/\left(2^{5/2}J\right)}{(2/3)\csc^2\psi\,(1-\cos\psi) - \cos\psi} + \frac{5(1+e)}{2^{3/2}J} \right\} T_h^{1/2},$$
(11)

where $B = 12\pi/2^{1/2}$ and an energy flux given as

$$Q_B = S u_B - \frac{2^{3/2}(1 - \cos\psi)\csc^2\psi\,(1-\epsilon)}{\pi^{1/2}L_h} T_h^{1/2}.$$
(12)

In (11) and (12), T_h and L_h are the granular temperature and correlation length evaluated at $y = h$.

At $y = h - \delta$, the interface between the fast and the slow flows, we employ the boundary condition for the energy flux at an erodible boundary [23], modified by the introduction of the correlation length,

$$Q_E = -2(1 + 0.6g\delta) \left[\frac{3M(1 - \epsilon)}{\pi L_{h-\delta}} \right]^{1/2} T_{h-\delta}^{1/2},$$
(13)

where $T_{h-\delta}$ and $L_{h-\delta}$ are the granular temperature and correlation length evaluated at $y = h - \delta$. We also fix the solid volume fraction there to be equal to ν_E. Finally, we require the value u_E of the particle velocity at $y = h - \delta$ to be continuous with that in the bed, determined analytically in the next section.

The five boundary conditions $u(y = h) = V - u_B$, $u(y = h - \delta) = u_E$, $\nu(y = h - \delta) = \nu_E$, $Q(y = h) = -Q_B$ and $Q(y = h - \delta) = Q_E$ permit the solution of the system of differential equations (8) through (10) using the Matlab® routine 'bvp4c', with the thickness δ and the value of the uniform shear stress S determined as part of the solution.

2.2 Slow Flow

In the slow flow, for $y \leq h - \delta$ in which the solid volume fraction exceeds the greatest for which shearing takes place without expansion, the stresses are likely generated by physical mechanisms besides momentum exchange in random collisions. In simple shearing, for instance, if the spheres are sufficiently compliant, there is an additional, elastic component of the stresses [20]. On the other hand, recent numerical simulations [10] showed that the constitutive relations for compliant spheres [20] do not always apply, especially in the case of wall-bounded,

inhomogeneous flows. Another physical mechanism, such as the development of spatial anisotropy in the network of contacts is likely to be involved. In shearing flows, it is probable that such a mechanism affects the particle shear stress and pressure in a similar way, so that their ratio remains equal to the ratio of (3) to (2). This assumption seems corroborated by a preliminary analysis of the numerical measurements [10] on inhomogeneous flows, and it permits the reproduction of the results of numerical simulations of simple shearing [20]. With this

$$\frac{S}{p} = \frac{4J}{5\pi^{1/2}(1+e)} \frac{u'}{T^{1/2}}. \tag{14}$$

We also assume, as elsewhere [20, 24], that the fluctuation energy balance in this slow flow region reduces to a balance between the diffusion and the collisional dissipation of energy—that is, the rate of energy production due to the working of the shear stress is negligible. As shown in [23], this results in a differential equation for the granular temperature of the form:

$$T'' = \frac{T}{\lambda^2}, \tag{15}$$

where $\lambda^2 = LM / [3(1 - \epsilon)]$, differing from that of [23] because of the introduction of the correlation length. For simplicity, we take L to be equal to its value in simple shearing [20],

$$L = 1 + \frac{26(1 - \epsilon)}{15} \frac{\nu_c - 0.49}{0.64 - \nu_c}. \tag{16}$$

The analytical solution of (15) is

$$T = T_{h-\delta} \exp\left(-\frac{h - \delta - y}{\lambda}\right). \tag{17}$$

Using (17) in (14), with (1), and integrating, with the boundary condition $u = 0$ when $y = 0$, gives

$$u = \frac{5\pi^{1/2}(1+e)}{4J} \frac{ST_{h-\delta}^{1/2}}{0.6g} \exp\left(\frac{1 + 0.6g\delta}{1.2g\lambda}\right)$$
$$\times \left[-\text{Ei}\left(-\frac{1 + 0.6g(h - y)}{1.2g\lambda}\right) + \text{Ei}\left(-\frac{1 + 0.6gh}{1.2g\lambda}\right)\right], \tag{18}$$

where $\text{Ei}(x) = \int_{-\infty}^{x} \exp(t)/t \, dt$ is the exponential integral. When $y = h - \delta$, (18) provides the value of the velocity u_E to be used as the boundary condition in the

numerical solution of the fast flow of the previous section:

$$u_E = \frac{5\pi^{1/2}(1+e)}{4J} \frac{ST_{h-\delta}^{1/2}}{0.6g} \exp\left(\frac{1+0.6g\delta}{1.2g\lambda}\right)$$
$$\times \left[-\mathrm{Ei}\left(-\frac{1+0.6g\delta}{1.2g\lambda}\right) + \mathrm{Ei}\left(-\frac{1+0.6gh}{1.2g\lambda}\right)\right]. \tag{19}$$

From (18) and (19), we obtain the expression of the scaled velocity profile in the slow flow:

$$\frac{u}{u_E} = \frac{-\mathrm{Ei}\left(-\frac{1+0.6g(h-y)}{1.2g\lambda}\right) + \mathrm{Ei}\left(-\frac{1+0.6gh}{1.2g\lambda}\right)}{-\mathrm{Ei}\left(-\frac{1+0.6g\delta}{1.2g\lambda}\right) + \mathrm{Ei}\left(-\frac{1+0.6gh}{1.2g\lambda}\right)}. \tag{20}$$

2.3 Results

We now indicate the results of the present theory for a representative set of parameters. We take $e = 0.9$ and $\nu_c = 0.587$, appropriate for particles of surface friction $\mu = 0.5$ [27], with $\epsilon = 0.7$ [18]; $\nu_E = 0.58$ (the solid volume fraction at the interface between the fast flow and the bed in numerical simulations of laterally confined, inclined flows of frictional spheres [22]) and $\psi = \pi/6$. We take $h = 70$ and use different values of dimensionless velocity V and dimensionless gravity g to determine the influence of these parameters on the results.

Figure 2 shows the dimensionless average particle velocity as a function of the distance from the moving plane. In a semi-log plot, it is possible to appreciate the exponential behaviour of (18) in the slow flow. The thickness of the fast flow, marked by the knee in the velocity profiles of Fig. 2, increases with increasing dimensionless V and decreasing dimensionless g. This is more evident in Figs. 3 and 4 where δ is plotted as a function of V and g, respectively. For $g = 0.05$, the fast flow disappears when V is less than 0.25 (Fig. 3). For a given velocity of the moving plane, the fast flow shrinks when dimensionless gravity increases (Fig. 4).

Unlike the thickness of the fast flow, the particle shear stress always increases with both increase in V and g (Figs. 5 and 6). In other words, pulling a plane over a granular assembly is increasingly more difficult if we increase the velocity of the plane and/or the gravity, relative to the applied pressure, as expected.

Experimental profiles of the velocity of glass spheres in a layer sheared by a slider pulled at constant velocity have been measured in Siavoshi et al. [25]. In dimensionless terms, those experiments were performed with $V = 0.0015$ and $g = 0.24$ by changing the total thickness h. Based on Figs. 3 and 4, we do not expect a fast flow to be present. The velocity profile is, therefore, analytical and given by (20). Figure 7 shows that our predictions are in good agreement with the experiments.
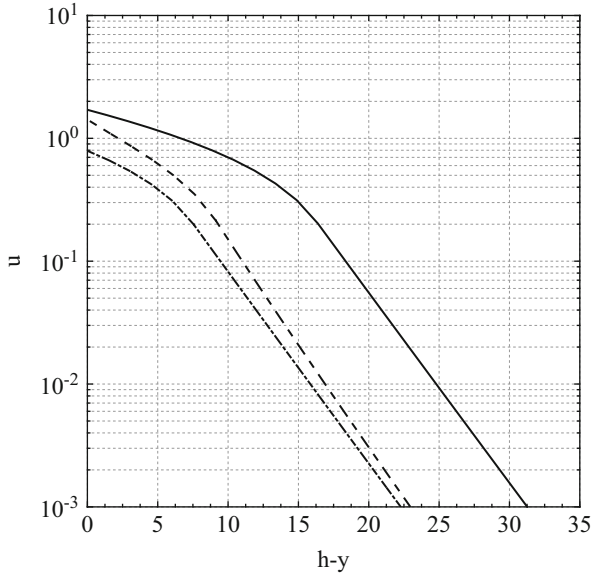
Fig. 2 Dimensionless velocity profiles for $h = 70$ and $V = 2$ and $g = 0.05$ (solid line); $V = 2$ and $g = 0.5$ (dashed line); and $V = 1$ and $g = 0.05$ (dot-dashed line)
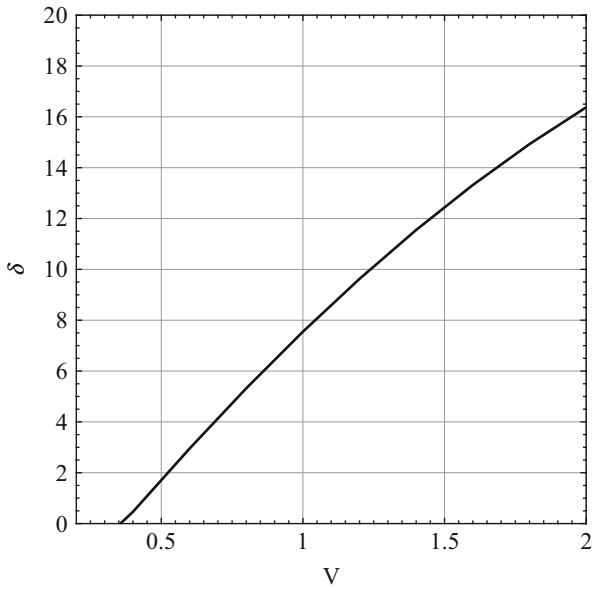
Fig. 3 Thickness of the fast flow as a function of the dimensionless velocity of the moving plane for $h = 70$ and $g = 0.05$

Fig. 4 Thickness of the fast
flow as a function of
dimensionless gravity for
$h = 70$ and $V = 2$
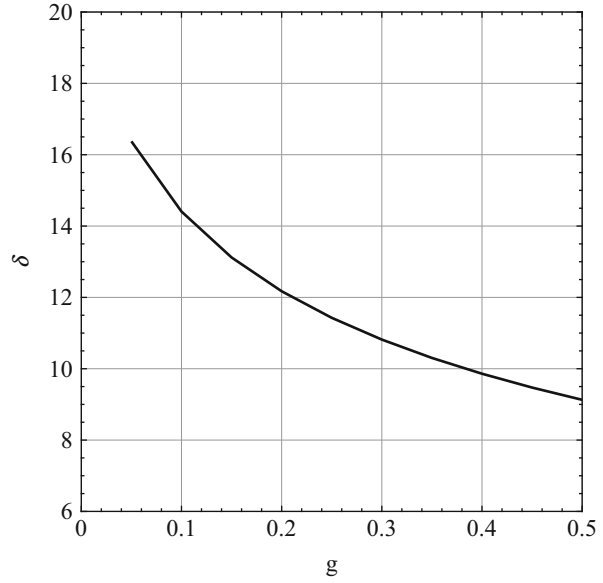
Fig. 5 Shear stress as a
function of the dimensionless
velocity of the moving plane
for $h = 70$ and $g = 0.05$
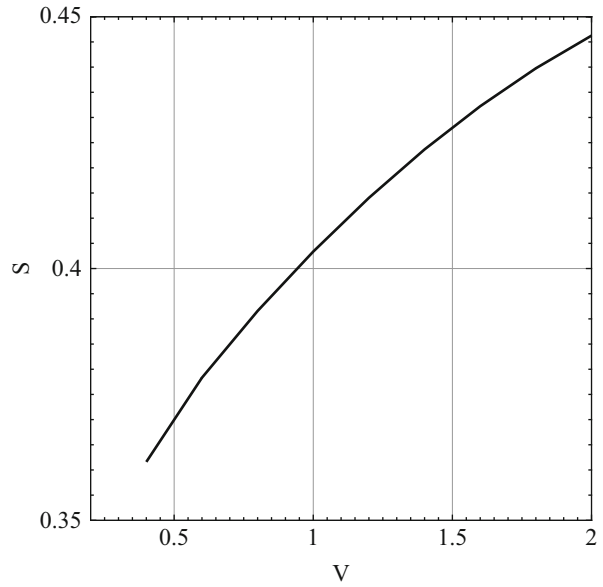
Fig. 6 Shear stress as a function of dimensionless gravity for $h = 70$ and $V = 2$
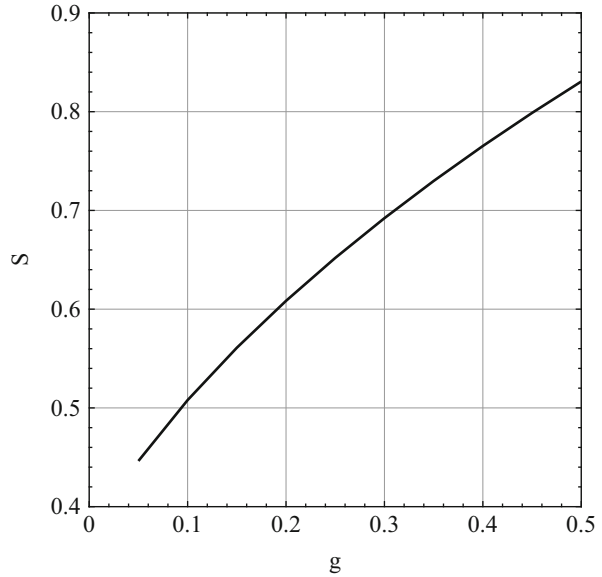
Fig. 7 Experimental (symbols, after Siavoshi et al. [25]) and predicted (lines, (20)) scaled velocity in the slow flow when $V = 0.0015$, $g = 0.24$ and $h = 4$ (dot-dashed line and squares); $h = 7$ (dashed line and triangles); $h = 10$ (solid line and circles)
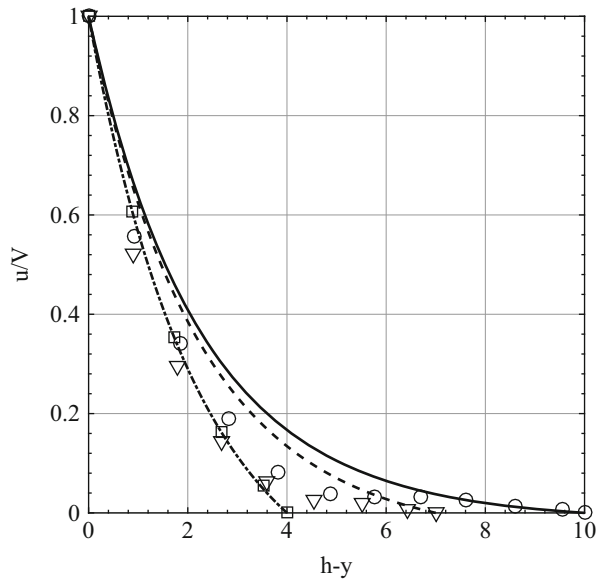
3 Annular Shearing

We now assume that the identical spheres are sheared between two coaxial cylinders in the absence of gravity, with the inner cylinder moving at constant angular velocity. As for the case of planar shearing with gravity, the surfaces of the cylinders are made bumpy by gluing a layer of spheres, identical to those of the flow, in a
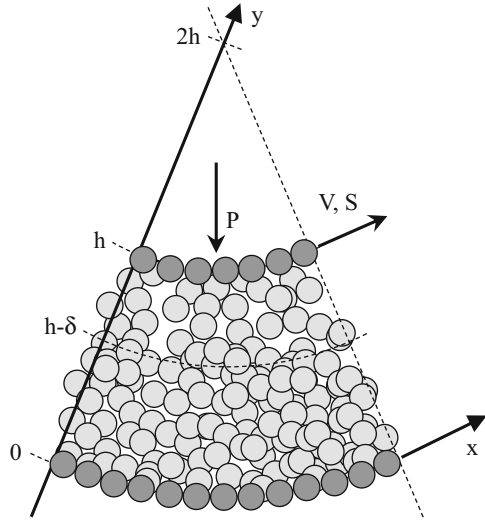
regular, hexagonal array. We take x and y to be the directions locally tangential and perpendicular to the cylinders, respectively (the inner and the outer cylinders are at $y = h$ and $y = 0$). The tangential component of the velocity, the only one present, is u. The distance, h, between the inner and the outer cylinder and the tangential velocity, V, of the inner cylinder are the control variables of the system (as in Koval et al. [8], we assume that the radius of the inner cylinder is equal to h). The flow configuration is depicted in Fig. 8.

As measured in numerical simulations [8], we take the particle pressure to be uniform and equal to P and the particle shear stress to be

$$s = S \left(\frac{h}{2h - y} \right)^2 , \tag{21}$$

where S is the particle shear stress at the inner cylinder. Also in this case, we focus on dense situations. The flow domain can still be divided into two sub-regions: a fast flow adjacent to the moving boundary of thickness δ and a slow flow of thickness $h - \delta$ (Fig. 8). We use the criterion based on the largest solid volume fraction for which the granular material can be sheared without expanding, ν_E, to distinguish the two regions.

3.1 Fast Flow

In the fast flow, Eqs. (2) through (7) are still valid. As in the previous case, we make lengths dimensionless by d, velocities by $(P/\rho_p)^{1/2}$, stresses by P, and energy

flux by $(P^3/\rho_p)^{1/2}$. Then, the dimensionless forms of the inner cylinder tangential velocity and the gap between the cylinders are $V\rho_p^{1/2}/P^{1/2}$ and h/d, respectively. For simplicity, in what follows, we employ the same notation, even if we refer to dimensionless quantities.

In the annular shearing, the derivative of the pressure (2) with respect to y vanishes. Then, with (1) and (5), we obtain a differential equation for the solid volume fraction [28]:

$$\nu' = \frac{\pi^{1/2} Q}{4M \left(\nu^2 g_0\right)_\nu T^{3/2}}, \tag{22}$$

where, from (1) and the uniform distribution of pressure, $T = \left[2(1+e)\nu^2 g_0\right]^{-1}$. The differential equation for the particle velocity is obtained by inverting (3),

$$u' = \frac{5\pi^{1/2} s}{8J\nu^2 g_0 T^{1/2}}. \tag{23}$$

Finally, the differential equation for the energy flux is, from (4) with (6) and (23),

$$Q' = \frac{5\pi^{1/2} s^2}{8J\nu^2 g_0 T^{1/2}} - \frac{12\left(1 - \epsilon^2\right) \nu^2 g_0 T^{3/2}}{\pi^{1/2} L}, \tag{24}$$

where L is calculated from (7) and (23). The system of three differential equations, (22) though (24), permits the determination of the distribution of ν, u and Q in the fast flow, with the boundary conditions: $u(y = h) = V - u_B$, with u_B given in (11); $u(y = h - \delta) = u_E$ (velocity at the interface with the slow flow determined in the next section); $\nu(y = h - \delta) = \nu_E$; $Q(y = h) = -Q_B$, with Q_B given in (12); and $Q(y = h - \delta) = Q_E$, with

$$Q_E = -2\left[\frac{3M(1 - \epsilon)}{\pi L_{h-\delta}}\right]^{1/2} T_{h-\delta}^{1/2}, \tag{25}$$

different from (13), because of the uniform distribution of particle pressure.

3.2 Slow Flow

In the slow flow region, the distribution of granular temperature is still given by (17). We still assume that the stress ratio is equal to

$$\frac{s}{p} = \frac{4J}{5\pi^{1/2}(1+e)} \frac{u'}{T^{1/2}}. \tag{26}$$

We can then invert (26) and obtain the equation that governs the distribution of the shear rate in the slow flow, using the distributions of the stresses in the annular shearing:

$$u' = \frac{5\pi^{1/2}(1+e)}{4J} Sh^2 T_{h-\delta}^{1/2} \frac{1}{(2h-y)^2} \exp\left(-\frac{h-\delta-y}{2\lambda}\right). \tag{27}$$

Integrating, with the boundary condition $u = 0$ at $y = 0$, gives

$$\begin{aligned}
u =\ & \frac{5\pi^{1/2}(1+e)}{4J} Sh^2 T_{h-\delta}^{1/2} \\
& \times \left[\frac{1}{2\lambda} \exp\left(\frac{h+\delta}{2\lambda}\right) \mathrm{Ei}\left(-\frac{2h-y}{2\lambda}\right) + \frac{1}{2h-y} \exp\left(-\frac{h-\delta-y}{2\lambda}\right) \right. \\
& \left. - \frac{1}{2\lambda} \exp\left(\frac{h+\delta}{2\lambda}\right) \mathrm{Ei}\left(-\frac{h}{\lambda}\right) - \frac{1}{2h} \exp\left(-\frac{h-\delta}{2\lambda}\right) \right].
\end{aligned} \tag{28}$$

When $y = h - \delta$, (28) provides the value of the velocity u_E to be used as the boundary condition in the numerical solution of the fast flow of the previous section:

$$\begin{aligned}
u_E =\ & \frac{5\pi^{1/2}(1+e)}{4J} Sh^2 T_{h-\delta}^{1/2} \\
& \times \left[\frac{1}{2\lambda} \exp\left(\frac{h+\delta}{2\lambda}\right) \mathrm{Ei}\left(-\frac{h+\delta}{2\lambda}\right) + \frac{1}{h+\delta} \right. \\
& \left. - \frac{1}{2\lambda} \exp\left(\frac{h+\delta}{2\lambda}\right) \mathrm{Ei}\left(-\frac{h}{\lambda}\right) - \frac{1}{2h} \exp\left(-\frac{h-\delta}{2\lambda}\right) \right].
\end{aligned} \tag{29}$$

3.3 Results

We now make qualitative comparisons between the results of the present theory for annular shearing and the numerical simulations on disks in an annular shear cell [8]. We take $e = 0.7$ and $\nu_c = 0.587$, appropriate for particles of surface friction $\mu = 0.5$ [27], with $\epsilon = 0.5$ [18]; $\nu_E = 0.58$ and $\psi = \pi/6$. We then vary h and V to check their influence on the results.

Figure 9 shows the particle velocity, scaled with the tangential velocity of the inner cylinder, as a function of the distance from the inner cylinder. As seen by Koval et al. [8], there is a slip velocity at $y = h$, an exponential behaviour in the slow flow; and when $h = 50$ and $V = 2.5$, there is a change in the concavity of the velocity profile in the fast flow. The thickness of the fast flow, marked by the knee in the velocity profiles of Fig. 9, apparently increases with increasing h and V.

The behaviour of δ with V is non-monotonic, as shown in Fig. 10 for the case $h = 50$. The thickness δ is zero when V is less than 0.1, and has a maximum when
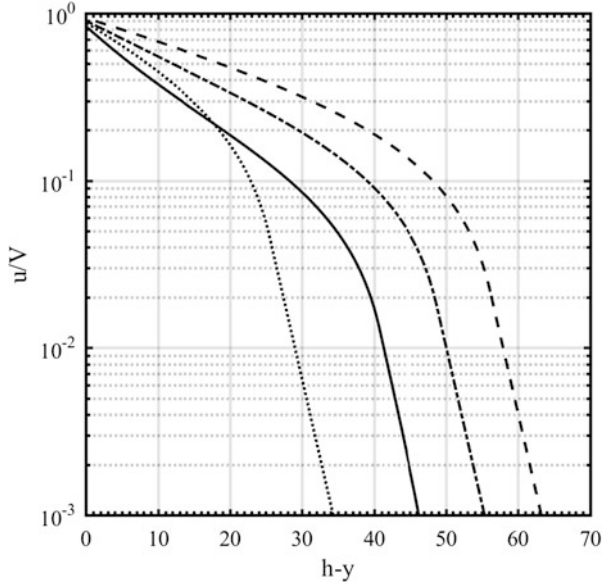
Fig. 9 Scaled velocity profiles for: $h = 50$ and $V = 2.5$ (solid line); $h = 100$ and $V = 2.5$ (dashed line); $h = 200$ and $V = 2.5$ (dot-dashed line); and $h = 50$ and $V = 1$ (dotted line)
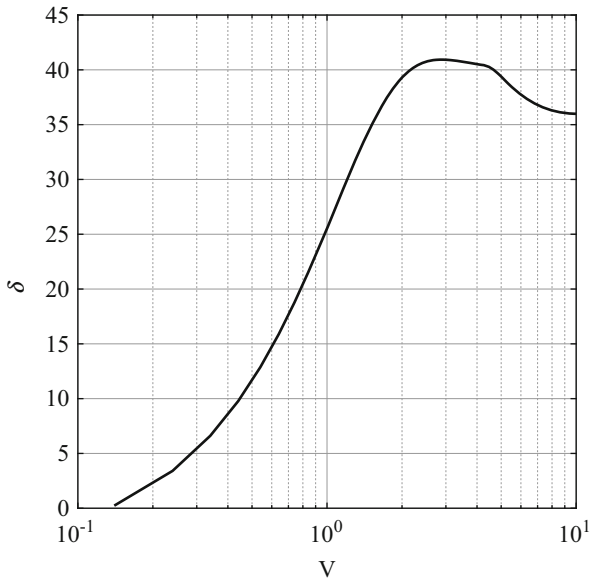
Fig. 10 Thickness of the fast flow as a function of the dimensionless tangential velocity of the inner cylinder for $h = 50$
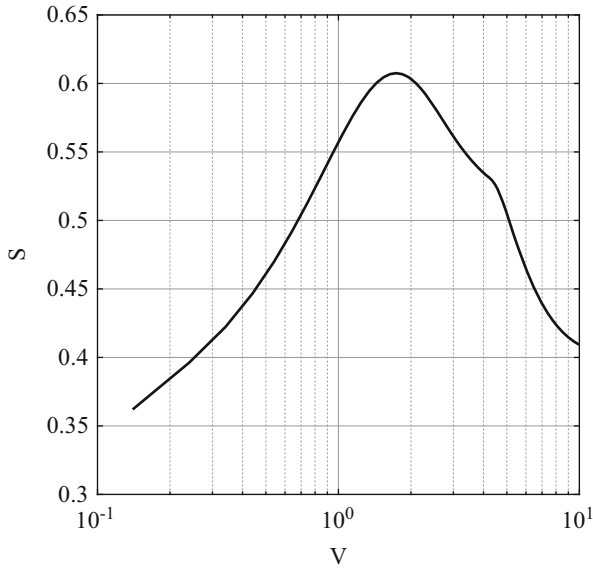
Fig. 11 Shear stress as a function of the dimensionless tangential velocity of the inner cylinder for $h = 50$

V is near 2.5; for large values of V, it decreases slightly and seems to saturate for even larger values. This is qualitatively similar to the relation between the shear stress at $y = h$ and the tangential velocity of the inner cylinder depicted in Fig. 11, although in that case the decrease after the peak is much more pronounced. Koval et al. [8] measured monotone increase of δ and S with V. However, they did not perform simulations for V larger than 2.5, and their Figs. 9a and 3b seem to confirm that the measurements are approaching a maximum at that value. However, it may be possible that the solutions showing a decrease of δ and S with V are actually unstable.

4 Conclusions

We have made use of recent extensions of kinetic theory for dense, dissipative shearing flows to phrase and solve boundary-value problems for steady, inhomogeneous flows of a relatively dense aggregate of identical frictional spheres. We have considered two configurations: planar granular shearing in a gravitational field between horizontal, rigid, bumpy boundaries due to the motion of the upper boundary; and annular shearing between coaxial, bumpy cylinders, with the inner cylinder in motion at constant angular velocity. In both cases, the flow consisted of a region of rapid, collisional shearing and a denser region of slower shearing

in which more enduring particle contacts played a role. In the denser region, or bed, we assumed that the collisional production of energy is negligible and the anisotropy of the contact forces influences the shear stress and the pressure in the same way. The resulting profiles of average velocity show an exponential decay into the bed, in qualitative and quantitative accordance with numerical simulations and physical experiments. We have also shown that the thickness of the fast flow and the shear stress increase as the boundary velocity is increased at fixed pressure or as the pressure is decreased at fixed velocity. Although the results of the present theory are in good qualitative agreement with 2D discrete numerical simulations and in quantitative agreement with some physical experiments, 3D discrete numerical simulations are required to fully test the capability of the theory to reproduce dense granular flows in inhomogeneous configurations. We hope that the predictions included above will inspire such simulations to test them.

In our view, the analyses that we have performed indicate the relationship between applications of the extended kinetic theory to dense, steady, inhomogeneous flows and the nonlocal extensions of the μ-I rheology developed by Kamrin and collaborators [7, 9, 10]. We hope to explore this relationship further in other contexts.

References

1. Jenkins, J.T., Savage, S.B.: A theory for the rapid flow of identical, smooth, nearly elastic, spherical particles. J. Fluid Mech. 130, 187–202 (1983). https://doi.org/10.1017/S0022112083001044
2. Garzó, V., Dufty, J.W.: Dense fluid transport for inelastic hard spheres. Phys. Rev. E 59, 5895–5911 (1999). https://doi.org/10.1103/PhysRevE.59.5895
3. Goldhirsch, I.: Introduction to granular temperature. Powd. Tech. 182, 130–136 (2008). https://doi.org/10.1016/j.powtec.2007.12.002
4. GDR MiDi: On dense granular flows. Eur. Phys. J. E 14, 341–365 (2004). https://doi.org/10.1140/epje/i2003-10153-0
5. da Cruz, F., Emam, S., Prochnow, M., Roux, J.-N., Chevoir, F.: Rheophysics of dense granular materials: Discrete simulation of plane shear flows. Phys. Rev. E 72, 021309 (2005). https://doi.org/10.1103/PhysRevE.72.021309
6. Jop, P., Forterre, Y., Pouliquen, O.: Crucial role of side walls for granular surface flows: consequences for the rheology. J. Fluid Mech. 541, 167–192 (2005). https://doi.org/10.1017/S0022112005005987
7. Kamrin, K., Henann, D.L.: Nonlocal modeling of granular flows down inclines. Soft Matt. 11, 179–185 (2014). https://doi.org/10.1039/c4sm01838a
8. Koval, G., Roux, J.-N., Corfdir, A., Chevoir, F.: Rheology of Confined Granular Flows: Annular shear of cohesionless granular materials: From the inertial to quasistatic regime. Phys. Rev. E 79, 021306 (2009). https://doi.org/10.1103/PhysRevE.79.021306
9. Kamrin, K., Koval, G.: Nonlocal Constitutive Relation for Steady Granular Flow. Phys. Rev. Lett. 108, 178301 (2012). https://doi.org/10.1103/PhysRevLett.108.178301
10. Zhang, Q., Kamrin, K.: Microscopic Description of the Granular Fluidity Field in Nonlocal Flow Modeling. Phys. Rev. Lett. 118, 058001 (2017). https://doi.org/10.1103/PhysRevLett.118.058001

11. Jenkins, J.T.: Dense shearing flows of inelastic disks. Phys. Fluids 18, 103307 (2006). https://doi.org/10.1063/1.2364168
12. Jenkins, J.T.: Dense inclined flows of inelastic spheres. Granul. Matt. 10, 47–52 (2007). https://doi.org/10.1007/s10035-007-0057-z
13. Berzi, D.: Extended kinetic theory applied to dense, granular, simple shear flows. Acta Mech. 225, 2191–2198 (2014). https://doi.org/10.1007/s00707-014-1125-1
14. Mitarai, N., Nakanishi, H.: Bagnold Scaling, Density Plateau, and Kinetic Theory Analysis of Dense Granular Flow. Phys. Rev. Lett. 94, 128001 (2005). https://doi.org/10.1103/PhysRevLett.94.128001
15. Mitarai, N., Nakanishi, H.: Velocity correlations in dense granular shear flows: Effects on energy dissipation and normal stress. Phys. Rev. E 75, 031305 (2007). https://doi.org/10.1103/PhysRevE.75.031305
16. Kumaran, V.: Dynamics of dense sheared granular flows. Part II. The relative velocity distributions. J. Fluid Mech. 632, 145–198 (2009). https://doi.org/10.1017/S0022112009006958
17. Jenkins, J.T., Zhang, C.: Kinetic theory for identical, frictional, nearly elastic spheres. Phys. Fluids 14, 1228–1235 (2002). https://doi.org/10.1063/1.1449466
18. Larcher, M., Jenkins, J.T.: Segregation and mixture profiles in dense, inclined flows of two types of spheres. Phys. Fluids 25, 113301 (2013). https://doi.org/10.1063/1.4830115
19. Berzi, D., Vescovi, D.: Different singularities in the functions of extended kinetic theory at the origin of the yield stress in granular flows. Phys. Fluids 27, 013302 (2015). https://doi.org/10.1063/1.4905461
20. Berzi, D., Jenkins, J.T.: Steady shearing flows of deformable, inelastic spheres. Soft Matt. 11, 4799–4808 (2015). https://doi.org/10.1039/c5sm00337g
21. Komatsu, T.S., Inagaki, S., Nakagawa, N., Nasuno, S.: Creep Motion in a Granular Pile Exhibiting Steady Surface Flow. Phys. Rev. Lett. 86, 1757–1760 (2001). https://doi.org/10.1103/PhysRevLett.86.1757
22. Richard, P., Valance, A., Meťayer, J.-F., Sanchez, P., Crassous, J., Louge, M., Delannay, R.: Rheology of Confined Granular Flows: Scale Invariance, Glass Transition, and Friction Weakening. Phys. Rev. Lett. 101, 248002 (2008). https://doi.org/10.1103/PhysRevLett.101.248002
23. Jenkins, J.T., Askari, E.: Boundary conditions for rapid granular flows: phase interfaces. J. Fluid Mech. 223, 497–508 (1991). https://doi.org/10.1017/S0022112091001519
24. Berzi, D., Jenkins, J.T.: Dense, inhomogeneous shearing flows of spheres. EPJ Web of Conferences 140, 11006 (2017). https://doi.org/10.1051/epjconf/201714011006
25. Siavoshi, S., Orpe, A.V., Kudrolli, A.: Friction of a slider on a granular layer: Nonmonotonic thickness dependence and effect of boundary conditions. Phys. Rev. E 73, 010301 (2006). https://doi.org/10.1103/PhysRevE.73.010301
26. Richman, M.W.: Boundary conditions based upon a modified Maxwellian velocity distribution for flows of identical, smooth, nearly elastic spheres. Acta Mech. 75, 227–240 (1988). https://doi.org/10.1007/BF01174637
27. Chialvo, S., Sun, J., Sundaresan, S.: Bridging the rheology of granular flows in three regimes. Phys. Rev. E 85, 021305 (2012). https://doi.org/10.1103/PhysRevE.85.021305
28. Jenkins, J.T., Berzi, D.: Dense inclined flows of inelastic spheres: tests of an extension of kinetic theory. Granul. Matt. 12, 151–158 (2010). https://doi.org/10.1007/s10035-010-0169-8

The Effective Stress of Unsaturated Soils: Thermodynamic Connections to Intrinsic and Measured Suctions

Itai Einav and Mario Liu

Abstract The effective stress of unsaturated soil media is defined in most rigorous way using Landau's hydrodynamic procedure, and its structure derived under conditions that are close to thermodynamic equilibrium. This derivation is complete and accurate for soils with negligible cohesion effects (degrees of saturation $\gtrsim$ 2–3%). The richness in the effective stress found by former experimental evidences is demonstrated to be explainable. The effective stress is strictly linked to the intrinsic suction in the soil, itself being strictly linked to the externally measured (or imposed) suction. Staggeringly, although the difference between those suctions has not been considered or appropriately quantified prior to our work, it is shown that their values can be entirely different. Finally, a discussion is provided on the extension of the hydrodynamic formulation for the very small saturations ($\lesssim$ 2–3%) and for conditions that are not in thermodynamic equilibrium, which would capture transient features such as hystereses in soil water retentions.

Keywords Hydrodynamics · Effective stress · Intrinsic suction · Measured suction

1 Introduction

The constitutive description of unsaturated soil media is significant for geotechnical engineering, yet is far from being complete. Previous research has acknowledged the need to first define the meaning and structure of effective stress (σ_{ij}^{eff}) of such materials, before moving on to resolve the rest of the constitutive relationships. The purpose of the current paper is to review the results of two recent papers

I. Einav (✉)
The University of Sydney, Sydney, NSW, Australia
e-mail: itai.einav@sydney.edu.au

M. Liu
Universität Tübingen, Tübingen, Germany

where the meaning [1] and precise structure [2] of the effective stress was indeed revealed under thermodynamic equilibrium conditions, using only a minimal number of highly plausible physical assumptions. The derivation was based on the *hydrodynamic procedure*, which was first proposed by Landau and later presented in the books on Newtonian and superfluid liquids [3–5]. It was generalised to liquid crystals by de Gennes [6], and more recently to granular materials by Jiang and Liu [7]. As detailed most generally by Einav and Liu [1], within the hydrodynamic procedure both the first and second laws of thermodynamics, as well as Truesdell's physical constraints of material objectivity and symmetry, are fully contained.

Whereas soil scientists tend to interpret soil moisture measurements using pseudo potentials, soil mechanicians usually opt to use pressure-like quantities such as measured suction, and measured air and water pressures, as those are pertinent for mechanical stress calculations. However, the 'measured suction'—the difference between the air and water pressures in measurement cells—should not be confused with the difference of those pressures in the soil mixture itself. As highlighted in [8] some constitutive models have incorrectly identified measured suction with the capillary component of the matrix potential of the soil.

The source for this confusion seems to have been initiated as a result of simplifications made during some of the earlier works in soil sciences. For example, starting with the earlier attempt by Day [9] to interpret soil moisture measurements, soil scientists have tacitly postulated that the chemical potential μ (the derivative of free energy with respect to density at constant temperature) could be decomposed into separate decoupled terms. Indeed, the chemical potential is an important thermodynamic variable that controls the equilibrium of mass transfer. Unfortunately, any assumption requiring to decompose it into decoupled terms cannot be sufficiently general, and thus a more rigorous thermodynamic treatment was required.

This erroneous concept of decomposing the overall chemical potential into decoupled ingredients was then taken even further in soil sciences [10–12], by further splitting the chemical potential into even more individual uncoupled terms. For example, Sposito [12] assumed that the chemical potential could be decoupled into a sum of the so-called matrix, pneumatic, and envelope-pressure potentials, while Babcock and Overstreet [11] further split the matrix potential into the so-called capillary-pressure and adsorption potentials. Indeed, many papers still frequently use those pseudo-physical potentials to interpret measured data of soil water retention. However, it should be noted that neither of those 'potential' terms is a true thermodynamic potential. This is unlike the internal free energy, from which all the constitutive laws of said material can be derived, and which may actually be decomposed into additive free energy terms. Therefore, from a thermodynamics viewpoint, the dependence of each of the assumed pseudo-physical ingredients of the chemical potential on the various densities may contradict the dependence of the other ingredients on the same densities, unless they could be shown to be derivable from the internal free energy.

Our rigorous thermodynamic treatment does not require to employ such ad hoc decompositions of chemical potentials. We resolve the problem of the interpretation

of experimental soil water retention data by distinguishing between the externally measured/applied pressures and the intrinsic pressures developing within the soil itself, as well as between intrinsic and measured suctions, while maintaining the equilibrium between the chemical potentials in the soil mixture and measurement cells.

In describing the behaviour of partially saturated soils many thermodynamic works have advanced the description of internal constitutive properties in the soil mixture (e.g., see [13–23] to name a few). For example, some papers attempt to track the complex shapes and distribution of interfaces, which are not easily accessible experimentally. Surface tensions are typically homogenised to recover the measured suction, with an inevitable loss in accuracy. The current paper avoids this complex strategy by inverting the logic. This is done by introducing the measured suction explicitly into the thermodynamic description, such that the role of interfaces on the effective material behaviour could be captured implicitly though more accurately.

2 General Hydrodynamic Effective Stress (for Any Media)

Following from Landau's complete thermodynamic formulation of continua, which is known in physics as the 'hydrodynamic procedure', the elastic stress σ_{ij}^e for any continuum media is defined as the derivative of the free energy per unit volume $f = f(\varepsilon_{ij}^e, \varrho, T, \dots)$ with respect to the elastic strain ε_{ij}^e:

$$\sigma_{ij}^e \equiv \frac{\partial f}{\partial \varepsilon_{ij}^e}, \tag{1}$$

where ϱ is the total partial density (mass per unit volume) and T the temperature. The use of '...' in the f represents the remaining set of independent internal variables required to capture the full free energy state of the material at hands.

Note—when one takes f to be independent of total density ϱ, the elastic stress becomes the total Cauchy stress $\sigma_{ij}^e = \sigma_{ij}$ under small deformation rates, as we shall return to this point later when dealing with purely continuous solid media without internal pores. Although soils are discontinuous and have internal pores, most previous thermodynamic derivations of constitutive models in geotechnics ignored the density dependence of the free energy of the soil material. Density, however, is a measurable variable in porous media, and should definitely be considered in soil mechanics. For example, elastic stiffness is known to be a function of density (as usually expressed in terms of void ratio or porosity), and this should be reflected in the free energy.

As a useful first step we identify the effective stress of any media with the elastic stress:

$$\sigma_{ij}^{eff} = \sigma_{ij}^e, \tag{2}$$

and therefore the elastic stiffness of the system is related explicitly to the effective stress and not to the total stress. For example, in granular materials it is the fabric of the elastic contact force chains that directly determines the elastic stiffness of the system, and not the presence of fluids in between the grains, whose forces dissipative over time and are thus inelastic.

The work input into any continuum media can always be defined consistently with previous thermodynamic formulations (e.g. [24]):

$$w \equiv \varrho \mathrm{d}_t e + \nabla_i q_i, \tag{3}$$

where $q_i = -Tf_i$ being the heat flux; f_i the dissipative entropy current; e the internal energy per unit mass $e \equiv e(\varepsilon_{ij}^e, \varrho, \eta, \dots) = f + T\eta$; and T the temperature. (Here, the definition is consistent with Rational Mechanics [24], which is slightly more general than the one in [25, 26]), as it captures convective terms using the material derivative $\mathrm{d}_t e \equiv \dot{e} + v_k \nabla_k e$ of the internal energy, that advects with the barycentric velocity vector v_k).

Although the hydrodynamic procedure provides the complete set of constitutive relationships for any continuum media (as solids, fluids, or their mixtures), without needing to employ the work input on the left-hand side of Eq. (3), it is still interesting to use hydrodynamics to reveal the explicit expression for that work input in Eq. (3), as this will highlight the relation of hydrodynamics with other rigorous formulations. In fact, it turns out from hydrodynamics that the particular form of the work input expression depends on the constitution of the medium itself [1], in a way that is fully consistent with Rational Mechanics [24].

For **single-component continuum media** the hydrodynamic procedure reveals that the work input in Eq. (3) takes the following form [1]:

$$w = \sigma_{ij} \dot{\varepsilon}_{ij}, \tag{4}$$

where σ_{ij} is the total Cauchy stress, and $\dot{\varepsilon}_{ij}$ is the total strain rate. There is, of course, nothing new with this expression above. Indeed, this hydrodynamic result [1] is entirely consistent with previous findings in Rational Mechanics, as described, for example, by Gurtin et al. [24]. As shown by Einav and Liu [1] there is full consistency between these two thermodynamic formulations—this is not surprising, since after all they both come to represent most rigorously the same physical reality. Where Rational Mechanics arrive to this work input expression through the localisation of global energy and power balances, the hydrodynamic procedure is fully operating at the local volume element level, and does not require to go back and forth between the global and local scales.

For **two-component continuum media**, such as saturated soil media, the hydrodynamic procedure reveals that the work input in Eq. (3) takes the following explicit form (see [1]):

$$w = \sigma_{ij} \dot{\varepsilon}_{ij} + \nabla_i \left(J_i^F (\mu_F - \mu_S) \right), \text{ with } J_i^F = \varrho_F (v_i - v_i^F), \tag{5}$$

where ϱ_F is the partial fluid density; $\mu_F = \partial f/\partial \varrho_F$ is the chemical potential of the fluid phase; v_i is the baricentric velocity, and v_i^F is the fluid velocity. Again, the result above is fully consistent with Rational Mechanics, as described by Gurtin et al. [24] for substitutional alloys, which essentially embody similar mixtures as in unsaturated soils. Unfortunately, their fundamental result generally did not transpire to mainstream soil mechanicians, with some papers missing the crucial role of the last term in the above equation. (This can be connected most often to the fact that those works typically ignored the physical dependence of the free energy on the partial densities, and thus avoided to deal with chemical potentials.)

Finally, for **multi-component continuum media**, such as three-component unsaturated soil media (with $\beta = \{S,W,A\}$ for solids, water, and air, respectively), the work input in Eq. (3) becomes (see [1]):

$$w = \sigma_{ij}\dot{\varepsilon}_{ij} + \sum_{\beta} \nabla_i \left(J_i^{\beta} \mu_{\beta} \right), \text{ with } J_i^{\beta} = \varrho_{\beta}(v_i - v_i^{\beta}) \qquad (6)$$

which is again fully consistent with Rational mechanics [24].

As shown through Eqs. (4), (5), and (6) the explicit expressions for the work input depend on the total Cauchy stress σ_{ij}, and not on the elastic/effective stress σ_{ij}^e. Therefore, it follows that the work input itself cannot directly reveal the thermodynamic meaning of the elastic/effective stress σ_{ij}^{eff} in a way that is fully faithful to thermodynamic principles.

On the other hand, according to the hydrodynamic procedure one can also identify the (strictly non-negative total) dissipation R, which unlike w does actually depend on the elastic stress σ_{ij}^e (see Einav and Liu [1]):

$$R = f_i \nabla_i T + \sigma_{ij}^e \dot{\varepsilon}_{ij}^p + \sigma_{ij}^D \dot{\varepsilon}_{ij} + \cdots \geq 0, \qquad (7)$$

where the term '...' comes to represent any additional dissipative contribution arising from changes to any corresponding internal variable that does not have a mass balance.

Also based on the hydrodynamic procedure, the stress quantity σ_{ij}^D is identified as the viscous stress, and is found to obey the following general relation (see a step-by-step derivation in [1]):

$$\sigma_{ij}^D = \sigma_{ij} - \sigma_{ij}^e - P_T \delta_{ij}, \quad P_T \equiv -\frac{\partial(f/\varrho)}{\partial(1/\varrho)} = \mu\varrho - f, \qquad (8)$$

where δ_{ij} is the Kronecker delta; $\mu = \partial f/\partial \varrho$ is the chemical potential of the whole media; and P_T is the thermodynamic stress defined by the derivative of the specific free energy (free energy per unit mass, f/ϱ) with respect to the specific volume (volume per mass, $1/\varrho$).

The positiveness of R suggests that the viscous stress scales to a first order as $\sigma_{ij}^D \propto \dot{\varepsilon}_{ij}$ (a more complete scaling is given by the set of Onsager's relationships, see

details in [1]). Therefore, close to thermodynamic equilibrium the viscous stress is negligible, and thus according to Eq. (2) the effective stress could be most generally defined for any material as:

$$\sigma_{ij}^{eff} \equiv \sigma_{ij} - P_T \delta_{ij}, \quad P_T \equiv -\frac{\partial(f/\varrho)}{\partial(1/\varrho)} = \mu\varrho - f. \tag{9}$$

Finally, based on the hydrodynamic procedure, we note that the entire constitutive relationships of any material can be entirely derived from the definition of the free energy f and the dissipation inequality in Eq. (7). The strict connection of the elastic strain to the elastic stress (as embodied in Eq. (1)), and the fact that R is also a function of that elastic stress, suggest that the material depends on the elastic stress and not on total Cauchy stress. A material is entirely described by [elastic stress]–[elastic strain] relationship and not by stress–strain relationship. Once the elastic stress is known, one should then go on to calculate the total Cauchy stress using Eq. (9), and then take it into the momentum equation (while there is never a need to calculate the total strain).

In fact, this general result of the effective stress in Eq. (9) is not really a new result; it follows directly from Landau's work. On the other hand, the precise specification of this general result for continuum mixtures such as saturated and unsaturated soil media was only recently resolved through the work of Jiang et al. [2]. The first key point required for their solution is the recognition of the general relation for the effective stress in Eq. (9). The second key point is to identify how exactly P_T depends the medium partial density ϱ for the different applications, where various species densities interact. For example, in partially saturated media, this overall partial density ϱ is the sum of three other densities, which interacts through internal processes related to the surface tensions between the components. Based on a minimal number of highly plausible assumptions, these interactions and issues were then resolved most rigorously [2]. Below, some of the key points and outcomes of this rigorous derivation are discussed.

3 Single-Component Media

The discussion on effective stress is rather trivial for single-component media, yet it is worthwhile to go through this step before continuing to describe the more subtle derivation results. Indeed, the total density ϱ of single-component media is simply the intrinsic material density of that single component (which is not the case for multi-component media). In this case, the definition of the work input in Eq. (3) yields the conventional result $w = \sigma_{ij}\dot{\varepsilon}_{ij}$ as in Eq. (4). On the other hand, the effective stress of a single-component media depends on whether it is solid or fluid:

In a **single-component solid** (which does not include internal pores) the free energy $f = f(\varepsilon_{ij}^e, \dots)$ does not generally depend on the solid density and thus

the thermodynamic pressure is generally zero, and therefore the effective stress is simply the total stress $\sigma_{ij}^{eff} = \sigma_{ij}$, and one can write $w = w^{eff} = \sigma_{ij}^{eff} \dot{\varepsilon}_{ij}$.

In a **single-component fluid** (such as pure water or pure air) the density is that of the fluid, while the free energy $f = f(\varrho, \dots)$ does not depend on the elastic strain, which is zero, and thus the elastic stress is also zero. Take, for example, non-viscous water, in which case $\sigma_{ij} = P_T \delta_{ij} = u_W \delta_{ij}$ with the water pressure $u_W = -\frac{\partial(f/\varrho)}{\partial(1/\varrho)}$ following the definition of P_T in Eq. (9). In this case, the work input in Eq. (4) is only due to volumetric contribution of the water pressure, in which case we find $w = u_W \dot{\varepsilon}_v$, with $\dot{\varepsilon}_v = \dot{\varepsilon}_{ii}$ being the volumetric strain rate. Furthermore, we note that in single-component non-viscous fluids the elastic stress is identically zero, $\sigma_{ij}^{eff} = 0$, and thus $w = u_W \dot{\varepsilon}_v \neq [\sigma_{ij}^{eff} \dot{\varepsilon}_{ij} = 0]$. This simple example, by itself, already demonstrates that the meaning of effective stress should not come from the work input, and rather should come from the total dissipation R.

The above results are obviously not surprising, yet they demonstrate the necessity (and physical correctness) for defini most generally the free energy f both in terms of elastic strain (ε_{ij}^e) and density (ϱ).

4   Saturated Soil Media

Unlike single-component media, when two or more mesoscopic components are mixed both the total stress and thermodynamic pressure are generally non-zero. In the following we consider finely dispersed mixtures, which consist of two single-component domains sufficiently macroscopic for thermodynamics to hold in each of them. The case of binary mixtures (saturated soil media) is discussed, where the problem is the existence of more than the one overall density ϱ, such that partial densities ϱ_β must be defined for the two species. In saturated soils there are indeed only two components, which will be designated by the index $\beta = \{S, F\}$ (a mixture of solid grains S surrounded by fluid F). In the following we use $F = A$ for gas such as air and $F = W$ for liquid such as water (therefore $\beta = \{S, W\}$ denotes soils saturated in water; while $\beta = \{S, A\}$ represents soils saturated in air). The partial densities are then defined as the ratio of the mass of the given species by the total volume, while the intrinsic densities $\hat{\varrho}_\beta$ defined by the ratio of the mass of the species by the corresponding volume of the species.

In such bi-mixture media surface tensions cannot develop between the components, and thus intrinsic pressures in the two components are identical $\hat{P}_S = \hat{P}_F$. In order to measure those intrinsic pressures it is possible to insert a measurement device (such as a piezometer) into the soil, which is entirely full of fluid. Once equilibrium is achieved between the measured pressure in the fluid within the external device u_F and the intrinsic pressure of fluid $\hat{P}_F$ in the soil, we find $u_F = \hat{P}_S = \hat{P}_F$. Since the measurement device contains only fluid, the thermodynamic pressure of the soil mixture is also in equilibrium with the other pressures, thus

$P_T = u_F$ such that using Eq. (9) the effective stress reduces to:

$$\sigma_{ij}^{eff} \equiv \sigma_{ij} - u_F \delta_{ij}, \tag{10}$$

which is fully consistent with Terzaghi's effective stress principle. In fact, the fluid pressure in the measurement device satisfies $u_F = -\frac{\partial(\hat{f}_F/\hat{\varrho}_F)}{\partial(1/\hat{\varrho}_F)}$, with $\hat{f}_F$ designating both the intrinsic and partial free energy of that fluid (since the device contains only fluid, the intrinsic and the partial energies within it are equal).

5 Unsaturated Soil Media

In unsaturated soils there are three components designated by an index $\beta = \{S,W,A\}$. The mixture is considered to consist three finely dispersed single-component domains sufficiently macroscopic for thermodynamics to hold in each of them. The soil has a volume V and its components have a mass M_S, M_W, and M_A; as such, in this case three thermodynamic partial densities can be identified, whose addition give the overall partial density:

$$\varrho_S \equiv M_S/V, \quad \varrho_W \equiv M_W/V, \quad \varrho_A \equiv M_A/V, \tag{11}$$

$$\varrho \equiv \varrho_S + \varrho_W + \varrho_A. \tag{12}$$

We can also define the water and air concentrations:

$$c_W \equiv \varrho_W/\varrho, \quad c_A \equiv \varrho_A/\varrho. \tag{13}$$

Therefore, the free energy (per unit volume) can be written either in terms of the three partial densities or using the total partial density and two concentrations:

$$f = f(\varrho_S, \varrho_W, \varrho_A, \cdots) = f(\varrho, c_W, c_A, \cdots).$$

Each of these density variables follows its own mass conservation, and for now we neglect the possibility of mass exchange between the species. Notice that the general effective stress definition in Eq. (9) is expressed in terms of only the overall partial density ϱ, and thus the relationships between partial densities make the derivation much more involved than for the dry and fully saturated cases.

As each of the three components occupies a subvolume, V_S, V_W, V_A, with $V = V_S + V_W + V_A$, the averaged true or *intrinsic densities* and the single-component intrinsic free energies are

$$\hat{\varrho}_\beta \equiv M_\beta/V_\beta, \quad \hat{f}_\beta = \hat{f}_\beta(\hat{\varrho}_\beta), \quad \beta = S, W, A. \tag{14}$$

Using the above, it is possible to define the volume fractions ϕ_β, porosity n and degree of saturation S_r as follows:

$$\phi_\beta \equiv \frac{V_\beta}{V} = \frac{\varrho_\beta}{\hat{\varrho}_\beta}, \quad \sum_\beta \phi_\beta = 1, \tag{15}$$

$$n \equiv \frac{V - V_S}{V} = \phi_W + \phi_A, \quad S_r \equiv \frac{V_W}{V - V_S} = \frac{\phi_W}{n}, \quad e \equiv \frac{V_A + V_W}{V_S} = \frac{n}{1 - n}.$$

Furthermore, noting the additivity property of energy, it is most accurate to express the free energy per unit volume f of unsaturated soils by summing up the volumetric contributions from the three distinct components using:

$$f = \sum_\beta \phi_\beta \hat{f}_\beta(\hat{\varrho}_\beta) = \sum_\beta (\varrho_\beta/\hat{\varrho}_\beta) \hat{f}_\beta, \tag{16}$$

where the possibility of temperature dependence of $\hat{f}_\beta$ was neglected, as it is not central to accounting for the phenomenon of suction. If temperature dependence would be needed, it is sufficient to include it in $\hat{f}_\beta = \hat{f}_\beta(T, \hat{\varrho}_\beta)$.

With the f given in terms of the three intrinsic free energies of the different components $\hat{f}_\beta$, the thermodynamic pressure $P_T \equiv \varrho(\partial f/\partial\varrho) - f = \sum \varrho_\beta(\partial f/\partial\varrho_\beta) - f$ and partial chemical potentials $\mu_\beta \equiv \partial f/\partial\varrho_\beta$ are (for those interested in the details, see the rather subtle derivation in [2])

$$P_T = \sum_\beta \hat{P}_\beta \left[1 - \varrho \frac{\partial}{\partial\varrho}\right] \phi_\beta, \tag{17}$$

$$\mu_\beta = \hat{\mu}_\beta - \sum_\alpha \hat{P}_\alpha \frac{\partial\phi_\alpha}{\partial\varrho_\beta}, \tag{18}$$

where

$$\hat{P}_\beta \equiv -\frac{\partial(\hat{f}_\beta/\varrho_\beta)}{\partial(1/\hat{\varrho}_\beta)}, \tag{19}$$

$$\hat{\mu}_\beta \equiv \frac{\partial \hat{f}_\beta}{\partial\hat{\varrho}_\beta}, \tag{20}$$

express the intrinsic pressure and chemical potential of the β component, respectively.

We therefore see from Eq. (17) that P_T is made of two terms. The first term, i.e. $\sum_\beta \hat{P}_\beta \phi_\beta$, represents a simple volumetric average of intrinsic pressures of the three components, while the second term provides a further correction due to surface tensions. Similarly, the last term in Eq. (18) for μ_β vanishes for saturated soils, and thus it designates the differences in unsaturated soils between partial and intrinsic

chemical potentials arising due to surface tensions that differentiate between the intrinsic pressures. In saturated soils, in the absence of surface tensions, the intrinsic pressures are equal, and thus the intrinsic chemical potentials are also equal to the partial chemical potentials. The distinction between intrinsic and partial chemical potentials is therefore pivotal for the interpretation of suctions in unsaturated soil.

5.1 Deviations from Common Pressure

If there were no surface tensions, force equilibrium would imply equal intrinsic pressures, which could be designated by a 'common pressure' [2] $P_0 \equiv \hat{P}_\beta$. However, in unsaturated soils one does actually have to deal with surface tensions, and thus those intrinsic pressures deviate from that common pressure:

$$\Delta \hat{P}_\beta = \hat{P}_\beta - P_0. \tag{21}$$

These deviations in the intrinsic pressures from the common pressure depend on their corresponding intrinsic densities, and those dependencies can most generally be represented in terms of simple first order linear elastic compression laws:

$$\Delta \hat{P}_\beta = K_\beta \frac{\Delta \hat{\varrho}_\beta}{\hat{\varrho}_\beta}, \tag{22}$$

where $\hat{\varrho}_\beta^0$ is the intrinsic density at the suctionless limit and $\Delta \hat{\varrho}_\beta = \hat{\varrho}_\beta - \hat{\varrho}_\beta^0$; and $K_\beta = \hat{\varrho}_\beta \frac{\partial \hat{P}_\beta}{\partial \hat{\varrho}_\beta}$ is the compressibility of the β components. Here, the compressibilities of the three components are all approximated to be density-independent. This is actually a fairly accurate relation due to the expectedly very small values of those intrinsic pressure deviations from the common pressure P_0 (deviations from a so-called, the 'suctionless limit').

5.2 Energy Minimisation

Next, we note that given an explicit expression for the free energy in Eq. (16), both the thermodynamic pressure in Eq. (17) and the effective stress in Eq. (9) could now be expressed explicitly in terms of six densities: three partial densities, ϱ_β, and three intrinsic ones, $\hat{\varrho}_\beta$. While the partial densities are actually state variables, which one can control, the intrinsic densities vary as a function of the partial ones and the medium in hand. Therefore, the final solution requires three additional conditions, in order to be able to express P_T and σ_{ij}^{eff} in terms of only the partial densities. One known condition is the additivity relation in the volume fraction in Eq. (15). The two remaining conditions are those proposed in [2], which come to respect the

actual material in hand, in terms of energy minimisation that accounts for the species compressibilities, and water retention curves, which both encode the material in terms of how the intrinsic densities adjust for the given set of partial densities. Those three conditions can be considered by minimising the free energy with constraints.

Generally speaking, for fix contents of species, the soil minimises its energy such that the air pressure increases and the water pressure decreases due to the smaller surface energy for solid–water interfaces than solid–air interfaces (which implies reduced interfaces with air). The phenomenon of reduced water pressure is frequently called *suction*. The effective stress of unsaturated media is usefully measured by eliminating from the externally imposed/measured air pressure u_A, the externally imposed/measured water pressure u_W, similarly the '*measured suction*' quantity is then tracked experimentally

$$s = u_A - u_W,\tag{23}$$

where plotting this suction quantity versus the various densities is commonly known in the literature as the 'water retention curve'.

Following Jiang et al. [2], it is pivotal to recognise that the important (yet usually forgotten) fact that the measured suction s is generally not the '*intrinsic suction*':

$$\hat{s} \equiv \hat{P}_A - \hat{P}_W,\tag{24}$$

which actually amounts the difference between the intrinsic pressures within the soil itself. The differences between $\hat{s}$ and s will later be evaluated by employing the equilibrium conditions on chemical potentials for the fluid transfers across the boundaries between the material and the measurement cells.

Since the intrinsic suction encodes the actual properties of the soil and its interfaces with the surrounding fluids, the energy minimisation should be made by respecting this property $\hat{s} \equiv \hat{P}_A - \hat{P}_W$. In addition, the minimisation should also acknowledge the additivity of the volume fractions $\phi = \sum_\beta \phi_\beta$ [2]:

$$\delta \int (f - L_1 \sum_\beta \phi_\beta - L_2[\hat{P}_A - \hat{P}_W])\mathrm{d}^3 r = 0,$$

where L_1 and L_2 are the Lagrange multipliers for the two corresponding constraints, such that through the minimisation we find $\hat{P}_S = \hat{P}_W + L_2 K_W/\phi_W = \hat{P}_A - L_2 K_A/\phi_A = L_1 = P_0 + \Delta P_0$, which in return implies $\hat{s} \equiv \hat{P}_A - \hat{P}_W = L_2(K_A/\phi_A + K_W/\phi_W)$. Finally, the result could be simplified further by acknowledging that air compressibility is much smaller than water compressibility: $K_A \ll K_W$, which yields the following reduced condition:

$$\hat{P}_A = \hat{P}_S = \hat{P}_W + \hat{s} = P_0 + \Delta P_0,\tag{25}$$

such that using Eq. (22) and the small compressibility of air, we find:

$$\Delta \hat{P}_A = \Delta \hat{P}_S = \Delta P_0 = 0, \tag{26}$$

and therefore, using Eq. (21), we also find

$$\hat{s} = \Delta \hat{P}_A - \Delta \hat{P}_W = -\Delta \hat{P}_W = -K_W \frac{\Delta \hat{\varrho}_W}{\hat{\varrho}_W}. \tag{27}$$

5.3 Chemical Potentials, Intrinsic and Measured Suctions

Consider a conventional measurement cells with stiff porous walls permitting only water or only air to penetrate through them, such that the corresponding cells contain only water or air (see Fig. 1). For a given temperature, the cell fluids are characterised by their respective density $\varrho_\beta^{\text{cell}}$, free energy $f_\beta^{cell} \equiv \hat{f}_\beta(\varrho_\beta^{\text{cell}})$, chemical potential μ_β^{cell}, and pressure u_β, such that

$$\mu_\beta^{cell} = \hat{\mu}_\beta(\varrho_\beta^{\text{cell}}), \quad u_\beta = \hat{P}_\beta(\varrho_\beta^{\text{cell}}), \quad \beta = A, W, \tag{28}$$

where u_β are the externally measured pressures. Having measured u_A and u_W, we can therefore rescue the cell densities. We also note that the measured suction is
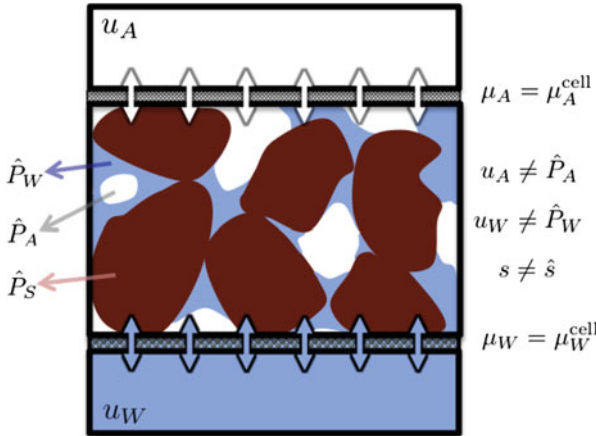
Fig. 1 The subtleties of dealing with 'suctions', as rigorously described by Jiang et al. [2]: Thermodynamic equilibrium along walls require the chemical potentials in the soil (μ_A and μ_W) to match those in the measurement cells (μ_A^{cell} and μ_W^{cell}). It does not require equality between the intrinsic (hatted quantities) and measured (non-hatted) pressures. Subsequently, we must distinguish between intrinsic ($\hat{s} = \hat{P}_A - \hat{P}_W$) and measured ($s = u_A - u_w$) suctions

conventionally given through their difference

$$s = \hat{P}_A(\varrho_A^{\text{cell}}) - \hat{P}_W(\varrho_W^{\text{cell}}), \tag{29}$$

which is not the intrinsic suction

$$\hat{s} = \hat{P}_A(\hat{\varrho}_A) - \hat{P}_W(\hat{\varrho}_W). \tag{30}$$

In order to eventually be able to amount the difference between the measured and intrinsic suctions, one should also recall that equilibrium with respect to mass transfers between the soil and the cells is expressed by equating the corresponding partial chemical potentials across the soil boundaries with the measurement cells

$$\mu_\beta(\varrho_A, \varrho_W, \varrho_S) = \mu_\beta^{\text{cell}}(\varrho_\beta^{\text{cell}}). \tag{31}$$

Figure 1 provides a useful illustration for this fundamental difference between the intrinsic and measured suctions and for the equilibrium condition between the chemical potentials across the boundaries with the measurement cells.

5.4   From non-Bishop Solution to Bishop Solution

The above result is a complete theory, from which the exact analytic solution for P_T and thus for σ_{ij}^{eff} were drawn as a function of the measured air and water pressures (see [2]). Unfortunately, the end expressions extend over several pagers, and therefore were not spelled out in a paper, as it would be far from being illuminating. Nevertheless, this analytic solution has actually been used to validate a separate approximation scheme, as detailed in length in [2]. Here, it is sufficient to extract some important outcomes of this approximation scheme, as the corresponding derivation was rather involved.

Briefly speaking, the corresponding derivation involved a second order Taylor approximation for the free energy. Specifically, we find

$$\Delta u_\alpha = u_\alpha - P_0 = \sum_\beta \left[\frac{\hat{\varrho}_\alpha \phi_\beta}{2K_\beta} \frac{\partial(\Delta \hat{P}_\beta)^2}{\partial \varrho_\alpha} \right]. \tag{32}$$

Continuing with Eqs. (26) and (27) yields

$$\Delta u_\beta = \frac{\phi_W \hat{s}}{K_W} \hat{\varrho}_\beta \hat{s}_\beta, \quad \text{where} \quad \hat{s}_\beta = \frac{\partial \hat{s}}{\partial \varrho_\beta}. \tag{33}$$

We can also express the deviation in the thermodynamic pressure from the common pressure with

$$\Delta P_T = \sum \phi_\beta \hat{\varrho}_\beta \Delta \mu_\beta = \sum \phi_\beta \Delta u_\beta,$$

and therefore, the general solution for the thermodynamic pressure is then given as:

$$P_T = P_0 + \sum_\beta \phi_\beta \Delta u_\beta = \sum \phi_\beta u_\beta = u_A + \sum_\beta \phi_\beta (u_\beta - u_A), \qquad (34)$$

which can be compared to the Bishop's equation [27] $P_T = u_A - \chi(u_A - u_W)$ with the Bishop's coefficient calculable from

$$\chi = \phi_W + \phi_S(u_A - u_S)/(u_A - u_W). \qquad (35)$$

5.5 General Expression for the Effective Stress

Considering Eqs. (33), (34), and (35), we can finally find most general expressions for the thermodynamic pressure, Bishop's coefficient, and measured suction s (measured water retention curve), in a way that strictly links them all to the intrinsic suction of the most general form $\boxed{\hat{s} \equiv \hat{s}(\varrho_A, \varrho_W, \varrho_S)}$ as follows:

$$P_T = u_A - \chi(u_A - u_W), \qquad (36a)$$

$$\chi \equiv \chi(\varrho_A, \varrho_W, \varrho_S) = \phi_W + \phi_S \left[\frac{\hat{\varrho}_A \hat{s}_A - \hat{\varrho}_S \hat{s}_S}{\hat{\varrho}_A \hat{s}_A - \hat{\varrho}_W \hat{s}_W} \right], \qquad (36b)$$

$$s \equiv s(\varrho_A, \varrho_W, \varrho_S) = \frac{\phi_W \hat{s}}{K_W} \left(\hat{\varrho}_A \hat{s}_A - \hat{\varrho}_W \hat{s}_W \right), \qquad (36c)$$

with $\hat{s}_\beta = \partial \hat{s}/\partial \varrho_\beta$. We note that our analytic approximation for the Bishop's coefficient described above could be compared with the exact (and longer) analytic solution. From this evaluation, for all practical purposes the analytic Bishop approximation above could be considered exact, for saturation degrees $\gtrsim$2–3%. Also, the above equations present an intimate relationship between χ and s (i.e., between the effective stress principle and the water retention curves), through their mutual dependence on $\hat{s}$, which supports the observation of [28, 29] based on empirical and micro-structural arguments.

This is an extraordinarily general thermodynamic solution to the Bishop's coefficient [27], though unlike Bishop, one which reveals the strict thermodynamic dependencies on all the three partial densities (ϱ_W, ϱ_S, and ϱ_A). Considering the links between Eqs. (36) and (33) we therefore find that for this general case the soil

water retention curve may depend on the measured air pressure u_A, even for fixed suction. Previously, not much attention has been paid to recovering this type of dependence, which should certainly require a most careful experimental evaluation. In fact, soil water retention curves are often recovered experimentally by accepting the *axis translation* concept that requires one to neglect any dependence of s on u_A. However, some authors have questioned the validity of this simplification [8, 30], which does actually hint for possible dependence of s on u_A.

5.6 Reduced Expressions for the Effective Stress

The result expressed in Eq. (36) applies to any soil, with any properties of water retention curves, where most generally one may have $\hat{s} \equiv \hat{s}(\varrho_A, \varrho_W, \varrho_S)$. However, most usually water retention curves are expressed in ways that do not show dependence on air density, where one can write $\hat{s} \equiv \hat{s}(\varrho_W, \varrho_S)$. Since the water and solid partial densities can be expressed in terms of index properties as in Eqs. (15), one can, for example, always replace the partial water and solid densities with the saturation degree (S_r) and porosity (n). Thus, for the case $\boxed{\hat{s} \equiv \hat{s}(S_r, n)}$ it was found that [2]:

$$P_T = u_A - \chi(u_A - u_W), \tag{37a}$$

$$\chi \equiv \chi(S_r, n) = S_r - n(1-n)\frac{\partial \hat{s}/\partial n}{\partial \hat{s}/\partial S_r}, \tag{37b}$$

$$s \equiv s(S_r, n) = -\frac{S_r}{K_W}\frac{\partial \hat{s}}{\partial S_r}\hat{s}. \tag{37c}$$

Of course, it is always possible to replace the porosity with the void ratio (e), such that for water retentions obeying $\boxed{\hat{s} \equiv \hat{s}(S_r, e)}$ we find

$$P_T = u_A - \chi(u_A - u_W), \tag{38a}$$

$$\chi \equiv \chi(S_r, e) = S_r - e\frac{\partial \hat{s}/\partial e}{\partial \hat{s}/\partial S_r}, \tag{38b}$$

$$s \equiv s(S_r, e) = -\frac{S_r}{K_W}\frac{\partial \hat{s}}{\partial S_r}\hat{s}. \tag{38c}$$

It could be shown that the relationship above between χ and the intrinsic suction $\hat{s}$ is remarkably identical to the one proposed simultaneously by Vaunat and Casini [29] using simplified micro-structural considerations. The above set of equations further provide the connection between the intrinsic suction $\hat{s}$ to the

externally measured/imposed suction s, while also showing that they are only a subset of the more general possible case in Eq. (36).

Finally, we note that in the absence of any dependence on the void ratio or porosity, that is for the case of $\boxed{\hat{s} \equiv \hat{s}(S_r)}$, we have

$$P_T = u_A - \chi(u_A - u_W), \tag{39a}$$

$$\chi \equiv \chi(S_r) = S_r, \tag{39b}$$

$$s \equiv s(S_r) = -\frac{S_r}{K_W} \frac{\partial \hat{s}}{\partial S_r} \hat{s}. \tag{39c}$$

All of the above reveals the strict restrictions thermodynamics impose on the structure of the effective stress, along with its relationships to the intrinsic suction. Since the intrinsic suction is not generally easily accessible, the fact that the above equations also connect the intrinsic suction to the measured suction is highly useful. Therefore, from a thermodynamics standpoint the effective stress of unsaturated media is strongly connected to the water retention curves.

5.7 Connecting Effective Stress to Water Retention

The two previous Sects. 5.5 and 5.6 thermodynamically formulate how the effective stress should be defined for any given soils in relations to its water retention curves. At first, one needs to identify how their measured/imposed suction s depends on the imposed/measured partial densities ϱ_β. Since, in most cases researchers have opted to use an s independent of air density, they would normally require something like $s = s(S_r, n)$ or $s = s(S_r, e)$.

For example, consider the case with $s = s(S_r, e)$, where the definition of the effective stress is given by Eqs. (38). First, one should carry out experiments to establish the specific dependence of the water retention curves on S_r and e, which could take, for example, a possible form such as $s = A(1 + e)^{-\beta} \left[\frac{1 - S_{re}}{S_{re}^\alpha} \right]$, where $S_{re} = \left\langle \frac{S_r - S_{res}}{1 - S_{res}} \right\rangle$ is the effective saturation degree; S_{res} the residual saturation degree; the function $\langle x \rangle \equiv \frac{1}{2}(|x| + x)$; while A, β, and α being water retention parameters controlling the shape of the water retention curves. Next, given this particular experimentally fitted family of lines, one should integrate s to get $\hat{s}$ using Eq. (38c) under constant void ratio e, while considering the condition of $\hat{s}$ being zero when $S_r = 1$. Finally, upon differentiation of $\hat{s}$ with respect to both S_r and e, one can obtain the Bishop's parameter χ using Eq. (38b). For the current example, the

strict connections between the effective stress and the two suctions can be written explicitly as:

$$s \equiv s(S_r, e) = A(1 + e)^{-\beta} \left[\frac{1 - S_{re}}{S_{re}^{\alpha}} \right], \tag{40a}$$

$$\hat{s} = \hat{s}(S_r, e) = \sqrt{2AK_W(1 + e)^{-\beta} \left[\frac{1 - \alpha + \alpha S_{re} - S_{re}^{\alpha}}{\alpha(1 - \alpha)S_{re}^{\alpha}} \right]}, \tag{40b}$$

$$\chi \equiv \chi(S_r, e) = S_r \left(1 - \beta(1 - S_{res}) \frac{e}{1 + e} \left[\frac{1 - \alpha + \alpha S_{re} - S_{re}^{\alpha}}{\alpha(1 - \alpha)(1 - S_{re})} \right] \right), \tag{40c}$$

where χ is dependent on both S_r and e, in terms of three parameters (S_{res}, α, β). For soils with residual degrees of saturation $S_{res} = 0$ the above model reduces to the example given in [2].

According to either of these models, for soils whose soil water retention that is insensitive to void ratio variations (when $\beta = 0$), the parameter χ is simply becoming the degree of saturation S_r. However, since soil water retention curves are actually strongly sensitive for variations in void ratio, we most generally expect $\chi \neq S_r$. Although the model above is only one possible example, it can already explain the possibility for such a wide range of experimental χ data. For example, in our previous paper [2] we already showed how the above model (for the case of $S_{res} = 0$, and under constant void ratio) is capable of rationalising the empirical suggestions by both Aitchison [32] (using $\alpha = 1$) and Khalili and Khabbaz [33] (using $\alpha = 1.75$), for their different suggestions of the constant slope of the asymptote of the plot of χ versus the logarithm of measured suction for growing suctions.

As another example, the above model can also explain the extremely broad range of observable trends for χ against S_r, which were experimentally found for different soils in the classical work by Jennings and Burland [31], as shown in Fig. 2. Note, however, that Jennings and Burland unfortunately did not describe the water retention curves and how they depend on saturation and void ratio, and thus we had some freedom in choosing the parameters. We therefore encourage interested authors to carry out future experimental campaigns that would require to establish careful data for the dependence of both the Bishop's parameter and the water retention curves on the various densities. Also note that during their experiments the void ratios along each of the lines for χ could have varied, but for simplicity they were kept constant when determining the model parameters.

It is also interesting to estimate the difference between the intrinsic and measured suctions. Take, for example, the parameters used to fit curves 1 and 5 in Fig. 2. Case 1 with $\alpha = 1.75$, $\beta = 8$, $S_{res} = 0.2$, with a fixed void ratio $e = 1$. Case 5 with $\alpha = 2$, $\beta = -2.75$, $S_{res} = 0$, and the same fixed void ratio $e = 1$. Also note that the coefficient A does not affect χ (see Eq. (40c)), so given the absence of experimental data for the soil water retention curves, A was here selected arbitrarily for the two cases such that their measured soil water retention curves could show approximately
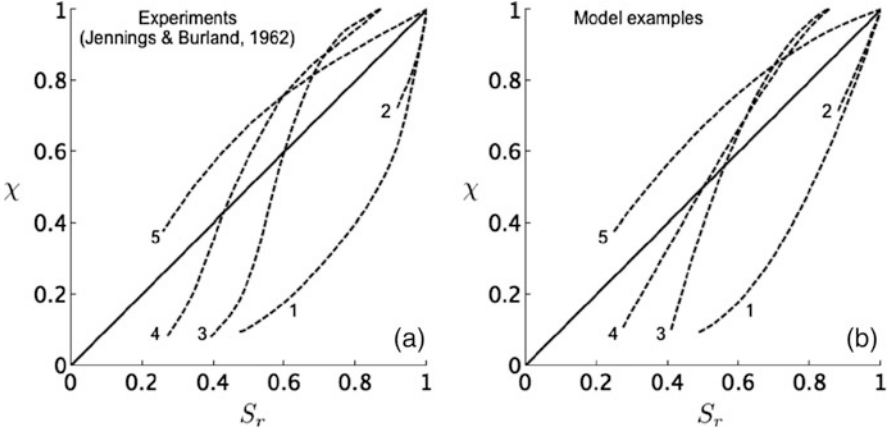
Fig. 2 Bishop's χ parameter plotted against saturation degree S_r for a wide range of soils (including clays, silts, and their mixtures): (**a**) Experimental data by Jennings and Burland [31]; (**b**) Model results using different soil water retention parameters. In both cases, the simple line $\chi = S_r$ was added to guide the eye (which is the theoretical line for water retentions independent of void ratio). Notice that the model can give $\chi > 1$ and that those large values were not shown, as they seem to have also been excluded experimentally
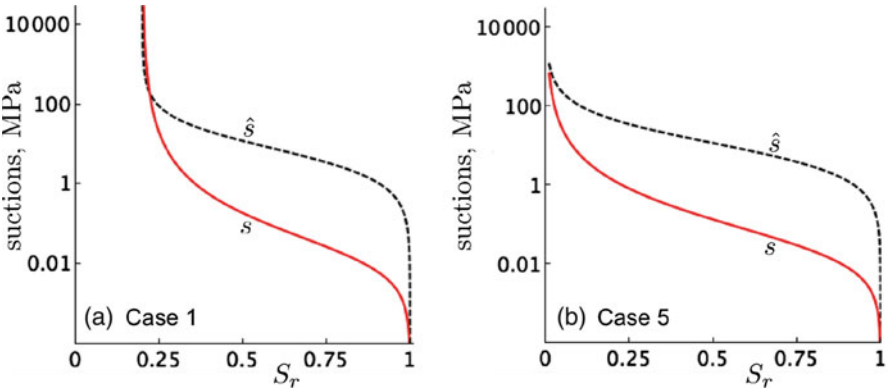
Fig. 3 Comparison between the measured s and intrinsic $\hat{s}$ suctions for the parameters used to model cases 1 and 5 shown in Fig. 2

the same levels of suctions at high saturations. Finally, to determine the intrinsic suction we use the bulk modulus of water, $K_W = 2 \cdot 10^3$ MPa. Accordingly, the difference between the intrinsic and measured suctions for this case is portrayed in Fig. 3. As is highlighted, although there is a certain qualitative agreement between those suctions, they are quantitatively different, at some degrees of saturation by up to two orders of magnitude.

To explore the often neglected effect of void ratio on the Bishop's parameter, we plot the latter against the degree of saturation, for both positive and negative β values

Fig. 4 Example for the possible dependencies of the Bishop's parameter χ on the void ratio e, for positive and negative β parameters
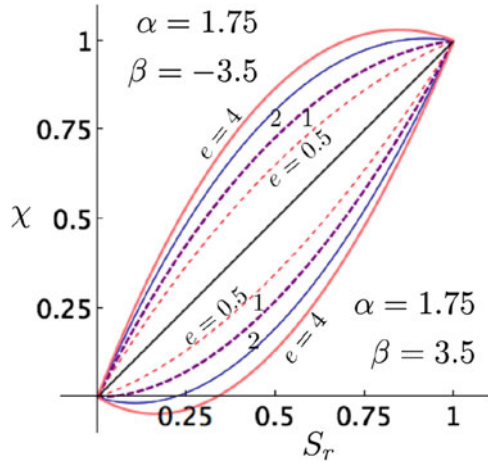
and for various void ratios e in Fig. 4. As shown, thermodynamically speaking, there are no restrictions on χ from being either negative or over unity under large void ratios. According to the current model, a positive β parameter may yield negative χ, while a positive β parameter can yield a χ larger than unity, but in both cases those extreme scenarios may be expected under very large void ratios.

6 Discussion

The definition of effective stress in unsaturated soil media has been a stubborn problem for more than six decades. The more physically based attempts to formulate the problem were strongly dependent on a large number of strong simplifying assumptions, ranging from neglecting the role of surface tension to incorporating homogenisation procedures that have nothing to do with thermodynamics. Some of the more complicated formulations have attempted to follow the complex interfacial physics developing within the soil, but the related surfaces are knowingly so geometrically complicated that it became impossible to adopt this line of work without introducing, again, extremely strong assumptions that simplify the geometrical picture.

The net result of these various physically inspired formulations has therefore yielded results that could not explain the plethora of empirically observed effective stresses, such as shown in Fig. 2. Subsequently, having to deal with this observable reality, a high number of researchers have decided to ignore the physical laws of nature, and rather continue in a purely phenomenological way, simply by trying to come up with some ad hoc curves that best fit the experimental observations at hand. Once new observations become available, those curves will be modified. Unfortunately, of course, this non-scientific approach does not help our progress in

the field, as every soil and every loading condition would have nothing to do with the original fits, and thus one will gain nothing but finding what they already knew from the available data.

Finally, none of these previous attempts (either physically based or empirically based) had appropriately addressed the intimate links, yet strong differences, between the externally measured/applied suction and the intrinsic suction within the soil.

This paper reviewed the essential points that we recently adopted in our recent paper [2] to finally resolve the problem of effective stress in unsaturated media. In summary, some of those key novel points include:

1. Using the hydrodynamic procedure (see relevant details in [1]) to identify the general meaning of effective stress in Eq. (9), as the total Cauchy stress minus the thermodynamic pressure (itself connected to the overall partial density of the mixture).
2. Expanding the dependence of the thermodynamic pressure with respect to all the three partial densities in soil mixtures (see for example Eq. (17)).
3. Acknowledging the additivity of the partial free energy, and taking it as the sum of the species' volume fractions times the correspondingly known intrinsic free energies within those species (see Eq. (16)).
4. Reducing the complexity of having a partial free energy dependent on six densities (three partial, and three intrinsic ones), by respecting that the sum of volume fractions is unity, that the bulk modulus of the air is much smaller than that of water, and carrying out energy minimisation.
5. Subjecting the energy minimisation to a constraint that takes along the knowledge of intrinsic suction, itself being connected to the measured suction through equilibrium of chemical potentials across the boundaries of the soil with the measurement cells.
6. While the problem at this stage was solved analytically, the complexity of the solution was further reduced using a second order Taylor's approximation around a 'suctionless limit', an approximation that yields an effective stress that generally follows Bishop's equation and further provides the analytic solution for the Bishop's coefficient (see general result in Eq. (36), followed by special cases in Eqs. (37), (38), and (39)).

Although we have managed to address the key challenges for establishing the effective stress of unsaturated soils, there are still a few special phenomena that require development within the hydrodynamic procedure. For example, the hydrodynamic solution in this paper was based on requiring thermodynamic equilibrium. Although the effective stress result should still hold, the treatment of hysteresis in water retention curves during drying and wetting cycles would require to accept additional state variables whose evolution laws relax towards equilibrium. Based on our work in progress, we envisage that the deviation of the intrinsic suction itself from an equilibrium suction state will be one of those variables. In order to follow different water retention branches upon continuous wetting and drying, the formulation will also expectedly include an additional mesoscopic temperature

variable that represents the degrees of freedom of mesoscopically vibrating internal surfaces.

At small degrees of saturation the response of the soil mixture might also depend on cohesion effects that arise due to disconnected and small capillary water bridges which energetically bind grains, thus leading to intricate new phenomena [34]. We expect that this might be solved by adding terms to the free energy. The net result might explain the problem of diverging measured suctions at very low saturations, which often seems to defy the incapacity of water to carry indefinitely high tensile forces. With the help of cohesion, the divergence in measured suctions would not carry itself into the interpreted intrinsic suction, which may quite intuitively go back to zero with S_r approaching to zero. On the other hand, the cohesion effects will expectedly die off under larger saturations (greater than $\approx$2–3%, as evidenced, for example, through the vanishing role of cohesion on the overall dynamic friction coefficient of increasingly wetted sand [34]), thus producing effectively the same results presented in this paper.

References

1. Itai Einav and Mario Liu. Hydrodynamic derivation of the work input to fully and partially saturated soils. *Journal of the Mechanics and Physics of Solids*, 110:205–217, 2018.
2. Y. Jiang, I. Einav, and M. Liu. A thermodynamic treatment of partially saturated soils revealing the structure of effective stress. *Journal of the Mechanics and Physics of Solids*, 100:131–146, 2017.
3. L.D. Landau and E.M. Lifshitz. *Statistical Physics*. Butterworth-Heinemann, 1980.
4. L. D. Landau and E. M. Lifshitz. *Fluid Mechanics*. Butterworth-Heinemann, 1987.
5. I. M. Khalatnikov. *Introduction to the Theory of Superfluidity*. Benjamin, New York, 1965.
6. P.G. de Gennes and J. Prost. *Continuum Mechanics*. Clarendon Press, Oxford, 1993.
7. Yimin Jiang and Mario Liu. Granular solid hydrodynamics. *Granular Matter*, 11:139, 2009.
8. Rafael Baker and Sam Frydman. Unsaturated soil mechanics: Critical review of physical foundations. *Engineering Geology*, 106(1–2):26–39, 2009.
9. Paul R. Day. The moisture potential of soils. *Soil Science*, pages 391–400, 1942.
10. N. E. Edlefsen and A. B. C. Anderson. Thermodynamics of soil moisture. *Hilgardia*, 15(2):31–298, February 1943.
11. K. L. Babcock and R. Overstreet. The extra-thermodynamics of soil moisture. *Soil Science*, 83(6):455–464, 1957.
12. Garrison Sposito. *The thermodynamics of soil solutions*. Oxford University Press Oxford ; New York, 1981.
13. Kanthasamy K. Muraleetharan and Changfu Wei. Dynamic behaviour of unsaturated porous media: governing equations using the theory of mixtures with interfaces (TMI). *International Journal for Numerical and Analytical Methods in Geomechanics*, 23(13):1579–1608, 1999.
14. K. Hutter, L. Laloui, and L. Vulliet. Thermodynamically based mixture models of saturated and unsaturated soils. *Mechanics of Cohesive-frictional Materials*, 4(4):295–338, 1999.
15. William G Gray and Bernhard A Schrefler. Thermodynamic approach to effective stress in partially saturated porous media. *European Journal of Mechanics - A/Solids*, 20(4):521–538, 2001.
16. B. A. Schrefler. Mechanics and thermodynamics of saturated/unsaturated porous materials and quantitative solutions. *Applied Mechanics Reviews*, 55(4):351–388, 2002.

17. Lyesse Laloui, Georg Klubertanz, and Laurent Vulliet. Solid–liquid–air coupling in multiphase porous media. *International Journal for Numerical and Analytical Methods in Geomechanics*, 27(3):183–206, 2003.
18. R. de Boer. *Trends in Continuum Mechanics of Porous Media*. Theory and Applications of Transport in Porous Media. Springer Netherlands, 2005.
19. William G. Gray, Bernhard A. Schrefler, and Francesco Pesavento. Work input for unsaturated elastic porous media. *Journal of the Mechanics and Physics of Solids*, 58(5):752–765, 2010.
20. Olivier Coussy, Jean-Michel Pereira, and Jean Vaunat. Revisiting the thermodynamics of hardening plasticity for unsaturated soils. *Computers and Geotechnics*, 37(1–2):207–215, 2010.
21. C. G. Zhao, Y. Liu, and F. P. Gao. Work and energy equations and the principle of generalized effective stress for unsaturated soils. *International Journal for Numerical and Analytical Methods in Geomechanics*, 34(9):920–936, 2010.
22. Ehsan Nikooee, Ghassem Habibagahi, S. Majid Hassanizadeh, and Arsalan Ghahramani. Effective stress in unsaturated soils: A thermodynamic approach based on the interfacial energy and hydromechanical coupling. *Transport in Porous Media*, 96(2):369–396, 2012.
23. G. Buscarnera and I. Einav. The yielding of brittle unsaturated granular soils. *Géotechnique*, 62(2):147–160, 2012.
24. M.E. Gurtin, E. Fried, and L. Anand. *The Mechanics and Thermodynamics of Continua*. Cambridge University Press, 2010.
25. H. Ziegler. *An introduction to thermomechanics*. North-Holland series in applied mathematics and mechanics. North-Holland Pub. Co., 1977.
26. I.F. Collins and G.T. Houlsby. Application of thermomechanical principles to the modelling of geotechnical materials. In *Proceedings of the Royal Society of London A: Mathematical, Physical and Engineering Sciences*, volume 453, pages 1975–2001. The Royal Society, 1997.
27. A. W. Bishop. The principle of effective stress. *Teknisk Ukeblad*, 106(39):859–863, 1959.
28. E.E. Alonso, J.-M. Pereira, J. Vaunat, and S. Olivella. A microstructurally based effective stress for unsaturated soils. *Géotechnique*, 60(12):913–925, 2010.
29. Jean Vaunat and F Casini. A procedure for the direct determination of bishop's χ parameter from changes in pore size distribution. *Géotechnique*, 67(7):631–636, 2017.
30. Dani Or and Markus Tuller. Cavitation during desaturation of porous media under tension. *Water Resources Research*, 38(5):19–1–19–14, 2002.
31. J. E. B. Jennings and J. B. Burland. Limitations to the use of effective stresses in partly saturated soils. *Géotechnique*, 12(2):125–144, 1962.
32. G. D. Aitchison. Relationships of moisture stress and effective stress functions in unsaturated soils. In *Golden Jubilee of the International Society for Soil Mechanics and Foundation Engineering: Commemorative Volume*, pages 20–25. Engineers Australia, Barton, ACT: Institution of Engineers, Australia, 1985.
33. Khalili N. and Khabbaz M. H. A unique relationship for χ for the determination of the shear strength of unsaturated soils. *Géotechnique*, 48(5):681–687, 1998.
34. Abdoulaye Fall, B Weber, M Pakpour, Nicolas Lenoir, N Shahidzadeh, J Fiscina, C Wagner, and Daniel Bonn. Sliding friction on wet and dry sand. *Physical review letters*, 112(17):175502, 2014.

Notes on Constitutive Relations for Porous Solids

Pasquale Giovine

Abstract The thermo-mechanical balance and constitutive equations for a porous material with large irregular pores are investigated by imposing internal kinematic and thermal constraints on ellipsoidal microstructures, in order to involve in the constitutive relations higher-order derivatives of macro- and micro-displacements and/or temperature avoiding classical incompatibilities.

Keywords Continuum with affine microstructure · Internal constraints · Solid with nano-pores · Constitutive relations · Higher-order continua · Heat propagation

1 Introduction

The theories of porous materials, fully or partially saturated with fluids, are of interest in seismology, geotechnics, and other fields within the frame of soil mechanics. First efforts to derive the governing balance equations were obtained in [4], and after in [5], from purely mechanical considerations, in a somewhat intuitive way. Extensive literature on this topic, many details concerning pioneering works and some new tendencies in the theories of porous media, are available in the essays [3, 24, 28].

In short, Biot's pioneering approach had a homogenization view on the matter. Biot's set of equations involves the balance of momentum pertaining to the matrix and Darcy's law describing fluid motion inside and across pores [4]. Such an approach addressed several works on this matter from mechanical and analytical viewpoints (see [2, 19]).

P. Giovine (✉)
Department of Civil, Energy, Environment, and Materials Engineering (DICEAM),
University 'Mediterranea' of Reggio Calabria, Reggio Calabria, Italy
e-mail: giovine@unirc.it; http://www.unirc.it/scheda_persona.php?id=361

In 1979, Nunziato and Cowin [58] characterized porous solids with an approach falling within the general model-building framework of the mechanics of complex materials [8, 52]. In that view, the void volume fraction is considered as an independent variable with time rate associated with pore-scale peculiar interactions, considered in a sense as perturbations of standard contact actions.

However, pores do not exist per se: they are determined by the surrounding material. Consequently, it seems to be reasonable considering the void volume fraction (or the fluid partially saturating voids) constrained to be connected with the macroscopic strain. In this sense we are in the case of what we call latent microstructures in the terminology of the mechanics of complex materials [7, 52].

When the pores are small and finely dispersed, as in "Voids theories," an isotropic tensor can describe possible pore homogeneous vibrations (see [58] and §4 of [14]); alternatively, in the case in which each material element of the body contains a large cavity filled with an inviscid fluid or an elastic inclusion, both of negligible mass, a microstretch tensor would be more appropriate to characterize the possible micro-motions that allows the body to have distinct micro-strains along the principal axes of micro-deformation, in the absence of micro-rotations (see [31, 33, 34, 37, 59]). Even in this case, if vugs or voids like them are devoid of matter, the microstate is completely determined by the macro-strain, so that only an indirect trace of the microstructure remains: it becomes "latent" [7, 52] and remains internally bound to the left (macro) Cauchy–Green tensor [38, 41].

In the latter case, the Cauchy stress tensor might depend on higher-order time and/or spatial derivatives of displacement and, in general, it could result not symmetric [39]. Thermodynamic compatibility of higher-order strain gradients requires an influx of mechanical energy across the border of any part of the body, what is called a interstitial working in [26, 35]. Such an additional term depends on internal micro-actions and in excess with respect to the one due only to macro-tractions. The interpretation of those constitutive laws are in line with an old remark of Toupin [60] on the desirability of seeing hyperelastic materials of the second grade such as continua with affine microstructure of Cosserat type with constrained micro-rotations (see, also, [21, 44, 53]).

In this work we present some new suggestions concerning the constitutive prescriptions for a model of porous materials, as already introduced in §8.3 of [40] for the incompressible fluid-filled case, which generalize the theories of voids and take into account remarks [50] on the impossibility of such theories to predict size effects in torsion, as they occur in bone mechanics [22] or rod-shaped specimens of dense polyurethane foams [51]. Surely those remarks stimulate a discussion starting from the more general principles of thermodynamics, even in the context of the entropy principle proposed in [57] and already used in soil mechanics for granular materials [36, 42].

An additional analysis of peculiar internal constraints is useful for obtaining primary examples: first, a model for a thermoelastic material with pores of different shapes and sizes, such as materials with evolving microstructures [32, 59] or cancellous bones [23], in which the theory of voids is recovered when the cavities are tiny and poorly distributed; secondly, a general description of microstructural

changes in a macroscopically partially saturated porous conductor with rigid skeleton, a conductor in which we recover, by following the proposal in [54], a finite speed heat propagation.

2 Continua with Affine Microstructure

For a continuous material medium occupying a fit region $\mathcal{B}$, we suppose that each material element is capable of an affine strain distinct from (and independent of) the macroscopic one.

We fix a "natural" reference placement $\mathcal{B}_*$ in the three-dimensional Euclidean space $\mathcal{E}$ [61]). A generic material point of $\mathcal{B}_*$ is denoted by $\mathbf{x}_*$. A motion of duration $\bar{\tau}$ ($\bar{\tau} > 0$) for $\mathcal{B}$, as a continuum with affine microstructure, is described by the following pair of smooth mappings on $\mathcal{B}_* \times [0, \bar{\tau}]$:

$$\mathbf{x} = \mathbf{x}(\mathbf{x}_*, \tau) \in \mathcal{E} \quad \text{and} \quad \mathbf{G} = \mathbf{G}(\mathbf{x}_*, \tau) \in \text{Lin}^+, \tag{1}$$

where $\mathbf{x}$ is the spatial position at time $\tau \in [0, \bar{\tau}]$ of the material point, which occupied the position $\mathbf{x}_*$ in the reference placement $\mathcal{B}_*$, and $\mathbf{G}$ the tensor field value describing the local affine structure; Lin^+ is the set of second-rank tensors with positive determinant (see, also, [33]).

The map $\mathbf{x}(\cdot, \tau)$ is a one-to-one correspondence, for each τ, between the reference placement $\mathcal{B}_*$ and the current placement $\mathcal{B}_\tau = \mathbf{x}(\mathcal{B}_*, \tau)$ of the body $\mathcal{B}$ and, so, the deformation gradient

$$\mathbf{F} := \nabla \mathbf{x}(\mathbf{x}_*, \tau) \ \left(= \frac{\partial \mathbf{x}}{\partial \mathbf{x}_*}(\mathbf{x}_*, \tau) \right) \tag{2}$$

is a double vector assumed to have positive determinant ι ($\iota := \det \mathbf{F} > 0$). $\mathbf{G}$ can be also considered of as a double vector, as is $\mathbf{F}$, and, consequently, we will denote its Cartesian components with one small and one capital index: G_{iJ}: J refers to coordinates in $\mathcal{B}_*$, while i to those in the current configuration $\mathcal{B}_\tau$. By referring only to orthogonal frames, we shall not make distinction between covariant and contravariant components.

Thus, a rigid rotation of the whole body, characterized by the proper orthogonal tensor $\mathbf{Q} \in \text{Orth}^+$ (the collection of all orthogonal tensor fields of the second-order with positive determinant, namely the rotations), changes the value of $\mathbf{G}$ everywhere into $\mathbf{QG}$; in components, we will write:

$$G_{iJ}^{\mathbf{s}} = Q_{ik} G_{kJ}, \tag{3}$$

where the convention, according to which repeated indices are summed, is adopted here and throughout the paper.

Hence, using the following compact notation for the rotation $\mathbf{Q}$ of the observer of characteristic vector $\mathbf{s}$

$$\mathbf{Q} = e^{-\varepsilon \mathbf{s}}, \tag{4}$$

where e is the basis of natural logarithms and ε is the third-rank Ricci's permutation index, we can compute the so-called infinitesimal generator $\mathcal{A}$ of the group of rotations on the microstructure in Lin^+, i.e., the operator describing the effect of observer rotation on the value $\mathbf{G^s}$ of the microstructure; to the first order in $\mathbf{s}$, $\mathcal{A}$ is defined by

$$\mathcal{A}(\mathbf{G}) := \left. \frac{d\mathbf{G^s}}{d\mathbf{s}} \right|_{\mathbf{s}=\mathbf{0}} \tag{5}$$

(see §3 of [8]), that is, a third-rank tensor with components

$$\mathcal{A}_{iJk} = \varepsilon_{ikm} G_{mJ}. \tag{6}$$

From definitions (1), we can define the fields of velocity and of microvelocity over the current placement $\mathcal{B}_\tau$ of the body by

$$\mathbf{v}(\mathbf{x}, \tau) := \dot{\mathbf{x}}(\mathbf{x}_*(\mathbf{x}, \tau), \tau) \quad \text{and} \quad \mathbf{V}(\mathbf{x}, \tau) := \dot{\mathbf{G}}(\mathbf{x}_*(\mathbf{x}, \tau), \tau), \tag{7}$$

respectively, where the superposed dot means material time derivative:

$$\dot{f} := \frac{\partial f}{\partial \tau} + (\mathrm{grad}\, f)\mathbf{v}. \tag{8}$$

For our purposes, we will limit ourselves only to the bodies with affine microstructures in which the density per unit mass of the kinetic energy is additively decomposed into the sum of two terms, the classical translational one and one related to affine changes of the microstructure

$$\frac{1}{2}\mathbf{v}^2 + \kappa(\mathbf{G}, \mathbf{V}); \tag{9}$$

this extra term is a scalar function, homogeneous in $\mathbf{G}$, such that

$$\kappa(\mathbf{G}, \mathbf{V}) \geq 0, \quad \kappa(\mathbf{G}, \mathbf{0}) = 0, \quad \frac{\partial^2 \kappa}{\partial \mathbf{V}^2} \neq \mathbf{0} \tag{10}$$

and is related to the kinetic co-energy $\chi(\mathbf{G}, \mathbf{V})$ by the Legendre transform

$$\frac{\partial \chi}{\partial \mathbf{V}} \cdot \mathbf{V} - \chi = \kappa; \tag{11}$$

of course, if χ were homogeneous of second degree in $\mathbf{V}$, it would coincide with κ, with no vice versa (see, also, [1, 9]).

The kinetic co-energy χ, and also κ, must have the same value for all observers at rest, that is, χ must be invariant under the Eulerian group and hence satisfy the condition

$$\dot{\mathcal{A}}^* \frac{\partial \chi}{\partial \mathbf{V}} = -\mathcal{A}^* \frac{\partial \chi}{\partial \mathbf{G}}, \tag{12}$$

where $\mathcal{A}^*$ is the adjoint of $\mathcal{A}$ with the following property: $(\mathcal{A}^* \mathbf{C}) \cdot \mathbf{c} := \mathbf{C} \cdot (\mathcal{A} \mathbf{c})$, for any double vector $\mathbf{C}$ and vector $\mathbf{c}$ [56], so, for relation (6),

$$\mathcal{A}^*_{kiJ} = \mathcal{A}_{iJk} = \varepsilon_{ikm} G_{mJ}. \tag{13}$$

By inserting relation (13) into Eq. (12) and applying the Ricci tensor ε on the left on both sides, we find the following kinematic compatibility relation:

$$\mathrm{skw} \left(\frac{\partial \chi}{\partial \mathbf{V}} \mathbf{V}^T + \frac{\partial \chi}{\partial \mathbf{G}} \mathbf{G}^T \right) = \mathbf{0}, \tag{14}$$

where "skw" denotes the skew part of a second-rank tensor

$$\mathrm{skw} \, (\cdot) := \frac{1}{2} \left[(\cdot) - (\cdot)^T \right], \tag{15}$$

the symmetrical part being

$$\mathrm{sym} \, (\cdot) := \frac{1}{2} \left[(\cdot) + (\cdot)^T \right]. \tag{16}$$

3 Balance Laws

Let us introduce now some classical fields that arise in continuum theories with the affine microstructure: ρ is the mass density on $\mathcal{B}_\tau$ and ρ_* its referential value defined on $\mathcal{B}_*$; $\mathbf{f}$ is the external vector of body forces per unit mass; $\mathbf{T}$ is Cauchy's stress tensor; $\rho \mathbf{H}$ and $\mathbf{Z}$ are second-rank tensor densities per unit volume of external bulk interactions acting on the microstructure and internal self-actions, respectively; $\mathbf{\Sigma}$ is the third-rank tensor of microstress; ϵ is the specific density of internal energy per unit mass; $\mathbf{q}$ is the vector of heat flux; λ the rate of heat generation per unit mass, due to irradiation.

Therefore, all the admissible thermokinetic processes for such a media are governed by the following general system of balance equations (see [8, 33, 52]):

- the *conservation of mass*,

$$\dot{\rho} + \rho \, \mathrm{tr} \, \mathbf{D} = 0, \tag{17}$$

where $\mathbf{D}$ is the stretching, i.e., the symmetric part of the velocity gradient with respect to current coordinates $\mathbf{L} := \operatorname{grad} \mathbf{v} \left(= \dot{\mathbf{F}} \mathbf{F}^{-1}\right)$, while $\operatorname{tr} \mathbf{D} := \mathbf{D} \cdot \mathbf{I}$ is the trace of $\mathbf{D}$ and $\mathbf{I}$ the identity tensor (we presume to choose a flat metric in space, i.e., to refer our calculations to orthonormal frames);

- the *linear momentum balance (Cauchy)*,

$$\rho \dot{\mathbf{v}} = \rho \mathbf{f} + \operatorname{div} \mathbf{T}, \tag{18}$$

where $\operatorname{div}(\cdot)$ denotes the divergence of $(\cdot)$;

- the *balance law for micromomentum (Capriz)*,

$$\rho \left[\frac{d}{d\tau} \left(\frac{\partial \chi}{\partial \mathbf{V}} \right) - \frac{\partial \chi}{\partial \mathbf{G}} \right] = \rho \mathbf{H} - \mathbf{Z} + \operatorname{div} \mathbf{\Sigma}; \tag{19}$$

- the *non-classical balance of moment of momentum*

$$\varepsilon \mathbf{T} = \mathcal{A}^* \mathbf{Z} + (\operatorname{grad} \mathcal{A}^*) \mathbf{\Sigma}, \tag{20}$$

where the compatibility condition (12) was used in the integral balance of angular momentum (see equation (9.11) of [8]);

- the *local energy balance*

$$\rho \dot{\epsilon} = \rho \lambda - \operatorname{div} \mathbf{q} + \mathbf{T} \cdot \mathbf{L} + \mathbf{Z} \cdot \mathbf{V} + \mathbf{\Sigma} \cdot \operatorname{grad} \mathbf{V}. \tag{21}$$

By using expression (13) of $\mathcal{A}^*$ in Eq. (20) and multiplying again both sides of it by a half of the Ricci tensor ε, we get

$$\operatorname{skw} \mathbf{T} = \operatorname{skw} \left(\mathbf{G} \mathbf{Z}^T + \operatorname{grad} \mathbf{G} \odot \mathbf{\Sigma} \right), \tag{22}$$

where the operator $\odot$ between third-rank tensors is defined by $(\operatorname{grad} \mathbf{G} \odot \mathbf{\Sigma})_{ij} := G_{iJ,l} \Sigma_{jJl}$.

Actually, to recognize our mechanical equations (19), (21), and (22) as balance laws that appear, e.g., in the dynamics of discrete bodies with affine structure [12] or of micromorphic continua [29], we must take the co-energy χ to be quadratic in $\mathbf{V}$, namely

$$\chi = \frac{1}{2} (\mathbf{V} \mathbf{J}_*) \cdot \mathbf{V}, \tag{23}$$

where we have to observe that the symmetric reference microinertia tensor field $\mathbf{J}_*$ in the reference placement $\mathcal{B}_*$ is directly related to Euler's microinertia tensor per unit mass $\mathbf{J}$ of the generic material element with respect to its center of mass $\mathbf{x}$ at time τ by the relation

$$\mathbf{J} = \mathbf{G} \mathbf{J}_* \mathbf{G}^T \in \operatorname{Sym}^+ \tag{24}$$

(see definition (2.10) in [14]) with Sym$^+$ the set of positive definite symmetric tensors. With the choice (23) the compatibility relation (14) is automatically checked because the tensor in the round brackets results symmetric.

By inserting (23) in Capriz's balance (19), we obtain

$$\rho \dot{\mathbf{V}} \mathbf{J}_* = \rho \, \mathbf{H} - \mathbf{Z} + \operatorname{div} \boldsymbol{\Sigma}; \tag{25}$$

moreover, using (24) in (25), transposing it and multiplying both sides by the microstructural double vector variable $\mathbf{G}$, we find

$$\rho \mathbf{J} (\dot{\mathbf{V}} \mathbf{G}^{-1})^T = \rho \mathbf{G} \mathbf{B}^T - \left(\mathbf{G} \mathbf{Z}^T + \operatorname{grad} \mathbf{G} \odot \boldsymbol{\Sigma} \right) + \operatorname{div} \tilde{\boldsymbol{\Sigma}}, \tag{26}$$

where $\tilde{\boldsymbol{\Sigma}}$ is the third-rank hyperstress tensor defined by $\tilde{\boldsymbol{\Sigma}} := \mathbf{G} \oslash {}^{t}\boldsymbol{\Sigma}$, wherein the tensor product $\oslash$ between tensors of second and third rank is $(\mathbf{A} \oslash \boldsymbol{\Phi})_{ikl} := \mathbf{A}_{iJ} \boldsymbol{\Phi}_{Jkl}$, while the definition of the left-transpose of a third-rank tensor is, in components, ${}^{t}\boldsymbol{\Sigma}_{Jkl} := \boldsymbol{\Sigma}_{kJl}$. By using the angular momentum balance in the form (22), we get

$$\rho \mathbf{J} (\dot{\mathbf{V}} \mathbf{G}^{-1})^T = \rho \tilde{\mathbf{B}} - \operatorname{skw} \mathbf{T} - \tilde{\mathbf{Z}} + \operatorname{div} \tilde{\boldsymbol{\Sigma}}, \tag{27}$$

with the second-rank tensors of external body couples $\tilde{\mathbf{B}}$ and generalized moment of momentum of internal micro-forces $\tilde{\mathbf{Z}}$ defined as

$$\tilde{\mathbf{B}} := \mathbf{G} \mathbf{B}^T \quad \text{and} \quad \tilde{\mathbf{Z}} := \operatorname{sym} \left(\mathbf{G} \mathbf{Z}^T + \operatorname{grad} \mathbf{G} \odot \boldsymbol{\Sigma} \right) \in \operatorname{Sym}, \tag{28}$$

respectively.

We also define the second-rank whorl tensor $\mathbf{W}$ by

$$\mathbf{W}(\mathbf{x}, \tau) := \left(\mathbf{V}(\mathbf{x}, \tau) \, \mathbf{G}^{-1}(\mathbf{x}, \tau) \right)^T, \tag{29}$$

which satisfies the elementary kinematical relationship

$$\dot{\mathbf{J}} = \mathbf{J} \mathbf{W} + \mathbf{W}^T \mathbf{J}, \tag{30}$$

sometimes called the equation of "*conservation of microinertia*," and parallel, in a certain sense, to the continuity equation (17) for macro-motion (see, e.g., Theorem 5 in [29]): here, however, it appears as a trivial consequence of the definition (24).

Now, by inserting the whorl $\mathbf{W}$ and using relation (30) on the left-hand side of Eq. (27), we find

$$\rho \left[\overline{(\dot{\mathbf{J}} \mathbf{W})} - \mathbf{W}^T \mathbf{J} \mathbf{W} \right] = \rho \tilde{\mathbf{B}} - \tilde{\mathbf{Z}} - \operatorname{skw} \mathbf{T} + \operatorname{div} \tilde{\boldsymbol{\Sigma}}, \tag{31}$$

while the local energy balance (21) is

$$\rho\dot{\epsilon} = \rho\lambda - \text{div}\,\mathbf{q} + \mathbf{T}\cdot\mathbf{L} + (\tilde{\mathbf{Z}} + \text{skw}\,\mathbf{T})\cdot\mathbf{W} + \tilde{\boldsymbol{\Sigma}}\cdot\text{grad}\,\mathbf{W}, \tag{32}$$

so they take a form commonly presented in the current literature (see (4.17) and (4.18) of [16]).

4 Entropy Principle and Jump Conditions

To account for pore contributions to entropy flux, otherwise not considered in pertinent previous analyses [38, 58], we adopt here Müller's proposal [57] of introducing entropy flux and source additional to those determined by heat flux and source (that voids may induce an extra entropy flux has been accepted in describing microcracking in [55]; such a flux determines also yield-type criteria).

More precisely, the entropy flux vector $\mathbf{p}$, as well as the entropy supply μ, are not considered equal to the heat flux $\mathbf{q}$ and the heat supply λ divided by the temperature θ, respectively: a field considered here as a phenomenological quantity defined by the rules it satisfies and which we suppose is always possible to assign as a positive function $\theta(\mathbf{x}_*, \tau)$ to each $\mathbf{x}_* \in \mathcal{B}_*$.

Intrinsic production of entropy is always non-negative during every admissible thermodynamic process for the body. It is given by the rate of variation of the entropy, with density per unit mass η, less the rate of entropy exchange due to a flux of entropy through the boundary of vector $\mathbf{p}$ and a production owing to distributed entropy sources of specific density per unit mass μ; therefore, the local form of the principle is given by the following inequality:

$$\rho\dot{\eta} + \text{div}\,\mathbf{p} - \rho\mu \geq 0. \tag{33}$$

Here, we refer to an extra entropy flux $\mathbf{k}$, signifying the difference between the entropy flux $\mathbf{p}$ and the heat flux $\mathbf{q}$ over the absolute temperature θ, and an extra entropy supply ϖ given by the difference between the entropy source μ and the energy supply λ divided by the same temperature (see [42, 57]):

$$\mathbf{k} = \mathbf{p} - \frac{\mathbf{q}}{\theta}, \quad \varpi = \mu - \frac{\lambda}{\theta}. \tag{34}$$

As usual, the specific Helmholtz free energy per unit mass ψ is given by

$$\psi := \epsilon - \theta\eta \tag{35}$$

and we use Eq. (21) to obtain a reduced version of the inequality (33), i.e.,

$$\rho\left(\dot{\psi} + \eta\dot{\theta}\right) + \theta^{-1}\mathbf{q}\cdot\mathbf{g} \leq w + \theta\left(\text{div}\,\mathbf{k} - \rho\varpi\right), \tag{36}$$

with $\mathbf{g} := \operatorname{grad} \theta$ and w the density of stress power defined by

$$w := \mathbf{T} \cdot \mathbf{L} + \mathbf{Z} \cdot \mathbf{V} + \mathbf{\Sigma} \cdot \operatorname{grad} \mathbf{V}. \tag{37}$$

The reduced version of the entropy principle (36) becomes the classical Clausius–Duhem inequality [20], if the extra entropy flux $\mathbf{k}$ and supply ϖ disappear.

Remark In order to compare our approach with Dunn's and Serrin's interstitial working u [26, 27], necessary to describe, e.g., Korteweg-type materials (see [48] or §18 of [8]) and, more generally, higher-gradient materials in appropriate, broader, thermodynamic structures, we get the flux $\mathbf{q}$ from the relation $(34)_1$,

$$\mathbf{q} = \theta\,\mathbf{p} - \theta\,\mathbf{k}; \tag{38}$$

therefore, we recognize two contributions to it, the first $\theta\,\mathbf{p}$ is purely thermal and the second one $\theta\,\mathbf{k}$ is due to an interstitial work flux across the boundary $\partial\mathcal{B}$ of the body $\mathcal{B}$ due to longer range spatial macro- and micro-interactions: so, if $\hat{\mathbf{n}}$ is the outer unit normal to the boundary, we have that the interstitial working coincides with the normal component of $\theta\,\mathbf{k}$, i.e., $u = \theta\,\mathbf{k}\cdot\hat{\mathbf{n}}$. Thus, although differently motivated, our theory has formal similarities with that of Dunn and Serrin [26], where even there the classical link between the fluxes of heat and entropy is definitively chop off.

Now, if we use in the definition of stress power (37) the standard decomposition of the velocity gradient

$$\mathbf{L} = \mathbf{D} + \mathbf{Y}, \tag{39}$$

where $\mathbf{D} := \operatorname{sym}\mathbf{L}$ and $\mathbf{Y} := \operatorname{skw}\mathbf{L}$ are the spin tensor and the rate of deformation, respectively (see definitions (16) and (15)). Therefore, we have

$$w = \operatorname{sym}\mathbf{T} \cdot \mathbf{D} + \operatorname{skw}\left(\mathbf{GZ}^T + \operatorname{grad}\mathbf{G} \odot \mathbf{\Sigma}\right) \cdot \mathbf{Y} + \mathbf{Z} \cdot \mathbf{V} + \mathbf{\Sigma} \cdot \operatorname{grad}\mathbf{V} = \tag{40}$$

$$= \operatorname{sym}\mathbf{T} \cdot \mathbf{D} + \mathbf{Z} \cdot (\mathbf{V} - \mathbf{YG}) + \mathbf{\Sigma} \cdot \operatorname{grad}(\mathbf{V} - \mathbf{YG}) + \left[\varepsilon \odot \left(\mathbf{G} \oslash {}^{t}\mathbf{\Sigma}\right)\right] \cdot \operatorname{grad}\mathbf{r};$$

in Eq. (40) we used angular momentum balance (22), properties of minor left-transposition of a third-rank tensor and the tensor product $\oslash$ between tensors of the second and the third rank.

In the previous formula, the spin vector $\mathbf{r}$ is defined by

$$\mathbf{r} := -\frac{1}{2}\varepsilon\mathbf{Y} = \frac{1}{2}\operatorname{curl}\mathbf{v}, \tag{41}$$

where for a vector $\mathbf{u}$, $\operatorname{curl}\mathbf{u} := -\varepsilon(\operatorname{grad}\mathbf{u})$.

The difference $\check{\mathbf{V}} := \mathbf{V} - \mathbf{YG}$ represents the corotational time derivative of the microspeed $\mathbf{V}$ due to the spin tensor $\mathbf{Y}$; so, $\mathbf{D}$, $\check{\mathbf{V}}$, $\operatorname{grad}\check{\mathbf{V}}$ and $\operatorname{grad}\mathbf{r}$ in Eq. $(40)_2$ are frame indifferent (see equation (36.13) of [61] or, in particular, §2.8.2.4 of [47] for porous media).

Finally, the presence of discontinuity surfaces (or interfaces) is a recurrent phenomenon in solids with material microstructure, so, in addition to the equations of balance (17)–(19) and (21)–(22) and the entropy inequality (33), we need to discuss how interactions can be balanced across an interface. The simplest way to characterize interfaces is to imagine them only as purely mathematical surfaces free of any form of own structure, namely a propagating wave Ω.

As it is customary, we suppose that a smooth moving surface Ω crosses the body $\mathcal{B}$, oriented by the unit normal vector $\hat{\mathbf{n}}$. At $\mathbf{x}$ and τ it has non-zero normal speed φ in $\mathcal{B}$. We further assume that some fields defined on $\mathcal{B}$ (excepting $\mathbf{x}$, $\mathbf{G}$ and θ) suffer jump discontinuity across Ω and so we employ the usual notation for jumps

$$[\![\, f \,]\!] = f^+ - f^-, \tag{42}$$

where f^+ or f^- are outer and inner traces of f, respectively.

Therefore, we can write classical Kotchine's equations, as modified in order to take into account microstructural effects, and a relation that restricts the jump of micromomentum (see, also, [17, 25, 39]) as it follows:

$$[\![\, \rho(\varphi - \mathbf{v} \cdot \mathbf{n}) \,]\!] = 0, \ [\![\, \rho\varphi\mathbf{v} + \mathbf{T}\,\mathbf{n} \,]\!] = \mathbf{0}, \ \mathcal{A}^* \left[\!\left[\, \rho\varphi\frac{\partial\chi}{\partial\mathbf{V}} + \boldsymbol{\Sigma}\,\mathbf{n} \,\right]\!\right] = \mathbf{0}, \tag{43}$$

$$\left[\!\left[\, \rho\varphi\left(\epsilon + \frac{1}{2}\mathbf{v}^2 + \kappa\right) \,\right]\!\right] = [\![\, \mathbf{q}\cdot\mathbf{n} - \mathbf{v}\cdot\mathbf{T}\mathbf{n} - \mathbf{V}\cdot\boldsymbol{\Sigma}\mathbf{n} \,]\!], \ [\![\, \rho\varphi\eta \,]\!] \geq [\![\, \mathbf{p}\cdot\mathbf{n} \,]\!].$$

The form of the jumps across a propagating wave of higher-order time derivatives of principal fields can be easily obtained from the balance equations (17)–(19), and (21).

If we insert the expressions (13), (23), and (34)$_1$ in jumps (43)$_{3,5}$, we obtain the following reduced forms for them:

$$\text{skw} [\![\, (\rho\varphi\mathbf{V}\mathbf{J}^* + \boldsymbol{\Sigma}\,\mathbf{n})\,\mathbf{G}^T \,]\!] = \mathbf{0} \quad \text{and} \quad [\![\, \rho\varphi\theta\eta \,]\!] \geq [\![\, \mathbf{q}\cdot\mathbf{n} + \theta\,\mathbf{k}\cdot\mathbf{n} \,]\!]. \tag{44}$$

In the previous expressions we assume that the surface Ω is not structured, i.e., it does not sustain neither surface stress nor surface microstress and self-actions (surface micro-actions appeared first in reference [25], while the discussion of surface standard stresses dates back reference [45]).

5 Internal Constraints for Materials with Nano-Pores

Let us constraint the microstructural variable $\mathbf{G}$ to be a symmetric tensor field with positive determinant. We exclude local pore rotations and consider in place of $\mathbf{G}$ just the micro-dilatation $\mathbf{U}' \in \text{Sym}^+$ at time τ given by $\mathbf{U}'^2 = \mathbf{G}\mathbf{G}^T$, the left Cauchy–Green tensor of the micro-deformation.

In particular, if $\mathbf{G} \equiv \mathbf{U}'\mathbf{R}'$ is the polar right decomposition of $\mathbf{G}$ with $\mathbf{R}' \in \mathrm{Orth}^+$, the kinematic constraint we consider is

$$\mathbf{R}' = \mathbf{I}. \tag{45}$$

Also, we decompose the microstretch $\mathbf{U}'$ into its isotropic and traceless parts indicated, respectively, by sph and dev , namely

$$\mathbf{U}' = \mathrm{sph}\,\mathbf{U}' + \mathrm{dev}\,\mathbf{U}', \tag{46}$$

where

$$\mathrm{sph}\,\mathbf{U}' := \omega\,\mathbf{I}, \ \ \text{with } \omega := \frac{1}{3}(\mathrm{tr}\,\mathbf{U}'), \quad \text{and} \quad \mathrm{dev}\,\mathbf{U}' := \mathbf{U}' - \mathrm{sph}\,\mathbf{U}'. \tag{47}$$

Then, we link $\mathrm{dev}\,\mathbf{U}'$ to the macro-strain, because pores, considered empty, are determined by the surrounding matter. At variance, if vugs are partially filled by an inviscid fluid or an elastic inclusion, both of negligible mass, we can consider the body as a material with ellipsoidal microstructure (see [33] or, after, [31, 32]).

Since the deformation gradient

$$\mathbf{F} = \mathbf{UR}, \tag{48}$$

with $\mathbf{U} = \sqrt{\mathbf{FF}^T} \in \mathrm{Sym}^+$ and $\mathbf{R} \in \mathrm{Orth}^+$, the second kinematical constraint considered is

$$\mathrm{dev}\,\mathbf{U}' = \mathrm{dev}\,\mathbf{U}: \tag{49}$$

the microstretch must be spherical.

Now, we use the constraint (45) to define tensor fields $\bar{\mathbf{Z}} := \mathbf{Z}\,\mathbf{I}^T$ and $\bar{\boldsymbol{\Sigma}} := \mathbf{I} \oslash {}^t\boldsymbol{\Sigma}$ with the following components:

$$\bar{Z}_{ij} = Z_{iL}\,\delta_{jL}, \quad \bar{\Sigma}_{ijk} = \delta_{iL}\,\Sigma_{jLk}. \tag{50}$$

By introducing the other constraint (49) with (50) in the balance of angular momentum (22) and the stress power (37), we get

$$\mathrm{skw}\,\mathbf{T} = \mathrm{skw}\left[\mathbf{Z}\,\mathrm{dev}\,\mathbf{U} - \omega\mathbf{Z} + \mathrm{str}\,\boldsymbol{\Sigma} \otimes \mathrm{grad}\,\dot{\omega} - \boldsymbol{\Sigma} \odot \mathrm{grad}\,(\mathrm{dev}\,\dot{\mathbf{U}})\right] \tag{51}$$

and

$$w = \mathbf{T} \cdot \dot{\mathbf{F}}\mathbf{F}^{-1} + \mathbf{Z} \cdot \dot{\mathbf{U}}' + \boldsymbol{\Sigma} \cdot \mathrm{grad}\,\dot{\mathbf{U}}' =$$
$$= \left(\mathbf{TU}^{-1}\right) \cdot \left(\dot{\mathbf{U}} + \mathbf{U}\dot{\mathbf{R}}\mathbf{R}^T\right) + \mathbf{Z} \cdot (\dot{\omega}\,\mathbf{I} + \mathrm{dev}\,\dot{\mathbf{U}}) + \boldsymbol{\Sigma} \cdot \mathrm{grad}\,(\dot{\omega}\,\mathbf{I} + \mathrm{dev}\,\dot{\mathbf{U}}) =$$

$$= \dot{\omega}\,\mathrm{tr}\,\mathbf{Z} + \mathrm{dev}\,\mathbf{Z}\cdot\mathrm{dev}\,\dot{\mathbf{U}} + \left(\mathbf{T}\mathbf{U}^{-1}\right)\cdot\left(\dot{\upsilon}\,\mathbf{I} + \mathrm{dev}\,\dot{\mathbf{U}} + \mathbf{U}\dot{\mathbf{R}}\mathbf{R}^{T}\right) +$$

$$+\mathrm{ldev}\,\boldsymbol{\Sigma}\cdot\mathrm{grad}\,(\mathrm{dev}\,\dot{\mathbf{U}}) + \boldsymbol{\Sigma}\cdot(\mathbf{I}\otimes\mathrm{grad}\,\dot{\omega}) =$$

$$= \dot{\upsilon}\,\mathrm{sym}\,\mathbf{T}\cdot\mathbf{U}^{-1} + \dot{\omega}\,\mathrm{tr}\,\mathbf{Z} + \mathrm{dev}\,\left(\mathbf{T}\mathbf{U}^{-1} + \mathbf{Z}\right)\cdot\mathrm{dev}\,\dot{\mathbf{U}} +$$

$$+\mathrm{skw}\,\left(\mathbf{U}\mathbf{T}\mathbf{U}^{-1}\right)\cdot\dot{\mathbf{R}}\mathbf{R}^{T} + \mathrm{ldev}\,\Sigma\cdot\mathrm{grad}\,(\mathrm{dev}\,\dot{\mathbf{U}}) + \mathrm{str}\,\boldsymbol{\Sigma}\cdot\mathrm{grad}\,\dot{\omega}, \qquad (52)$$

where we avoid using the bar accents to make the notations more compact.

In Eqs. (51) and (52) scalar υ is defined by $\upsilon := \frac{1}{3}(\mathrm{tr}\,\mathbf{U})$; moreover, the operator left-deviator ldev $(\cdot)$ computes the deviatoric component of the second-rank tensor $\boldsymbol{\Sigma}\mathbf{w}$, for any vector $\mathbf{w}$, that is $(\mathrm{ldev}\,\boldsymbol{\Sigma})_{ijk}\mathbf{w}_{k} = [\mathrm{dev}\,(\boldsymbol{\Sigma}\mathbf{w})]_{ij}$, and the operator semi-trace str $(\cdot)$ contracts the first two indices of the operand, i.e., $(\mathrm{str}\,\boldsymbol{\Sigma})_{j} := \Sigma_{iij}$.

It is necessary at this point to assign a meaning to the notion of *perfect thermo-mechanical constraint*. We accept the following general statements as valid (see [15, 46] and, also, §27 of [8]):

 (i) Each entity, to which we assign a constitutive prescription in absence of constraints, i.e., ψ, η, ϵ, $\mathbf{q}$, $\mathbf{k}$, $\mathbf{T}$, $\mathbf{Z}$ and $\boldsymbol{\Sigma}$, is now the sum of *active* and *reactive* components:

$$\psi = \psi_a + \psi_r,\ \eta = \eta_a + \eta_r,\ \epsilon = \epsilon_a + \epsilon_r,\ \text{etc.} \qquad (53)$$

 (ii) *Perfect* (i.e., internally frictionless) *constraints* are those such that the pertinent reactive entities do not contribute to the inequality (36) and thus satisfy the equation

$$\rho\eta_r\,\dot{\theta} + \theta^{-1}\mathbf{q}_r\cdot\mathbf{g} = \mathbf{T}_r\cdot\mathbf{L} + \mathbf{Z}_r\cdot\mathbf{V} + \boldsymbol{\Sigma}_r\cdot\mathrm{grad}\,\mathbf{V} + \theta\,(\mathrm{div}\,\mathbf{k}_r - \rho\varpi)\,, \qquad (54)$$

where we follow [43] and do not include the reaction term ψ_r for the free energy (in fact, if we enclose such quantity, the conclusion would be that it is constant in every process).

(iii) Only the active components are connected by appropriate constitutive rules to the independent thermokinetic variables and their values reduce to fields in the orthogonal complement of the respective reaction functional (see, also, (5.2) of [13]).

By using relations (45) and (49) and the resulting representation (52)₄ of the stress power w in Eq. (54), we have

$$\rho\eta_r\dot{\theta} + \theta^{-1}\mathbf{q}_r\cdot\mathbf{g} = \dot{\upsilon}\,\mathrm{sym}\,\mathbf{T}_r\cdot\mathbf{U}^{-1} + \dot{\omega}\,\mathrm{tr}\,\mathbf{Z}_r +$$

$$+\mathrm{dev}\,\left(\mathbf{T}_r\mathbf{U}^{-1} + \mathbf{Z}_r\right)\cdot\mathrm{dev}\,\dot{\mathbf{U}} + \mathrm{skw}\,\left(\mathbf{U}\mathbf{T}_r\mathbf{U}^{-1}\right)\cdot\dot{\mathbf{R}}\mathbf{R}^{T} +$$

$$+\mathrm{str}\,\boldsymbol{\Sigma}_r\cdot\mathrm{grad}\,\dot{\omega} + \mathrm{ldev}\,\boldsymbol{\Sigma}_r\cdot\mathrm{grad}\,(\mathrm{dev}\,\dot{\mathbf{U}}) + \theta\,(\mathrm{div}\,\mathbf{k}_r - \rho\varpi)\,, \qquad (55)$$

for every choice of $\dot{\theta}, \dot{\upsilon}, \dot{\omega},$ and θ among scalars, $\mathbf{g}$ and $\operatorname{grad}\dot{\omega}$ between vectors, $\mathbf{U}$ amid symmetric tensors, $\operatorname{dev}\dot{\mathbf{U}}$ and $\operatorname{grad}(\operatorname{dev}\dot{\mathbf{U}})\mathbf{w}$ amid deviators of second rank, for any vector $\mathbf{w}$, and $\dot{\mathbf{R}}\mathbf{R}^T$ amongst skew tensors. The arbitrariness of these variables implies

$$\eta_r = 0, \quad \mathbf{q}_r = \mathbf{0}, \quad \operatorname{sym}\mathbf{T}_r = \mathbf{0}, \quad \operatorname{tr}\mathbf{Z}_r = 0,$$

$$\operatorname{dev}\left(\mathbf{T}_r\mathbf{U}^{-1} + \mathbf{Z}_r\right) = \mathbf{0}, \quad \operatorname{skw}\left(\mathbf{U}\mathbf{T}_r\mathbf{U}^{-1}\right) = \mathbf{0},$$

$$\operatorname{str}\mathbf{\Sigma}_r = \mathbf{0}, \quad \operatorname{ldev}\mathbf{\Sigma}_r = \mathbf{0}, \quad \operatorname{div}\mathbf{k}_r = \rho\varpi; \tag{56}$$

hence, from relations $(56)_{3-5}$, we find that reactions must be such that

$$\mathbf{T}_r \in \operatorname{Skw} \quad \mathbf{Z}_r \in \operatorname{Dev} \oplus \operatorname{Skw}, \quad \text{with} \quad \operatorname{dev}\mathbf{Z}_r = -\mathbf{T}_r\mathbf{U}^{-1}, \tag{57}$$

because $\operatorname{tr}\left(\mathbf{T}_r\mathbf{U}^{-1}\right) = \mathbf{T}_r \cdot \mathbf{U}^{-1} = 0$, and so $\mathbf{T}_r\mathbf{U}^{-1} \in \operatorname{Dev}$, while, from conditions $(56)_{7,8}$, we deduce that

$$\mathbf{\Sigma}_r\,\mathbf{w} \in \operatorname{Skw}, \quad \forall\,\mathbf{w}. \tag{58}$$

Also, due to the statement (iii), it is necessary that

$$\mathbf{T}_a \in \operatorname{Sym}, \quad \mathbf{Z}_a \in \operatorname{Sph}, \quad \text{and} \quad \mathbf{\Sigma}_a\,\mathbf{w} \in \operatorname{Sym}, \forall\,\mathbf{w}. \tag{59}$$

Then, from relations (35) and (56)–(59), it follows that

$$\psi = \psi_a, \ \eta = \eta_a, \ \epsilon = \epsilon_a, \ \mathbf{q} = \mathbf{q}_a, \ \mathbf{k} = \mathbf{k}_a + \mathbf{k}_r, \ \mathbf{T} = \mathbf{T}_a + \mathbf{T}_r,$$

$$\mathbf{Z} = \frac{1}{3}(\operatorname{tr}\mathbf{Z}_a)\,\mathbf{I} - \mathbf{T}_r\mathbf{U}^{-1} + \operatorname{skw}\mathbf{Z}_r, \quad \mathbf{\Sigma} = \mathbf{\Sigma}_a + \mathbf{\Sigma}_r, \tag{60}$$

with

$$\operatorname{div}\mathbf{k}_r = \rho\varpi, \ \mathbf{T}_a \in \operatorname{Sym}, \ \mathbf{T}_r \in \operatorname{Skw}, \ \mathbf{\Sigma}_a \in \operatorname{lSym}, \ \mathbf{\Sigma}_r \in \operatorname{lSkw}, \tag{61}$$

where lSym and lSkw indicate the sets of third-rank tensor fields symmetric and skew in the first two indices, respectively.

6 Pure Equations of Motion

Our aim is to get now equations that rule the thermo-mechanical evolution of porous solids, excluding interactions not specified by constitutive laws.

The first step is to split Capriz's balance law (25) into its isotropic, traceless and antisymmetric parts, calculating the trace, the deviator and the skew part of both sides to obtain

$$\text{div}\,(\text{str}\,\boldsymbol{\Sigma}_a) - \text{tr}\,\mathbf{Z}_a = \rho\left(\ddot{\omega}\,\text{tr}\,\mathbf{J}_* + \mathbf{J}_* \cdot \text{dev}\,\ddot{\mathbf{U}} - \text{tr}\,\mathbf{H}\right), \tag{62}$$

$$\text{dev}\left(\mathbf{T}_r\mathbf{U}^{-1} + \text{div}\,\boldsymbol{\Sigma}_a\right) = \rho\,\text{dev}\left[\ddot{\omega}\,\mathbf{J}_* + (\text{dev}\,\ddot{\mathbf{U}})\mathbf{J}_* - \mathbf{H}\right], \tag{63}$$

$$\text{div}\,\boldsymbol{\Sigma}_r - \text{skw}\,\mathbf{Z}_r = \rho\,\text{skw}\left[(\text{dev}\,\ddot{\mathbf{U}})\mathbf{J}_* - \mathbf{H}\right], \tag{64}$$

where we used relations $(60)_{8,9}$ and the decomposition of $\mathbf{V}$, i.e.,

$$\mathbf{V} = \dot{\mathbf{U}}' = \dot{\omega}\,\mathbf{I} + \text{dev}\,\dot{\mathbf{U}}. \tag{65}$$

As a second step, we need to express the Cauchy stress tensor in a reaction-free form using the relations $(60)_{7-9}$ and the angular momentum balance (22), other than the constrained decomposition of $\mathbf{U}'$; therefore, we have

$$\begin{aligned}
\text{skw}\,\mathbf{T} \;=\; \mathbf{T}_r &= \text{skw}\,\Big\{\big[\mathbf{I}\otimes\text{grad}\,\omega + \text{grad}\,(\text{dev}\,\mathbf{U})\big]\odot(\boldsymbol{\Sigma}_a + \boldsymbol{\Sigma}_r) + \\
&\quad + (\omega\mathbf{I} + \text{dev}\,\mathbf{U})\left[\frac{1}{3}(\text{tr}\,\mathbf{Z}_a)\,\mathbf{I} - \text{dev}\left(\mathbf{T}_r\mathbf{U}^{-1}\right) + \text{skw}\,\mathbf{Z}_r\right]^T\Big\} = \\
&= \text{skw}\,\Big\{\mathbf{U}'\,(\text{div}\,\boldsymbol{\Sigma}_r - \text{skw}\,\mathbf{Z}_r) - \text{dev}\,\mathbf{U}\Big[\text{dev}\left(\mathbf{T}_r\mathbf{U}^{-1} + \text{div}\,\boldsymbol{\Sigma}_a\right)\Big] + \\
&\quad + \text{div}\left(\text{dev}\,\mathbf{U}\oslash\text{ldev}\,\boldsymbol{\Sigma}_a\right) + \text{div}\,(\mathbf{U}'\oslash{}^t\boldsymbol{\Sigma}_r)\Big\}, \tag{66}
\end{aligned}$$

where we used the symmetry properties of $\mathbf{U}'$, $\boldsymbol{\Sigma}_a$ and the deviator operator.

The first two terms of relation $(66)_3$ on the right-hand side can be expressed as a function of the right-hand sides of Eqs. (63) and (64), where only the deviatoric and skew parts of the resultant tensor densities per unit volume of external bulk interactions acting on the microstructure are present. About the last term, we use Remark 1 of §3 in [13], because an essential ambiguity is left in the definition of contact micro-force density in Eq. (64): by supposing that $(\mathbf{U}'\oslash{}^t\boldsymbol{\Sigma}_r)$ satisfies the conditions of null hyperstress field on $\mathcal{B}$, an arbitrary null stress field $\mathbf{T}^0 := \text{div}\,(\mathbf{U}'\oslash{}^t\boldsymbol{\Sigma}_r)$ in Skw exists and satisfies the condition $\text{div}\,\mathbf{T}^0 = \mathbf{0}$; so we can absorb formally $\mathbf{T}^0$ into $\mathbf{T}$ and disregard it in the Cauchy's equation (18) to obtain the pure equation of macro-motion

$$\rho\dot{\mathbf{v}} = \rho\,\mathbf{f} + \text{div}\,\tilde{\mathbf{T}}, \tag{67}$$

with

$$\begin{aligned}
\tilde{\mathbf{T}} = \mathbf{T}_a + \text{skw}\,\Big\{&\rho\,\mathbf{U}'\,\text{skw}\left[(\text{dev}\,\ddot{\mathbf{U}})\mathbf{J}_* - \mathbf{H}\right] + \text{div}\,(\text{dev}\,\mathbf{U}\oslash\text{ldev}\,\boldsymbol{\Sigma}_a) - \\
&- \rho\,(\text{dev}\,\mathbf{U})\,\text{dev}\left[\ddot{\omega}\,\mathbf{J}_* + (\text{dev}\,\ddot{\mathbf{U}})\mathbf{J}_* - \mathbf{H}\right]\Big\}; \tag{68}
\end{aligned}$$

the reduced stress tensor $\tilde{\mathbf{T}}$ is clearly not symmetric, in general, and will be the object of constitutive prescriptions for $\mathbf{T}_a$ and $\mathbf{\Sigma}_a$, in addition to the assignment of the densities of the microstructural volume forces.

The only pure balance for the micro-motion is Eq. (62). Consequently, the extended energy balance (21) takes the simple form

$$\rho\,\dot{\epsilon}_a = \rho\,\lambda - \mathrm{div}\,\mathbf{q}_a + \mathbf{T}_a\cdot\mathbf{D} + \dot{\omega}\,\mathrm{tr}\,\mathbf{Z}_a + \mathrm{str}\,\mathbf{\Sigma}_a\cdot\mathrm{grad}\,\dot{\omega} + \mathrm{ldev}\,\mathbf{\Sigma}_a\cdot\mathrm{grad}\,(\mathrm{dev}\,\dot{\mathbf{U}}). \quad (69)$$

Once we find a solution of the pure balance equations, the corresponding reaction constraints are obtained from conditions (63) and (64) for $\mathbf{T}_r$ and for $\mathbf{Z}_r$ and $\mathbf{\Sigma}_r$, respectively, within the intrinsic indeterminacy generated by equations themselves, as pointed out in sections 205 and 227 of [62] or, again, in Remark 1 of §3 in [13].

Remark 1 Here we observe that the microstress vector (str $\mathbf{\Sigma}_a$) in equation (62) could assume a different physical nature in relation to the size of the pores.

In particular, if the lacunes are very large, interconnected, and constitute a series of linked canaliculi in which fluids can flow, we can think it possible of acting on the pores through the boundary, as for the rare phenomena of micro-earthquakes in the basin of the caldera in the Phlegraean Fields [30].

At variance, if the voids are small, spherical and finely dispersed in the matrix material, we find it difficult to imagine a direct way to assign prescribed boundary conditions on them and recognize boundary microtractions, with the consequence that there is no physically significant microstress vector [10], rather, only the sum [div (str Σ_a) − tr $\mathbf{Z}_a$] of two formally distinct terms has physical meaning and should be considered and interpreted as an indicator of weakly nonlocal effects (see [6], page 21 of [49], pages 26–27 of [8] and [11]): the distinction between micro-forces and the divergence of an improperly termed "microstress" has no physical substance [10].

Remark 2 Finally, in order to establish a comparison with the field equations used in [58] for thermoelastic materials with voids, where pores are small, spherical and finely dispersed, we first consider the constant microinertia tensor field $\mathbf{J}_*$ to be spherical, i.e., $\mathbf{J}_* = \kappa\,\mathbf{I}$ (with κ a positive constant of the material), as well as the left-symmetric microstress $\mathbf{\Sigma}_a$, in the sense that $\mathbf{\Sigma}_a := \frac{1}{3}\,\mathbf{I}\otimes\tilde{\mathbf{h}}$, with $\tilde{\mathbf{h}}$ a vector field, and so ldev $\mathbf{\Sigma}_a = \mathbf{O}$; therefore, Eqs. (62) and (69) are now reduced to the following expressions:

$$3\rho\,\kappa\,\ddot{\omega} = \rho\,\mathrm{tr}\,\mathbf{H} + \mathrm{div}\,\tilde{\mathbf{h}} - \mathrm{tr}\,\mathbf{Z}_a, \quad (70)$$

$$\rho\,\dot{\epsilon}_a = \rho\,\lambda - \mathrm{div}\,\mathbf{q}_a + \mathbf{T}_a\cdot\mathbf{D} + \dot{\omega}\,\mathrm{tr}\,\mathbf{Z}_a + \tilde{\mathbf{h}}\cdot\mathrm{grad}\,\dot{\omega}. \quad (71)$$

It is clear that the pure equations (17) and (67) should coincide with (2.7) and (2.8) in [58], respectively (although in the referential version). However, our Eq. (68) above shows that the reduced Cauchy stress $\tilde{\mathbf{T}}$ need not in general be symmetric, as instead explicitly required by equation (2.9) of [58]; in addition, we could suppose

that even the body micro-actions $\mathbf{H}$ are spherical and nevertheless observe that the stress tensor $\tilde{\mathbf{T}}$ is reduced to

$$\tilde{\mathbf{T}} = \mathbf{T}_a - \rho\,\kappa\,\mathrm{skw}\left[(\mathrm{dev}\,\mathbf{U})(\mathrm{dev}\,\ddot{\mathbf{U}})\right], \tag{72}$$

still keeping in our theory a skew part related to a microstructural inertial term derived from the pore constraint (49).

At the end, the balance equations (2.10) and (2.11) of [58] should match our (70) and (71), *modulo* some simple changes in notation. In particular, Nunziato and Cowin use a single kinematic microstructural variable, "the *volume fraction* ν of the solid material found at the point $\mathbf{x}_*$ at time τ and hence is a measure of the volume change of the bulk material which results from void compaction or distention" (page 177 of [58]), and we too have the single degree of freedom ω at microscopic (or mesoscopic) scale, therefore we set that

$$\dot{\nu} = \dot{\omega}\,\omega^{-1} \quad \text{and} \quad k = 3\,\kappa\,\omega^2, \tag{73}$$

where k is the *equilibrated inertia*, depending on void geometrical features. After identifying the referential fields, the extrinsic equilibrated body force l, the *equilibrated stress* $\mathbf{h}$, and the *intrinsic equilibrated body force g* read

$$l := \omega\,\mathrm{tr}\,\mathbf{H}, \quad \mathbf{h} := \iota\,\omega\,\mathbf{F}^{-1}\tilde{\mathbf{h}}, \quad g := \frac{1}{2}\rho_*\dot{k}\dot{\nu} - \iota\left(\omega\,\mathrm{tr}\,\mathbf{Z}_a + \tilde{\mathbf{h}}\cdot\mathrm{grad}\,\omega\right). \tag{74}$$

Then, we obtain a full identification between the linear micro-momentum balance (70), multiplied by ω, and the energy balance (71) with equations (2.10) and (2.11) of [58], respectively.

In the end we recover the substance of the voids theory in [58] for porous materials with small holes, still eliminating some kinematic terms such as, e.g., $\frac{1}{2}\rho_*\dot{k}\dot{\nu}$ from their energy balance (2.11) and in their definition (3.5) of the dissipation function (see, also, §4 of [14]).

7 Thermodynamic Restrictions for Solids with Large Pores

7.1 The Thermoelastic Case

Here, we generalize the constitutive prescriptions presented in [32, 34, 58], by considering both inelastic surface effects associated with changes in the deformation of nano-pores near hole boundaries as well as heat conduction, and we assume that the overall response depends upon the isotropic variations in void volume ω, its gradient $\mathrm{grad}\,\omega$, the gross deformation gradient $\mathbf{F}$, and temperature θ.

We call *elastic state* of the solid with nano-pores the array of independent variables $\mathcal{S} \equiv \{\omega, \mathbf{w} := \mathrm{grad}\,\omega, \mathbf{F}, \theta\}$. We postulate the principle of equipresence,

which requires that each dependent constitutive field be given by a smooth function of the same set of independent variables, i.e.,

$$\{\psi_a,\ \eta_a,\ \mathbf{q}_a,\ \mathbf{k}_a,\ \mathbf{T}_a,\ \operatorname{tr}\mathbf{Z}_a,\ \boldsymbol{\Sigma}_a\} = \left\{\hat{\psi},\ \hat{\eta},\ \hat{\mathbf{q}},\ \hat{\mathbf{k}},\ \hat{\mathbf{T}},\ \hat{\zeta},\ \hat{\boldsymbol{\Sigma}}\right\}(\mathcal{S},\dot{\omega},\mathbf{g}); \qquad (75)$$

moreover, we check the compatibility of these prescriptions with the reduced version (36) of the extended Clausius–Duhem inequality, taking into account not only the condition of perfect constraint (54), but also relations (59) and (65). Then, we get

$$\rho\left(\dot{\psi}_a + \eta_a\,\dot{\theta}\right) + \theta^{-1}\mathbf{q}_a \cdot \mathbf{g} \leq \mathbf{T}_a \cdot \mathbf{D} + \dot{\omega}\operatorname{tr}\mathbf{Z}_a +$$
$$+ \operatorname{str}\boldsymbol{\Sigma}_a \cdot \operatorname{grad}\dot{\omega} + \operatorname{ldev}\boldsymbol{\Sigma}_a \cdot \operatorname{grad}(\operatorname{dev}\dot{\mathbf{U}}) + \theta\operatorname{div}\mathbf{k}_a. \quad (76)$$

For the functional dependence of the free energy ψ_a and the active component $\mathbf{k}_a$ of the extra entropy flux, by using the chain rule and the identity

$$\overline{\operatorname{grad}\alpha} = \operatorname{grad}\dot{\alpha} - \mathbf{L}^T\operatorname{grad}\alpha, \qquad (77)$$

for each scalar function α, we require that the entropy imbalance (76) holds for any choice of the fields in the set $(\mathcal{S},\dot{\omega},\mathbf{g})$; consequently, when the terms are properly ordered, the inequality reads

$$\rho\left(\hat{\eta} + \hat{\psi}_{,\theta}\right)\dot{\theta} + \left(\theta^{-1}\hat{\mathbf{q}} - \theta\,\hat{\mathbf{k}}_{,\theta}\right)\cdot\mathbf{g} + \left(\rho\hat{\psi}_{,\omega} - \hat{\zeta}\right)\dot{\omega} + \rho\hat{\psi}_{,\dot{\omega}}\ddot{\omega} + \rho\hat{\psi}_{,\mathbf{g}}\cdot\operatorname{grad}\dot{\theta} -$$
$$- \left[\hat{\mathbf{T}} - \rho\operatorname{sym}\left(\hat{\psi}_{,\mathbf{F}}\mathbf{F}^T - \mathbf{g}\otimes\hat{\psi}_{,\mathbf{g}} - \mathbf{w}\otimes\hat{\psi}_{,\mathbf{w}}\right)\right]\cdot\mathbf{D} - \operatorname{ldev}\hat{\boldsymbol{\Sigma}}\cdot\operatorname{grad}(\operatorname{dev}\dot{\mathbf{U}}) -$$
$$+\rho\operatorname{skw}\left(\hat{\psi}_{,\mathbf{F}}\mathbf{F}^T - \mathbf{g}\otimes\hat{\psi}_{,\mathbf{g}} - \mathbf{w}\otimes\hat{\psi}_{,\mathbf{w}}\right)\cdot\mathbf{Y} + \left(\rho\hat{\psi}_{,\mathbf{w}} - \theta\,,\hat{\mathbf{k}}_{,\dot{\omega}} - \operatorname{str}\hat{\boldsymbol{\Sigma}}\right)\cdot\operatorname{grad}\dot{\omega} +$$
$$-\theta\left(\hat{\mathbf{k}}_{,\mathbf{w}}\cdot\operatorname{grad}\mathbf{w} + \hat{\mathbf{k}}_{,\mathbf{g}}\cdot\operatorname{grad}\mathbf{g} + \hat{\mathbf{k}}_{,\omega}\cdot\mathbf{w} + \hat{\mathbf{k}}_{,\mathbf{F}}\cdot\operatorname{grad}\mathbf{F}\right) \leq 0, \qquad (78)$$

where the comma with a subscript denotes the partial differentiation with respect to the field shown, e.g., $\hat{\psi}_{,\mathbf{g}} := \frac{\partial\hat{\psi}}{\partial\mathbf{g}}$.

Since one can imagine, for each material element of the porous body, thermo-mechanical processes along which the following fields assume arbitrary values at a given instant: $\dot{\theta}$, $\ddot{\omega}$, $\operatorname{grad}\dot{\theta}$, $\mathbf{D}$, $\operatorname{grad}(\operatorname{dev}\dot{\mathbf{U}})$, $\mathbf{Y}$, $\operatorname{grad}\dot{\omega}$, $\operatorname{grad}\mathbf{w}$, $\operatorname{grad}\mathbf{g}$, and $\operatorname{grad}\mathbf{F}$, and since the left-hand side of the inequality (78) must always hold up, therefore its fulfillment implies that the coefficients in the linear expression of these quantities must all vanish, i.e.,

$$\mathbf{T}_a = \rho\operatorname{sym}\left(\hat{\psi}_{,\mathbf{F}}\mathbf{F}^T - \mathbf{w}\otimes\hat{\psi}_{,\mathbf{w}}\right), \qquad \rho\operatorname{skw}\left(\hat{\psi}_{,\mathbf{F}}\mathbf{F}^T - \mathbf{w}\otimes\hat{\psi}_{,\mathbf{w}}\right) = \mathbf{0},$$

$$\operatorname{str}\boldsymbol{\Sigma}_a = \rho\hat{\psi}_{,\mathbf{w}} - \theta\,\hat{\mathbf{k}}_{,\dot{\omega}}, \qquad \operatorname{ldev}\boldsymbol{\Sigma}_a = \mathbf{0}, \qquad \eta_a = -\hat{\psi}_{,\theta},$$

$$\left(\theta^{-1}\mathbf{q}_a - \theta\,\hat{\mathbf{k}}_{,\theta}\right)\cdot\mathbf{g} + \left(\rho\hat{\psi}_{,\omega} - \operatorname{tr}\mathbf{Z}_a\right)\dot{\omega} - \theta\hat{\mathbf{k}}_{,\omega}\cdot\mathbf{w} \leq 0, \qquad (79)$$

while the active part of the free energy of Helmholtz ψ_a is a function only of the elastic state $\mathcal{S}$ and a potential function just for active parts of entropy η^a, stress $\mathbf{T}_a$, and microstress semi-trace str $\mathbf{\Sigma}_a$. Moreover, the active extra entropy flux $\mathbf{k}_a$ must be independent of $\mathbf{w}$, $\mathbf{F}$, and $\mathbf{g}$. Thus, the following reduced form holds:

$$\mathbf{k}_a = \hat{\mathbf{k}}(\omega, \dot{\omega}, \theta), \tag{80}$$

but there is no isotropic vectorial function of only scalars, and thus the reduced form (80) necessarily implies

$$\mathbf{k}_a = \mathbf{0}, \tag{81}$$

for thermoelastic bodies with big pores, i.e., vugs (see, also, §6 of [57]). Therefore, the extra entropy flux $\mathbf{k}$ has only the reactive part $\mathbf{k}_r$ different from zero and whose divergence field cancels the extra entropy flux per unit volume $\rho\varpi$ for the constitutive relation (61).

In such a material, the sum $(\text{div}\,\mathbf{p} - \rho\mu)$, which appears in the entropy principle (33), satisfies the identity

$$\text{div}\,\mathbf{p} - \rho\mu = \text{div}\,\mathbf{k}_a + \text{div}\,\mathbf{k}_r + \text{div}\left(\frac{\mathbf{q}_a}{\theta}\right) - \rho\varpi - \rho\frac{\lambda}{\theta} = \text{div}\left(\frac{\mathbf{q}_a}{\theta}\right) - \rho\frac{\lambda}{\theta}, \tag{82}$$

due to relations $(61)_1$ and (80). Therefore, in such materials, the general entropy principle (33) for continua with affine microstructure has the classical form, usually assumed as a postulate.

The compatibility condition $(79)_2$ for the free energy ψ_a simply expresses the condition of frame-indifference with respect to vectorial and tensorial arguments, namely,

$$\hat{\psi}\left(\omega, \mathbf{Qw}, \mathbf{QF}, \theta\right) = \hat{\psi}\left(\omega, \mathbf{w}, \mathbf{F}, \theta\right), \tag{83}$$

for each $\mathbf{Q} \in \text{Orth}^+$, while in the expression $(79)_1$ for the active part of the Cauchy stress $\mathbf{T}_a$ we recognize a stress of Ericksen's type, namely $[-\rho\,\text{sym}\,(\mathbf{w} \otimes \hat{\psi}_{,\mathbf{w}})]$, in addition to the standard expression of stress tensor for thermoelastic media.

According to the result (80), response functions str $\hat{\mathbf{\Sigma}}, \hat{\mathbf{q}}$ and $\hat{\zeta}$ obey the new constitutive relation $(79)_3$ and the residual dissipation inequality $(79)_6$, respectively:

$$\text{str}\,\hat{\mathbf{\Sigma}} = \rho\hat{\psi}_{,\mathbf{w}}, \quad \mathcal{D} := \theta^{-1}\hat{\mathbf{q}} \cdot \mathbf{g} + \delta\,\dot{\omega} \leq 0, \tag{84}$$

where $\mathcal{D} = \hat{\mathcal{D}}(\mathcal{S}, \dot{\omega}, \mathbf{g})$ defines the dissipation functional of the thermokinetic process and $\delta := \rho\hat{\psi}_\omega - \hat{\zeta}$ its scalar part of internal micro-actions.

The dissipation inequality $(84)_2$ asserts that the heat flux $\mathbf{q}_a$ must form an obtuse angle with $\mathbf{g}$, while δ must be opposite in sign to $\dot{\omega}$, and, consequently, the dissipation function $\mathcal{D}$ must vanish whenever and $\mathbf{g} = \mathbf{0}$ and $\dot{\omega} = 0$; i.e.,

$$\hat{\mathbf{q}}(\mathcal{S}, 0, \mathbf{0}) = \mathbf{0} \quad \text{and} \quad \delta(\mathcal{S}, 0, \mathbf{0}) = \rho\hat{\psi}_{,\omega}(\mathcal{S}) - \hat{\zeta}(\mathcal{S}, 0, \mathbf{0}) = \mathbf{0}. \tag{85}$$

Furthermore, the evolution equation for temperature follows from the energy equation (69), which is considerably simplified, when we use the definition of Helmholtz free energy (35) and the constitutive relations (79)$_{1,2,4,5}$ and (84)$_1$, reducing to

$$\rho\theta\frac{d\hat{\psi}_\theta}{d\tau} + \rho\lambda = \operatorname{div}\hat{\mathbf{q}} + \delta\,\dot{\omega}, \tag{86}$$

where the influence of the microstructure, and, in particular, of the inelastic pores surface effects, is evident in the last member on the right-hand side. Instead, the micromomentum balance of pore dilatation (62) is, now,

$$\rho\left(\ddot{\omega}\operatorname{tr}\mathbf{J}_* + \mathbf{J}_*\cdot\operatorname{dev}\ddot{\mathbf{U}}\right) = \rho\operatorname{tr}\mathbf{H} + \operatorname{div}\left(\rho\hat{\psi}_{,\mathbf{w}}\right) - \rho\hat{\psi}_{,\omega} + \delta, \tag{87}$$

where $\rho\operatorname{tr}\mathbf{H}$ represents the external dilatational force, $\rho\hat{\psi}_{,\mathbf{w}}$ the dilating microstress vector, $\rho\hat{\psi}_{,\omega}$ the internal forces of dilatancy, and δ the dissipation due to pores.

In this context, the latter is the only pure equation, derived from Capriz's balance (25), which rules the micro-motion, the macro-motion being governed by conservation of mass (17) and Cauchy's balance of linear momentum (67), with

$$\tilde{\mathbf{T}} = \rho\operatorname{sym}\left(\hat{\psi}_{,\mathbf{F}}\,\mathbf{F}^T - \mathbf{w}\otimes\hat{\psi}_{,\mathbf{w}}\right) + \rho\operatorname{skw}\left\{\omega\left[(\operatorname{dev}\ddot{\mathbf{U}})\mathbf{J}_* - \mathbf{H}\right] + \right. \tag{88}$$
$$\left. + (\operatorname{dev}\mathbf{U})\left\{\operatorname{skw}\left[(\operatorname{dev}\ddot{\mathbf{U}})\mathbf{J}_* - \mathbf{H}\right] - \operatorname{dev}\left[\ddot{\omega}\,\mathbf{J}_* + (\operatorname{dev}\ddot{\mathbf{U}})\mathbf{J}_* - \mathbf{H}\right]\right\}\right\},$$

due to relations (68) and (79)$_{1,4}$, and the decomposition (47) of $\mathbf{U}'$ with the constraint (49); the evolution of the temperature is regulated by the pure equation (86).

7.2 Finite Speed Heat Propagation for the Rigid Instance

In this section we consider the particular case in which large pores are at least partially filled by a non-viscous fluid of negligible mass, such as a gas or a liquid which, subjected to heating or cooling, could change phase and/or increase or reduce its own volume, developing a new thermodynamic constraint linking the microstructural variable ω to the temperature θ [7].

To analyze this phenomenon we suppose that the sole admissible (macroscopic) deformations are isometric and orientation-preserving: a circumstance that does not exclude the possibility of microscopic changes in the pores due to variations of the temperature. These microscopic changes occur at a spatial scale lower than that of observations with the naked eye: such changes are alterations of the low-scale geometry in volume of vugs (see, also, the general theory developed in [54]).

Therefore, we exclude here the macroscopic motions of the body and any external actions performing power in a change of place. We consider only variations in time

of the microstructure and, consequently, we define the external power just performed by these actions in the first law of thermodynamics (21) in local form; furthermore, we disregard both relative microstructural inertia and direct actions of external mass on the microstructure.

The previous hypotheses imply

$$\rho = \rho_*, \ \mathbf{v} = \mathbf{f} = \mathbf{0}, \ \mathbf{T} = \mathbf{J}_* = \mathbf{H} = \mathbf{0}, \ \dot{\mathbf{U}}' = \dot{\omega}\,\mathbf{I} \quad \text{and} \quad \omega = \hat{\omega}(\theta(\mathbf{x}, \tau)). \tag{89}$$

Hence, the micromomentum balance (25) is now

$$\mathbf{Z} = \operatorname{div} \boldsymbol{\Sigma}, \tag{90}$$

and the balance of energy reduces to

$$\rho_* \dot{\epsilon} = \rho\,\lambda - \operatorname{div} \mathbf{q} + \operatorname{div}\,(\dot{\omega}\operatorname{str} \boldsymbol{\Sigma})\,, \tag{91}$$

where an additional flux $(\dot{\omega}\operatorname{str} \boldsymbol{\Sigma})$ appears clearly due to the microstructural variations. The entropy inequality (36) becomes

$$\rho_* \left(\dot{\psi} + \eta\,\dot{\theta} \right) + \theta^{-1}\mathbf{q} \cdot \mathbf{g} \leq \operatorname{div}\,(\dot{\omega}\operatorname{str} \boldsymbol{\Sigma}) + \theta\,(\operatorname{div} \mathbf{k} - \rho\varpi)\,. \tag{92}$$

In particular, due to condition (ii) on the new constraint $(89)_4$, the reactive components of constitutive fields are such that

$$[\rho_*\eta_r + \operatorname{div}\,(\varsigma\operatorname{str} \boldsymbol{\Sigma}_r)]\,\dot{\theta} + \theta^{-1}\mathbf{q}_r \cdot \mathbf{g} + \varsigma\operatorname{str} \boldsymbol{\Sigma}_r \cdot \operatorname{grad} \dot{\theta} = \theta\,(\operatorname{div} \mathbf{k}_r - \rho_*\varpi) \tag{93}$$

for every choice of θ and $\dot{\theta}$ among scalars and $\mathbf{g}$ and $\operatorname{grad} \dot{\theta}$ between vectors, with $\varsigma := -\frac{d\omega}{d\theta}$; thus, we have

$$\eta_r = 0, \ \operatorname{div} \mathbf{k}_r = \rho_*\varpi, \ \mathbf{q}_r = \mathbf{0}, \ \operatorname{str} \boldsymbol{\Sigma}_r = \mathbf{0}. \tag{94}$$

Here, likewise to the procedure of Sect. 7.1, we obtain

$$\rho_* \left(\dot{\psi}_a + \eta_a\,\dot{\theta} \right) + \theta^{-1}\mathbf{q}_a \cdot \mathbf{g} + \operatorname{div}\,\left(\varsigma\,\dot{\theta}\operatorname{str} \boldsymbol{\Sigma}_a \right) \leq \theta\operatorname{div} \mathbf{k}_a. \tag{95}$$

By using the principle of equipresence, we introduce the array $\mathcal{S}' \equiv \{\theta, \mathbf{g}\}$ of independent variables to verify the compatibility of the constitutive fields $\psi_a, \eta_a, \mathbf{q}_a, \operatorname{str} \boldsymbol{\Sigma}_a$ and $\mathbf{k}_a$ with inequality (95) to get to the following ones

$$\left[\rho_* \left(\eta_a + \hat{\psi}_{,\theta} \right) + \operatorname{div}\,(\varsigma\operatorname{str} \boldsymbol{\Sigma}_a) \right]\dot{\theta} + \left(\rho_*\hat{\psi}_{,\mathbf{g}} + \varsigma\operatorname{str} \boldsymbol{\Sigma}_a \right) \cdot \operatorname{grad} \dot{\theta} +$$
$$+ \left(\theta^{-1}\mathbf{q}_a - \theta\,\hat{\mathbf{k}}_{,\theta} \right) \cdot \mathbf{g} - \theta\,\hat{\mathbf{k}}_{,\mathbf{g}} \cdot \operatorname{grad} \mathbf{g} \leq 0, \tag{96}$$

where we used the chain rule for differentiations and the relation (77) with $\mathbf{L} = \mathbf{0}$, for $(89)_2$.

The left-hand side of inequality (96) is linear in $\dot\theta$, grad $\dot\theta$ and grad $\mathbf{g}$; therefore, the pertinent coefficients must vanish. Also, as already pointed out in the previous section, there is no isotropic vectorial functional of a scalar, thus we have

$$\mathbf{k}_a \equiv \mathbf{0}. \tag{97}$$

Then, the following constitutive prescriptions are valid:

$$\text{str } \mathbf{\Sigma}_a = -\rho_* \varsigma^{-1} \hat\psi_{,\mathbf{g}}, \quad \eta_a = \text{div } \hat\psi_{,\mathbf{g}} - \hat\psi_{,\theta}, \tag{98}$$

$$\theta^{-1} \mathbf{q}_a \cdot \mathbf{g} \le 0, \tag{99}$$

where the prime $'$ denotes differentiation with respect to the independent variable θ and the material is considered homogeneous at gross scale, i.e., ρ_* constant.

Now, we are able to insert peculiar constitutive rules, satisfying the relations (94), (98), and (99), in Eq. (91). In particular, we assume, as in the classical case, that the internal energy depends only on θ (i.e., $\epsilon_r = \psi_r = $ constant and $\epsilon_a (= \psi_a + \theta\, \eta_a) = \hat\epsilon(\theta)$, for relation (35)) and that the Fourier's law for a thermally isotropic porous material, which is a definite heat conductor [18], is valid, i.e.,

$$\mathbf{q}_a = -\xi \text{ grad } \theta, \tag{100}$$

with the heat conductivity $\xi = \hat\xi(\theta) \ge 0$.

Therefore, by using Eq. (21), we get

$$\rho_* c_v \dot\theta = \rho_* \lambda + \xi\, \Delta\theta + \xi'(\text{grad }\theta)^2 - \varsigma \text{ str } \mathbf{\Sigma}_a \cdot \text{grad } \dot\theta - \dot\theta \text{ div } (\varsigma \text{ str } \mathbf{\Sigma}_a), \tag{101}$$

where $c_v = \epsilon' = \frac{d\hat\epsilon}{d\theta}$ is the specific heat at constant volume; Eq. (101) can be rewritten as

$$\mathbf{h} \cdot \text{grad } \dot\theta - \tilde\xi\, \Delta\theta + (1 + \phi)\, \dot\theta - \hat\xi (\text{grad }\theta)^2 = \tilde\lambda, \tag{102}$$

where we have indicated

$$\mathbf{h} := \frac{\varsigma(\theta)}{\rho_* c_v(\theta)} \text{ str } \mathbf{\Sigma}_a, \quad \tilde\xi := \frac{\xi(\theta)}{\rho_* c_v(\theta)}, \quad \phi := \frac{\text{div } (\varsigma(\theta) \text{str } \mathbf{\Sigma}_a)}{\rho_* c_v(\theta)},$$

$$\hat\xi := \frac{\xi'(\theta)}{\rho_* c_v(\theta)}, \quad \tilde\lambda := \frac{\lambda}{c_v(\theta)}. \tag{103}$$

Equation (102) is the heat equation that regulates the evolution of temperature in a rigid porous conductor. In the simple case, when both c_v and ξ are constant, as well as $\mathbf{h}$, and $\lambda = 0$, the equation takes the form

$$\mathbf{h} \cdot \text{grad } \dot\theta - \tilde\xi\, \Delta\theta + \dot\theta = 0. \tag{104}$$

This equation is hyperbolic. In fact, since $\mathbf{v} = \mathbf{0}$, material and partial time derivatives are equivalent by definition (8), i.e., $\dot{\theta} = \frac{\partial \theta}{\partial \tau}$, and, in components, Eq. (104) reads

$$h_i \frac{\partial^2 \theta}{\partial x_i \partial \tau} = \tilde{\xi} \, \frac{\partial^2 \theta}{\partial x_i \partial x_i} - \frac{\partial \theta}{\partial \tau}, \tag{105}$$

where the summation over repeated indices is understood. The subsequent analysis, carried out at the end of §4 in [54], where an analogous equation is obtained for macroscopically rigid bodies with general microstructures, without exploiting reactive stresses, assures us of the hyperbolicity of Eq. (105); it follows the propagation at finite speed of the temperature changes and so, here, we avoids Fourier's heat paradox for the classical rigid conductor.

Obviously, when microstructural actions are neglected, with the disappearance of $\mathbf{h}$ and ϕ, we recover the parabolic nature of Eq. (102) with the associated recurrence of Fourier's paradox (see, also [54]).

8   Closure

We have analyzed the thermomechanics of a complex material, the porous solid, in a scheme in which the kinematic order parameters describing the microstate, are partially constrained to macro-strain, while the independent variable is directly correlated to the volume fraction of the matrix material and, therefore, is like a measure of the volume variation of the bulk material that results from void compaction or dilation. Pure balance equations (i.e., equations expressed only in terms of active stresses) are obtained for both macro- and micro-motions by using constraint reaction.

The Cauchy stress tensor results not symmetric, in general, and also depending on acceleration gradients and on a term of Ericksen's type, clearly due to microstructural actions, even in the case of small pores. Moreover, the dissipation functional puts in evidence the effects associated only with void closure and inelastic pore-surface effects. Furthermore, we show that the extra entropy flux, introduced in accordance with Müller's theory, is of reactive origin and balances the extra entropy supply.

Finally, to study the evolution of temperature in a non-deforming porous conductor, the microstructural variable are linked to the temperature, obtaining hyperbolic-type evolution of temperature disturbances due to a flux that mimics the interstitial working of Dunn and Serrin, a flux due only to microstructural actions.

References

1. Amoddeo, A., Giovine, P.: Micromechanical modelling of granular materials and FEM simulations. Meccanica 54, 609–630 (2019)
2. Barbu, V., Da Prato, G., Röckner, M.: Stochastic Porous Media Equations. Springer, Berlin (2016)
3. Bear, J.: Dynamics of fluids in porous media. Dover Publications Inc., New York (1988)
4. Biot, M.A.: General theory of three-dimensional consolidation. J. Appl. Phys. 12, 155–164 (1941)
5. Biot, M.A.: Theory of propagation of elastic waves in a fluid-saturated porous solid. I. Low-frequency range. J. Acoust. Soc. Am. 28, 168–178 (1956)
6. Bridgman, P.W.: Reflections on thermodynamics. Proc. Am. Acad. Arts Sci. 82, 301–309 (1953)
7. Capriz, G.: Continua with latent microstructure. Arch. Ration. Mech. Analysis 90(1), 43–56 (1985)
8. Capriz, G.: Continua with Microstructure. Springer Tracts in Natural Philosophy, vol. 35. Springer-Verlag, Berlin (1989)
9. Capriz, G., Giovine. P.: On microstructural inertia. Math. Mod. Meth. Appl. Sciences 7, 211–216 (1997)
10. Capriz, G., Giovine. P.: Remedy to omissions in a tract on continua with microstructure. Atti XIII° Congresso AIMETA '97, Siena, Meccanica Generale, Vol. I, pp.1–6 (1997)
11. Capriz, G., Giovine, P.: Weakly nonlocal effects in mechanics. In: Contributions to Continuum Theories, Krzysztof Wilmanski's Anniversary Volume. Weierstrass Institute for Applied Analysis and Stochastics, Berlin, Report n.**18**, pp. 37–44 (2000). ISSN 0946-8838
12. Capriz, G., Podio Guidugli, P.: Discrete and continuous bodies with affine structure. Annali Mat. Pura Appl. (IV) 111, 195–211 (1976)
13. Capriz, G., Podio Guidugli, P.: Formal structure and classification of theories of oriented materials. Annali Mat. Pura Appl. (IV) 115, 17–39 (1977)
14. Capriz, G., Podio Guidugli, P.: Materials with spherical structure. Arch. Ration. Mech. Anal. 75, 269–279 (1981)
15. Capriz, G., Podio Guidugli, P.: Internal constraints. In: Truesdell, C.: Rational Thermodynamics, Appendix 3A, 2nd edition. Springer-Verlag, New York, pp. 159–170 (1984)
16. Capriz, G., Podio Guidugli P., Williams, W.: On balance equations for materials with affine structure. Meccanica 17, 80–84 (1982)
17. Capriz, G., Virga, E.G.: On singular surfaces in the dynamics of continua with microstructure. Quart. Appl. Math. 52, 509–517 (1994)
18. Chadwick P., Currie P.K.: The propagation of acceleration waves in heat conducting elastic materials. Arch. Rational Mech. Anal. 49, 137–158 (1972)
19. Cheng, A.H.-D.: Poroelasticity. Springer, Berlin (2016)
20. Coleman, B.D., Noll, W.: The thermodynamics of elastic materials with heat conduction and viscosity. Arch. Rational Mech. Anal. 13, 245–261 (1963)
21. Cosserat, E., Cosserat, F.: Théorie des corps déformables. Hermann, Paris (1909)
22. Cowin, S.C.: Stress functions for Cosserat elasticity. Int. J. Solids Struct. 6, 389–398 (1970)
23. Cowin, S.C., Weinbaum, S., Zeng, Y.: A case for bone canaliculi as the anatomical site of strain generated potentials. J. Biomechanics 28, 1281–1297 (1995)
24. de Boer, R.: Theory of Porous Media. Highlights in the Historical Development and Current State. Springer, Berlin (2000)
25. de Fabritiis, C., Mariano, P.M.: Geometry of interactions in complex bodies. J. Geom. Physics 54, 301–323 (2005)
26. Dunn, J.E., Serrin, J.: On the thermomechanics of interstitial working. Arch. Ration. Mech. Anal. 88, 95–133 (1985)
27. Dunn, J.E.: Interstitial working and a nonclassical continuum thermodynamics. In: Serrin, J. (ed) New Perspectives in Thermodynamics. Springer-Verlag, Berlin, pp. 187–222 (1986)

28. Ehlers, W.: Continuum and numerical simulation of porous materials in science and technology. In: Capriz, G., Ghionna, V.N., Giovine, P. (eds), Modeling and Mechanics of Granular and Porous Materials. Series on Modeling and Simulation in Science, Engineering and Technology. Birkhäuser, Boston, pp. 245–292 (2002)

29. Eringen, A.C.: Mechanics of micromorphic continua. In: Kröner, E. (ed) Proc. IUTAM Symposium on Mechanics of Generalized Continua, Freudenstadt and Stuttgart, 1967 Springer, Berlin Heidelberg New York, pp. 18–35 (1968)

30. Esposito, R., Badescu, K., Steele-MacInnis, M., Cannatelli, C., De Vivo, B., Lima, A., Bodnar, R.J., Manning, C.E.: Magmatic evolution of the Campi Flegrei and Procida volcanic fields, Italy, based on interpretation of data from well-constrained melt inclusions. Earth-Science Reviews 185, 325–356 (2018)

31. Forest, S., Sievert, R.: Nonlinear microstrain theories. Int. J. Solids Struct. 43, 7224–7245 (2006)

32. Giacobbe, V., Giovine, P.: Plane waves in linear thermoelastic porous solids. In: Ganghoffer, J.-F., Pastrone, F. (eds) Mechanics of Microstructured Solids: Cellular Materials, Fibre Reinforced Solids and Soft Tissues. Series: Lecture Notes in Applied and Computational Mechanics. Springer Verlag, Berlin, 46, pp. 71–80 (2009)

33. Giovine, P.: Porous solids as materials with ellipsoidal structure. In: Batra, R.C., Beatty, M.F. (eds) Contemporary Research in the Mechanics and Mathematics of Materials. CIMNE, Barcelona, pp. 335–342 (1996)

34. Giovine, P.: A linear theory of porous elastic solids. Transp. Porous Media 34, 305–318 (1999)

35. Giovine, P.: Nonclassical thermomechanics of granular materials. Math. Phys. Analys. Geom. 2(2), 179–196 (1999)

36. Giovine, P.: Remarks on constitutive laws for dry granular materials. In: Giovine, P., Goddard, J.D., Jenkins, J.T. (eds), IUTAM-ISIMM Symposium on Mathematical Modeling and Physical Instances of Granular Flows, Amer. Inst. Physics Conference Proceed. Vol. 1227, AIP, New York, USA, pp. 314–322 (2010)

37. Giovine, P.: Linear wave motions in continua with nano-pores. In: Giovine, P. (ed) Wave Processes in Classical and New Solids, Intech, Rijeka, pp. 61–86 (2012)

38. Giovine, P.: Nano-pores in a thermo-elastic continuum with strain gradient effects. In: Ascione, L., Berardi, V.P., Feo, L., Fraternali F., Tralli, A.M. (eds) Proceedings of the XXIII Conference of the Italian Association of Theoretical and Applied Mechanics (AIMETA), September 2017, Salerno, Italy, Vol. 1, pp. 50–59 (2017)

39. Giovine, P.: Strain gradient effects in a thermo-elastic continuum with nano-pores. J. Mech. Engng. Automation 7(7), 348–355 (2017)

40. Giovine, P.: Internal constraints in the theories of immiscible mixtures for soils. Int. J. Solids Struct., 187, 3–22 (2020)

41. Giovine, P., Margheriti, L., Speciale, M.P.: On wave propagation in porous media with strain gradient effects. Comp. Math. Applications 55, 307–318 (2008)

42. Goodman, M.A., Cowin, S.C.: A continuum theory for granular materials. Arch. Ration. Mech. Anal. 44, 249–266 (1972)

43. Green, A.E., Naghdi, P.M., Trapp, J.A.: Thermodynamics of a continuum with internal constraints. Int. J. Eng. Sci. 8, 891–908 (1970)

44. Grioli, G.: Microstructures as a refinement of Cauchy theory. Problems of physical concreteness. Continuum Mech. Thermodyn. 15, 441–450 (2003)

45. Gurtin, M.E., Murdoch, A.I.: A continuum theory of elastic material surfaces Arch. Rational Mech. Anal. 57, 291–323 (1975)

46. Gurtin, M.E., Podio-Guidugli, P.: The thermodynamics of constrained materials. Arch. Rational Mech. Anal. 51, 192–208 (1973)

47. Ichikawa, Y., Selvadurai, A.P.S.: Transport phenomena in porous media: aspects of micro/macro behaviour. Springer, Berlin-Heidelberg (2012)

48. Korteweg, D.J.: Sur la forme que prennent les equations du mouvement des fluides si l'on tient compte des forces capillaires causees par des variations de densite considerables mais connues et sur la theorie de la capillarite dans l'hypothese d'une variation continue de la densite. Arch. Neerl. Sci. Exactes Nat. 6(2), 1–24 (1901)

49. Kunin, I.A.: Elastic media with microstructure II. Springer Series in Solid-State Sciences, Vol. 44. Springer-Verlag, Berlin (1983)

50. Lakes, R.S.: Size effects and micromechanics of a porous solid. J. Mat. Science 18, 2572–2580 (1983)

51. Lakes, R.S.: Experimental microelasticity of two porous solids. Int. J. Solids Struct. 22, 55–63 (1986)

52. Mariano, P.M.: Multifield theories in mechanics of solids. Adv. Appl. Mech. 38, 1–93 (2002)

53. Mariano, P.M.: Second-neighbor interactions in classical field theories: invariance of the relative power and covariance. Math. Meth. Appl. Sci. 40, 1316–1332 (2017)

54. Mariano, P.M.: Finite speed heat propagation as a consequence of microstructural changes. Continuum Mech. Thermodyn. 29, 1241–1248 (2017)

55. Mariano, P.M., Augusti, G.: Multifield description of microcracked continua: a local model. Math. Mech. Solids 3(2), 183–200 (1988)

56. Mariano, P.M., Stazi, F.L.: Computational aspects of the mechanics of complex materials. Arch. Comput. Meth. Engng. 12, 391–478 (2005)

57. Müller, I.: On the entropy inequality. Arch. Ration. Mech. Anal. 26, 118–141 (1967)

58. Nunziato, J. W., Cowin, S. C.: A nonlinear theory of elastic materials with voids. Arch. Ration. Mech. Anal. 72, 175–201 (1979)

59. Ponte-Castañeda, P., Zaidman, M.: Constitutive models for porous materials with evolving microstructure. J. Mech. Phys. Solids 42, 1459–1497 (1994)

60. Toupin, R. A.: Theories of elasticity with couple-stress. Arch. Ration. Mech. Anal. 17, 85–112 (1964)

61. Truesdell, C., Noll, W.: The Non-Linear Field Theories of Mechanics. 2nd edition, Springer-Verlag, Berlin (1992)

62. Truesdell, C., Toupin, R.A.: The Classical Field Theories. In: Flügge, S. (ed) Handbuch der Physik, Vol. III/1. Springer-Verlag, Berlin, pp. 226–793 (1960)

Hyperplasticity: From Micro to Macro

Guy T. Houlsby

Abstract A simple model is presented in which the hyperplasticity approach is used to develop a model at the micro-scale, with energy and dissipation terms then being integrated over a Representative Volume Element to deduce the macroscopic response. Strong kinetic or kinematic assumptions do not need to be made, as the perturbations from affine deformation are automatically treated within the formulation. The model is developed here in four stages. First a simple assembly of elastic bars is considered. Plastic deformation is then added. As a precursor to modelling a granular material the possibility of tangential as well as axial movement of the bars is considered. Finally a simple no-tension frictional model is implemented at the particle "contacts", for which some simplifying geometrical assumptions are made. It is shown that the models successfully exhibit features of both elastic and plastic deformation behaviour.

Keywords Modelling · Hyperplasticity · Micro · Macro

1 Introduction

The hyperplasticity method allows constitutive models to be developed based on hypotheses for the storage and dissipation of energy. Such hypotheses are usually based on macroscopic quantities (stresses and strains). However, an obvious extension is to develop the hypotheses in terms of microscopic quantities, i.e., in terms of particles and contacts. The macroscopic response may then be deduced by integrating the microscopic contributions to the stored and dissipated energy.

In this paper we develop such an approach to derive a model for a simple analogue of a granular material. It would be possible to deduce the mechanical behaviour of the model we develop using alternative numerical techniques, but

G. T. Houlsby (✉)
Department of Engineering Science, Oxford University, Oxford, UK
e-mail: guy.houlsby@eng.ox.ac.uk

the hyperplasticity approach permits a particularly simple and concise formulation. The results can be expressed entirely in terms of matrix operations, allowing a straightforward implementation in computer code.

2 A Brief Summary of the Hyperplastic Formulation

Hyperplasticity [1] is an approach to plasticity theory, based on thermodynamic principles, in which the entire material response is derived from knowledge of two potential functions. It has its origins in the work of Ziegler [2], and his orthogonality principle is central to the method. The following is a brief summary of the key elements of the theory. Consider a system in which the mechanical behaviour is expressed in terms of strain ε and stress σ. The "state" of the material is also assumed to depend on "internal variables" α, which often (but not necessarily) play the role of plastic strain. Here we are deliberately unspecific about the detailed nature of the internal variables. They can be in principle scalars, tensors or multiple sets of tensors. In the case that the internal variables become an internal function (in effect an infinite number of variables), the potential functions become functionals, and the derivatives must be interpreted as Frechet derivatives (see [3] for details).

The formulation begins with the specification of a Helmholtz free energy $f(\varepsilon, \alpha)$, and a dissipation function $d(\varepsilon, \alpha, \dot{\alpha}) \geq 0$, which must be a homogeneous first order function of $\dot{\alpha}$ for a rate-independent ("plastic") material, i.e., $d(\varepsilon, \alpha, \mu\dot{\alpha}) = \mu d(\varepsilon, \alpha, \dot{\alpha})$. The formulation then defines:

$\sigma = \dfrac{\partial f}{\partial \varepsilon}$, $\overline{\chi} = -\dfrac{\partial f}{\partial \alpha}$ and $\chi = \dfrac{\partial d}{\partial \dot{\alpha}}$, where $\overline{\chi}$ and χ are "generalized stresses" conjugated to the internal variable α. It can be shown from thermodynamics that $(\overline{\chi} - \chi)\dot{\alpha} = 0$. If, however, we make the stronger assumption $\overline{\chi} = \chi$ (equivalent to the orthogonality postulate [2]), then it follows that the entire constitutive response can be derived without any further assumptions being necessary.

2.1 Alternative Forms

The formulation allows a variety of different potentials to be defined, and these are related by Legendre Transforms (or more generally Fenchel Duals). For instance, rather than specifying the Helmholtz free energy $f(\varepsilon, \alpha)$, it is possible to define the Gibbs free energy $g(\sigma, \alpha)$, defined by the Legendre transform $f + (-g) = \sigma\varepsilon$. In this case $\varepsilon = -\dfrac{\partial g}{\partial \sigma}$ and $\overline{\chi} = -\dfrac{\partial g}{\partial \alpha}$.

Instead of specifying the dissipation $d(\ldots, \dot{\alpha})$ it is possible to specify the yield function in the form $y(\ldots, \chi) = 0$. Here $\ldots$ stands for (ε, α) or (σ, α) whichever is the most convenient form. The yield function may be written in a variety of ways, including a canonical form $y(\ldots, \chi) = \gamma(\ldots, \chi) - 1$, where $\gamma(\ldots, \chi)$ is the polar

dual of $d\,(\ldots,\dot{\alpha})$ defined by $\gamma\,(\ldots,\chi) = \sup\limits_{0\neq\dot{\alpha}} \dfrac{\chi\alpha}{d\,(\ldots,\dot{\alpha})}$. The function $\gamma\,(\ldots,\chi)$ is first order in χ, thus $\gamma\,(\ldots,\mu\chi) = \mu\gamma\,(\ldots,\chi)$. In this case yield occurs when $y\,(\ldots,\chi) = 0$ and the plastic strain rates are determined by $\dot{\alpha} = \lambda\dfrac{\partial y}{\partial \chi}$, where λ is a multiplier that becomes determined by the consistency condition $y = 0$. The so-called Karush–Kuhn–Tucker (KKT) conditions apply: $y\lambda = 0$ and $y \leq 0,\ \lambda = 0$ or $y = 0,\ \lambda \geq 0$. The method can be extended to include rate-dependence, see [4] for details.

2.2 Application to Granular Materials

An important feature of the hyperplasticity approach is the role of internal variables. One set of variables that appear in the formulation discussed here are the perturbations of the particle displacements from the affine displacement field. These perturbations may be determined by exploiting the hyperplasticity approach which automatically furnishes the internal equilibrium equations.

In the following, for didactic purposes, we initially develop a simple model involving nodes connected by elastic springs. We develop this into a plasticity model, and then into a model that allows for both radial and tangential relative movement between nodes. Finally this is developed into a simple model of a granular assembly.

3   Model 1: An Elastic Model Based on Micromechanics

In the hyperplastic approach, if the free energy per unit volume is $f = f(\varepsilon)$, then the stresses are given by $\sigma = \partial f/\partial \varepsilon$. If the total free energy in a 2D Representative Volume Element (RVE) of dimension $a \times a$ is $F = fa^2$, then it follows $\sigma = \dfrac{1}{a^2}\dfrac{\partial F}{\partial \varepsilon}$.

Consider an RVE consisting of an assembly of N springs (each with stiffness k_n and extension e_n) connected at M nodes as shown in Fig. 1. The free energy is simply the sum of the stored energies in the individual springs: $F = \sum\limits_{n=1}^{N} \dfrac{k_n}{2}e_n^2$.
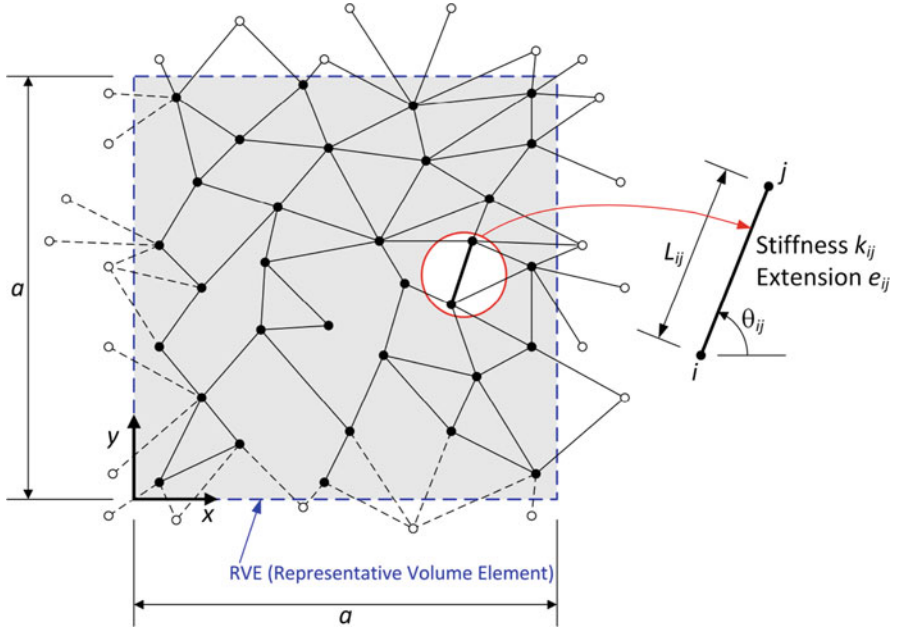
Fig. 1 A 2D assembly of springs

If the strains of the RVE are $\varepsilon_x = \dfrac{\partial u}{\partial x}$, $\varepsilon_y = \dfrac{\partial v}{\partial y}$ and $\gamma = \dfrac{\partial v}{\partial x} + \dfrac{\partial u}{\partial y}$, and the (anticlockwise) rotation is $\omega = \dfrac{1}{2}\left(\dfrac{\partial v}{\partial x} - \dfrac{\partial u}{\partial y}\right)$, then $\dfrac{\partial u}{\partial y} = \dfrac{\gamma - 2\omega}{2}$ and $\dfrac{\partial v}{\partial x} = \dfrac{\gamma + 2\omega}{2}$ we can write the displacements of the nodes as

$$u_m = u_0 + \varepsilon_x x_m + \frac{\gamma - 2\omega}{2} y_m + p_m, \quad m = 1 \dots M \tag{1}$$

$$v_m = v_0 + \frac{\gamma + 2\omega}{2} x_m + \varepsilon_y y_m + q_m \tag{2}$$

where (p_m, q_m) are perturbations on the average (affine) displacement field defined by the strains. The extension of the bar connecting node j to node i is therefore:

$$e_{ij} = (u_j - u_i)\cos\theta_{ij} + (v_j - v_i)\sin\theta_{ij} \tag{3}$$

We define bar n uniquely by requiring $j > i$ and then defining $L_n = L_{ij}$, $\theta_n = \theta_{ij}$. We then define the connectivity of the assembly through a connectivity matrix C_{mn} of dimension $M \times N$. Each row represents a node and each column a bar. If bar n connects nodes i and j, with $j > i$, $C_{in} = -1$, $C_{jn} = 1$ and $C_{mn} = 0$ for the

remaining elements in the column. This allows the bar extensions to be expressed as

$$e_n = \sum_{m=1}^{M} C_{mn} \left(u_m \cos \theta_n + v_m \sin \theta_n \right)$$

$$= \sum_{m=1}^{M} C_{mn} \left(\varepsilon_x x_m + \frac{\gamma - 2\omega}{2} y_m + p_m \right) \cos \theta_n \tag{4}$$

$$+ \sum_{m=1}^{M} C_{mn} \left(\frac{\gamma + 2\omega}{2} x_m + \varepsilon_y y_m + q_m \right) \sin \theta_n$$

Noting that we can write $\left(x_j - x_i \right) = L_n \cos \theta_n$ or $\sum_{m=1}^{M} C_{mn} x_m = L_n \cos \theta_n$, and $\left(y_j - y_i \right) = L_n \sin \theta_n$ or $\sum_{m=1}^{M} C_{mn} y_m = L_n \sin \theta_n$ this leads to

$$e_n = \varepsilon_x L_n \cos^2 \theta_n + \frac{\gamma - 2\omega}{2} L_n \sin \theta_n \cos \theta_n + \sum_{m=1}^{M} C_{mn} p_m \cos \theta_n$$

$$+ \frac{\gamma + 2\omega}{2} L_n \cos \theta_n \sin \theta_n + \varepsilon_y L_n \sin^2 \theta_n + \sum_{m=1}^{M} C_{mn} q_m \sin \theta_n \tag{5}$$

$$= \varepsilon_x L_n \cos^2 \theta_n + \varepsilon_y L_n \sin^2 \theta_n + \gamma L_n \sin \theta_n \cos \theta_n$$

$$+ \sum_{m=1}^{M} C_{mn} \left(p_m \cos \theta_n + q_m \sin \theta_n \right)$$

Note the elimination of the rotation ω.

Applying the chain rule we then have

$$\sigma_x = \frac{1}{a^2} \frac{\partial F}{\partial \varepsilon_x} = \frac{1}{a^2} \sum_{n=1}^{N} k_n e_n \frac{\partial e_n}{\partial \varepsilon_x} = \frac{1}{a^2} \sum_{n=1}^{N} k_n e_n L_n \cos^2 \theta_n \tag{6}$$

and similar expressions for σ_y and the shear stress τ

$$\sigma_y = \frac{1}{a^2} \frac{\partial F}{\partial \varepsilon_y} = \frac{1}{a^2} \sum_{n=1}^{N} k_n e_n \frac{\partial e_n}{\partial \varepsilon_y} = \frac{1}{a^2} \sum_{n=1}^{N} k_n e_n L_n \sin^2 \theta_n \tag{7}$$

$$\tau = \frac{1}{a^2}\frac{\partial F}{\partial \gamma} = \frac{1}{a^2}\sum_{n=1}^{N}k_n e_n \frac{\partial e_n}{\partial \gamma} = \frac{1}{a^2}\sum_{n=1}^{N}k_n e_n L_n \sin\theta_n \cos\theta_n \tag{8}$$

After substituting for the extensions, the above gives the stresses in terms of the strains and the $2M$ perturbations p_m, q_m. However, the hyperplasticity framework treats the perturbations as *internal variables* and provides the supplementary equations $0 = \dfrac{\partial F}{\partial p_m}$, $0 = \dfrac{\partial F}{\partial q_m}$ (after removing a factor of $1/a^2$). These are in effect the internal equilibrium equations. There are $2M$ equations of the form:

$$0 = \frac{\partial F}{\partial p_m} = \sum_{n=1}^{N}k_n e_n \frac{\partial e_n}{\partial p_m} = \sum_{n=1}^{N}k_n e_n C_{mn}\cos\theta_n \tag{9}$$

$$0 = \frac{\partial F}{\partial q_m} = \sum_{n=1}^{N}k_n e_n \frac{\partial e_n}{\partial q_m} = \sum_{n=1}^{N}k_n e_n C_{mn}\sin\theta_n \tag{10}$$

which are the equilibrium conditions at the nodes. In principle these allow solution for the perturbations, but there are two linear dependencies in the above equations. We arbitrarily set the perturbation to zero at one node (the first), and discard the first equation in each of (9) and (10).

3.1 Matrix Analysis

In order to solve the above sets of equations it is most convenient to cast them in matrix form. Define

$$\boldsymbol{\sigma} = \begin{bmatrix} \sigma_x & \sigma_y & \tau \end{bmatrix}^T \qquad \text{(dimension 3)} \tag{11}$$

$$\boldsymbol{\varepsilon} = \begin{bmatrix} \varepsilon_x & \varepsilon_y & \gamma \end{bmatrix}^T \qquad \text{(dimension 3)} \tag{12}$$

$$\mathbf{p} = \begin{bmatrix} p_1 & q_1 & \dots & p_m & q_m \end{bmatrix}^T \qquad \text{(dimension } 2M) \tag{13}$$

$$\mathbf{e} = \begin{bmatrix} e_1 & \dots & e_n \end{bmatrix}^T \qquad \text{(dimension } N) \tag{14}$$

We can then write

$$\mathbf{e} = \mathbf{A}\boldsymbol{\varepsilon} + \mathbf{Bp} \qquad \text{(expresses equation 5)} \tag{15}$$

$$\boldsymbol{\sigma} = \mathbf{Fe} = \mathbf{FA}\boldsymbol{\varepsilon} + \mathbf{FBp} \qquad \text{(expresses equation 6,7,8)} \tag{16}$$

$$\mathbf{0} = \mathbf{Ge} = \mathbf{GA}\boldsymbol{\varepsilon} + \mathbf{GBp} \qquad \text{(expresses equation 9,10)} \tag{17}$$

Table 1 Dimensions of variables in analysis

Variable	Models 1 and 2	Models 3 and 4
σ, ε	3	3
p	$2M$	$3M$
e	N	$2N$
A, L	$N \times 3$	$2N \times 3$
B	$N \times 2M$	$2N \times 3M$
F	$3 \times N$	$3 \times 2N$
G	$2M \times N$	$3M \times 2N$
$GA, \overline{GA}$	$2M \times 3$	$3M \times 3$
$GB, \overline{GB}$	$2M \times 2M$	$3M \times 3M$
D	3×3	3×3

For convenience the dimensions of all matrices used in the model are presented in Table 1.

In order to fix perturbation of the first node as zero we modify **GA** by setting the first two rows as zero, and **GB** by setting the first two rows as zero except for unity on the leading diagonal. We call these modified matrices $\overline{\mathbf{GA}}$ and $\overline{\mathbf{GB}}$. Then

$$\mathbf{p} = - \left(\overline{\mathbf{GB}}\right)^{-1} \overline{\mathbf{GA}} \boldsymbol{\varepsilon} \qquad (18)$$

It then follows that:

$$\boldsymbol{\sigma} = \mathbf{FA}\boldsymbol{\varepsilon} - \mathbf{FB} \left(\overline{\mathbf{GB}}\right)^{-1} \overline{\mathbf{GA}}\boldsymbol{\varepsilon}$$

$$= \mathbf{F} \left[\mathbf{A} - \mathbf{B} \left(\overline{\mathbf{GB}}\right)^{-1} \left(\overline{\mathbf{GA}}\right) \right] \boldsymbol{\varepsilon} = \mathbf{FL}\boldsymbol{\varepsilon} = \mathbf{D}\boldsymbol{\varepsilon} \qquad (19)$$

If the perturbations are suppressed by artificially constraining the nodes to a homogeneous (affine) deformation, then we obtain simply $\boldsymbol{\sigma} = \mathbf{FA}\boldsymbol{\varepsilon}$.

3.2 Example: Elastic Response

Using the example illustrated in 1, with $a = 1$ and the stiffness of each bar set as $k_n = 100$, the stiffness matrix for the assembly can be calculated as

$$\begin{bmatrix} \sigma_x \\ \sigma_y \\ \tau \end{bmatrix} = \begin{bmatrix} 33.7 & 19.8 & -2.3 \\ 19.8 & 42.7 & -5.9 \\ -2.3 & -5.9 & 10.1 \end{bmatrix} \begin{bmatrix} \varepsilon_x \\ \varepsilon_y \\ \gamma \end{bmatrix} \qquad (20)$$

Whilst if the perturbations are suppressed, a significantly higher stiffness is obtained:

$$\begin{bmatrix} \sigma_x \\ \sigma_y \\ \tau \end{bmatrix} = \begin{bmatrix} 129.4 & 44.7 & -1.1 \\ 44.7 & 86.3 & 0.7 \\ -1.1 & 0.7 & 44.7 \end{bmatrix} \begin{bmatrix} \varepsilon_x \\ \varepsilon_y \\ \gamma \end{bmatrix} \tag{21}$$

Note that in each case the calculated matrix is symmetric. However, it does not represent isotropic behaviour, for instance, there are coupling terms between, for example, σ_x and γ that would not be present in the case of an isotropic material.

4 Model 2: Extension to Plasticity

If each element is replaced by an element of the form in Fig. 2, then the theory can be extended to plasticity.

The energy stored in each spring is now $\dfrac{k_n}{2}(e_n - \alpha_n)^2$ and the dissipation rate is $c_n |\dot{\alpha}_n|$. The development proceeds exactly as before with $F = \sum\limits_{n=1}^{N} \dfrac{k_n}{2}(e_n - \alpha_n)^2$ and $D = \sum\limits_{n=1}^{N} c_n |\dot{\alpha}_n|$. The formalism gives the N necessary addition equations to eliminate the α_n variables:

$$0 = \frac{\partial F}{\partial \alpha_n} + \frac{\partial D}{\partial \dot{\alpha}_n} \tag{22}$$

which are each of the form:

$$0 = -k_n (e_n - \alpha_n) + c_n S(\dot{\alpha}_n) \tag{23}$$

where $S(\ldots)$ is a modified signum function (defined by $S(x) = -1$, $x < 0$, $-1 \le S(0) \le 1$, $S(x) = 1$, $x > 0$. Alternatively, the yield surface can be obtained as a Legendre–Fenchel transform of the dissipation function, using infimal convolution as the transform of the summation. The simplest way to express the result is by introducing the generalised force $\chi_n = \dfrac{\partial D}{\partial \dot{\alpha}_n} = c_n S(\dot{\alpha}_n) = \overline{\chi}_n =$

Fig. 2 A simple sliding element

Slider strength c Spring stiffness k
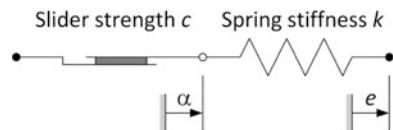
$-\dfrac{\partial F}{\partial \alpha_n} = k_n\,(e_n - \alpha_n)$ and then expressing the individual yield functions for the links as $y_n = \chi_n^2 - c_n^2$ together with the flow condition $\dot{\alpha}_n = \lambda_n\dfrac{\partial y_n}{\partial \chi_n}$, where $y_n \le 0$, $\lambda_n \ge 0$ and $y_n\lambda_n = 0$ (the so-called Karush–Kuhn–Tucker conditions). The formalism then requires

$$\chi_n = k_n\,(e_n - \alpha_n) \tag{24}$$

$$\dot{\alpha}_n = \lambda_n\frac{\partial y_n}{\partial \chi_n} = 2\lambda_n\chi_n \tag{25}$$

The solution for the stresses therefore uses the equations:

$$\sigma_x = \frac{1}{a^2}\sum_{n=1}^{N} k_n\,(e_n - \alpha_n)\,L_n\cos^2\theta_n \tag{26}$$

$$\sigma_y = \frac{1}{a^2}\sum_{n=1}^{N} k_n\,(e_n - \alpha_n)\,L_n\sin^2\theta_n \tag{27}$$

$$\tau = \frac{1}{a^2}\sum_{n=1}^{N} k_n\,(e_n - \alpha_n)\,L_n\sin\theta_n\cos\theta_n \tag{28}$$

$$0 = \frac{\partial F}{\partial p_m} = \sum_{n=1}^{N} k_n e_n\frac{\partial e_n}{\partial p_m} = \sum_{n=1}^{N} k_n\,(e_n - \alpha_n)\,C_{mn}\cos\theta_n \tag{29}$$

$$0 = \frac{\partial F}{\partial q_m} = \sum_{n=1}^{N} k_n e_n\frac{\partial e_n}{\partial q_m} = \sum_{n=1}^{N} k_n\,(e_n - \alpha_n)\,C_{mn}\sin\theta_n \tag{30}$$

The solution must proceed incrementally. For each plastic element, if at the beginning of an increment $y_n = y_{n0} \le 0$, then that element remains elastic in the increment so $\dot{\alpha}_n = 0$, whilst if $y_{n0} > 0$ the element deforms plastically and the consistency condition $\dot{y}_n = 0$ applies. In numerical implementation it is expedient to "correct" the generalised stress to the yield surface, so we write the modified form $\dot{y}_n = -f y_{n0} = 2\chi_n\dot{\chi}_n = 2\chi_n k_n\,(\dot{e}_n - \dot{\alpha}_n)$ where $0 \le f \le 1$ is an appropriate scalar factor.

4.1 Matrix Analysis

The above equations can also be cast in incremental form and solved by matrix methods. Defining also $\boldsymbol{\alpha} = \begin{bmatrix}\alpha_1 & \dots & \alpha_N\end{bmatrix}^T$ (dimension N) and $\boldsymbol{\chi} = \begin{bmatrix}\chi_1 & \dots & \chi_N\end{bmatrix}^T$

(dimension N) we can now write

$$\dot{\mathbf{e}} = \mathbf{A}\dot{\boldsymbol{\varepsilon}} + \mathbf{B}\dot{\mathbf{p}} \quad \text{(expresses equation (5) as befor but in incremental form)} \qquad (31)$$

$$\dot{\boldsymbol{\sigma}} = \mathbf{F}\,(\dot{\mathbf{e}} - \dot{\boldsymbol{\alpha}}) \quad \text{(expresses equations (26) to (28) in incremental form)} \qquad (32)$$

$$\mathbf{0} = \mathbf{G}\,(\dot{\mathbf{e}} - \dot{\boldsymbol{\alpha}}) \quad \text{(expresses equations (29) and (30) in incremental form)} \qquad (33)$$

$$\dot{\boldsymbol{\chi}} = \mathbf{K}\,(\dot{\mathbf{e}} - \dot{\boldsymbol{\alpha}}) \quad \text{(expresses equation (24) in incremental form)} \qquad (34)$$

Note that $\mathbf{K}$ is a diagonal matrix.

   We accommodate the plastic behaviour by noting that in the summations used in forming equations (32) and (33), in each case where $y_{n0} \leq 0$ then $\dot{\alpha}_n = 0$ and where $y_{n0} > 0$ then $k_n\,(\dot{e}_n - \dot{\alpha}_n) = -fy_{n0}/2\chi_n$. This allows equation (32) to be rewritten as $\dot{\boldsymbol{\sigma}} = \mathbf{F}^*\dot{\mathbf{e}} - \mathbf{P}$ and (33) as $\mathbf{0} = \mathbf{G}^*\dot{\mathbf{e}} - \mathbf{Q}$. From this we obtain $\mathbf{0} = \mathbf{G}^*\,(\mathbf{A}\dot{\boldsymbol{\varepsilon}} + \mathbf{B}\dot{\mathbf{p}}) - \mathbf{Q}$ or $\mathbf{G}^*\mathbf{B}\dot{\mathbf{p}} = -(\mathbf{G}^*\mathbf{A}\dot{\boldsymbol{\varepsilon}}) - \mathbf{Q}$. We set the increment of perturbation of the first node to an arbitrary value by modifying $\mathbf{G}^*\mathbf{A}$ and $\mathbf{G}^*\mathbf{B}$ in a similar way to before, and then obtain

$$\dot{\mathbf{p}} = -\left(\overline{\mathbf{G}^*\mathbf{B}}\right)^{-1}\left(\overline{\mathbf{G}^*\mathbf{A}}\dot{\boldsymbol{\varepsilon}} - \mathbf{Q}\right) \qquad (35)$$

It follows that:

$$\begin{aligned}
\dot{\boldsymbol{\sigma}} &= \mathbf{F}^*\left[\mathbf{A}\dot{\boldsymbol{\varepsilon}} - \mathbf{B}\left(\overline{\mathbf{G}^*\mathbf{B}}\right)^{-1}\left(\overline{\mathbf{G}^*\mathbf{A}}\dot{\boldsymbol{\varepsilon}} - \mathbf{Q}\right)\right] - \mathbf{P} \\
&= \mathbf{F}^*\left[\mathbf{A} - \mathbf{B}\left(\overline{\mathbf{G}^*\mathbf{B}}\right)^{-1}\left(\overline{\mathbf{G}^*\mathbf{A}}\right)\right]\dot{\boldsymbol{\varepsilon}} + \mathbf{F}^*\mathbf{B}\left(\overline{\mathbf{G}^*\mathbf{B}}\right)^{-1}\mathbf{Q} - \mathbf{P} \qquad (36) \\
&= \mathbf{D}\dot{\boldsymbol{\varepsilon}} - \mathbf{R}
\end{aligned}$$

The generalised forces must be updated. We do this as follows. First calculate the incremental extensions through: $\dot{\mathbf{e}} = \mathbf{A}\dot{\boldsymbol{\varepsilon}} - \mathbf{B}\left(\overline{\mathbf{G}^*\mathbf{B}}\right)^{-1}\left(\overline{\mathbf{G}^*\mathbf{A}}\dot{\boldsymbol{\varepsilon}} - \mathbf{Q}\right)$, then for all the elements that are initially elastic calculate $\dot{\chi}_n = k_n\dot{e}_n$ and for those that are initially plastic calculate $\dot{\chi}_n = -fy_{n0}/2\chi_n$.

   Note that the entire process just involves simple matrix manipulation and logical operations. The only matrix that has to be inverted is $\overline{\mathbf{G}^*\mathbf{B}}$ (which is of dimension $2M \times 2M$). All other operations just involve matrix multiplication, which is quadratic in the number of nodes or links.

4.2   Example: Elastic-Plastic Response

As an example, Fig. 3 shows the result when the bar assembly of Fig. 1 is subjected to uniaxial strain in the x-direction. The strengths of each of the links is set to
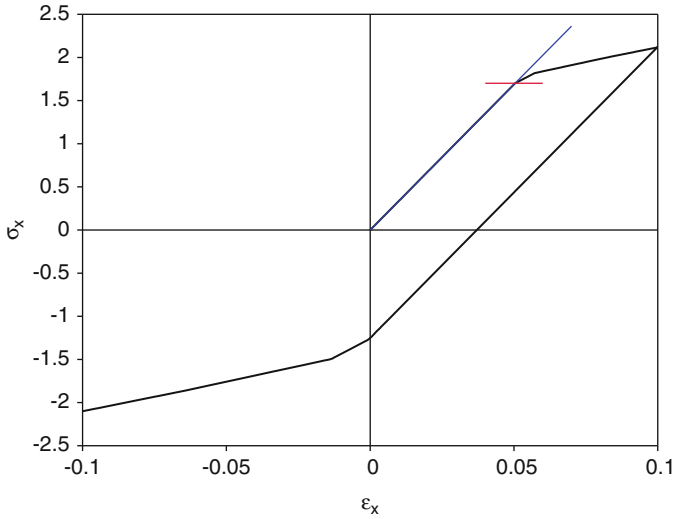
Fig. 3 A stress-strain curve for the bar assembly in Fig. 1 under uniaxial strain

$c_n = 1$. The initial stiffness as computed from the elastic calculation is shown by the blue line, and initial yield by the red bar. Note the unloading behaviour which is correctly modelled as initially elastic. The unloading response corresponds to the well-known Masing relationships, which apply for simple plasticity models of this sort.

4.3 Example: Yield and Failure Surfaces

Figure 4 shows the initial yield surface in (σ_x, σ_y) space for the same assembly, for $\tau = 0$. The blue envelope indicates the initial yield surface, that is, the stress state for which the first bar yields. The red envelope shows the ultimate failure surface, that is, the stress states achieved at large strain (strictly these are not at precisely $\tau = 0$). These surfaces are computed for equal strengths of the links in compression and tension, $c_n = 1$. The innermost, small envelope indicates initial yield surface when the strength of the links in compression is reduced to one tenth of the tensile value. This is computed as a precursor to later developments for a granular material when there will be an asymmetry between compression and tension. Note that the small inner surface is not symmetric about the origin.
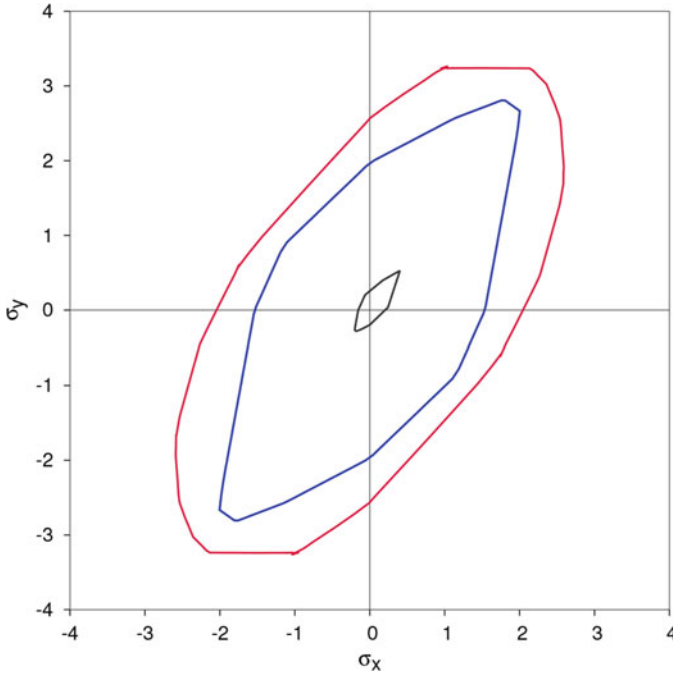
Fig. 4 Yield surface for bar assembly in Fig. 1

5 Model 3: Towards an Assembly of Particles

We now introduce a tangential motion as well as a normal one. As a preliminary, consider the mechanics of the tangential motion also to be governed by a simple plasticity law. The mechanics can be described by the expressions:

$$f = \frac{k_n^r}{2} \left(e_n^r - \alpha_n^r\right)^2 + \frac{k_n^t}{2} \left(e_n^t - \alpha_n^t\right)^2 \tag{37}$$

$$d = c_n^r \left|\dot{\alpha}_n^r\right| + c_n^t \left|\dot{\alpha}_n^t\right| \tag{38}$$

where e_n^r, e_n^t are the normal and tangential displacements, k_n^r, k_n^t stiffnesses and c_n^r, c_n^t the strengths. The model is shown conceptually in Fig. 5.

We can now treat the M nodes as if they were particles. The particle centres have velocities as before:

$$u_m = u_0 + \varepsilon_x x_m + \frac{\gamma - 2\omega}{2} y_m + p_m \tag{39}$$

$$v_m = v_0 + \frac{\gamma + 2\omega}{2} x_m + \varepsilon_y y_m + q_m \tag{40}$$
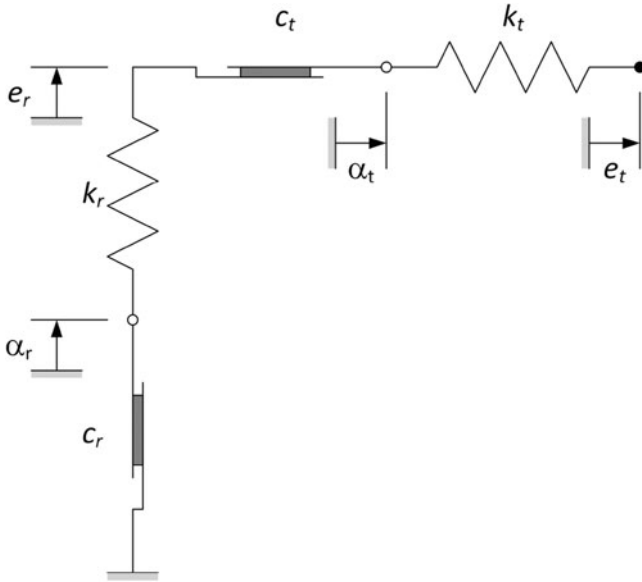
Fig. 5 Plastic element with normal and tangential components

and in addition each particle rotates (anticlockwise) an amount $\omega + \beta_m$, in other words β_m is the perturbation on the average rotation ω.

For the time being we shall assume for simplicity that the particle-to-particle contact occurs at the midpoint of the line between the two particle centres, and that the contact occurs on plane normal to this line. Both of these restrictions could easily be relaxed later, at the expense of making the geometry a little more complicated. We have as before:

$$
\begin{aligned}
e_n^r =& \varepsilon_x L_n \cos^2 \theta_n + \varepsilon_y L_n \sin^2 \theta_n + \gamma L_n \sin \theta_n \cos \theta_n \\
&+ \sum_{m=1}^{M} C_{mn} \left(p_m \cos \theta_n + q_m \sin \theta_n \right)
\end{aligned}
\tag{41}
$$

and in addition can determine the tangential displacement:

$$
e_{ij}^t = \left(u_j - u_i \right) \sin \theta_{ij} - \left(v_j - v_i \right) \cos \theta_{ij} + L_{ij} \left(\omega + \beta_i + \omega + \beta_j \right)
\tag{42}
$$

$$
e_n^t = \sum_{m=1}^{M} \left[C_{mn} \left(u_m \sin \theta_n - v_m \cos \theta_n \right) + |C_{mn}| \frac{L_n}{2} \beta_n \right] + L_n \omega
$$

$$
= \sum_{m=1}^{M} \left[C_{mn} \left(\begin{array}{l} \left(\varepsilon_x x_m + \dfrac{\gamma - 2\omega}{2} y_m + p_m \right) \sin \theta_n \\[2mm] - \left(\dfrac{\gamma + 2\omega}{2} x_m + \varepsilon_y y_m + q_m \right) \cos \theta_n \end{array} \right) + |C_{mn}| \frac{L_n}{2} \right] \tag{43}
$$

$$
+ L_n \omega
$$

$$
e_n^t = \left(\varepsilon_x - \varepsilon_y \right) L_n \sin \theta \cos \theta - \frac{\gamma}{2} L_n \left(\cos^2 \theta_n - \sin^2 \theta_n \right)
$$

$$
+ \sum_{m=1}^{M} \left[C_{mn} \left(p_m \sin \theta - q_m \cos \theta \right) + |C_{mn}| \frac{L_n}{2} \beta_m \right] \tag{44}
$$

Noting again that the terms in ω cancel. We can now write for the whole assembly:

$$
F = \sum_{n=1}^{N} \left[\frac{k_n^r}{2} \left(e_n^r - \alpha_n^r \right)^2 + \frac{k_n^t}{2} \left(e_n^t - \alpha_n^t \right)^2 \right] \tag{45}
$$

$$
D = \sum_{n=1}^{N} \left[c_n^r \left| \dot{\alpha}_n^r \right| + c_n^t \left| \dot{\alpha}_n^t \right| \right] \tag{46}
$$

$$
\sigma_x = \frac{1}{a^2} \frac{\partial F}{\partial \varepsilon_x} = \frac{1}{a^2} \sum_{n=1}^{N} \left[k_n^r \left(e_n^r - \alpha_n^r \right) \frac{\partial e_n^r}{\partial \varepsilon_x} + k_n^t \left(e_n^t - \alpha_n^t \right) \frac{\partial e_n^t}{\partial \varepsilon_x} \right]
$$

$$
= \frac{1}{a^2} \sum_{n=1}^{N} \left[\begin{array}{l} k_n^r \left(e_n^r - \alpha_n^r \right) L_n \cos^2 \theta_n + \\ k_n^t \left(e_n^t - \alpha_n^t \right) L_n \sin \theta_n \cos \theta_n \end{array} \right] \tag{47}
$$

$$
\sigma_y = \frac{1}{a^2} \frac{\partial F}{\partial \varepsilon_y} = \frac{1}{a^2} \sum_{n=1}^{N} \left[k_n^r \left(e_n^r - \alpha_n^r \right) \frac{\partial e_n^r}{\partial \varepsilon_y} + k_n^t \left(e_n^t - \alpha_n^t \right) \frac{\partial e_n^t}{\partial \varepsilon_y} \right]
$$

$$
= \frac{1}{a^2} \sum_{n=1}^{N} \left[\begin{array}{l} k_n^r \left(e_n^r - \alpha_n^r \right) L_n \sin^2 \theta_n + \\ k_n^t \left(e_n^t - \alpha_n^t \right) L_n \sin \theta_n \cos \theta_n \end{array} \right] \tag{48}
$$

$$\tau = \frac{1}{a^2} \frac{\partial F}{\partial \gamma} = \frac{1}{a^2} \sum_{n=1}^{N} \left[k_n^r \left(e_n^r - \alpha_n^r \right) \frac{\partial e_n^r}{\partial \gamma} + k_n^t \left(e_n^t - \alpha_n^t \right) \frac{\partial e_n^t}{\partial \gamma} \right]$$

$$= \frac{1}{a^2} \sum_{n=1}^{N} \left[\begin{array}{c} k_n^r \left(e_n^r - \alpha_n^r \right) L_n \sin \theta_n \cos \theta_n + \\ k_n^t \left(e_n^t - \alpha_n^t \right) \frac{L_n}{2} \left(\cos^2 \theta_n - \sin^2 \theta_n \right) \end{array} \right]$$

(49)

The perturbations lead to the internal equilibrium equations:

$$0 = \frac{\partial F}{\partial p_m} = \sum_{n=1}^{N} \left[k_n^r \left(e_n^r - \alpha_n^r \right) \frac{\partial e_n^r}{\partial p_m} + k_n^t \left(e_n^t - \alpha_n^t \right) \frac{\partial e_n^t}{\partial p_m} \right]$$

$$= \sum_{n=1}^{N} C_{mn} \left[k_n^r \left(e_n^r - \alpha_n^r \right) L_n \cos \theta_n + k_n^t \left(e_n^t - \alpha_n^t \right) L_n \sin \theta_n \right]$$

(50)

$$0 = \frac{\partial F}{\partial q_m} = \sum_{n=1}^{N} \left[k_n^r \left(e_n^r - \alpha_n^r \right) \frac{\partial e_n^r}{\partial q_m} + k_n^t \left(e_n^t - \alpha_n^t \right) \frac{\partial e_n^t}{\partial q_m} \right]$$

$$= \sum_{n=1}^{N} C_{mn} \left[k_n^r \left(e_n^r - \alpha_n^r \right) L_n \sin \theta_n + k_n^t \left(e_n^t - \alpha_n^t \right) L_n \cos \theta_n \right]$$

(51)

$$0 = \frac{\partial F}{\partial \beta_m} = \sum_{n=1}^{N} \left[k_n^r \left(e_n^r - \alpha_n^r \right) \frac{\partial e_n^r}{\partial \beta_m} \right] = \sum_{n=1}^{N} \left[k_n^r \left(e_n^r - \alpha_n^r \right) \frac{L_n}{2} \left| C_{mn} \right| \right]$$

(52)

5.1 Matrix Analysis

The above equations can again be cast in incremental form and solved by matrix methods. The matrix equations are cast in exactly the same way as in the previous section. We define now:

$$\mathbf{p} = \begin{bmatrix} p_1 & q_1 & \beta_1 & \cdots & p_m & q_m & \beta_m \end{bmatrix}^T \quad \text{(dimension } 3M) \quad (53)$$

$$\mathbf{e} = \begin{bmatrix} e_1^r & e_1^t & \cdots & e_n^r & e_n^t \end{bmatrix}^T \quad \text{(dimension } 2N) \quad (54)$$

$$\boldsymbol{\alpha} = \begin{bmatrix} \alpha_1^r & \alpha_1^t & \cdots & \alpha_n^r & \alpha_n^t \end{bmatrix}^T \quad \text{(dimension } 2N) \quad (55)$$

$$\boldsymbol{\chi} = \begin{bmatrix} \chi_1^r & \chi_1^t & \cdots & \chi_n^r & \chi_n^t \end{bmatrix}^T \quad \text{(dimension } 2N) \quad (56)$$

We can then write

$$\dot{\mathbf{e}} = \mathbf{A}\dot{\boldsymbol{\varepsilon}} + \mathbf{B}\dot{\mathbf{p}} \qquad \text{(equations (41) and (44) in incremental form)} \qquad (57)$$

$$\dot{\boldsymbol{\sigma}} = \mathbf{F}\,(\dot{\mathbf{e}} - \dot{\boldsymbol{\alpha}}) \qquad \text{(equations (47) to (49) in incremental form)} \qquad (58)$$

$$\mathbf{0} = \mathbf{G}\,(\dot{\mathbf{e}} - \dot{\boldsymbol{\alpha}}) \qquad \text{(equations (50) to (52) in incremental form)} \qquad (59)$$

$$\dot{\boldsymbol{\chi}} = \mathbf{K}\,(\dot{\mathbf{e}} - \dot{\boldsymbol{\alpha}}) \qquad \text{(generalisation of equations (24) in incremental form)} \qquad (60)$$

Note that **K** is a diagonal matrix.

The structure of the analysis then follows exactly as before, although the dimensions of the equations are now different.

5.2 Example: Elastic-Plastic Behaviour

Figure 6 shows the computed stress-strain behaviour for a uniaxial tension test, followed by unloading into uniaxial compression. Note again the transition from elastic to nonlinear response and the fact that the unloading corresponds to the Masing relationships.
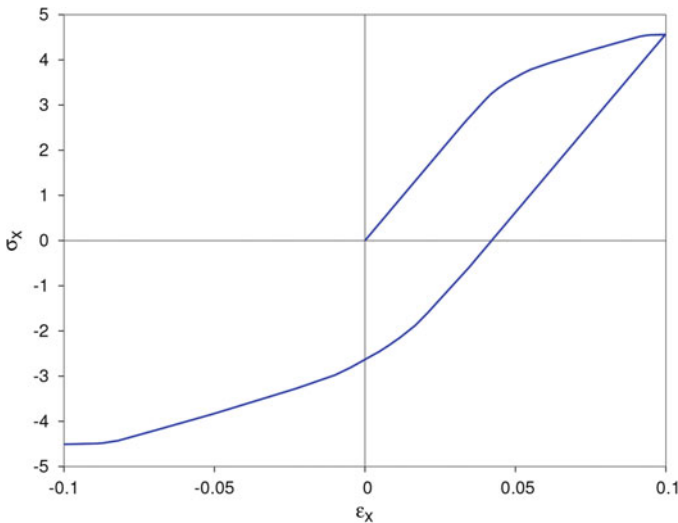
Fig. 6 Stress-strain behaviour for plastic model with tangential components

6 Model 4: Particles with Frictional Contact

Finally we modify the above model to introduce a more physically reasonable model of the particle-to-particle contact. We neglect the possibility of plastic deformation in compression, and assume that contact is simply broken in tension. We assume that plastic shear deformation is governed by a frictional relationship. These results are achieved by the expressions:

$$f = \frac{k_n^r}{2}\langle -e_n^r \rangle^2 + \frac{k_n^t}{2}\left(e_n^t - \alpha_n^t\right)^2 \tag{61}$$

$$d = \mu_n k_n \langle -e_n^r \rangle^2 \left|\dot{\alpha}_n^t\right| \tag{62}$$

The model is shown conceptually in Fig. 7. In the numerical application the presence of the Macaulay bracket in Eq. (61) (which results in zero normal stiffness in tension) is implemented by applying a very small multiplier to elastic stiffness for any element in tension. As there is no plastic yield in the normal direction in compression, this is simply implemented by a very high value of the normal yield stress. The yield surface in the tangential direction is implemented in the form:

$$y_n = \chi_t^2 - (c_t - \mu k_n e_n)^2 \tag{63}$$

where c_t is an arbitrarily small shear strength included for numerical stability. The consistency condition becomes

$$dy_n = -f y_{n0} = 2\chi_t d\chi_t + 2\left(c_t - \mu k_n e_n\right)\mu k_n de_n \tag{64}$$

Fig. 7 A simple contact model
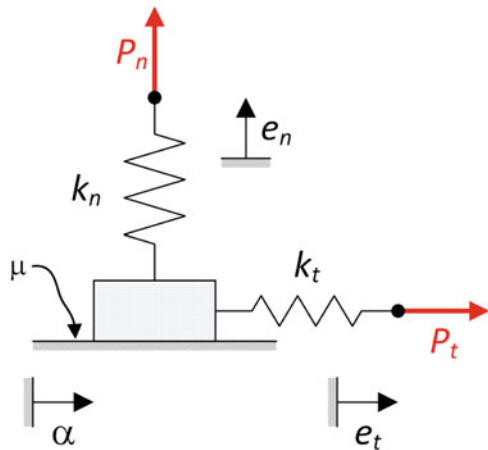
which we can re-arrange in the form:

$$dy_n = k_t \left(de - d\alpha \right) = -\frac{f y_{n0}}{2\chi_t} - \frac{\left(c_t - \mu k_n e_n \right) \mu k_n}{2\chi_t} de_n$$

$$\simeq -\frac{f y_{n0}}{2\chi_t} - S\left(\chi_t \right) \mu k_n de_n$$

(65)

where $S(x)$ is a signum function. The above form again allows reformulation of Eqs. (58) and (59) in the form $\dot{\boldsymbol{\sigma}} = \mathbf{F}^* \dot{\mathbf{e}} - \mathbf{P}$ and (33) as $\mathbf{0} = \mathbf{G}^* \dot{\mathbf{e}} - \mathbf{Q}$, and the incremental solution can proceed as before.

6.1 Example

Figure 8 presents the results of two tests using the analogue of a granular material. Unlike the previous results this is presented using the compressive positive conventional in soil mechanics. The sample is first brought to an isotropic stress state of $\sigma_x = \sigma_y = 2$ (compressive). This stage is not shown on the figure.

The blue trace in Fig. 8a then shows the stress-strain curve for a "drained" compressive test at constant mean stress, shown in terms of $\left(\sigma_x - \sigma_y \right) / 2$ vs $\varepsilon_x - \varepsilon_y$. As before there is an initial stiff response followed by plasticity. On unloading there is again an initial stiff response followed by reverse plasticity. This time the Masing rules are not exactly followed because of the tension/compression asymmetry in the model.

Figure 8b shows the corresponding volumetric response in terms of volumetric strain $\varepsilon_x + \varepsilon_y$ vs $\varepsilon_x - \varepsilon_y$. For this case, which effectively represents a rather loose granular material, plastic deformation is associated with compression. It is assumed that this is because those elements where sliding is triggered contribute to compressive strains. Note that when the stress reversal occurs plastic compression again takes place, confirming that this is a plastic rather than elastic process.

The red trace in Fig. 8a shows the stress-strain curve for a "drained" compressive test initially sheared in the opposite direction. The characteristics are broadly as for the first test, and Fig. 8b again shows that during plastic deformation compression occurs.

7 Discussion and Conclusions

A preliminary model has been presented in which the hyperplasticity framework is used to formulate a micromechanical model. Simple hypotheses are made for the stored and dissipated energy at a particle level. These are integrated over a Representative Volume Element to obtain the macroscopic response. An important
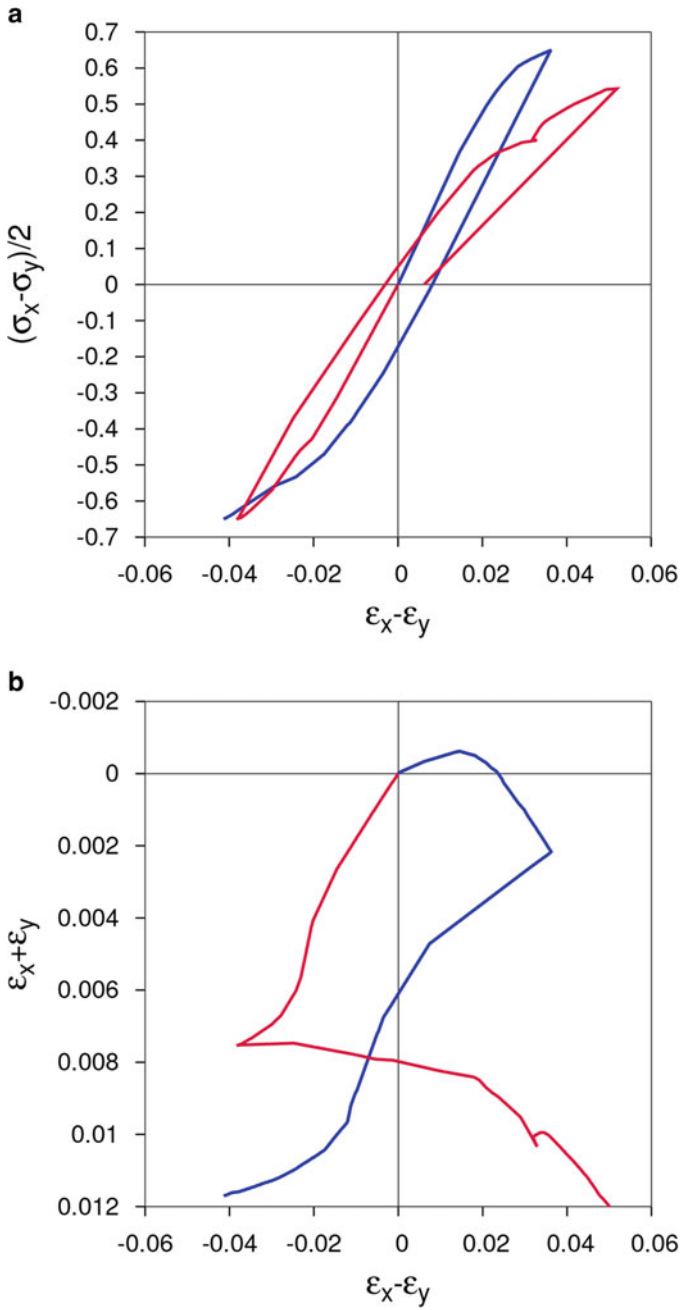
Fig. 8 (**a**) Deviatoric stress-strain behaviour for frictional model, (**b**) compressive strains during plastic shearing

feature of the hyperplasticity approach is that the perturbations on the affine deformation field are regarded as internal variables, which are eliminated from the overall equations through use of what are in effect the internal equilibrium equations at a particle level.

The whole formulation is expressed for computational purposes in terms of matrix operations. This allows a relatively quick and simple coding. Of course there are other ways of formulating an equivalent model. A conventional plasticity theory approach could be adopted. Alternatively a very similar model could be expressed in terms of Discrete Element coding, solving the dynamic equations explicitly. It remains to be seen whether the method adopted here would prove more efficient or less for large particle assemblies. However, given that one of the principle challenges of bridging the gap between micro- and macro-mechanics for granular assemblies is the ability to handle a reasonably large number of particles efficiently, it is worth exploring whether hyperplasticity offers an efficient route to calculation.

It is emphasised that the model described here is preliminary only, containing a few key features of typical granular material behaviour: principally that of frictional contact between particles. In order to develop the model a more sophisticated approach would be needed to establishing the positions and orientations of contacts in a realistic assembly. Furthermore, the movement of particles would need to be tracked, and appropriate updating of the "links" between particles made as contacts are broken and new contacts made. The issue of updating particle positions and the making and breaking of contacts has not been addressed here. Nevertheless, the approach shows sufficient promise to be worth pursuing.

References

1. Houlsby G.T., Puzrin, A.M.: Principles of Hyperplasticity: an Approach to Plasticity Theory Based on Thermodynamic Principles. Springer Verlag, London (2006).
2. Ziegler H.: An Introduction to Thermomechanics. North Holland, Amsterdam (1977, 2nd edition 1983).
3. Puzrin A.M., Houlsby G.T.: A thermomechanical framework for rate-independent dissipative materials with internal functions, International Journal of Plasticity 17, 1147–1165 (2001).
4. Houlsby G.T., Puzrin A.M.: Rate-dependent plasticity models derived from potential functions. Journal of Rheology, 46, 113–126 (2002).

Wave Propagation and Elasticity in Granular Soils: A Numerical Approach for a Micromechanical Perspective

Vanessa Magnanimo

Abstract In this work we propose an overview of results about propagation of waves and elasticity in soils over the last 30 years. Remarkably, the chapter attempts to frame and compare contributions from soil mechanics, solid mechanics and physics. In a wide landscape, we focus on the micromechanical approach to the topic. Numerical simulations, based on the Discrete Element Method, have revealed the outmost role of the microstructure in characterising the elastic behaviour of granular soils. Following this evidence, microstructure-based continuum models have been developed and are discussed here, starting from the classical Effective Medium Theory. Finally, the chapter describes how micromechanical models can be extended to the case of immersed granular soils, and compares the new model with experiments on sand soils in a wide range of saturation degrees.

Keywords Granular materials · Wave propagation · Elasticity · Micromechanics · Discrete Element Method

1 Introduction: Overview

For many geotechnical structures under working loads, the deformations are small. The regime of deformation where the behaviour of soils can be considered linear elastic is infinitesimal, with nonlinear and irreversible effects present already at small strains. Nevertheless, characterisation of the stiffness of soils is of outmost importance, as it provides an anchor on which to attach the subsequent stress-strain response [6, 39].

V. Magnanimo (✉)
MultiScale Mechancs (MSM), TFE, Mesa+, University of Twente, Enschede, Netherlands

Construction Management & Engineering (CME), University of Twente, Enschede, Netherlands
e-mail: v.magnanimo@utwente.nl, https://www.utwente.nl

Despite the long-standing debate across the geomechanical, mechanical and physics communities, basic features of the physics of granular elasticity are currently unresolved, like the definition of a proper set of state variables to characterise the effective moduli. In early studies, macroscopic variables measurable in laboratory experiments were thought to be sufficient. Based on those information, many empirical relations have been proposed, where the elastic moduli are functions of pressure and void ratio, e.g., [4, 16, 17, 46]. However, such formulations miss a first order mechanical interpretation and coefficients have to be back-calculated case by case from experiments, based on the specific material and stress path. Moreover, experimental evidences [7, 13, 27, 44], along with many numerical studies [2, 35], show that stress and volume fraction are not sufficient to characterise granular elasticity.

On the other hand, conventional approaches in the framework of solid-state elasticity [31] consider a uniform strain at all scales, with the displacement field of the grains following the macroscopic deformation (affine approximation). These Effective Medium Theories (EMT) developed by Digby and Walton [10, 52] in the 1980s are the first, simplest attempt for a micromechanical approach to the elasticity of granular soils. EMT predicts the moduli of an isotropic granular material in terms of the external pressure, the void ratio and average coordination number (p_0, e, Z). In particular, the pressure dependency is $G \sim K \sim p_0^{1/3}$, a direct consequence of the Hertz interaction between particles. However, such scaling is not recovered in experiments and previous works (see [15] for a review) raise serious questions about the validity of these generally accepted theoretical elastic formulations.

Empirical relations coming from experiments and micromechanical EMT equations show many similarities and the two approaches can fruitfully inform each other. Following one of the paths suggested already in [15] and further developed in [33, 35], this chapter shows that when the evolution of the microstructure is properly modelled, the set of state variables to describe granular elasticity is complete, and experiments follow the trend predicted by the model. This is obtained with the aid of Discrete Element Simulations (DEM) that uniquely allow to monitor the kinematics at the microscale and establish a link it with the macroscale.

However, the EMT framework still largely overpredicts the elastic moduli of loose samples, especially when shear is involved. The difficulty in describing theoretically the shear modulus is due to the complex relaxation of the particles as related to the structural disorder in the packing [35]. Sophisticated theories in which collective fluctuations and relaxation of the particles are explicitly accounted for are needed to recover quantitative agreement. Here we briefly illustrate the mechanics beyond these theories and compare the results with numerical simulations.

This chapter has the ambition to link the work on wave propagations and granular elasticity from different scientific communities. The work offers a wide perspective, even if non-comprehensive, to elucidate on the microscopic origin of macroscopic phenomena related to elasticity and wave propagation in particulate media. For the sake of simplicity, here we focus on of an isotropic materials to illustrate traditional models and new findings.

Additionally we extend our study, by illustrating a recent work where the simple EMT has been successfully combined with a geomechanical framework to provide a micromechanical model for unsaturated sand [42]. The model is able to interpret experimental results, and to elucidate the mechanisms underlying different patterns of the shear modulus in unsaturated materials observed in the literature.

The chapter is organised as follows: in Sect. 2, the classical relations between wave velocity and elastic moduli in a solid are derived; Sect. 3 introduces the specific features of waves in granular materials as observed at macroscopic level and the empirical models based on them; Sect. 4 describes the micromechanical approach based on the Effective Medium Theory and Sect. 5 compares the predictions of EMT theory with DEM simulations; in Sect. 6, advanced micromechanical models accounting for fluctuations are introduced and compared with DEM data. Finally in Sect. 7, the micromechanical approach is extended to describe wave propagation in unsaturated soils.

2 Waves in Solids: The Duality Between Waves and Elasticity

A wave is an elastic perturbation that propagates between two points through a body (volume waves) or on the surface (surface waves) without material displacement [3]. In the case of volume waves the acoustic-elastic effect is related to the change in the wave velocity of small amplitude waves due to the stress state of the body. Differently from liquids, in a solid material three acoustic polarisations exist, more specifically a longitudinal and two transversal branches. In the present section, we will derive the relations between the elastic characteristics and the velocities of acoustic waves, in the longitudinal and transversal directions.

Let us consider a three-dimensional body with density ρ, homogeneous, isotropic and elastic. The stress change due to the propagation of the wave in the body is given by the Newton's second law applied to the volume element ρdV [9]:

$$\frac{\partial \sigma_{ij}}{\partial x_j} = \rho \ddot{u}_i, \tag{1}$$

with σ_{ij} stress and u_i displacement of the volume element in directions $i, j = 1, 2, 3$. On the other hand, the constitutive relation for the elastic body holds that relates the stress tensor to the strain ϵ_{ij} via the stiffness tensor C_{ijkl}

$$\dot{\sigma}_{ij} = C_{ijkl}\dot{\epsilon}_{kl}. \tag{2}$$

In the isotropic case, Eq. (2) becomes (Lamé equation)

$$\dot{\sigma}_{ij} = \lambda\Theta\delta_{ij} + 2G\epsilon_{ij}, \tag{3}$$

where $\Theta = \sum_{i=1}^{3} \epsilon_{ii}$, G and λ are the shear modulus and Lamé coefficient, respectively, and the incremental strain tensor is given by

$$\epsilon_{ij} = \frac{1}{2} \left(\frac{\partial u_i}{\partial x_j} + \frac{\partial u_j}{\partial x_i} \right). \tag{4}$$

The bulk modulus is related to the previous quantities as $K = \lambda + 2/3G$.

Using Eqs. (3–4) in Eq. (1) and the relation $\Theta = \dfrac{\partial u_i}{\partial x_i}$, the equation of motion becomes

$$\rho \frac{\partial^2 u_i}{\partial t^2} = \frac{\partial}{\partial x_j} \left(\lambda \frac{\partial u_i}{\partial x_i} \right) + G \frac{\partial^2 u_i}{\partial x_j^2} + G \frac{\partial}{\partial x_i} \left(\frac{\partial u_i}{\partial x_j} \right). \tag{5}$$

From Helmholtz decomposition, the displacement vector $\boldsymbol{u}$ can be written in terms of a scalar potential ϕ and a vector potential $\boldsymbol{\psi}$ as

$$\boldsymbol{u} = \nabla\phi + \nabla \times \boldsymbol{\psi}, \tag{6}$$

with

$$\nabla \times (\nabla\phi) = \boldsymbol{0} \qquad \text{and} \qquad \nabla \cdot (\nabla \times \boldsymbol{\psi}) = 0, \tag{7}$$

due to the properties of divergence and curl. Note the tensorial notation has been introduced here for the sake of brevity.

By using the decomposition in Eq. (6), Eq. (5) becomes

$$\nabla \left[\rho \frac{\partial^2 \phi}{\partial t^2} - \left(\lambda + \frac{4}{3}G \right) \nabla^2 \phi \right] + \nabla \times \left[\rho \frac{\partial^2 \boldsymbol{\psi}}{\partial t^2} - G\nabla^2 \boldsymbol{\psi} \right] = \boldsymbol{0}. \tag{8}$$

Equation (8) is known as the wave equation and predicts longitudinal and transversal modes of propagation. The first term depends only on ϕ and is related to the propagation of waves in the longitudinal direction, while the second term depends on the vector potential $\boldsymbol{\psi}$ and is associated with transversal waves. Both terms must be separately zero to satisfy Eq. (8), that is, the two propagation modes, longitudinal and transversal, are independent.

Let us define the longitudinal and shear components of the displacement as

$$\boldsymbol{u}_P = \nabla\phi \qquad \text{and} \qquad \boldsymbol{u}_S = \nabla \times \boldsymbol{\psi}. \tag{9}$$

The combination of Eqs. (7) and (9) leads to constrains for $\boldsymbol{u}_P$ and $\boldsymbol{u}_S$. Because of $\nabla \times \boldsymbol{u}_P = \boldsymbol{0}$, there are no angular displacements and rotations associated with $\boldsymbol{u}_P(\phi)$, being this a characteristic of longitudinal waves. Similarly, $\nabla \cdot \boldsymbol{u}_S = 0$

assures that volume changes associated with $\boldsymbol{u}_S(\boldsymbol{\psi})$ are forbidden, as expected for transversal waves.

Finally, Eq. (8) results in the following two equations:

$$\frac{\partial^2 \boldsymbol{u}_P}{\partial t^2} = V_P^2 \nabla^2 \boldsymbol{u}_P \qquad \text{and} \qquad \frac{\partial^2 \boldsymbol{u}_S}{\partial t^2} = V_S^2 \nabla^2 \boldsymbol{u}_S, \tag{10}$$

where

$$V_P = \sqrt{\frac{(\lambda + 4/3G)}{\rho}} \qquad \text{and} \qquad V_S = \sqrt{\frac{G}{\rho}} \tag{11}$$

are the velocities of longitudinal and transversal waves in an isotropic elastic body.

From Eq. (11), we can immediately draw some interesting conclusions: (1) the propagation velocity increases with the stiffness of the material and decreases with its mass density (inertia), these characteristics being constants in a given solid body; (2) the velocity of transversal waves is smaller than the velocity of longitudinal waves, given the relative values of the moduli.

3 Waves in Granular Media

We move now our attention from solid to particulate materials. In this section we will highlight the most relevant features characteristic of wave propagation in granular materials.

When the wavelength is significantly longer than the internal scales of the material, such as particle or cluster size, the propagation velocity can be defined for the equivalent continuum, that is, Eqs. (11), where the elastic moduli and mass density refer to the bulk medium. Differently, for high frequencies and short wavelengths, the continuum assumption does not hold, due to the heterogeneity of the material at small scale and forces fluctuation [50]. With increasing frequencies, features related to the multiscale nature of soils become dominant, e.g., dispersion and frequency filtering. These aspects are beyond the scope of this work and in the next sections the focus will be on the long wave length limit.

Other than frequency, also amplitude is an important factor to take into account. The propagation of elastic waves is, by definition, a small perturbation phenomenon that does not alter the fabric or cause permanent (plastic) effects. This condition must be guaranteed for the continuum analogy to hold. This is shown by the degradation curve obtained in the resonant column device that provides values of the elastic shear stiffness G for increasing amplitude of the shear strain. A typical output of the resonant column experiment is given in Fig. 1. The figure shows that the response of granular materials is nonlinear and inelastic even at extremely small strains. The region of stress or strain in which granular materials can be described as truly elastic, producing an entirely recoverable response to
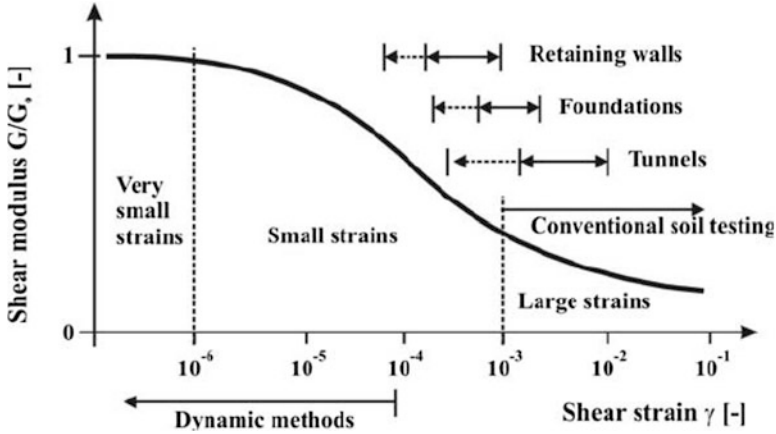
Fig. 1 Degradation curve for *G* with indication of typical soil tests and geotechnical applications per strain regime [34]

perturbations, the so-called small-strain stiffness G_{max}, is very small, corresponding to shear strains of the order of 10^{-6}. In turn, the size of the elastic, reversible regime depends on material characteristics, stress state, anisotropy: the elastic range increases with increasing asperities (particle friction) and pressure, but decreases with increasing anisotropy. Strain-amplitude-dependent moduli are not addressed further here, although its importance is widely recognised. In the following, all references will be to the small-strain shear modulus G_{max} and we will use simply *G* for it, unless otherwise stated.

If both conditions, long wavelength and small amplitude, are fulfilled, wave measurements (obtained, e.g., via wave transducers) can be used to infer elastic moduli and vice versa.

3.1 Macroscale Observations: Pressure-Dependent Elasticity

Several authors have carried on experiments to assess the influence of material characteristics and initial conditions on the elastic/wave properties of natural and synthetic granular materials, see, for example, [7, 17, 30] for experiments on sand in the resonant column device or [11, 29] for wave experiments on sand and glass beads. At the macroscopic level, all these studies lead to a similar conclusion that the initial soil stiffness is a nonlinear function of the stress, specifically the mean effective stress. Based on experiments, empirical expressions have been proposed for the shear stiffness of soils under isotropic conditions (e.g., [4, 16, 17, 30]):

$$G = Af(e)p_0^{\alpha} \qquad \text{hence} \qquad V_s = Af(e)p_0^{\alpha/2}, \tag{12}$$

where A and α are experimentally determined constants, p_0 is the hydrostatic pressure and $f(e)$ is a function that describes the effect of void ratio e again obtained empirically, e.g., [16]:

$$f(e) = \frac{(2.97 - e)^2}{(1 + e)}. \tag{13}$$

In Eq. (12) the exponent α and the factor A are assumed to be constants, related to the material characteristics and independent of the stress level. Differently from $f(e)$, there is no common interpretation for α and A and they must be retrieved case by case from experiments. Hardin [16, 17] has reported values of α around 0.25 for sands. The same value was confirmed in [30]. Domenico in [11] conducted experiments on dry/unsaturated glass beads and sands. He obtained a very similar expression to Eq. (12) with the exponent depending on the saturation degree. Values of α close to those reported by Hardin were found in the case of dry materials, with negligible differences between rounded sand and glass beads.

While the majority of these studies are restricted to isotropic loading conditions, in their initial work, Hardin and Black [16] suggested that Eq. (12) can be extended to anisotropic soils. Later on, modifications (see, for example, [4, 46]) have led to a generalised expression of the form:

$$G = A f(e) p_0^{1-\beta_i-\beta_j} \sigma_i^{\beta_i} \sigma_j^{\beta_j}, \tag{14}$$

where the directions i and j of polarisation and propagation coincide with the principal axes of stress and of anisotropy of the material [39]. The expression suggests that the stiffness depends on the principal stresses in the directions of polarisation and propagation. A wide range of values has been reported for β_i and β_j depending on the specific stress path.

Thus, extensive experimental evidences and theoretical studies support the choice of a power function to relate stiffness and stress. What is still missing is the physical interpretation of the parameters A and α in Eq. (12). An intriguing interpretation associates those to the structure of the granular soil, i.e., the fabric. Among others, the authors in [7] have related the dynamic shear modulus of glass beads in resonant column monotonic/cyclic tests to the fabric, as the sample was sheared in various directions with constant mean stress. Santamarina [47] has observed different scaling of the wave velocities at low/high stress and identified a transition between two regimes with varying and constant fabric, respectively. More recently, the authors in [13] have used bender elements to underline the effect of (inherent and induced) anisotropy on the elastic stiffness of sand under triaxial conditions. In these experiments features of the elastic behaviour of the material are linked to the internal structure. From there, the relation between the parameters in Eq. (12) and the fabric can be indirectly inferred.

In the next section we will use a different approach and derive the elastic properties of the bulk starting from the grain scale. Finally we will compare the

results with the empirical relations presented above. When general expressions are confirmed, wave velocities and stiffness experiments can be used as indirect measurement of the internal structure of the granular medium or to monitor fabric changes induced by loading.

4 Micromechanics

The experiments referred to in Sect. 3.1 are examples of approaches that rely on macro measurements. On the other hand, the state of the granular medium at the micromechanical level is defined by the distribution of contacts, forces and orientations. In turn, it is possible to describe the macroscopic stiffness of the granular medium in terms of its micromechanical characteristics.

In this section, we will derive the expression of the stiffness tensor for an isotropic assembly of identical spheres, starting from the grains interaction. Then we will compare the expression with Eq. (12) and show how micromechanics is able to explain the empirical coefficients obtained from experiments.

4.1 Interaction at the Grain Level

Kinematics We consider a dense aggregate of N_B identical, frictional elastic spheres with diameter d, isotropically compressed. The contact point c between two contacting particles A and B is identified by the unit vector n_i along the line that joins the centres of the two spheres. The unit vector t_i belongs to the plane tangent to the spheres in c. The kinematics of the pair $A - B$ is given by the incremental relative displacement between the centres

$$\dot{u}_i^{(BA)} = \dot{X}_i^B - \dot{X}_i^A - \frac{1}{2}\epsilon_{ijk}(\dot{\theta}_j^B - \dot{\theta}_j^A)n_k, \qquad (15)$$

where $\dot{X}_i^A, \dot{X}_i^B$ and $\dot{\theta}_i^A, \dot{\theta}_i^B$ are the increments in the centres translation and rotations, respectively, and ϵ_{ijk} is the permutation tensor. For the sake of simplicity, we will assume in the following that the rotational velocities are infinitesimally small. Thus $\dot{u}_i^{(BA)}$ can be expressed in terms of the normal component $\dot{\delta}_i$ and $\dot{s}_i$ with

$$\dot{\delta}_i = \dot{\delta}n_i = (\dot{X}_k^B - \dot{X}_k^A)n_k n_i \qquad (16)$$

and tangential component

$$\dot{s}_i = (\dot{X}_i^B - \dot{X}_i^A) - \dot{\delta}n_i. \qquad (17)$$

We also introduce here the branch vector l_i^c that connects the centres of A and B interacting at c and relates to the particle diameter as

$$l_i^c = (X_i^B - X_i^A) = dn_i. \tag{18}$$

Contact Force Contacting particles interact by means of contact forces. We denote by f_i^c the i-th component of the force exerted on particle A by particle B. Since we are interested in the incremental response of the aggregate, we will refer to the incremental force $\dot{f}_i^c$. In this case, when deformations are small, the incremental response is elastic, proportional to the relative displacement in both normal and tangential directions. If we denote by K_N and K_T the normal and tangential components of the stiffness the constitutive law at the contact is

$$\dot{f}_i^c = K_N \dot{\delta} n_i + K_T \dot{s}_i. \tag{19}$$

K_N and K_T are constant values if a linear contact model is considered. When Hertz contact interaction is assumed [18], K_N and K_T are functions of the normal component δ of the relative displacement, the diameter d of the spheres, and their material properties

$$K_N = \frac{G_g d^{1/2}}{1 - v} \delta^{1/2} \tag{20}$$

and

$$K_T = \frac{2G_g d^{1/2}}{2 - v} \delta^{1/2}, \tag{21}$$

where G_g and v are the shear modulus and Poisson's ratio of the individual particle.

Incremental Stress At the macroscale the relevant quantities are the incremental stress tensor $\dot{\sigma}_{ij}$ and the strain tensor $\dot{\epsilon}_{ij}$. Given the incremental force, the incremental stress tensor is determined by the particle arrangement as [26]

$$\dot{\sigma}_{ij} = \frac{1}{V} \sum_{\theta} \sum_{c \in N^c(\theta)} l_i^c \dot{f}_j^c, \tag{22}$$

that is, the average on the volume V of the Cauchy's stress [31], with N^c total number of contacts. The equation emphasises the dependence of the stress on the average of forces on equally oriented contacts. In the case of a regular array, the values of l_i^c and $\dot{f}_i^c$ are known for each contact and the components of $\dot{\sigma}_{ij}$ can be easily determined. For a random isotropic aggregate of particles of the number of contacts for each orientation θ is the same, and can be characterised by the scalar coordination number, i.e., the average number of contacts in the sample

$Z = 2N^c/N_B$, with N_B number of particles in V. Then, the incremental stress simplifies to the form

$$\dot{\sigma}_{ij} = \frac{Z}{V} \left\langle l_i^c \dot{f}_j^c \right\rangle. \tag{23}$$

4.2 Theoretical Modelling: The Effective Medium Theory

The Effective Medium Theory (EMT) assumes that the incremental displacement of each point X in the (discrete) body is given by the applied average strain $\dot{\epsilon}_{ij}$ [10, 52]. Following this hypothesis, the relative displacement between contacting particles is

$$\dot{u}_h^{(BA)} = \dot{X}_h^B - \dot{X}_h^A = \dot{\epsilon}_{hk} l_k^c = \dot{\epsilon}_{hk} d n_k, \tag{24}$$

thus, the normal and tangential components of the incremental displacement become

$$\dot{\delta} = d\dot{\epsilon}_{hk} n_h n_k \qquad \text{and} \qquad \dot{s}_j = \dot{\epsilon}_{jk} d n_k - d\dot{\epsilon}_{hk} n_h n_k n_j. \tag{25}$$

Using Eqs. (18) and (25) in Eq. (19) the incremental stress can be rewritten as

$$\dot{\sigma}_{ij} = \frac{d^2}{V} \sum_{\theta} \sum_{c \in N^c(\theta)} \left[\left\langle K_N \dot{\epsilon}_{hk} n_h n_k n_i n_j \right\rangle + \left\langle K_T \dot{\epsilon}_{jk} n_i n_k \right\rangle - \left\langle K_T \dot{\epsilon}_{hk} n_h n_k n_i n_j \right\rangle \right]. \tag{26}$$

Using Eq. (2) in its incremental form, after some further algebra, we find the following solution for the stiffness tensor:

$$C_{ijkh} = \frac{\dot{\sigma}_{ij}}{\dot{\epsilon}_{hk}} =$$

$$= \frac{d^2}{V} \sum_{\theta} \sum_{c \in N^c(\theta)} \left[\left\langle (K_N - K_T) n_h n_k n_i n_j \right\rangle \right] \tag{27}$$

$$+ \frac{d^2}{V} \sum_{\theta} \sum_{c \in N^c(\theta)} \frac{1}{4} \left[\left\langle K_T \delta_{jh} n_i n_k \right\rangle + \left\langle K_T \delta_{ik} n_j n_h \right\rangle + \left\langle K_T \delta_{ih} n_j n_k \right\rangle + \left\langle K_T \delta_{jk} n_i n_h \right\rangle \right].$$

In the case of a regular array of particles the values of n_i are known exactly, and the volume fraction and number of contacts are constant values in the unit cell of spheres. That is, the stiffness assumes simplified forms, for example, in the case of Face Centred Cubic (FCC) packing that will be treated in Sect. 5.1 or Square Cubic (SC) packing in Sect. 7.1.

For a random assembly of spheres, we can use the simplified Eq. (23) to obtain

$$C_{ijkh} = \frac{d^2 Z}{V} \left[\left\langle (K_N - K_T) n_h n_k n_i n_j \right\rangle \right] \tag{28}$$

$$+ \frac{d^2 Z}{V} \frac{1}{4} \left[\left\langle K_T \delta_{jh} n_i n_k \right\rangle + \left\langle K_T \delta_{ik} n_j n_h \right\rangle + \left\langle K_T \delta_{ih} n_j n_k \right\rangle + \left\langle K_T \delta_{jk} n_i n_h \right\rangle \right].$$

Finally, when Hertzian contacts are considered, subjected to an initial isotropic compression, the relative normal displacement δ is related with the hydrostatic pressure $p_0 = 1/3 \mathrm{tr}(\sigma_{ij})$ as

$$\delta = d \left[\frac{3\pi}{2} \frac{(1-v) p_0}{G_g Z \phi} \right]^{2/3}, \tag{29}$$

where $\phi = \pi d^3 N_B / 6V$ is the volume fraction. Equation (29) gives K_N and K_T in Eqs. (20) and (21) as functions of the state variables of the initial, reference state, p_0, ϕ, Z [20, 35]. The average strain assumption results in the following expression for the shear and bulk moduli G and K:

$$G = \frac{5 - 3v}{20} \phi^{2/3} Z^{2/3} p_0^{1/3} \left[12 \left(\frac{G_g}{\pi(1-v)} \right)^2 \right]^{1/3} \tag{30}$$

and

$$K = \frac{1}{3} \phi^{2/3} Z^{2/3} p_0^{1/3} \left[\frac{3}{2} \left(\frac{G_g}{\pi(1-v)} \right)^2 \right]^{1/3}. \tag{31}$$

The relations above show that the elastic properties of the granular material depend only on the material characteristics and the values of p_0, ϕ, Z in the reference state. They are not related explicitly to the previous history of the sample, other than through the values that such history assigns to the state variables.

We want now to compare the micromechanical expressions (Eq. (30)) for G with the empirical relations proposed by Hardin and other investigators (Eq. (12)). By adopting equations of the form (Eq. (12)) and given the relation between volume fraction and void ratio e

$$\phi = \frac{1 + 2e}{1 + e},$$

the parallelism appears to be remarkable. A first major difference involves the exponent of p_0. In EMT the exponent is a constant value that relates directly to the nature of the contact interaction, e.g., $\alpha = 1/3$ for Hertzian contacts as shown above. The exponent α in Eq. (12) is a fitting parameter, back-calculated from

experimental data. However, the experimental measurement of α requires data at different pressure values that involve changes in the number of contacts. Information on such evolution are not accessible from macroscopic observations that (usually) only provide ϕ and p_0, while it is well known that imperceptible changes in ϕ may lead to big changes in Z [48]. Hence, α represents not only the nature of the contact stiffness but also the effect of changes in contacts [48]. If this circumstance is assumed and two different exponents derived for pressure and coordination number, the Hertzian scaling reconciles with the experimental evidence. This is in the spirit of EMT that proposes ϕ, p_0 and Z as independent quantities.

In the following, we will introduce a numerical procedure to simulate wave propagation in granular materials. Based on the micromechanical insights from the simulations, we can improve the understanding about the dependence of the elastic moduli on the individual state variables, and the cross correlations between them.

5 Discrete Element Simulations

The Discrete Element Method (DEM) as introduced by Cundall and Strack [8] is a unique tool for direct exploration of the microstructure in a granular material. In the DEM method, the deformation of the assemblies is computed by numerically integrating in time the equations of motion of all particles, and the results can be employed to analyse the actual state of the material (at both macro- and microscale) and deformation mechanisms.

If the sum of all forces, $\sum_{c \in N^c(A)} f_i{}^c(A)$, acting on particle A, either from other particles, from boundaries or from external forces, is known, the problem is reduced to the integration of Newton's equations of motion for the translational and rotational degrees of freedom:

$$m^{(A)}\ddot{x}_i^{(A)} = \sum_{c \in N^c(A)} f_i^c(A) \qquad \text{and} \qquad I^{(A)}\ddot{\theta}_i^{(A)} = \sum M_i(A), \qquad (32)$$

with the mass $m^{(A)}$ of particle (A), its position $x_i^{(A)}$, its moment of inertia $I^{(A)}$, its angular velocity $w_i^{(A)} = \dot{\theta}_i^{(A)}$ and the total torque $\sum M_i(A)$. That is, the interaction between particles is given by a non-central contact force in which the normal component follows the expressions introduced in Sect. 4.1. In the tangential direction a bilinear force-displacement relationship is often used, elastic with Coulomb friction threshold. The micromechanical definition of stress given by Eq. (23) holds for a DEM assembly. Periodic boundary conditions are usually employed to reduce boundary effects, and gravity is neglected.

When looking at the microstructure, the coordination number Z is a quantity of interest as it characterises the contact arrangement. The simplest definition of the coordination number has been introduced in the previous section. However,

numerical simulations have revealed that at any time, during compression, there are some particles with no contacts and some particles with only one contact. Those particles do not meet the condition of equilibrium; hence, they are unloaded and do not contribute to the transmission of stress through sample. The mechanical coordination number was introduced in [51]:

$$Z = \frac{2N^c - N_1}{N_B - N_0 - N_1},$$ (33)

where N_1 and N_0 are the number of particles with only one or no contacts, respectively. When discussing DEM results, we will always refer to the mechanical coordination number, if not stated otherwise. In the case of isotropic systems the scalar quantity Z can be used as main descriptor of the microstructure for all samples. When anisotropic systems are considered, the fabric tensor, able to describe the orientation of the contact network, must be introduced, along with the coordination number.

In the following we will use DEM simulations to study the propagation of waves and elasticity in granular materials. We will analyse two cases, a regular structured array and a random, isotropic aggregate of spheres. In the first case (Sect. 5.1) waves are agitated by perturbation, at the one end of the granular packing, this resembling wave transducers tests [29]. For the random system, the elastic moduli are calculated directly (Sect. 5.2) via an overall strain perturbation applied to the particles. In this way, two numerical approaches are discussed, both suitable either for regular or random packings and leading to identical results for long wavelength and small-strain amplitude (as discussed in Sect. 3). DEM simulations offer direct access to microscale information, allow to verify the micromechanical assumptions proposed by the EMT and, in turn, formulate new, more sophisticated micromechanical models.

5.1 DEM Simulations of Structured Arrays of Particles

It is expected that a regular, structured packing of identical particles moves because of affine motion only and then follows the prediction of the Effective Medium Theory. Several authors have worked out this assumption. Among others, in [38] the authors have performed wave propagation DEM simulations on monodisperse, structured (crystal) packings and compared results with predictions from EMT theory. The configuration considered there is a dense, static, FCC packing, see Fig. 2. In this configuration, a unit cell (cuboid) has a volume $V_u = \sqrt{2}d^3$ and contains two particles with volume $2V_A = (\pi/3)d^3$ such that the volume fraction is $\phi = 2V_p/V_u = \pi/(3\sqrt{2}) \approx 0.74$. Each particle has four contacts inside each square-layer, and eight with particles in both neighbouring layers, corresponding to a coordination number $Z = 12$. Being the packing regular and homogeneous, the system is in a static equilibrium. A small overlap, i.e., contact deformation in
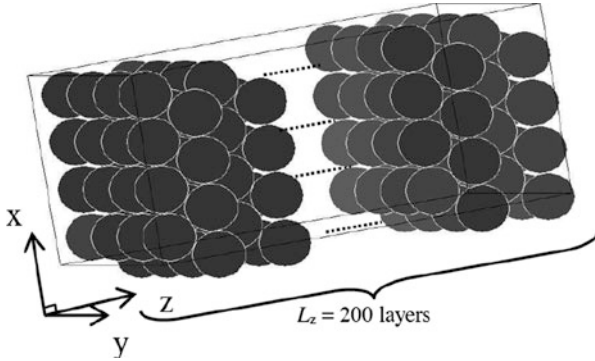
**Fig. 2** Snapshot of a typical body centred cuboid packing from [38]
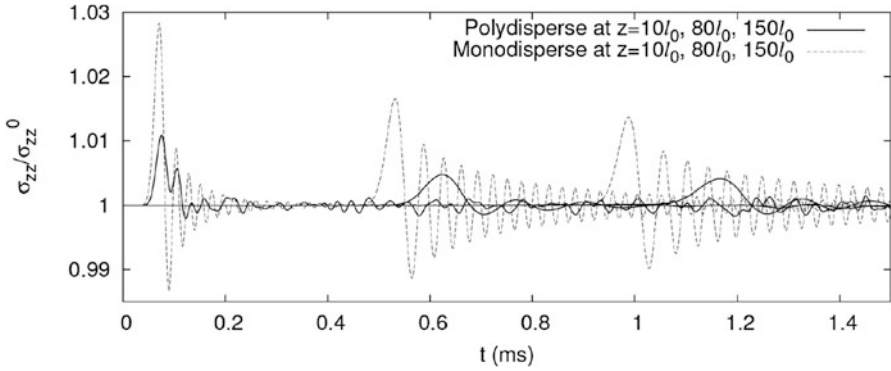
Fig. 3 Normal stress (σ_{zz}) scaled by the equilibrium stress (σ_{zz}^0) as function of time at different positions $z/l_0 = 10$, 80 and 150, with the distance from the source, z, and the layer distance l_0 [38]

normal direction, between all particle is applied, much smaller than the particle diameter, $\delta/d \approx 10^{-3}$. The applied overlap defines the stress state of the packing p_0. Waves are excited by applying a small perturbation at one side of the system, i.e., by shifting a layer of particles. Compressive (P) and shear (S) modes can be triggered by directing the perturbation parallel or perpendicular to the wave propagation direction, respectively. Perturbations of small amplitude with respect to the typical overlap are chosen, $\Delta z/\delta = 10^{-1}$, such that the structure does not change during the simulations. Since the system is made of layers, it is possible to "record" the pulse at each layer as a function of time. As an example, Fig. 3 shows the output of a numerical experiment where a plan compressive P-wave is created and propagated in z-direction. The scaled normal stress is plotted versus time at different positions along the wave propagation direction. The figure nicely resembles the travel of the wave as seen in experiments. By looking at the behaviour of stress over time in a given layer, it is possible to detect the arrival time. Since the distance L between

the source layer and the arrival layer is known, the velocity can then be calculated as $V_P = L/t_a$, with t_a arrival time. The simulation results can be compared with the wave speed predicted from Eq. (11) where Eq. (27) provides the elastic moduli. The assumption of a constant stiffness, which holds for small deformations and large wavelength limit, is respected in this case. A very good agreement is obtained between theory and simulations, where the discrepancy is only about 3%. cient, which is kept constant to = 0:5 and kt ness for which we performed a parameter study with the following erences of static and dynamic friction cients, or di erent magnitudes of , relevant here (data not shown). Of course by cially low value for (= 0:001), see [17], sliding contacts occur andThe ness tensor and using the simulation data in order to get the

Later on, the authors check the EMT for a slightly different system, by assigning a size distribution to the particles (Δa of the order of the overlap δ). As soon as polydispersity is introduced, and already for small values, the induced disorder in the micromechanical equilibrium forces particles to a kinematics more complex than the affine motion. Note that the coordination number of the relaxed is $Z = 9.975$. This represents a loss of 17% of the contacts as compared to the ordered system ($Z = 12$), but stays constant during propagation of waves. In this nonlinear context, the EMT immediately fails, with discrepancies up to 9% as shown in Fig. 4.
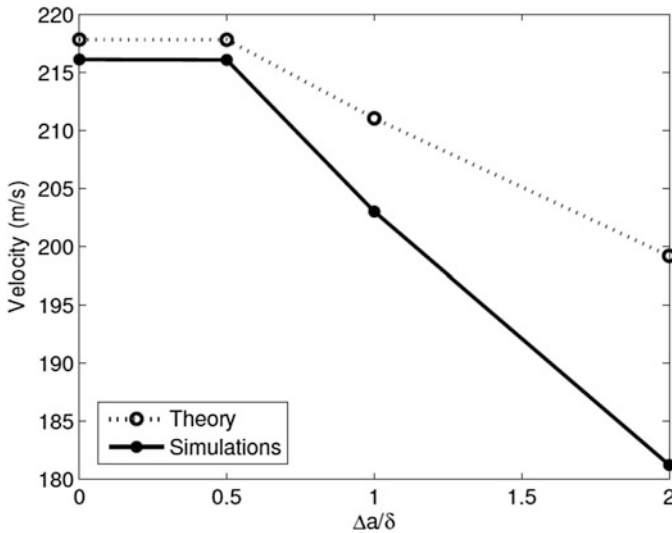
Fig. 4 P-wave velocities as function of polydispersity: comparison between simulations and EMT theory [38]

5.2 DEM Simulations of Random Aggregates

When moving from the regular packing of spheres, to random aggregates, the deviation from the predictions of the Effective Medium Theory becomes more dramatic. In particular, one would expect that an aggregate of random spheres in contact scales with pressure following the relation in Eqs. (30)–(31), i.e., the packing behaves as a collection of Hertzian springs. However, experimentally it is known that the bulk modulus K and shear modulus G of a granular assembly increase with pressure p_0 faster than the law predicted by EMT based on Hertz-Mindlin contact forces:

$$K(p_0) \sim p^{1/3} \qquad \text{and} \qquad G(p_0) \sim p^{1/3}.$$

Rather, numerous studies show values dependence of incremental elastic moduli on pressure p_0 as $p_0^{1/2}$, as already mentioned in Sect. 3.1. In [15], Goddard presents a comprehensive analysis comparing two alternative mechanisms for the anomalous pressure scaling: (1) the breakdown of the Hertz-Mindlin force law at the level of individual grains due to sharp asphericities at the contact departures; (2) the variation of the number of contacts during pressure increase. He shows that both mechanisms result in a $p_0^{1/2}$ pressure scaling at low pressure and both exhibit a high-pressure transition to $p_0^{1/3}$ scaling at a characteristic transition pressure value.

While Goddard privileges the first hypothesis, the study proposed in [35] supports the second hypothesis with the aid of DEM simulations. In this study, the elastic moduli of isotropic monodisperse packings are calculated directly, by applying an incremental strain to the sample and then measuring the resulting incremental stress. The friction coefficient is set on a very high value to prevent sliding among grains. When a shear strain, $\Delta \epsilon_{12}$ is applied and the change in stress σ_{12} is measured after relaxation, the shear modulus is recovered as $G = \Delta \sigma_{12}/\Delta \epsilon_{12}$. Similarly, an incremental isotropic strain, $\Delta v = \Delta \epsilon_{11} + \Delta \epsilon_{22} + \Delta \epsilon_{33}$, is applied to measure K. Other than the anomalous scaling with pressure, the shear modulus measured in the simulation is approximately 60% lower than that predicted by EMT (with discrepancies even more dramatic for frictionless spheres), while the difference in the measured and predicted bulk modulus is negligible. The authors in [35] conclude that EMT can describe the scaling between moduli and pressure observed in experiments if the increasing number of grain-grain contacts with p_0 is considered. The authors propose an empirical relation for the evolution of the coordination number with pressure of the form

$$\langle Z(p) \rangle = 6 + \left(\frac{p_0}{0.06 \, \text{MPa}} \right)^{1/3}. \tag{34}$$

Once this is properly included in the EMT, a good agreement between theory and simulations is recovered.

In the same years, an independent work by Aloufi and Santamarina [47] suggested a similar micromechanical interpretation to their wave transducer experiments on Houston sand. The authors observe a transition in the behaviour of shear wave with pressure and suggest the existence of two regimes: "plastic", i.e., where contacts change, for $p_0 < \overline{p}_0$, where $\overline{p}_0$ is the critical threshold, and "elastic", at constant fabric, for $p_0 > \overline{p}_0$.

More recently, Magnanimo et al. [33] have tested further the relation between microstructure and elastic moduli in isotropic granular assemblies. By using a specific numerical protocol, they succeeded to isolate three state variables and analyse their role independently, namely the pressure p_0, volume fraction ϕ and coordination number Z. Set of data prepared by increasing pressure and letting the coordination number free to change as well show a behaviour similar to experiments, with a relation between moduli and pressure not following the Hertzian prediction in Sect. 4.2 and dependent on the specific preparation protocol, see Fig. 5.

On the other hand, by collecting packings with similar Z and fixed volume fraction ϕ, the dependence of the elastic moduli on the confining pressure only can be analysed. Interestingly, in the case of constant structure, G and K both vary as $p_0^{1/3}$. That is, for packings with fixed Z, particles experience an increase of the contact overlap with the pressure and the behaviour of the aggregate naturally follows Hertz's law, see Fig. 6. Finally, the dependence of the elastic moduli on Z is shown by plotting the bulk and shear moduli normalised by the confining pressure $p_0^{1/3}$, in Fig. 7. In this case unique curves are obtained, showing that the moduli depend on the microstructure characterised by Z independently of pressure.

The findings support the micromechanical formulation of EMT. The work shows that (1) the behaviour of the elastic moduli with pressure is qualitatively recovered; (2) an independent relation of the moduli with Z must be considered. However, Fig. 7 also highlights that the scaling proposed in Eqs. (31) and (30) for the moduli with Z is not quantitative satisfactory. Highly coordinated packings converge to EMT with $G \sim K \sim Z^{2/3}$ and in turn converge to a constant value as expected in the "elastic" regime [47] where a very dense contact network prevents further rearrangements. Differently, data at low Z strongly deviate from the EMT prediction. Thus, we conclude that more sophisticated theories, taking in account relaxation of grains, due the disordered microstructure of the packing, are needed in order to capture the material behaviour over a wide range of pressure and coordination number. Those will be treated in the following section.
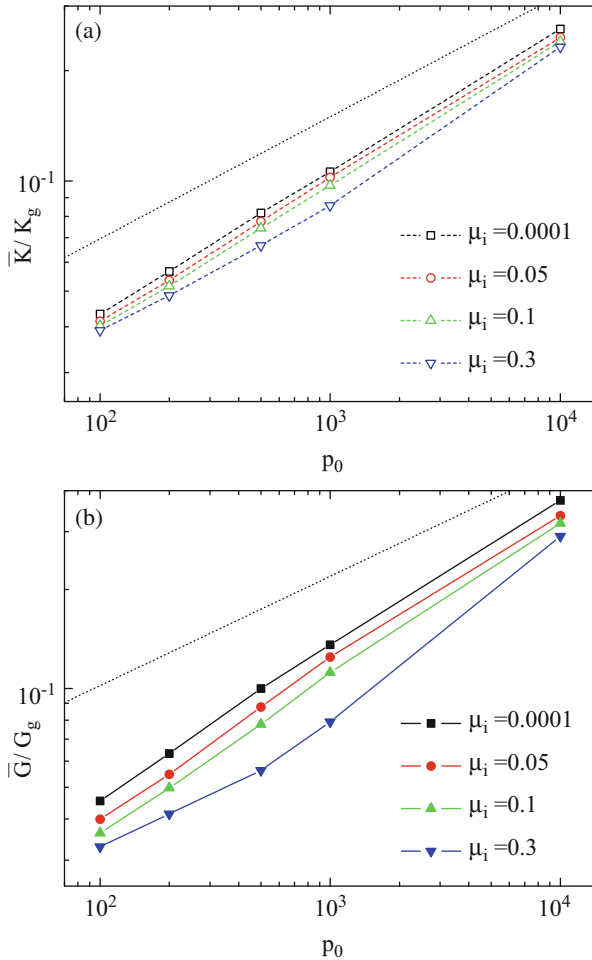
Fig. 5 Elastic moduli K and G, normalised by the material moduli K_g and G_g, vs. the confining pressure p_0, for four groups of packings. μ_i defines the preparation protocol [33]

6 Micromechanical Modelling Beyond EMT

In the last 30 years, efforts have been made to improve upon the Effective Medium Theory. The so-called fluctuations theories are micromechanically based and describe the particle displacements as the sum of a fluctuation component along with the average term. Koenders [32] was the first one to introduce fluctuation about the average deformation of contacting discs. Misra and Chang [37] for the first time applied a fluctuation in strain to the calculation of the stiffness of a packing of
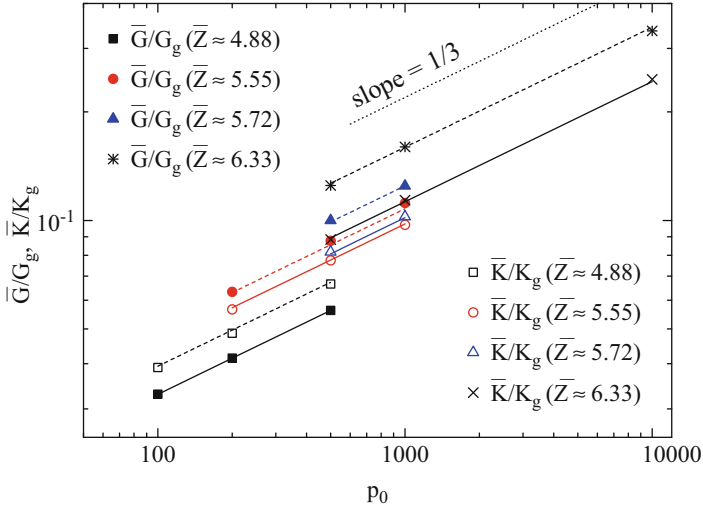
Fig. 6 Normalised elastic moduli, vs. confining pressure p_0, for four groups of packings with similar coordination numbers. G_g and K_g are the shear and bulk moduli of the individual particles [33]

disks, with good agreement with numerical results. Later on, [21, 43] focused on a typical pair of contacting particles that interact through both the average strain and the fluctuations, assuming that the neighbouring particles moved with the average strain.

An analytical formulation for the bulk and the shear moduli based on the pair-fluctuation method has been proposed in [20, 28]. This is briefly summarised here and we refer to the articles for details.

In the pair-fluctuation approach, the kinematics of two contacting particles is given by the average deformation and fluctuations in both translations and rotations:

$$\dot{u}_i^{(BA)} = \dot{\epsilon}_{ij} l_j^c + \dot{\Delta}_j^{(BA)} - \frac{1}{2}\epsilon_{ijk}\dot{S}_j^{(BA)} l_k^c, \tag{35}$$

where $u_i^{(BA)}, l_i^c$ have been introduced in Sect. 4, $\dot{\Delta}_j^{(BA)}$ is the increment in the difference of the fluctuations in displacement of the particles and $\dot{S}_j^{(BA)}$ is the increment in the sum of the fluctuations in the rotations about their centres. As main assumption of the fluctuation theory, all the other n-th particles in touch with the pair $A - B$ simply move with an average deformation.
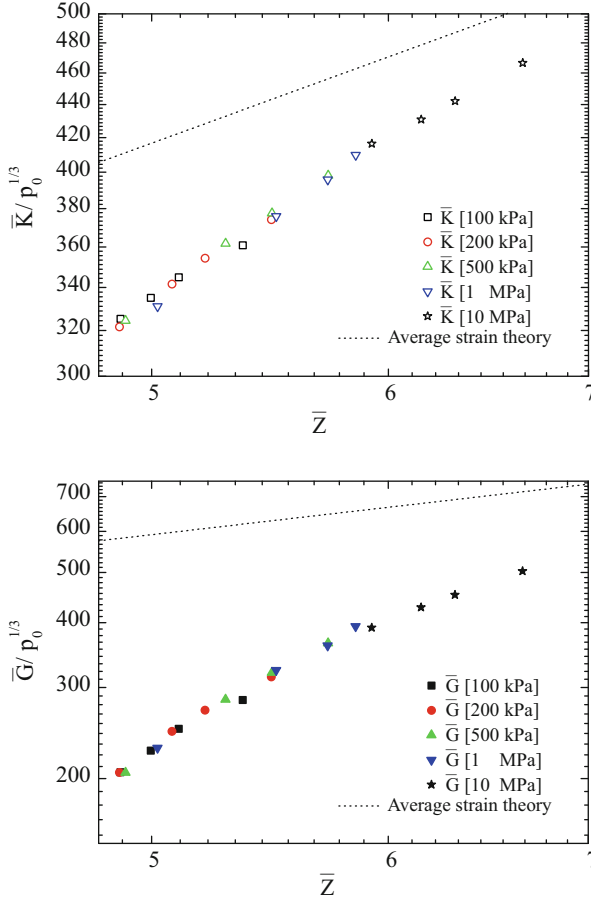
Fig. 7 Elastic moduli K and G, normalised by $p_0^{1/3}$, vs. the coordination number Z: all the data collapse into unique curves [33]

After some algebra [28], and restricting our cases to $K_N/K_T \sim 1$, the expressions for the effective shear and bulk moduli proposed by EMT, Eqs. (30) and (31) are modified as follows:

$$G = \frac{6\phi}{\pi d^3}\frac{\bar{Z}d^2}{30}(K_N - K_T)(1-2\zeta) + \frac{6\phi}{\pi d^3}\frac{\bar{Z}d^2}{30}K_T\left[\frac{5}{2} - 5\zeta - 3(\xi_3 - \xi_5)\right] \quad (36)$$

and

$$K = \frac{6\phi}{\pi d^3}\frac{\bar{Z}d^2}{18}K_N(1-2\zeta), \quad (37)$$

where the coefficients ζ, ξ_3, ξ_5 are functions only of the statistics of the aggregate [28], i.e., the local fabric. ζ, ξ_3, ξ_5 involve the standard deviation in particle coordination number as a statistical measure of the contact geometry. In particular the coefficient is obtained from the conditional contact distribution function, which gives the probability of finding a contact at an orientation given that another contact with certain orientation is present. Along with pressure, volume fraction and coordination number, as proposed initially by EMT, the new theory states that the fluctuation in coordination number must be taken into account to characterise the contact network, and in turn, the elastic moduli.

Equations above are the solutions for the fluctuation of a typical pair of particles to be in equilibrium, assuming that the other particles in the neighbour move with the average strain. We can further improve the kinematics of a typical pair by relaxing this hypothesis. For example, in [28], the solution of the fluctuation is implemented also in the interaction of the pairs with their neighbours. In Fig. 8 we report the DEM data on bulk and shear moduli $K(Z)$ and $G(Z)$ from Fig. 7 and compare them with predictions of EMT and fluctuation theory. As shown in the figure, the pair-fluctuation theory gives an excellent prediction of the bulk modulus over a wide range of Z. A very good approximation is obtained for the shear modulus in the intermediate-to-high Z regime, where the predicted shear modulus reduces to approximately 40% of its average strain prediction. For high coordination number EMT, fluctuation theory and DEM data converge, as highly coordinated packings of spheres tend to move according to the affine motion and the coefficients ζ, χ_3 and χ_5 in Eqs. (36), (37) approach zero. As expected, the role of fluctuations results particularly significant for loose, low-coordinated packings. This is also confirmed by [1], where the prediction of the moduli of two-dimensional, isotropic assemblies is extended over a significant range of coordination number. The authors adopt the "particle-fluctuation" method, complementary to the "pair-fluctuation" method in [20, 28]. However, in the former, complete knowledge of the contact geometry is required, generally only available from DEM simulations.

The fluctuation theory satisfactorily improves upon EMT for the description of granular elasticity and offers interesting insights. This analysis refers to the open question on what statistical measures are needed for a comprehensive description of the microstructure. For dense systems the coordination number (and its local fluctuations) seems to be a sufficient measure of the contact geometry (Fig. 8). Simulations and theory still diverge for poorly coordinated samples, when the jamming point is approached, i.e., the transition from solid to fluid state [19]. For those systems no statistical measure may be sufficient. In [25], the authors show that, by increasing the order (or size) the sub-assemblies, the predictions get closer to the true moduli determined from DEM simulations. In turn, the full knowledge of the contact geometry is required, for a correct prediction of the material response in the isostatic limit, since a small change leads to large rearrangement of contact forces. Specific issues related to low-coordinated packings are discussed in [2]. The authors suggest that collective effects determine the rigidity properties of tenuous networks in the low-Z limit, where the shear moduli vanish. In these circumstances, pair-fluctuations theory, based on the local equilibrium of one pair of grains embedded
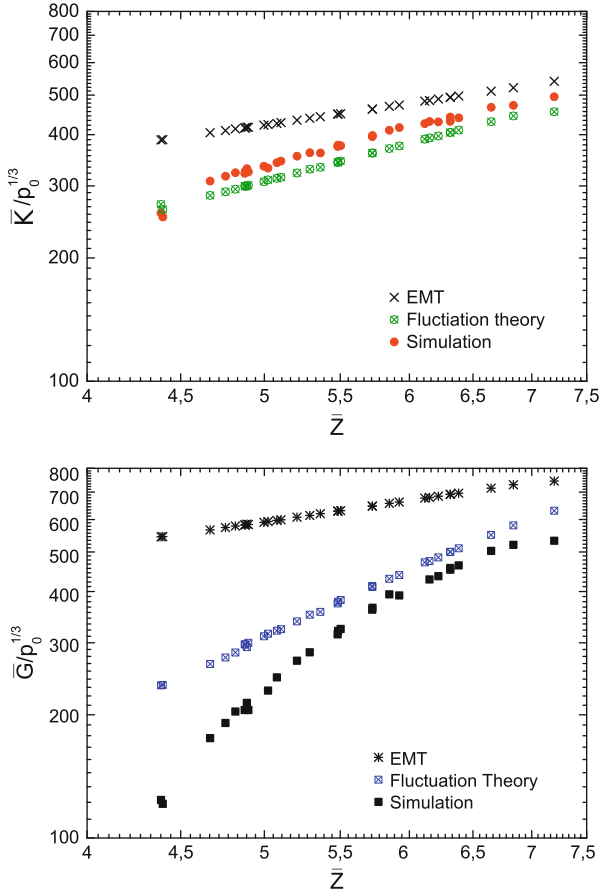
Fig. 8 Comparison between the numerical data and fluctuation theory for the normalised (left panel) bulk modulus and (right panel) shear modulus

in an elastic medium, does not correctly represent the granular system and is thus unable to capture its behaviour.

7 Toward Waves in Multiphase Granular Media

In this section the Effective Medium Theory introduced in Sect. 4.2 is extended to describe the elasticity of granular media immersed in a fluid phase. In particular, the complex case of unsaturated soils is treated, and EMT is applied to predict the nonlinear behaviour of shear stiffness.

7.1 Micromechanical Modelling of Unsaturated Soils

For the case of small-strain stiffness of soils in unsaturated state, a number of models have recently been proposed to quantify the shear modulus G over a wide range of degrees of saturation [12, 24, 36, 41, 49]. G is recognised to be affected by both suction and degree of saturation, which may vary independently because of the hydraulic hysteresis and the dependency of the void ratio on the water retention behaviour. A key question is how these two variables control the small-strain stiffness and whether they can be combined into a single variable. A common approach adopted by several authors [24, 41, 49] is to derive empirical or semi-empirical relationships for G using the product between suction and degree of saturation as a stress variable [22], often referred to as Bishop's effective stress for unsaturated soils:

$$\sigma_{ij}'' = \sigma_{ij} - u_a \delta_{ij} + (S_r s)\delta_{ij}, \qquad (38)$$

where σ is the total stress, u_a is the pore pressure, s is the suction, S_r is the degree of saturation and δ_{ij} is the Kronecker delta. An implicit assumption in this approach is that, at the same suction, the product $S_r s$ increases with an increase in degree of saturation. Since the degree of saturation along a drying path is higher than the degree of saturation along a wetting path, one would expect G to be higher along a drying path. Although an evidence of this has been observed experimentally [23], a number of experimental investigations show an opposite trend, i.e., the soil is observed to be significantly stiffer along a wetting path [24, 40]. Inspection of experimental data also reveals that the change of G with suction or degree of saturation occurs in either a monotonic or non-monotonic fashion [23, 45]. Ideally, a stiffness model should be capable of capturing the physics behind the two observed behaviours. However, no models presented so far are capable of addressing causes and differences.

A recent work [42] presents an experimental investigation of the independent effect of suction and degree of saturation on G along a full hydraulic hysteresis loop. An unsaturated sand specimen was tested in a modified triaxial cell apparatus equipped with bender elements using the hanging water column method (see [42] for details on the experiments). Then, a simple macroscopic model based on micromechanical insights from EMT is proposed in order to interpret and predict the evolution of G during hydraulic hysteresis. The proposed model is then challenged to elucidate a range of different responses observed in the literature.

The intergranular stress σ_{ij}^* induced by the degree of saturation/suction may be formulated by considering an idealised packing of equal spheres in an ordered structure. Let us consider the idealised unsaturated packing as shown in Fig. 9, and let us assume that the contact area of each pair of spherical particles is a point. The two-phase material can be described as the coexistence of a region fully occupied by

Fig. 9 Schematic
representation of the
unsaturated soil packing [42].
T is the surface tension at the
interface between particle and
water meniscus
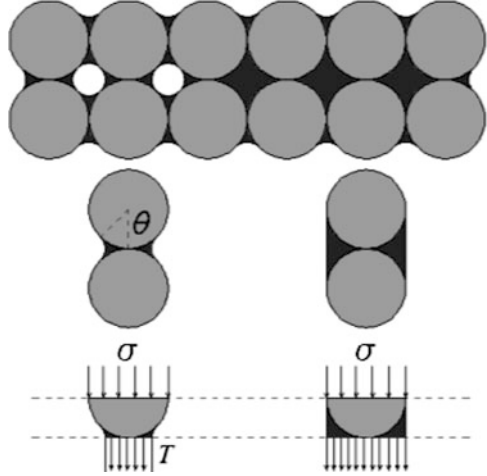
bulk water (saturated region) and a region occupied by the menisci alone. Boso et al.
[5] derived an expression of the intergranular stress σ_i of the unsaturated packing as

$$\sigma_{ij}^* = \sigma_{ij} + \left[\sigma_{ij}^{*b} \frac{S_r - S_{rm}}{1 - S_{rm}} + \sigma_{ij}^{*m} \left(1 - \frac{S_r - S_{rm}}{1 - S_{rm}} \right) \right], \tag{39}$$

where S_r is the total degree of saturation, S_{rm} is the residual degree of saturation
(degree of saturation of the region occupied by the menisci alone), σ_{ij} is the total
stress, σ_{ij}^{*b} is the intergranular stress in the bulk water region and σ_{ij}^{*m} is the
intergranular stress in the meniscus water region. The first term in square brackets
takes into account the contribution of suction to the intergranular stress in the
saturated region, which is directly proportional to the suction ($\sigma_{ij}^{*b} = s$). The second
term in square brackets indicates the contribution of suction to the intergranular
stress in the meniscus water region. The two contributions of suction in Eq. (39) are
weighed by functions of the degree of saturation.

By extending the analysis in [14] for spherical particles the stress in the menisci
region σ_{ij}^{*m} can be assumed independent of suction. As further step, we use the
Effective Medium Theory in the simplified case of a regular lattice to express the
shear modulus in terms of the intergranular stress. Starting from Eq. (27) applied,
for example, to a Cubic Square lattice shown in Fig. 9, the shear stiffness is

$$G = C_{1212} = \frac{2}{7} \frac{d^2}{V} \frac{3}{2} k_{n0}^{2/3} \left(\frac{p_0^*}{2d} V \right)^{1/3}, \tag{40}$$

with $d = D_{50}$ average diameter of the particles and the volume V is extended to the
whole experimental sample, and only the normal component of the intergranular
stress tensor has been considered $p_0^* = 1/3 \text{tr}(\sigma_{ij}^*)$. The proposed model was
calibrated and validated against the experimental results. Two model parameters

need to be identified, namely k_{n0} and p_0^{*m}. In the macroscopic model, these parameters should be intended as macroscopic parameters with an intuitive physical micromechanical meaning. In particular, k_{n0} is proportional to the interparticle stiffness K_N in Sect. 4, but it is assigned an extended physical meaning. k_{n0} is a model parameter that accounts for a number of characteristics of the real soil packing including the particle stiffness, particle shape, particle size distribution, particle arrangements, etc. With proper calibration, e.g., at saturation and at residual saturation, the two calibration parameters can be devised.

Figure 10 shows the comparison between the values of G obtained experimentally and the simulated stiffness C_{1212}. In order to take into account the variability of the degree of saturation within the specimen, bounding values of C_{1212} are considered, corresponding to the values of suction at the top/bottom of container. The model gives an accurate prediction of the small-strain shear modulus during hydraulic hysteresis. The variation of G with suction is well captured at a qualitative and quantitative level.

Moreover, the proposed model is able to elucidate the mechanisms behind different patterns of small-strain response in unsaturated granular materials. Two key responses can be successfully reproduced: soils have been observed to exhibit a stiffer behaviour along either a drying or a wetting path; G has been observed to vary in either a monotonic or non-monotonic fashion. By accounting for the independent effect of suction and degree of saturation on soil stiffness and with
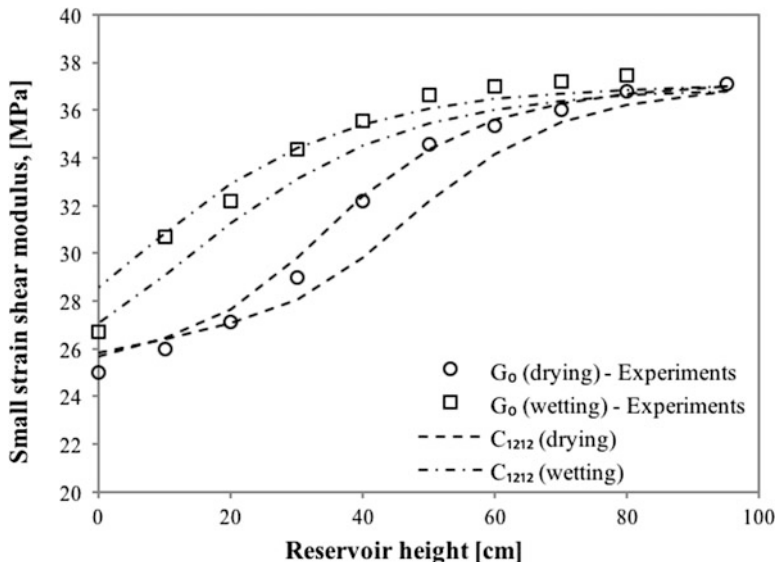
Fig. 10 Comparison of experimental data and prediction of the micromechanical model for small-strain stiffness during hydraulic hysteresis. The two dashed lines for the drying path (dashed-dotted for the wetting path) indicate the boundaries of the theoretical prediction for the two extreme values of suction at the top/bottom of the container [42]

proper calibration of only two constants, both mechanisms can be reproduced and interpreted from the micromechanical point of view at a qualitative and quantitative level. The model captures the higher stiffness observed along a wetting path that the stress variable obtained as the product suction times degree of saturation fails to predict. According to the proposed model, the evolution of G is controlled by the evolution of the intergranular stress induced by suction and degree of saturation during hydraulic hysteresis. This naturally leads to the conclusion that the breadth of the water retention curve and the intensity of the intergranular stress due to the presence of the menisci have an effect on the evolution of G and control its monotonic/non-monotonic behaviour. The reader is referred to [42] for details and more extended analysis.

8 Conclusions

We have given an overview of the most relevant theoretical approaches to describe the elastic responses of granular soils across the geomechanical, mechanical and physics communities. Via the between experiment-based empirical models and classical micromechanical Effective Medium Theory (EMT), we have investigated the relevant parameters needed to describe the elastic response of a dense granular soil.

The study has been further enriched through insights from Discrete Element simulations. First, we have shown that waves propagating in regular arrays of particles perfectly follow the prediction of EMT. Later on, we have employed DEM to show that, in the case of random isotropic aggregates, a non-trivial dependence between pressure p_0, volume fraction ϕ and coordination number exists. In particular, for packing with identical microstructure Z, the elastic moduli confirm the scaling $K \sim G \sim p_0^{1/3}$ expected because of the Hertzian interaction between spheres. In addition to p_0, ϕ, Z, we also considered the fluctuation in the number of contacts per particle and compared DEM simulations with the more sophisticated fluctuation theory that include the relaxation of grains kinematics, due to the disordered microstructure of the packing. We conclude that several regimes define the elastic behaviour of granular soils: at very high pressure (high coordination number), where contact rearrangements are impeded and the coordination number is constant, the aggregate behaves "elastically", i.e., $K \sim G \sim p_0^{1/3}$; when p_0 and Z decrease, changes in pressure induce changes in contacts and the behaviour becomes "plastic". For sufficiently high coordination number, where movement is limited and particles tend to follow the affine motion, the prediction of EMT $K \sim G \sim Z^{2/3}$ is confirmed by DEM. For lower values of Z, the elastic behaviour is qualitatively but not quantitatively captured by the Effective Medium Theory. In this regime, modifications that include the local distribution of contacts succeed to improve upon EMT, with fluctuations increasing with decreasing Z. In the limit of poorly coordinated systems, close to jamming, fluctuation theories fail to

describe granular elasticity, and contact fluctuations must be extended from local to collective, including the whole packing of particles.

Finally, we have extended the Effective Medium framework to describe unsaturated soils and shown validation of the model against laboratory experiments after proper calibration. Experimental results revealed that wave velocity and, hence, stiffness are not controlled by the product "suction times degree of saturation", traditionally used for describing the behaviour of shear waves in unsaturated sand. According to the simplified micromechanical model the evolution of the shear modulus G is controlled by the evolution of the suction-generated intergranular stress during drying-wetting cycles.

References

1. I. Agnolin and N. P. Kruyt. On the elastic moduli of two-dimensional assemblies of disks: Relevance and modeling of fluctuations in particle displacements and rotations. *Computers and Mathematics with Applications*, 55(2):245–256, 2008.
2. I. Agnolin and J.N. Roux. Internal states of model isotropic granular packings. III. Elastic properties. *Physical Review E*, 76(6):061304, 2007.
3. K. Aki and P. Richards. *Quantitative Seismology*. Freeman, New York, 1980.
4. R. Bellotti, M. Jamiolkowski, D.C.F. LoPresti, and D.A. O'Neill. Anisotropy of small strain stiffness in Ticino sand. *Géotechnique*, 46(1):115–131, 1996.
5. M. Boso, A. Tarantino, and L. Mongioví. *Shear strength behaviour of a reconstituted clayey silt. Unsaturated soils*, pages 9–14. Taylor & Francis Group, London, 2005.
6. J.B. Burland. Ninth Laurits Bjerrum memorial lecture: "small is beautiful" - the stiffness of soils at small strains. *Canadian Geotechnical Journal*, 26(4):499–516, 1989.
7. Y.-C. Chen, I. Ishibashi, and J.T. Jenkins. Dynamic shear modulus and fabric: part I, depositional and induced anisotropy. *Géotechnique*, 38(1):25–32, 1988.
8. P.A. Cundall and O.D.L. Strack. A discrete numerical model for granular assemblies. *Géotechnique*, 29(1):47–65, 1979.
9. J. David and N. Cheeke. *Fundamentals and Applications of Ultrasonic Waves*. CRC Press, Boca Raton, 2002.
10. P.J. Digby. The effective elastic moduli of porous granular rocks. *ASME Journal of Applied Mechanics*, 48(4):803–808, 1981.
11. S.N. Domenico. Elastic properties of unconsolidated porous sand reservoirs. *Geophysics*, 42(7):1339–1368, 1977.
12. Y. Dong and N. Lu. Correlation between small-strain shear modulus and suction stress in capillary regime under zero total stress conditions. *Journal of Geotechnical and Geoenvironmental Engineering*, 142(11):4016056, 2016.
13. A. Ezaoui and H. Di Benedetto. Experimental measurements of the global anisotropic elastic behaviour of dry Hostun sand during triaxial tests, and effect of sample preparation. *Géotechnique*, 59(7):621–635, 2009.
14. R.A. Fisher. On the capillary forces in an ideal soil; correction on formulae given by W.B. Haines. *Journal of Agricultural Science*, 16(3):492–505, 1926.
15. J.D. Goddard. Nonlinear Elasticity and Pressure-Dependent Wave Speeds in Granular Media. *Proceedings of the Royal Society A*, 430(1878):105–131, 1990.

16. B.O. Hardin and W.L. Black. Elastic wave velocities in granular soils. *Journal of Soil Mechanics and Foundations Division*, 92(2):27–42, 1966.

17. B.O. Hardin and F.E.Jr Richart. Elastic wave velocities in granular soils. *Journal of Soil Mechanics and Foundations Division*, 89(1):33–66, 1963.

18. H. Hertz. Über die berührung fester elastischer körper (on the contact of elastic solids). *J. Reine und Angewandte Mathematik*, 92:156–171, 1882.

19. H.M. Jaeger, S.R. Nagel, and R.P. Behringer. Granular solids, liquids and gases. *Review Modern Physics*, 68(4):1259–1273, 1996.

20. J. Jenkins, D. Johnson, L. La Ragione, and H.A. Makse. Fluctuations and the effective moduli of an isotropic, random aggregate of identical, frictionless spheres. *Journal of the Mechanics and Physics of Solids*, 53(1):197, 2005.

21. J.T. Jenkins. *Inelastic behavior of random arrays of identical spheres*, chapter Mechanics of Granular and Porous Materials, page 11. Kluwer, Amsterdam, 1997.

22. C. Jommi. Remarks on the constitutive modelling of unsaturated soils. In *Experimental evidence and theoretical approaches in unsaturated soils*, 2000.

23. A. Khosravi. Characterizing the variation of small strain shear modulus for silt and sand during hydraulic hysteresis. In *Proceedings of the 3rd European Conference on Unsaturated Soils E-UNSAT 2016*, number 9, page 10418. A.A. Balkema Publishers, 2016.

24. A. Khosravi and J.S. McCartney. Resonant column test for unsaturated soils with suction-saturation control. *Geotechnical Testing Journal*, 36(6):1–10, 2011.

25. N.P. Kruyt, I. Agnolin, S. Luding, and L. Rothenburg. Micromechanical study of elastic moduli of loose granular materials. *Journal of the Mechanics and Physics of Solids*, 58(9):1286–1301, 2010.

26. N.P. Kruyt and L. Rothemburg. Micromechanical definition of the strain tensor for granular materials. *Journal of Applied Mechanics*, 63(3):706–711, 1996.

27. R. Kuwano and Jardine R.J. On the applicability of cross-anisotropic elasticity to granular materials at very small strains. *Géotechnique*, 52(10):727–749, 2002.

28. L. La Ragione and J. Jenkins. The initial response of an idealized granular material. *Proceedings of the Royal Society A*, 463(2079):735–758, 2007.

29. J.-S. Lee and J.C. Santamarina. Bender elements: Performance and signal interpretation. *Journal of Geotechnical and Geoenvironmental Engineering*, 131(9):1063–1070, 2005.

30. D.C.F. LoPresti, M. Jamiolkowski, O. Pallara, A. Cavallaro, and S. Pedroni. Shear modulus and damping of soils. *Géotechnique*, 47(3):603–617, 1997.

31. A.E.H. Love. *A Treatise on the Mathematical Theory of Elasticity*. Cambridge University Press, Cambridge, 1927.

32. Koenders M.A. The incremental stiffness of an assembly of particles. *Acta Mechanica*, 70(1–4):31–49, 1987.

33. V. Magnanimo, L.L. La Ragione, J.T. T. Jenkins, P. Wang, and H.A.A. Makse. Characterizing the shear and bulk moduli of an idealized granular material. *Europhysics Letters*, 81(3):34006, 2008.

34. R.J. Mair. Developments in geotechnical engineering research: Application to tunnels and deep excavations. volume 97 of *Proceedings of the Institution of Civil Engineers-Civil Engineering*, pages 27–41. Thomas Telford-ICE Virtual Library, 1993.

35. H.A. Makse, N. Gland, D.L. Johnson, and L. Schwartz. Why effective medium theory fails in granular materials. *Physical Review Letters*, 83:5070, 1999.

36. C. Mancuso, R. Vassallo, and A. d'Onofrio. Small strain behaviour of a silty sand in controlled-suction resonant column-torsional shear tests. *Canadian Geotechnical Journal*, 39(1):22–31, 2002.

37. A. Misra and C.S. Chang. Effective elastic moduli of heterogeneous granular solids. *International Journal of Solids and Structures*, 30(18):2547–2566, 1993.

38. O. Mouraille, W.A. Mulder, and S. Luding. Sound wave acceleration in granular materials. *Journal of Statistical Mechanics: Theory and Experiments*, 2006(07):P07023, 2006.

39. D. Muir Wood. Life cycles of granular materials. *Philosophical Transactions of Royal Society London A*, 356(1747):2453–2470, 1998.

40. C.W.W. Ng and J. Xu. Effects of current suction ratio and recent suction history on small-strain behaviour of an unsaturated soil. *Canadian Geotechnical Journal*, 49(2):226–243, 2012.

41. W.T. Oh and S.K. Vanapalli. Semi-empirical model for estimating the small-strain shear modulus of unsaturated non-plastic sandy soils. *Geotechnical and Geological Engineering*, 32(2):259–271, 2014.

42. A. Pagano, A. Tarantino, and V. Magnanimo. A microscale-based model for small-strain stiffness in unsaturated granular geomaterials. *Géotechnique*, 69(8):687–700, 2019.

43. A.C. Paine. Calculation of the effective moduli of a random packing of spheres using a perturbation of the uniform strain approximation. In *Proceedings of Powders and Grains 1997*, 1997.

44. P. Philippe and D. Bideau. Compaction dynamics of a granular medium under vertical tapping. *Europhysics Letters*, 60(5):677, 2002.

45. X. Qian, D.H. Gray, and R.D. Woods. Voids and granulometry: effects on shear modulus of unsaturated sands. *Journal of Geotechnical Engineering*, 119(2):295–314, 1993.

46. S.K. Roesler. Anisotropic shear modulus due to stress anisotropy. *Journal of Geotechnical Engineering*, 105(7):871–880, 1979.

47. J.C. Santamarina. *Soils and waves: particulate materials behavior, characterization and process monitoring*. Wiley, 2001.

48. J.C. Santamarina and Cascante G. Stress anisotropy and wave propagation: a micromechanical view. *Canadian Geotechnical Journal*, 33(5):770–782, 1996.

49. A. Sawangsuriya, T.B. Edil, and P.J. Bosscher. *Journal of Geotechnical and Geoenvironmental Engineering*, 135(10):1390–1403, 2009.

50. E. Somfai, J.N. Roux, J.H. Snoeijer, M. van Hecke, and W. van Saarloos. Elastic wave propagation in confined granular systems. *Physical Review E*, 72(2):021301, 2005.

51. C. Thornton. Numerical simulations of deviatoric shear deformation of granular media. *Géotechnique*, 50(1):43–53, 2000.

52. K. Walton. The effective elastic moduli of a random packing of spheres. *Journal of Mechanics and Physics of Solids*, 35(2):213–226, 1987.

Macroscale Yield Criteria
for Geomaterials

Giuseppe Mortara

Abstract This paper deals with the formulation of yield criteria for geomaterials. Three kinds of approaches will be described: the first is called *coupled* because it gives rise to the natural coupling between the meridian and the deviatoric sections of the resulting yield surfaces; the second is called *uncoupled* because it is based on the definition of two distinct functions, one meridian and one deviatoric; the third is called *hybrid* and can be seen as intermediate between the *coupled* and the *uncoupled* approaches. The analysis is restricted to isotropic criteria. True triaxial tests obtained from numerical specimens are then used to validate the approaches.

1 Introduction

Yield criteria are fundamental for the definition of models based on elastoplasticity. The solution of boundary value problems requires their definition accounting for general stress conditions.

In his historical survey from *The Early Era* to *The Classical Era*, de Boer [1] reported the development of soil failure theories from the work by Coulomb (1773, see [1]), on the earth pressure on retaining walls, to those by Rankine [2] and Mohr (1900, see [1]). In particular, Rankine [2] wrote:

> The resistance to displacement by sliding along a given plane in a loose granular mass, is equal to the normal pressure exerted between the parts of the mass on either side of that plan, multiplied by a specific constant. The specific constant is the coefficient of friction of the mass, and is regarded as the tangent of an angle called the angle of repose.

G. Mortara (✉)
Department of Civil, Energy, Environment, and Materials Engineering (DICEAM),
University of Reggio Calabria, Reggio Calabria, Italy
e-mail: giuseppe.mortara@unirc.it

This can be summarised by the two equivalent equations

$$\tau = \sigma_n \tan \phi \tag{1}$$

$$\frac{\sigma_1 - \sigma_3}{\sigma_1 + \sigma_3} = \sin \phi \tag{2}$$

being τ, σ_n, σ_1, σ_3, and ϕ the shear and normal stresses, the largest and smallest principal stresses and the friction angle, respectively.

Later, Mohr (1900, see [1]) extended the failure condition to materials with cohesion obtaining what today is known as the Mohr–Coulomb (MC) criterion

$$\frac{\sigma_1 - \sigma_3}{2} = \frac{\sigma_1 + \sigma_3}{2} \sin \phi + c \cos \phi \tag{3}$$

being c the cohesion. Despite a long time passed from the early studies, that of failure criteria for soils is still an active field of research. Furthermore, numerical techniques such as the Discrete Element Method (DEM) allow the possibility to investigate in deep the behaviour at failure of identical numerical specimens subjected to different stress and strain paths (see e.g. [3]).

2 Invariants

In this paper the criteria will be formulated in terms of invariants of the Cauchy effective stress tensor σ_{ij} and of its deviator $s_{ij} = \sigma_{ij} - \sigma_{kk}\delta_{ij}/3$ being δ_{ij} the Kronecker delta. In the following three approaches will be defined: the *coupled* approach will make use of the principal invariants I_1, I_2, and I_3

$$I_1 = \sigma_{ii}$$

$$I_2 = \frac{1}{2}\left(\sigma_{ii}\sigma_{jj} - \sigma_{ij}\sigma_{ij}\right) \tag{4}$$

$$I_3 = \frac{1}{6}\left(\sigma_{ii}\sigma_{jj}\sigma_{kk} - 3\sigma_{ii}\sigma_{jk}\sigma_{jk} + 2\sigma_{ij}\sigma_{jk}\sigma_{ki}\right)$$

while the *uncoupled* and the *hybrid* approaches will be formulated in terms of p, q, and θ defined as

$$p = \frac{1}{3}\sigma_{ii}$$

$$q = \sqrt{\frac{3}{2}s_{ij}s_{ij}} \tag{5}$$

$$\theta = \frac{1}{3}\arccos\left(\frac{9}{2}\frac{s_{ij}s_{jk}s_{ki}}{q^3}\right)$$

that will be referred to as mean stress, deviatoric stress, and Lode's angle, respectively. The two sets of invariants are linked through the following relationships

$$I_1 = 3p$$

$$I_2 = 3p^2 - \frac{1}{3}q^2 \qquad (6)$$

$$I_3 = \frac{2}{27}q^3 \cos^2 3\theta - \frac{1}{3}pq^2 + p^3$$

3 The *Coupled* Approach

Figure 1, that is reported in many soil mechanics textbooks (see e.g. [4–6]), shows the deviatoric representation of the criteria by Mohr–Coulomb, and the two modern pioneering works on this subject formulated in 1970s by Matsuoka and Nakai (MN) [7] and Lade and Duncan (LD) [8]. The deviatoric surfaces are drawn for $\phi_0 = 30°$ being ϕ_0 the friction angle under triaxial compression. The axes scaling factor has
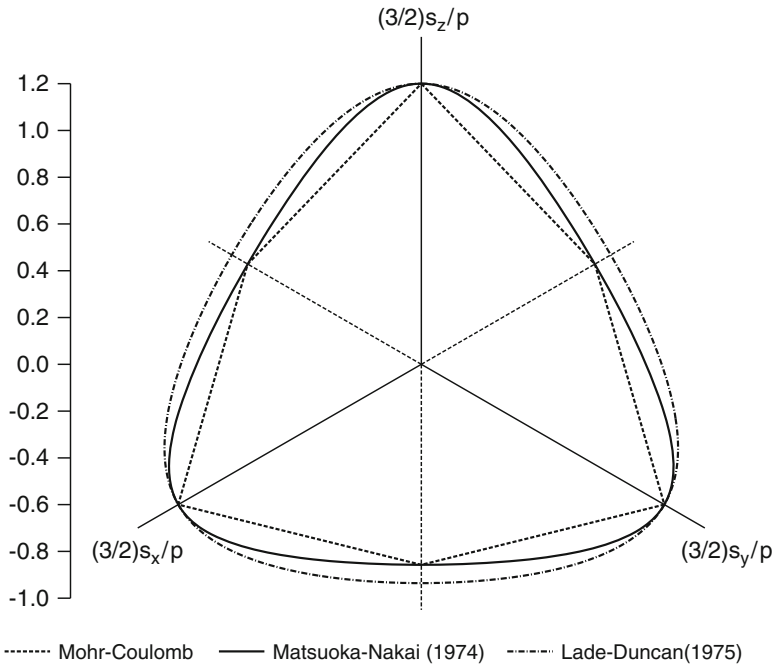
Fig. 1 Normalised deviatoric traces of the MC, MN, and LD criteria for $\phi_0 = 30°$

been selected in order to describe the evolution of the stress ratio $\eta = q/p$ with the Lode's angle.

The principal invariants written in terms of principal stresses simplifies as $I_1 = \sigma_1 + \sigma_2 + \sigma_3$, $I_2 = \sigma_1\sigma_2 + \sigma_2\sigma_3 + \sigma_3\sigma_1$, $I_3 = \sigma_1\sigma_2\sigma_3$. Under triaxial compression, that is for $\sigma_2 = \sigma_3$, using (2) one obtains

$$I_1 = \sigma_3 \frac{3 - \sin\phi_0}{1 - \sin\phi_0} \qquad I_2 = \sigma_3^2 \frac{3 + \sin\phi_0}{1 - \sin\phi_0} \qquad I_3 = \sigma_3^3 \frac{1 + \sin\phi_0}{1 - \sin\phi_0} \tag{7}$$

Using (7) it is simple to express the MN and LD criteria as

$$\frac{I_1 I_2}{I_3} = \frac{9 - \sin^2\phi_0}{1 - \sin^2\phi_0} = k_{MN} \tag{8}$$

$$\frac{I_1^3}{I_3} = \frac{(3 - \sin\phi_0)^3}{(1 + \sin\phi_0)(1 - \sin\phi_0)^2} = k_{LD} \tag{9}$$

Besides being formulated in terms of principal invariants, the common points of MN and LD are: (1) they are expressed in a non-dimensional form and (2) the triaxial compression friction angle influences not only the size but also the shape of the related surfaces. Both criteria, in fact, are represented by a circle for $\phi_0 = 0$ and by a triangle for $\phi_0 = 90°$ in the deviatoric representation.

In addition to the lack of I_2 in the LD criterion, the difference between MN and LD is explained by Houlsby [9] as follows:

> The main difference between the shapes suggested by Lade and Matsuoka is that while Matsuoka's gives the same equivalent angle of friction at both triaxial compression and extension, Lade's gives a slightly higher angle in extension. Evidence in favour of both has been obtained, and it is likely that neither is capable of modelling the failure of all soils.

Indeed, looking at the deviatoric traces of the MN and LD criteria, one could say "There must be something in between". Thus, having in mind a more general criterion, the Author [10, 11] tried to answer the simple question "Is there a unique criterion including the MN and LD criteria as special cases?". To this purpose, it is convenient to rewrite the LD criterion in a form equivalent to (9) but containing the missing invariant I_2

$$\frac{I_1^3 I_2^0}{I_3} = k_{LD} \tag{10}$$

Inspection of Eqs. (8) and (10) suggests that a general criterion, that can be called $3In$, can be written in the form

$$\frac{I_1^n I_2^{\frac{3-n}{2}}}{I_3} = \frac{(3 - \sin\phi_0)^n (3 + \sin\phi_0)^{\frac{3-n}{2}}}{(1 + \sin\phi_0)(1 - \sin\phi_0)^{\frac{1+n}{2}}} = \xi_0 \tag{11}$$
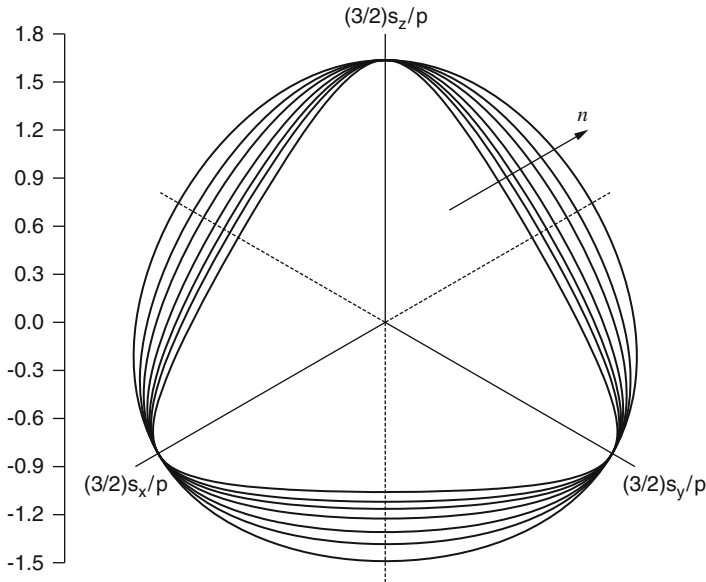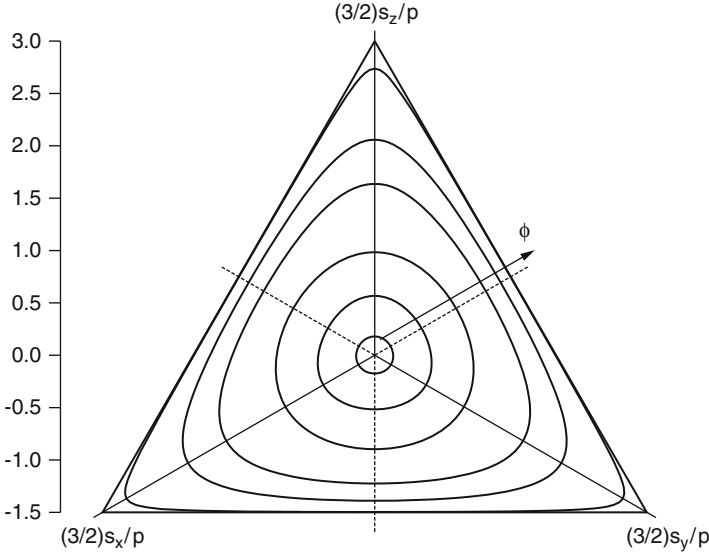
Fig. 2 Normalised deviatoric traces of the $3In$ criterion for $\phi_0 = 40°$ and $n = 1, 2, 3, 5, 10, 20, 100$

and that the original criteria (8) and (9) are now a particular case of (11) for $n = 1$ and $n = 3$, respectively. Clearly, the continuous variation of the new parameter n enables to "fill" the space between MN and LD and to go outside LD. This is shown in Fig. 2 where the effect of increasing parameter n on the deviatoric shape of (11) is depicted. The curves differ for the aspect ratio β defined as the ratio between the values of the deviatoric stress in triaxial extension and compression [12]. For constant values of I_1 one has $0.5 \leq \beta \leq 1$ for $90 \geq \phi_0 \geq 0°$. Values $n < 1$ in (11) are admitted but convexity of the related surfaces is not guaranteed [10].

Criterion (11) can be easily extended to frictional-cohesive soils by introducing the modified stress tensor $\overline{\sigma}_{ij} = \sigma_{ij} + t\delta_{ij}$ being t the isotropic tensile strength. For $n = 1$ the generalisation of the MN criterion to materials with friction and cohesion by Houlsby [13] is simply obtained.

Figure 3, that shows the effect of increasing ϕ_0 for the curves related to $n = 5$, clarifies the reason why this approach is termed *coupled*: it is evident that increasing values of ϕ_0 give rise to the change of shape of (11) in the deviatoric representation.

While for the MN and LD criteria the values of the aspect ratio depend only on ϕ_0 for the $3In$ criterion they depend also on the new parameter n. Equation (11) can be

Fig. 3 Normalised deviatoric traces of the $3In$ criterion for $n = 5$ and $\phi_0 = 5, 15, 25, 40, 50, 70, 90°$

rewritten using (6) for the extension condition, that is for $\cos 3\theta = -1$. Introducing the stress ratios in compression and extension

$$M_c = \frac{6 \sin \phi_0}{3 - \sin \phi_0} \tag{12}$$

$$M_e = \beta M_c \tag{13}$$

the generalised criterion takes the form

$$\left[\frac{1}{3} - 3\left(\frac{M_c \beta}{9}\right)^2\right]^{\frac{3-n}{2}} + \xi_0 \left[2\left(\frac{M_c \beta}{9}\right)^3 + \left(\frac{M_c \beta}{9}\right)^2 - \frac{1}{27}\right] = 0 \tag{14}$$

The plot of Eq. (14) for some values of ϕ_0 reveals that same values of β can be obtained for different combination of n and ϕ_0 and this means that the determination of parameter n needs data related to different mobilised friction angles (Fig. 4). From the figure it is also possible to observe that for each value of ϕ_0 the aspect ratio β increases as n increases and that it tends to an asymptotic value.

An important feature, that does not emerge from Fig. 2, is the variation of the friction angle with the Lode's angle for different values of parameter n. This is shown in Fig. 5 where the variation of ϕ_θ is plotted for values of n considered in Fig. 2. It is possible to see that for increasing values of n the maximum value of
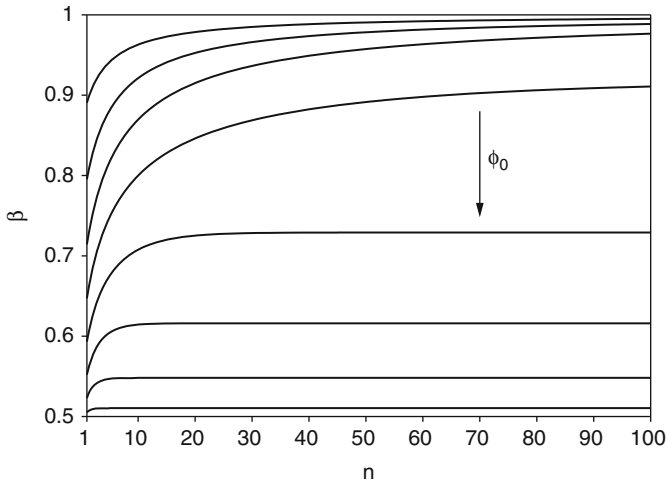
Fig. 4 Variation of the aspect ratio with n for $\phi_0 = 10, 20, 30, 40, 50, 70, 80°$
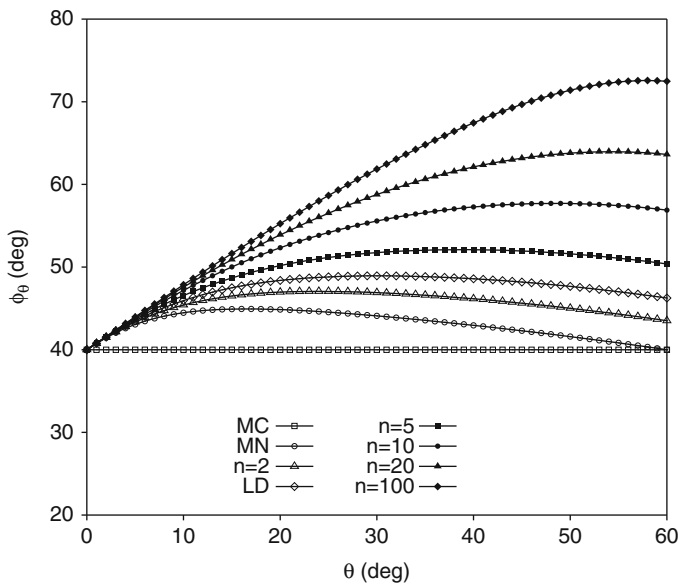
Fig. 5 Variation of the friction angle with θ for $\phi_0 = 40°$

ϕ_θ increases and the higher value related to each curve is obtained for different values of θ: in particular, for $n = 3$, that is for the LD criterion, the maximum is related to $\theta = 30°$, while for $n < 3$ and $n > 3$ the maximum is obtained for $\theta < 30°$ and $\theta > 30°$, respectively. As can be observed, for increasing values of n the maximum relative difference $\Delta\phi/\phi_0 = \phi_\theta/\phi_0 - 1$ increases considerably. It is

seen that $\Delta\phi$ depends on ϕ_0: for $n = 20$, for example, $\Delta\phi/\phi_0 = 60\%$ for $\phi_0 = 40°$ and $\Delta\phi/\phi_0 = 44\%$ for $\phi_0 = 30°$.

Criterion (11) has two serious drawbacks: (1) for some integer values of n it has *solutions outside the elastic domain of interest* [14] or, as defined by [15], it exhibits *false elastic domains*; (2) for non-integer values of n the criterion is not defined out of the positive octant of the stress space. These drawbacks will be addressed in the next sections. On the other hand, the advantage of the $3In$ criterion is that it does not require a tension cut-off since it is embedded in the formulation.

In the discussed approach the 3D surface is a cone, although the Author [10] also defined a hierarchical formulation able to include closed surfaces like those by [16, 17]. In the next section a meridian function will be developed in depth.

4   The *Uncoupled* Approach

Many Authors in literature [18–26] followed the *uncoupled* approach, namely that in which the 3D surface is obtained as the product of two functions, one meridian formulated in terms of invariants p and q (or invariants proportional to them) and one deviatoric formulated in terms of the Lode's angle θ. This approach offers a great versatility due to the possibility to formulate separately the two functions. As an example, the Mohr–Coulomb cone (3) can be reformulated in terms of invariants (5) as

$$q^2 = p^2 \left[\frac{6\sin\phi_0}{(3 - \sin\phi_0)\cos\theta + \sqrt{3}\,(1 + \sin\phi_0)\sin\theta} \right]^2 \tag{15}$$

The previous equation can be put in the general form

$$q^2 - \Phi_p \Phi_\rho^2 = 0 \tag{16}$$

The *uncoupled* approach is based on the definition of Φ_p and Φ_ρ.

4.1   Deviatoric Function Φ_ρ

The Lode's dependence Φ_ρ can be formulated by rewriting the MN criterion (8) in terms of invariants (5) using (6)

$$3p\left(3p^2 - \frac{q^2}{3}\right) - k_{MN}\left(\frac{2}{27}q^3\cos 3\theta - \frac{1}{3}pq^2 + p^3\right) = 0 \tag{17}$$

Normalising the previous equation by p^3 one obtains a third degree equation that can be put in the general form

$$\eta^3 \cos 3\theta + c_2 \eta^2 + c_0 = 0 \tag{18}$$

where c_2 and c_0 are determined by rewriting (18) for triaxial compression ($\cos 3\theta = 1$, $\eta = \eta_c$) and extension ($\cos 3\theta = -1$, $\eta = \eta_e = \beta \eta_c$)

$$\begin{cases} \eta_c^3 + c_2 \eta_c^2 + c_0 = 0 \\ -\eta_e^3 + c_2 \eta_e^2 + c_0 = 0 \end{cases} \tag{19}$$

Solving (19), Eq. (18) becomes

$$\eta^3 \cos 3\theta + \eta_c \frac{\beta^3 + 1}{\beta^2 - 1} \eta^2 - \eta_c^3 \left(\frac{\beta^3 + 1}{\beta^2 - 1} + 1 \right) = 0 \tag{20}$$

Defining

$$\rho = \frac{\eta}{\eta_c} \tag{21}$$

the further normalisation of Eq. (20) by $\eta_c^3 \cos 3\theta$ gives us

$$\rho^3 + \frac{1}{\cos 3\theta} \frac{\beta^3 + 1}{\beta^2 - 1} \rho^2 - \frac{1}{\cos 3\theta} \frac{\beta^3 + \beta^2}{\beta^2 - 1} = 0 \tag{22}$$

It is worth noting that the obtained third degree equation is a function of the Lode's angle only and thus the information on the meridian shape of the starting 3D criterion (17) has been lost. The three roots of (22) are

$$\rho_k = \frac{\sqrt{3}}{2} \frac{\beta}{\sqrt{\beta^2 - \beta + 1}} (-1)^k \frac{1 - 2 \cos \left[\dfrac{\omega + 2(4 - k)\pi}{3} \right]}{\cos \dfrac{\omega}{2}} \tag{23}$$

for $k = 1, 2, 3$ where

$$\omega = \arccos \left[-1 + \frac{27}{2} \frac{\beta^2 (1 - \beta)^2}{(\beta^2 - \beta + 1)^3} \cos^2 3\theta \right] \tag{24}$$

Only the solutions for $k = 1$ and $k = 2$ are of interest for the deviatoric function. In particular, function Φ_ρ is given by

$$\Phi_\rho = \begin{cases} \rho_1 & \text{for} \quad \cos 3\theta \leq 0 \\ \rho_2 & \text{for} \quad \cos 3\theta \geq 0 \end{cases} \tag{25}$$

After some manipulation of (23), the Lode's dependence is put in the form

$$\Phi_\rho = \frac{\sqrt{3}}{2} \frac{\beta}{\sqrt{\beta^2 - \beta + 1}} \frac{s_\theta}{\cos\left(\dfrac{4 + s_\theta}{3}\pi + \dfrac{\omega}{6}\right)} \tag{26}$$

where

$$s_\theta = 1 - |\mathrm{sgn}\,(\cos 3\theta)| + \mathrm{sgn}\,(\cos 3\theta) \tag{27}$$

Function (26) depends only on the aspect ratio β and its representation on the deviatoric plane results in the same shapes as those related to the $3In$ criterion.

Equation (26) provides the same values of the Ottosen criterion [21] that can be put in a form related to the function defined by Podgòrski [22]

$$\Phi_\rho = \frac{\cos\left\{\dfrac{1}{3}\arccos\,[-k]\right\}}{\cos\left\{\dfrac{1}{3}\arccos\,[k\cos(3\theta + \pi)]\right\}} \tag{28}$$

where $0 \leq k \leq 1$. The relationship between β and k is given by

$$\beta = \frac{\cos\left[\dfrac{1}{3}\arccos\,(-k)\right]}{\cos\left[\dfrac{1}{3}\arccos\,(+k)\right]} \tag{29}$$

The deviatoric shape of (26) can be modified making β a function of the Lode's angle. To maintain isotropy, a function of period $2\pi/3$ must be selected as done by the Author [26]

$$\beta = \beta_c + (\beta_e - \beta_c)\left|\sin\left(\frac{3}{2}\theta\right)\right| \tag{30}$$

In this way, the Lode's dependence (26) results as an envelope of functions obtained for different values of aspect ratios varying from β_c for $\theta = 0$ to β_e for $\theta = \pi/3$. Inserting (30) in (26) a more flexible deviatoric function is obtained. In Fig. 6 five functions are shown: the innermost and the outermost are characterised by $\beta_c =$
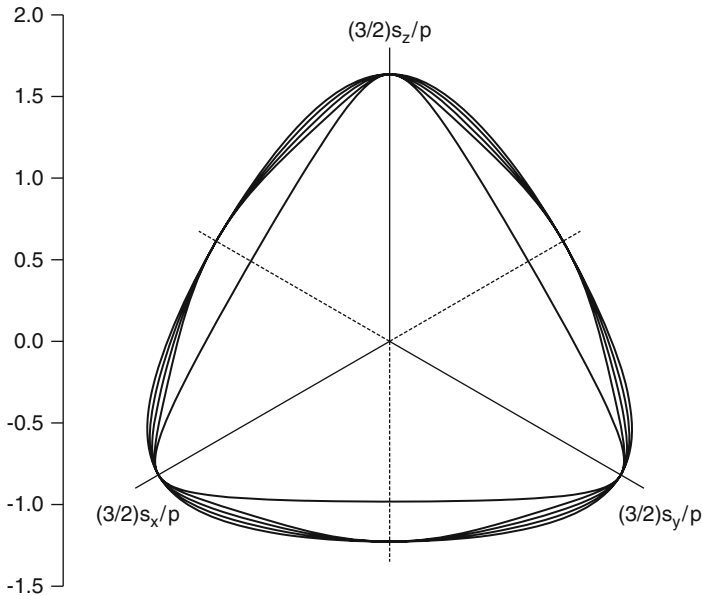
Fig. 6 Normalised deviatoric traces of the *uncoupled* criterion for $\phi_0 = 40°$ for $\beta_e = \beta_c = 0.60$, and for $\beta_e = 0.75$ and $\beta_c = 0.60, 0.65, 0.70, 0.75$

$\beta_e = 0.60$ and $\beta_c = \beta_e = 0.75$, respectively; the others are related to $\beta_e = 0.75$ and $\beta_c = 0.60, 0.65, 0.70$. While the functions with $\beta_c = \beta_e$ can be predicted by the $3In$ criterion, those related with $\beta_c \neq \beta_e$ offer a new possibility for interpreting the experimental data in particular when failure data of concrete are analysed [26]. It should be noted that the surfaces in Fig. 6 are related to a given value of ϕ_0: this value is at all arbitrary since the deviatoric curves have no any relationship with the selected value of the compression friction angle.

A value of ϕ_0 is necessary if one wants to highlight the variation of the friction angle for increasing values of the Lode's angle. Figure 7 shows the variation related to the curves shown in Fig. 6. A peculiarity can be noted for the curve related with $\beta_e = \beta_c = 0.60$ due to the value of the friction angle under the extension condition, which is lower than ϕ_0: this feature cannot be predicted by the *coupled* criterion for which the lowest values of ϕ for $\theta = 60°$ is related to $n = 1$, namely with the MN criterion, that predicts the value $\beta = (3 - \sin\phi_0)/(3 + \sin\phi_0)$. Thus, the minimum value of $\beta_e = \beta_c$ for $\phi_0 = 40°$ consistent with the *coupled* approach is 0.647. The other curves shown in Fig. 7 are related to the same values of the friction angles in compression and extension: this is a peculiarity impossible to be predicted with the $3In$ criterion. Furthermore, with the *uncoupled* approach, for some combinations of ϕ_0 and β_e the predicted curves are not able to fulfil the limit condition on the friction
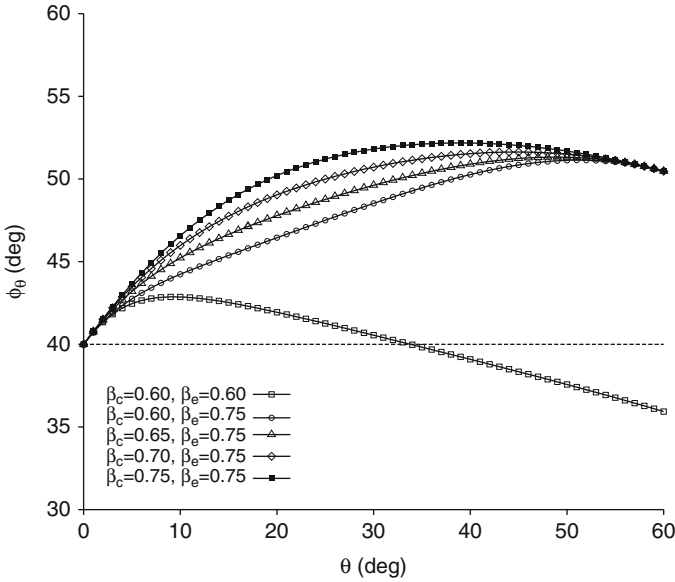
Fig. 7 Variation of the friction angle with θ for the curves shown in Fig. 6

angle $\phi_\theta \leq 90°$. Also, not all combinations of β_c and $\beta_e \neq \beta_c$ are consistent with the convexity of the Lode's dependence. Convexity is preserved if the condition

$$\Phi_\rho^2 + 2\left(\frac{\partial \Phi_\rho}{\partial \theta}\right)^2 - \Phi_\rho \frac{\partial^2 \Phi_\rho}{\partial \theta^2} \geq 0 \tag{31}$$

is fulfilled [27].

4.2 Meridian Function Φ_p

The most popular choices as yield surfaces in geomechanics are related to simple shapes as the cone [28] and the ellipse [29]. Unfortunately, these simple shapes cannot always account for the complex behaviour of soils. On the other hand, more complex functions can suffer of deficiencies related to *false elastic domains* or indefiniteness in some portions of the stress space.

Willing to define a function including such simple shapes, the Author [26, 30] formulated the following hierarchical function

$$\Phi_p = \text{sgn}\,(p_t + p)\,\alpha_d R_p^{n_\alpha} \left[1 - \text{sgn}\,(n_c)\,\text{sgn}\,(p_t + p)\,R_p^{n_c} \right] \tag{32}$$

where R_p, n_α, and α_d are given by

$$R_p = \left| \frac{p_t + p}{p_t + p_c} \right| \tag{33}$$

$$n_\alpha = \left[1 - \mathrm{sgn}\,(n_c) \right] 2n_d + \frac{n_c \left[1 - \mathrm{sgn}\,(n_c) + R_p \right]^{n_c}}{1 - \mathrm{sgn}\,(n_c) \left[1 - \mathrm{sgn}\,(n_c) + R_p \right]^{n_c}} \tag{34}$$

$$\alpha_d = \frac{1 - \mathrm{sgn}\,(n_c) + \mathrm{sgn}\,(n_c)\, R_p^{2-n_\alpha}}{1 - \mathrm{sgn}\,(n_c) \left[1 - \mathrm{sgn}\,(n_c) + R_p \right]^{n_c}} \left[\eta_h\,(p_t + p_c) \right]^2 \tag{35}$$

being R_h, n_c, and n_d parameters of the function while η_h, p_t, and p_c are size parameters (hardening variables). The term $\mathrm{sgn}\,(p_t + p)$ in (32) is necessary to avoid the presence of a *false elastic domain* for $p < p_t$. For $n_c = 0$ the function represents an open surface, while for $n_c > 0$ it is a closed surface. Parameter R_h represents the value of R_p for which the tangent to the surface is horizontal and must be specified in the range $0 < R_h < 1$. Figure 8 shows some example of shapes related to Eqs. (32) and (26): in particular, subfigures (a)–(d) show a cone, a hyperboloid, an ellipsoid, and a tear shape, respectively.
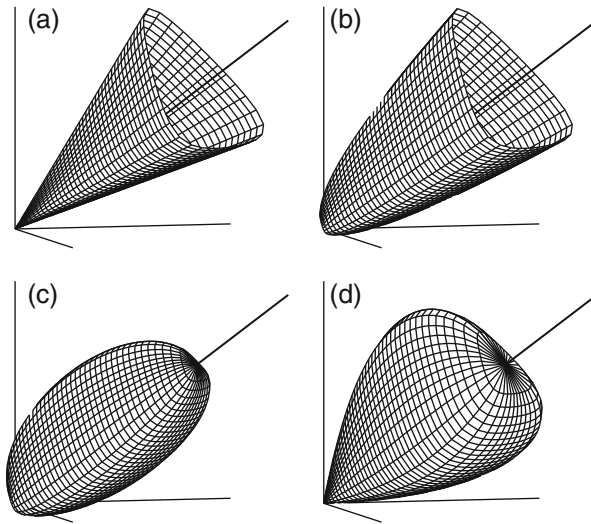
Fig. 8 3D shapes related to (26) for $\beta_c = \beta_e = 0.7$ and to (32). (**a**) Cone: $R_h = 0, n_c = 0, n_d = 1$; (**b**) paraboloid: $R_h = 0, n_c = 0, n_d = 0.5$; (**c**) ellipsoid: $R_h = 0.5, n_c = 1, n_d = 0$; (**d**) tear: $R_h = 0.7, n_c = 2, n_d = 0$

5 The *Hybrid* Approach

The *uncoupled* approach offers very high flexibility in shape but it has the feature of having a deviatoric trace independent of the friction angle. The consequence of this feature is shown in Fig. 9 where the traces of three cones related to $\beta_e = \beta_c = 0.8$ and different values of the triaxial compression friction angle are reported along with the limit (cut-off) surface, namely the Mohr–Coulomb surface for $\phi_0 = 90°$. It can be seen that for a limit value of the friction angle ($\phi_0 = 45.58°$) the trace of the cone and of the limit surface are tangent for $\theta = \pi/3$. For higher values of ϕ_0 (e.g. 50° in the figure) the surface highlights zones outside the positive octant of the stress space, thus predicting tensile stresses. It is simple to demonstrate [31] that the limit value of the friction angle is linked to the aspect ratio

$$\phi_{lim} = \arcsin\left(\frac{3}{4\beta + 1}\right) \tag{36}$$

Therefore, according to (36), the higher is the value of β, the lower is the value of ϕ_{lim}. This drawback can be eliminated by simply making the aspect ratio explicitly dependent on the friction angle. Clearly this function must fulfil the condition $0.5 \leq \beta \leq 1$ for $90 \geq \phi_0 \geq 0$. The following function is introduced [30]

$$\beta = \frac{3 + h}{3 + M_c + 2h} \tag{37}$$
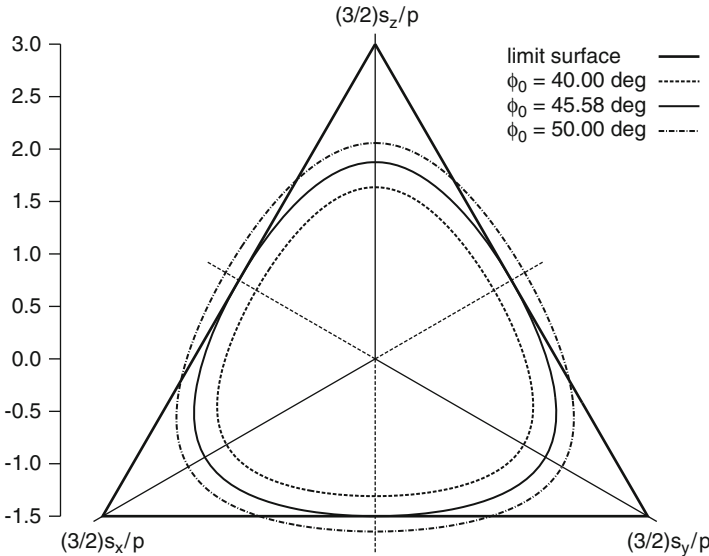
Fig. 9 Deviatoric traces of cones related to the *uncoupled* approach for $\beta_e = \beta_c = 0.8$ and different values of the triaxial compression friction angle
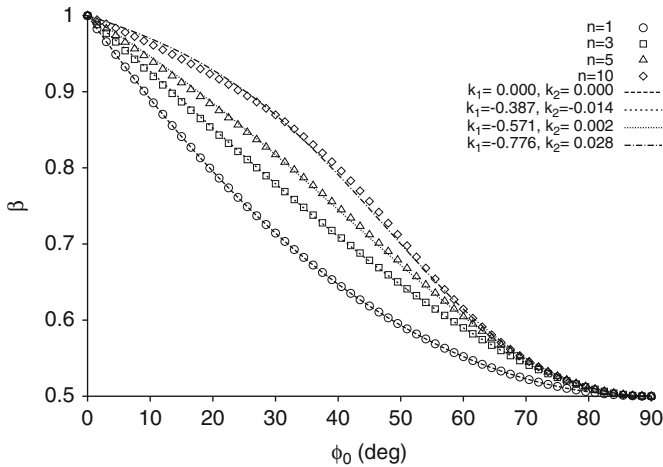
Fig. 10 Interpolation of the aspect ratio of the $3In$ model with Eq. (37)

where h is a function of M_c that must satisfy the constraint $h = 0$ for $\phi_0 = 0$. It is simple to infer that if $h = 0$ for each value of ϕ_0 the value of the aspect ratio $\beta = 3/(3 + M_c) = (3 - \sin \phi_0)/(3 + \sin \phi_0)$ is that predicted by the MN criterion. The following function is chosen

$$h = k_1 M_c + k_2 M_c^3 \tag{38}$$

where parameters k_1 and k_2 are computed from the minimum scatter between the values of the aspect ratio of the $3In$ model, computed using Eq. (14), and the values of β given by (37). Figure 10 shows that the agreement for $n \leq 10$ is very good. A deeper discussion is given in [31].

The *hybrid* approach consists in the introduction of (37) in the Lode's dependence (26) and in the choice of a suitable meridian function that does not violate the cut-off requirement under compression condition ($q/p \leq 3$). Unfortunately, the meridian function (32) presented in the previous section is not in general suitable because of the presence of exponent n_c. If $n_c > 0$, in fact, the surface is rounded for $p = p_t$ and due to this feature a more or less large portion of it results outside the positive octant of the principal stress space (see Fig. 8). Thus, function (32) can be used in the *hybrid* approach only if $n_c = 0$ and $n_d = 1$, namely if the surface is a cone. The definition of a suitable meridian function for the *hybrid* approach will avoid the problems related to the *coupled* and *uncoupled* approaches, that is the presence of *false elastic domains* and the occurrence of zones predicting tensile states of stress.

6 Failure Surfaces from DEM Experiments

The Discrete Element Method is a formidable tool for investigating the incremental behaviour of granular materials at the macroscale [3]. In DEM simulations many aspects of the complex macroscopic behaviour of granular materials, such as strong non-linearity, loading path dependency, stress dilatancy, anisotropy, non-coaxiality, critical state flow, grain breakage, liquefaction, and failure, can be explained from the description of such materials at the microscopic level [32]. In this section DEM experiments are used for the calibration of the parameters related to the criteria discussed in the previous sections.

Barreto and O'Sullivan [33] analysed the combined effects of the inter-particle friction μ and of the intermediate stress ratio $b = (\sigma_2 - \sigma_3)/(\sigma_1 - \sigma_3)$ by performing an extensive set of DEM simulations. In particular, after an isotropic compression stage to 200 kPa, drained true triaxial tests on isotropic specimens made by spheres at constant values of b for different values of the inter-particle friction $\mu = 0.140, 0.220, 0.325, 0.700$ where performed. The data in Fig. 11 have been plotted in terms of θ instead of b, as in the the original plot, using the relationship $\theta = \arctan[\sqrt{3}b/(2 - b)]$. From the figure it is possible to observe that the peak friction angle increases with μ for all the values of b considered. Furthermore, the values of parameters k_1 and k_2 of the *hybrid* approach as well as
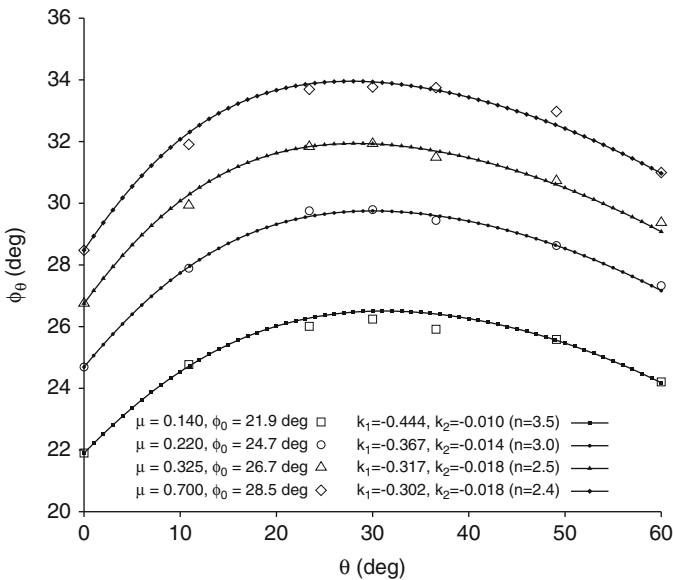
Fig. 11 Comparison between failure envelops obtained from DEM simulation related to different inter-particle friction coefficients and the *hybrid* approach (data from [33])

the value of n related to the *coupled* approach are shown. It is inferred that a little change of shape of the failure loci takes place for different inter-particle friction coefficients.

Galindo-Torres et al. [34] performed a DEM study related to the macroscopic shear strength characteristics of granular assemblies using three-dimensional complex-shaped particles with both isotropic and anisotropic geometries. In particular, true triaxial constant mean stress tests performed on cube assemblies of sphero-polyhedra for the isotropic granular geometry were performed. The results of the simulations show that under the compression condition a linear fitting can be adopted to model the peak stress points in the $p - q$ plane that are well represented by a friction angle $\phi_0 = 50°$. The Authors compared the results with the response obtained from two sphere assemblies: the results related to the complex-shaped particles highlight a considerably higher peak friction angle. The numerical failure points obtained from the simulation of true triaxial tests are compared in Fig. 12 with the deviatoric surface related to the *hybrid* (*coupled*) approach. As can be seen, the DEM results are very well matched by the model curve related to $k_1 = -0.232$ and $k_2 = -0.020$, corresponding to $n = 2$ for the *coupled* approach, thus just in the middle between the MN and the LD criteria. Anisotropy was investigated by performing tests on specimens made of particles with the z dimension flatter with respect to those related to the isotropic specimens. The failure envelope obtained is deformed and evidences cross-anisotropy as observed in real soils [26].
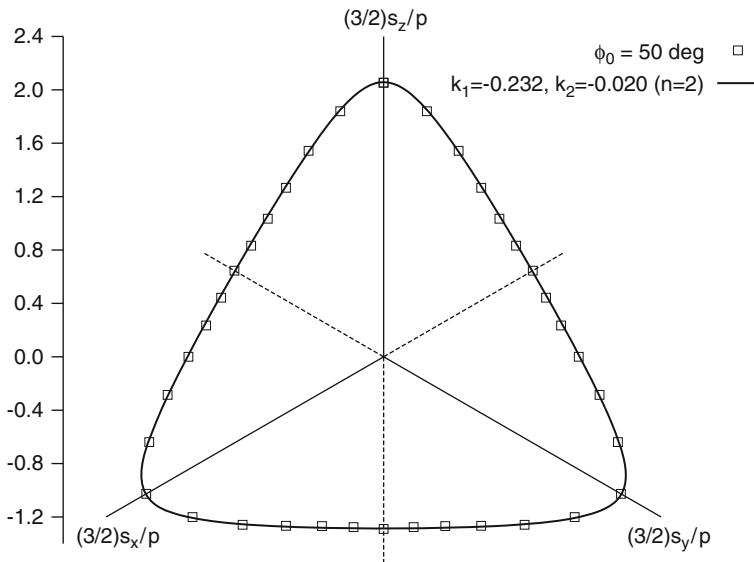

Fig. 12 Comparison between failure points obtained from DEM simulation and the *hybrid* approach (data from [34])

7 Conclusions

Different ways of formulating yield criteria for soils have been presented. In particular, three approaches called *coupled*, *uncoupled*, and *hybrid* have been defined and the drawbacks of each discussed. The *hybrid* approach is the only one that guarantees the absence of *false elastic domains* and avoid the presence of portions of the yield surfaces outside the positive octant of the stress space. However, the key point of the *hybrid* approach is the definition of a suitable meridian surface representative of closed surfaces. This problem has been recently addressed by the Author [31].

References

1. de Boer R.: Theory of porous media. Springer Verlag (2000).
2. Rankine W.J.M.: On the stability of loose earth. Philosophical Transactions of the Royal Society of London 147, 9–27 (1857).
3. Calvetti F., Viggiani G., Tamagnini G.: Micromechanical inspection of constitutive modelling. Workshop on Constitutive Modelling and Analysis of Boundary Value Problems in Geotechnical Engineering (3x4), Hevelius Edizioni, 187–216 (2003).
4. Davis R.O., Selvadurai A.P.S.: Plasticity and geomechanics. Cambridge University Press (2002).
5. Muir Wood D.: Geotechnical modelling. Spon Press (2004).
6. Nova R: Soil mechanics. John Wiley & Sons (2010).
7. Matsuoka H., Nakai T.: Stress-deformation and strength characteristics of soil under three different principal stresses. Proceeding Japan Society of Civil Engineers 232, 59–70 (1974).
8. Lade P.V., Duncan M.: Elastoplastic stress-strain theory for cohesionless soil. ASCE, Journal of the Geotechnical Engineering Division 101, 1037–1053 (1975).
9. Houlsby G.T.: A study of plasticity theories and their applicability to soils. PhD Thesis, University of Cambridge (1981).
10. Mortara G.: A new yield and failure criterion for geomaterials. Géotechnique 58, 125–132 (2008).
11. Mortara G.: A hierarchical single yield surface for frictional materials. Computers and Geotechnics 36, 960–967 (2009).
12. Bardet J.P.: Lode dependences for isotropic pressure-sensitive materials. ASME, Journal of Applied Mechanics 57, 498–506 (1990).
13. Houlsby G.T.: A general failure criterion for frictional and cohesive materials. Soils and Foundations 26, 97–101 (1986).
14. Bier W., Hartmann S.: A finite strain constitutive model for metal powder compaction using a unique and convex single surface yield function. European Journal of Mechanics A/Solids 25, 1009–1030 (2006).
15. Brannon R.M., Leelavanichkul S.: A multi-stage return algorithm for solving the classical damage component of constitutive models for rocks, ceramics, and other rock-like media. International Journal of Fracture 163, 133–149 (2010).
16. Lade P.V.: Elasto-plastic stress-strain theory for cohesionless soil with curved yield surfaces. International Journal of Solids and Structures 13, 1019–1035 (1977).
17. Kim M.K., Lade P.V.: Modeling of rock strength in three dimensions. International Journal of Rock Mechanics and Mining Sciences 21, 21–33 (1984).

18. Argyris J.H., Faust G., Szimmat J., Warnke E.P., Willam K.J.: Recent developments in the finite element analysis of prestressed concrete reactor vessels. Nuclear Engineering and Design 28, 42–75 (1974).
19. Gudehus G.: Elastoplastische stoffgleichungen fur trockenen sand. Ingenieur-Archiv 42, 151–169 (1973).
20. Willam K., Warnke E.P.: Constitutive model for the triaxial behavior of concrete. Seminar on concrete structure subjected to triaxial stresses. ISMES, Bergamo, Italy (1974).
21. Ottosen N.S.: A failure criterion for concrete. ASCE, Journal of the Mechanics Engineering Division 103, 527–535 (1977).
22. Podgòrski J.: General failure criterion for isotropic media. ASCE, Journal of Engineering Mechanics 111, 188–201 (1985).
23. van Eekelen H.A.M.: Isotropic yield surface in three dimensions for use in soil mechanics. International Journal for Numerical and Analytical Methods in Geomechanics 4, 89–101 (1980).
24. Sheng D., Sloan S.W., Yu H.S.: Aspects of finite element implementation of critical state models. Computational Mechanics 26, 185–196 (2000).
25. Bigoni D., Piccolroaz A.: Yield criteria for quasibrittle and frictional materials. International Journal of Solids and Structures 41, 2855–2878 (2004).
26. Mortara G.: A yield criterion for isotropic and cross-anisotropic cohesive-frictional materials. International Journal for Numerical and Analytical Methods in Geomechanics 34, 953–977 (2010).
27. Jiang J., Pietruszczak S.: Convexity of yield loci for pressure sensitive materials. Computers and Geotechnics 5, 51–63 (1988).
28. Drucker D.C., Prager W.: Soil mechanics and plastic analysis or limit design. Quarterly of Applied Mathematics 10, 157–165 (1952).
29. Burland J.B.: The yielding and dilation of clay. Géotechnique 15, 211–214 (1965).
30. Mortara G.: A constitutive framework for the elastoplastic modelling of geomaterials. International Journal of Solids and Structures 63, 139–152 (2015).
31. Mortara G.: A new yield criterion for soils with embedded tension cut-off. Meccanica 54, 683–696 (2019).
32. Zhao J., Jiang M., Soga K., Luding S.: Micro origins for macro behavior in granular media. Granular Matter 18, 1–5 (2016).
33. Barreto D., O'Sullivan C.: The influence of inter-particle friction and the intermediate stress ratio on soil response under generalised stress conditions. Granular Matter 14, 505–521 (2012).
34. Galindo-Torres S.A., Pedroso D.M., Williams D.J., Mühlhaus H.B.: Strength of non-spherical particles with anisotropic geometries under triaxial and shearing loading configurations. Granular Matter 15, 531–542 (2013).

Biological Driven Phase Transitions in Fully or Partly Saturated Porous Media: A Multi-Component FEM Simulation Based on the Theory of Porous Media

Tim Ricken, Andrea Thom, Tobias Gehrke, Martin Denecke, Renatus Widmann, Marcel Schulte, and Thorsten C. Schmidt

Abstract Bacterial methane oxidation in landfill cover soils, which turns the emitting methane caused by waste degradation into carbon dioxide, reduces the climate impact of landfill gas emissions significantly, since methane is estimated to have a global warming potential (GWP) of 25 over 100 years (GWP of CO_2 = 1). To understand and forecast the biological processes, a Finite-Element Model (FEM) is developed to simulate the behavior of methanotrophic layers. A multiphasic continuum mechanical approach based on the extended Theory of Porous Media (eTPM) is chosen, providing a macroscopic, multi-component view on the bacterial progress including the relevant gas transport processes of diffusion and advection in porous media as well as bacterial driven conversion processes. The presented thermodynamically consistent model also considers energy production within the gas phase resulting from exothermic reactions. An experimental setup was developed to validate the model also in terms of temperature development via the thermal imaging technique.

Keywords Bacterial methane oxidation · Extended Theory of Porous Media (eTPM) · Mixture theory · Multi-Component approach · Multiphysics · Thermodynamics · Model coupling · Finite-Element Method

T. Ricken (✉) · A. Thom
Institute of Mechanics, Structural Analysis and Dynamics, Faculty of Aerospace Engineering and Geodesy, University of Stuttgart, Stuttgart, Germany
e-mail: tim.ricken@isd.uni-stuttgart.de

T. Gehrke · M. Denecke · R. Widmann
Department of Water and Waste Management, University of Duisburg-Essen, Essen, Germany

M. Schulte · T. C. Schmidt
Department of Instrumental Analytical Chemistry, University of Duisburg-Essen, Essen, Germany

1 Introduction

Besides carbon dioxide (CO_2), methane (CH_4) is regarded as one of the global greenhouse gases which causes climate change. However, it must be noted that the GWP of CH_4 is considered with the factor 25 compared to the GWP = 1 of CO_2 over a period of 100 years, cf. [1]. Landfills emit CO_2 and CH_4 in equal shares and are one of the polluters of anthropogenic methane emissions. Figure 1 schematically shows the amount of methane produced over the years within a landfill, caused by the biological driven degradation and conversion of organic waste. During the first decades of operation and active aftercare phase the degradation of organic waste produces high methane emissions; these are technically captured and flared or used for biogas power plants. At a point where an active treatment of landfill gas is no longer economically efficient due to lean gas emissions, the biological oxidation of methane within the landfill cover layer can be taken as a passive treatment of the harmful emissions.

The so-called methanotrophic bacteria are ubiquitous in aerobic soil areas, thus also in cover soils of landfills, cf. Fig. 2, so that a passive treatment of methane
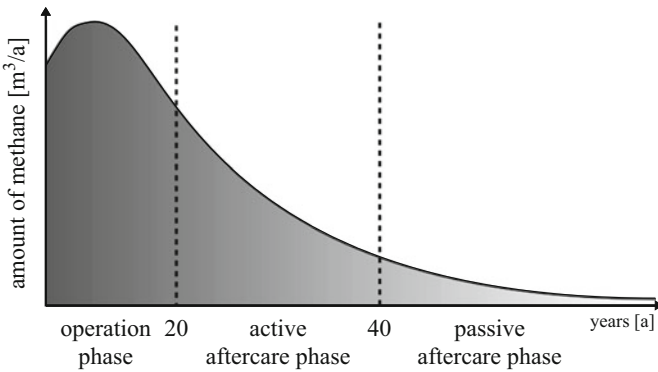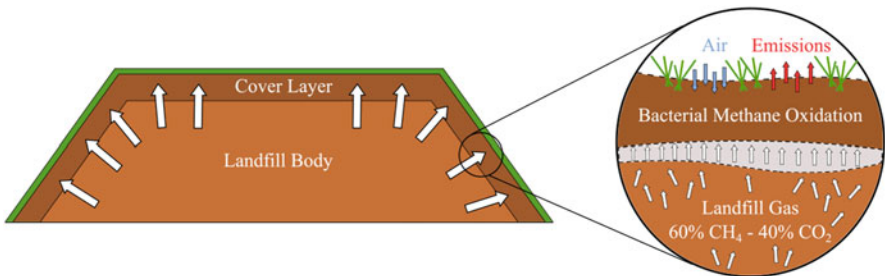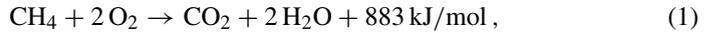

Fig. 1 Methane production of a landfill

Fig. 2 Methane oxidation in cover layer

emissions is automatically given. The exothermic reaction equation of bacterial methane oxidation is given with

$$CH_4 + 2\,O_2 \rightarrow CO_2 + 2\,H_2O + 883\,kJ/mol\,, \tag{1}$$

see [15]. Attenuation of landfill gas in cover soils is significantly affected by ingress of atmospheric oxygen into the soil, which generates conditions suitable for aerobic methane oxidation, cf. [17]. But still, a reliable forecast of the biological processes and methane conversion, which are influenced by a variety of environmental factors, is needed to confirm passive aftercare of landfill sites.

Hence, a fully coupled multiphasic and multi-component Finite-Element model (FE model), which reproduces the phenomena of bacterial activity, see [21], energy production, and the gas transport mechanisms of diffusion and advection, is developed and presented. The fundamentals are given with the continuum mechanical approach with the Theory of Porous Media (TPM) [2, 6, 8, 9]. A former model, predicting the gas production in landfills, can be found in [22, 25, 36]. Building on that, the new model for methane oxidation processes in landfill cover soils completes the overall computational simulation of landfill emissions. Former works regarding this model can be found in [21, 28–30, 34].

Several models describing methane oxidation have been developed in the past. Stein et al. [31] developed a simple 1D reactive transport model to determine the effects of soil moisture, the soil's relative air-filled porosity, CH_4 flux rate, and CH_4 oxidation rate. Molins et al., cf. [16, 17], also focus on the gas transfer using a multi-component reactive transport model. De Visscher et al. [37] developed a simulation model incorporating diffusion, methane oxidation, and methanotrophic growth. All previously mentioned models ignored the effects of water and heat transfer and the effects on the microbial activity. Hettiarachchi et al. [12] developed a 1D numerical model including all phenomena of heat transfer, gas transport, microbial reactions, and moisture transport as a tool in designing and operating methane biofilters. Xue et al. [38] present a 2D multiphase FE model (solid, liquid, gaseous) for a landfill cover system including dissolved air in the liquid phase as well as water vapor in the gaseous phase under thermal, hydro, and mechanical coupling effects, but excluding effects of methane oxidation, focusing on numerical simulations of cracking. Ng et al. [18] also present a 2D multiphase model for methane oxidation in landfill cover layers consisting of solid, liquid, and gas phase as a four-component gas mixture (CO_2, O_2, CH_4, N_2) including water-heat-coupling effects solved by commercial FE software focusing on influences of oxidation-generated water and heat on methane oxidation. Adopting this model, Feng et al. [10] present numerical studies of methane oxidation efficiency of sloping landfill covers.

The model presented in this work is composed of an incompressible porous solid matrix representing the cover soil, saturated by a compressible gas phase which is built as a mixture of the relevant gases composing air together with landfill gases, namely methane, oxygen, carbon dioxide, and nitrogen (CH_4, O_2, CO_2, N_2). The liquid phase is assumed to be included within the solid phase providing optimal environmental conditions for the bacteria population (biofilm), which in turn is

assumed to be fixed to the solid phase. The constitutive approaches for bacteria growth and the depending methane oxidation rates have been investigated in [21] and serve as the basis for this contribution. Nevertheless, the influence of a growing biofilm on the CH_4 oxidation as described in [13, 14] has to be investigated with the present model, since EPS (exopolymeric substances) production can reduce CH_4 oxidation capacity over time by limiting oxygen diffusion to sites of microbial activity. More alternative models concerning biofilm growth in porous media are given in [7, 11]. However, existing models are currently not able to holistically describe the multi-component bio-chemo-thermo coupled conversion processes including finite solid deformation in a continuum mechanical and thermodynamically consistent framework. It is the aim of this work to provide such a model.

The presented model will be validated by use of experimental data which are originally produced for this propose, cf. [26]. The model reproduces measured gas concentrations and indicates the highest bacterial activity also by heat generation. The continuum mechanical approach for the multi-component body including the gas concentrations is presented in Sect. 2, whereas the specific model assumptions are presented in Sect. 3. A thermodynamically consistent constitutive framework for the description of the stresses, interaction forces, phase transition, and energy production derived by evaluation of the entropy inequality based on [5] is presented in Sect. 4, whereas Sect. 5 gives a short overview of the numerical treatment of the governing equations and their weak formulations for the implementation into the Finite-Element (FE) code. For model validation, a new experimental setup using the thermal imaging technique was developed. This experiment technique provides an insight into the cover layer and visualizes the methane oxidation horizon via the energy production. The experiment and the corresponding simulations are presented in Sect. 6.

2 Basics

2.1 Theory of Porous Media (TPM)

Among others, geotechnical problems can be described with the help of the Theory of Porous Media (TPM). The TPM originates from the underlying Mixture Theory [4] enhanced by the concept of volume fractions, cf. [6, 9]. The TPM provides a continuum mechanical description of multiphasic systems consisting of different constituents. As described in [20] a (partially) saturated soil body in general is composed of a solid (**S**) matrix, which generates the control volume $B_\mathbf{S}$ with its boundary $\partial B_\mathbf{S}$, saturated by a liquid (**L**) or gas phase (**G**), or both. The phases are assumed to be statistically and homogeneously distributed over the control volume, immiscible and therefore mutually superimposed, see Fig. 3. After superposition of the homogenized phases each spatial point X is occupied by every constituent
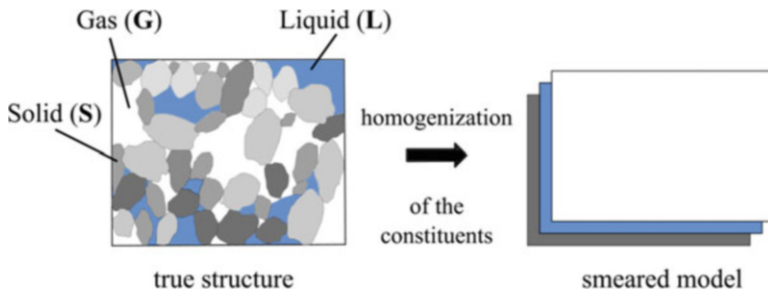
Fig. 3 Homogenization of the constituents

simultaneously. Following the concept of volume fractions, each phase φ^α ($\alpha =$ **S**, **L**, **G**) occupies its own volume fraction

$$n^\alpha = \frac{dv^\alpha}{dv} \, , \tag{2}$$

defined as the ratio between the volume of each constituent to the bulk volume. The partial density of the constituent φ^α is given as the product of the volume fraction and the realistic density $\rho^{\alpha R}$ with

$$\rho^\alpha = n^\alpha \rho^{\alpha R} \, . \tag{3}$$

The saturation condition, claiming that summing up all volume fractions n^α of the κ phases, leads to the overall mixture body is hence given with

$$\sum_{\alpha=1}^{\kappa} n^\alpha (\mathbf{x}, t) = \sum_{\alpha=1}^{\kappa} \frac{dv^\alpha}{dv} = \sum_{\alpha=1}^{\kappa} \frac{\rho^\alpha}{\rho^{\alpha R}} = 1, \tag{4}$$

with $\mathbf{x}$ as the position vector in the actual placement of the spatial point X.

The balance equations for mass, momentum, moment of momentum, and energy are valid for each constituent. Following the metaphysical principles of Truesdell, cf. [35], the mixture body has to behave like a one component continuum, so that additionally interaction forces ($\hat{\mathbf{p}}^\alpha$) and supply terms ($\hat{\rho}^\alpha$ for mass, $\hat{e}^\alpha$ for energy) have to be considered. The balance equations for the constituents in the local form in the above-mentioned sequence read

$$(\rho^\alpha)'_\alpha + \rho^\alpha \, \mathrm{div} \, \mathbf{x}'_\alpha = \hat{\rho}^\alpha \, , \tag{5}$$

$$\mathrm{div} \, \mathbf{T}^\alpha + \rho^\alpha \, (\mathbf{b} - \mathbf{x}''_\alpha) = \hat{\rho}^\alpha \, \mathbf{x}'_\alpha - \hat{\mathbf{p}}^\alpha \, , \tag{6}$$

$$\mathbf{T}^\alpha = (\mathbf{T}^\alpha)^{\mathrm{T}} \tag{7}$$

$$\rho^\alpha (\varepsilon^\alpha)'_\alpha - \mathbf{T}^\alpha \cdot \mathbf{D}_\alpha - \rho^\alpha \, r^\alpha + \mathrm{div} \, \mathbf{q}^\alpha = \hat{\varepsilon}^\alpha \, , \tag{8}$$

where the direct energy production term $\hat{\varepsilon}^{\alpha}$ is given with

$$\hat{\varepsilon}^{\alpha} = \hat{e}^{\alpha} - \hat{\mathbf{p}}^{\alpha} \cdot \mathbf{x}'_{\alpha} - \hat{\rho}^{\alpha} \left(\varepsilon^{\alpha} + \frac{1}{2} \mathbf{x}'_{\alpha} \cdot \mathbf{x}'_{\alpha} \right) . \tag{9}$$

The production terms follow the restrictions

$$\sum_{\alpha=1}^{\kappa} \hat{\rho}^{\alpha} = 0, \quad \sum_{\alpha=1}^{\kappa} \hat{\mathbf{p}}^{\alpha} = 0, \quad \sum_{\alpha=1}^{\kappa} \hat{e}^{\alpha} = 0. \tag{10}$$

Furthermore, $\mathbf{T}^{\alpha}$ denotes the partial Cauchy stress tensor, $\mathbf{b}$ the body force vector, and $\mathbf{D}_{\alpha}$ is defined as the symmetric part of the spatial velocity gradient, cf. Appendix 1. In addition, ε^{α}, $\mathbf{r}^{\alpha}$, and $\mathbf{q}^{\alpha}$ represent the specific internal energy, the specific external heat supply, and the heat flux over the surface, respectively. The specific internal energy can be given in terms of the specific entropy η^{α} and the Helmholtz free energy ψ^{α} with $\varepsilon^{\alpha} = \psi^{\alpha} + \theta^{\alpha} \eta^{\alpha}$. The operator "div" denotes the spatial divergence operator.

The second law of thermodynamics (entropy inequality) provides restrictions for constitutive modelling to derive a thermodynamic consistent description of the material behavior with

$$\sum_{\alpha=1}^{\kappa} [\rho^{\alpha} (\eta^{\alpha})'_{\alpha} + \hat{\rho}^{\alpha} \eta^{\alpha}] \geq \sum_{\alpha=1}^{\kappa} [\frac{1}{\theta^{\alpha}} \rho^{\alpha} \mathbf{r}^{\alpha} - \text{div} \, (\frac{1}{\theta^{\alpha}} \, \mathbf{q}^{\alpha})]. \tag{11}$$

Further details regarding the evaluation of the entropy inequality are given in Appendix 2.

2.2 Extended Theory of Porous Media (eTPM)

The extended TPM (eTPM) provides an approach for the case that the immiscible macroscopic phases φ^{α} are additionally composed of different substances. For example, the macroscopic liquid phase φ^{L} can consist of an incompressible carrier phase and therein dissolved substances, cf. [23, 24], or the macroscopic compressible gas phase φ^{G} is given as a mixture of different gases, as presented here. For this case, the mixture body φ can be described in a generalized approach with

$$\varphi = \sum_{\alpha=1}^{\kappa} \varphi^{\alpha} = \sum_{\alpha}^{\kappa} \left[\sum_{\gamma=1}^{\nu} \varphi^{\alpha\gamma} \right], \tag{12}$$

where the macroscopic main phase φ^{α} is composed of ν miscible substances φ^{γ}. The restrictions for the interaction and supply terms, cf. (10), are then given with

$$\sum_{\alpha=1}^{\kappa} \hat{\rho}^{\alpha} = \sum_{\alpha=1}^{\kappa} [(\sum_{\gamma=1}^{\nu} \hat{\rho}^{\alpha\gamma})] = 0,$$

$$\sum_{\alpha=1}^{\kappa} \hat{\mathbf{p}}^{\alpha} = \sum_{\alpha=1}^{\kappa} [(\sum_{\gamma=1}^{\nu} \hat{\mathbf{p}}^{\alpha\gamma})] = 0 \qquad (13)$$

$$\sum_{\alpha=1}^{\kappa} \hat{e}^{\alpha} = \sum_{\alpha=1}^{\kappa} [(\sum_{\gamma=1}^{\nu} \hat{e}^{\alpha\gamma})] = 0.$$

The compressible gas mixture can be described as a mixture of ideal gases, together they form the overall gas phase. The partial density of the gas component with the local mass dm^{γ} related to the overall bulk volume is defined as

$$\rho^{G\gamma} = \frac{dm^{\gamma}}{dv} = \frac{dv^{G}}{dv} \frac{dm^{\gamma}}{dv^{G}} = n^{G} \rho^{G\gamma x}, \qquad (14)$$

where use has been made of the definition of the partial density related to the gas volume element (partial gas density) given as

$$\rho^{G\gamma x} = \frac{dm^{\gamma}}{dv^{G}} = M_{mol}^{\gamma} \frac{dn_{mol}^{\gamma}}{dv^{G}}, \qquad (15)$$

where the molar mass M_{mol}^{γ} is given by the amount of substance n_{mol}^{γ}

$$M_{mol}^{\gamma} = \frac{dm^{\gamma}}{dn_{mol}^{\gamma}}. \qquad (16)$$

The definition of the molar concentration of gas component φ^{γ} and of the gas mixture φ^{G}, respectively,

$$c_{mol}^{G\gamma} = \frac{dn_{mol}^{\gamma}}{dv^{G}} \quad \text{and} \quad c_{mol}^{G} = \sum_{\gamma} c_{mol}^{G\gamma} \qquad (17)$$

leads to the molar fraction defined as

$$x_{mol}^{G\gamma} = \frac{dn^{\gamma}}{\sum_{\gamma} dn^{\gamma}} = \frac{c_{mol}^{G\gamma}}{\sum_{\gamma} c_{mol}^{G\gamma}} = \frac{c_{mol}^{G\gamma}}{c_{mol}^{G}}, \qquad (18)$$

so that the partial gas density can be written as

$$\rho^{G\gamma x} = M_{mol}^{\gamma} c_{mol}^{G} x_{mol}^{G\gamma} = M_{mol}^{\gamma} c_{mol}^{G\gamma} \, , \tag{19}$$

and the true gas density of the macroscopic main phase is calculated via

$$\rho^{GR} = \sum_{\gamma} \rho^{G\gamma x} \, . \tag{20}$$

In analogy to the macroscopic quantities, the kinematics presented in Appendix 1 is valid for the mixture components as well as the balance equations given in (5)–(8).

3   Assumptions for the Biphasic, Multi-Component Model

The system is investigated as a biphasic model consisting of two macroscopic immiscible phases φ^S (solid) and φ^G (gas) in accordance to Sect. 2.1,

$$\varphi = \underset{\alpha}{\cup} \varphi^{\alpha} = \varphi^S \cup \varphi^G, \quad \text{with} \quad \boldsymbol{\alpha} = \{S, G\} \, , \tag{21}$$

so that the saturation condition (4) reads

$$n^S + n^G = 1 \, . \tag{22}$$

The macroscopic gas phase φ^G is composed of the miscible gas components $\varphi^{G\gamma}$ in accordance to Sect. 2.2, yielding a four-component gas mixture of N_2, CH_4, O_2, and CO_2 with

$$\varphi^G = \underset{\gamma}{\cup} \varphi^{G\gamma} \quad \text{with} \quad \gamma = \{N, M, O, C\} \, , \tag{23}$$

cf. Fig. 4. The liquid phase φ^L is assumed to be contained within the solid phase φ^S providing optimal environmental conditions for the methanotrophic bacteria
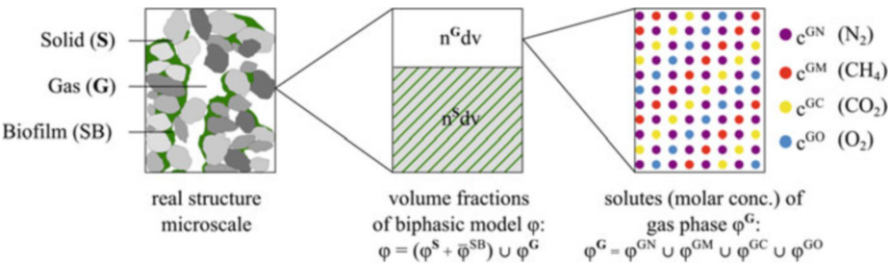
Fig. 4 Assumptions for the biphasic mixture model

$\bar{\varphi}^{SB}$. The solid matrix is considered to be incompressible, so that $(\rho^{SR})'_S = 0$ is valid, whereas density changes of the compressible gas phase depend on $\rho^{GR} = \rho^{GR}(\mathbf{x}, t, c_{mol}^{G\gamma})$. Mass transfer between the solid and gas phase is excluded, the exchange only takes place within the gas components, so that $(13)_1$ reduces to

$$\sum_\gamma \hat{\rho}^{G\gamma} = 0.$$ (24)

Moreover, the influence of the volume forces $\mathbf{b}$ is neglected for the gas components as well as the influence on the moment resulting from mass supply $\hat{\rho}^{G\gamma} \mathbf{x}'_{G\gamma}$. Additionally, the square of the velocities $\mathbf{x}'_\alpha \cdot \mathbf{x}'_\alpha$ and $\mathbf{x}'_{G\gamma} \cdot \mathbf{x}'_{G\gamma}$, respectively, and accelerations are neglected for both phases ($\mathbf{x}''_\alpha = \mathbf{0}$). The problem is investigated with varying temperature so that $(\theta)'_\alpha \neq 0$, but with identical temperatures for each phase at the same point X and hence each component temperature is referred to $\theta = \theta^S = \theta^G = \theta^{G\gamma}$. As a consequence, no energy supply between the phases occurs and the constraint from $(10)_3$ and $(13)_3$, respectively, is lapsed with $\hat{e}^S = \hat{e}^G = \hat{e}^{G\gamma} = 0$. At last, external heat supplies are excluded with $r^\alpha = 0$.

3.1 Field Equations

Following these assumptions, the coupled field equations describing the investigated biphasic, multi-component model are set up in the local form with the volume balances of the macroscopic solid and gas phase with

$$(n^S)'_S + n^S \operatorname{div} \mathbf{x}'_S = 0$$ (25)

$$(n^G)'_G + n^G \operatorname{div} \mathbf{x}'_G + \frac{n^G}{\rho^{GR}} (\rho^{GR})'_G = 0,$$ (26)

the concentration balances of the gas components

$$(n^G c_{mol}^{G\gamma})'_S + \operatorname{div} \mathbf{j}^{G\gamma} + n^G c_{mol}^{G\gamma} \operatorname{div} \mathbf{x}'_S = \hat{\rho}_{mol}^{G\gamma}$$ (27)

with $\hat{\rho}_{mol}^{G\gamma} = \hat{\rho}^{G\gamma}/M_{mol}^\gamma$ and $\mathbf{j}^{G\gamma} = n^G c_{mol}^{G\gamma} \mathbf{w}_{G\gamma S}$ describing the molar flux relative to the solid's movement with the difference velocity $\mathbf{w}_{G\gamma S} = \mathbf{x}'_{G\gamma} - \mathbf{x}'_S$, see also Sect. 4. Note that summing up the concentration balances (27) over all gas components yields (26). The set is completed with the momentum balances of the solid phase and gas components, since $\mathbf{T}^G = \sum_\gamma \mathbf{T}^{G\gamma}$, with

$$\operatorname{div} \mathbf{T}^S + \rho^S \mathbf{b} = -\hat{\mathbf{p}}^S,$$ (28)

$$\operatorname{div} \mathbf{T}^{G\gamma} + \rho^{G\gamma} \mathbf{b} = -\hat{\mathbf{p}}^{G\gamma},$$ (29)

the balance of energy for the mixture

$$\rho^{\mathbf{S}} \left[(\psi^{\mathbf{S}})'_{\mathbf{S}} + (\theta)'_{\mathbf{S}} \, \eta^{\mathbf{S}} + \theta \, (\eta^{\mathbf{S}})'_{\mathbf{S}} \right] - \mathbf{T}^{\mathbf{S}} \cdot \mathbf{D_S} +$$

$$\sum_\gamma \rho^{\mathbf{G}\gamma} \left[(\psi^{\mathbf{G}\gamma})'_{\mathbf{G}\gamma} + (\theta)'_{\mathbf{G}\gamma} \, \eta^{\mathbf{G}\gamma} + \theta (\eta^{\mathbf{G}\gamma})'_{\mathbf{G}\gamma} \right] - \sum_\gamma \mathbf{T}^{\mathbf{G}\gamma} \cdot \mathbf{D_{G\gamma}} + \tag{30}$$

$$\operatorname{div} \mathbf{q} + \sum_\gamma \hat{\mathbf{p}}^{\mathbf{G}\gamma} \cdot \mathbf{w_{G\gamma S}} + \sum_\gamma \hat{\rho}^{\mathbf{G}\gamma} \left(\psi^{\mathbf{G}\gamma} + \theta \eta^{\mathbf{G}\gamma} \right) = 0 \,,$$

where use has been made of $\operatorname{div} \mathbf{q}^{\mathbf{S}} + \sum_\gamma \operatorname{div} \mathbf{q}^{\mathbf{G}\gamma} = \operatorname{div} \mathbf{q}$.

4   Constitutive Theory

To develop a thermodynamic consistent approach, the entropy inequality was evaluated according to [5], see Appendix 2. The entropy is fulfilled for the following restrictions for the Cauchy stress tensors and the specific entropies with

$$\mathbf{T}^{\mathbf{S}} + n^{\mathbf{S}} \lambda \, \mathbf{I} = 2 \, \rho^{\mathbf{S}} \mathbf{F_S} \frac{\partial \psi^{\mathbf{S}}}{\partial \mathbf{C_S}} \mathbf{F_S^T} \,, \quad \mathbf{T}^{\mathbf{G}\gamma} + n^{\mathbf{G}} \mathbf{x}_{\text{mol}}^{\mathbf{G}\gamma} \lambda \, \mathbf{I} = \mathbf{0}$$

$$\tag{31}$$

$$\eta^{\mathbf{S}} = -\frac{\partial \psi^{\mathbf{S}}}{\partial \theta} \,, \quad \eta^{\mathbf{G}\gamma} = -\frac{1}{\rho^{\mathbf{G}\gamma \mathbf{x}}} \frac{\partial \psi^{\mathbf{G}\gamma \mathbf{x}}}{\partial \theta} \,,$$

where the weighted Lagrange multiplicator is given with

$$\mathbf{x}_{\text{mol}}^{\mathbf{G}\gamma} \lambda = \rho^{\mathbf{G}\gamma \mathbf{x}} \frac{\partial \psi^{\mathbf{G}\gamma \mathbf{x}}}{\partial \rho^{\mathbf{G}\gamma \mathbf{x}}} - \psi^{\mathbf{G}\gamma \mathbf{x}} \tag{32}$$

and the mass specific entropy $\eta^{\mathbf{G}\gamma}$

$$\eta^{\mathbf{G}\gamma \mathbf{x}} = \rho^{\mathbf{G}\gamma \mathbf{x}} \eta^{\mathbf{G}\gamma} \,. \tag{33}$$

Following the principle of effective stresses founded on [33], the effective stress part within the solid Cauchy stress tensor can be identified with

$$\mathbf{T}_{\mathbf{E}}^{\mathbf{S}} = 2 \, \rho^{\mathbf{S}} \, \mathbf{F_S} \, \frac{\partial \psi^{\mathbf{S}}(\mathbf{C_S}, \theta)}{\partial \mathbf{C_S}} \, \mathbf{F_S^T} \,, \tag{34}$$

and the Lagrange multiplicator λ as the overall pore pressure. In general, the pore pressure for a partially saturated medium is composed of a pressure part resulting from the liquid filled pore space $p^{\mathbf{LR}}$ and a pressure part developing from the gas filled pore space $p^{\mathbf{GR}}$ with $\lambda = p^{\mathbf{LR}} + p^{\mathbf{GR}}$. Since in this contribution the solid matrix

is only gas saturated, the overall pressure is given with $\lambda = p^{GR}$ and the solid stress tensor reads

$$\mathbf{T^S} = -n^S p^{GR} \mathbf{I} + \mathbf{T_E^S}. \tag{35}$$

According to Dalton's law the pore pressure is composed of the sum of the partial pressures $p^{G\gamma}$ with

$$\lambda = p^{GR} = \sum\nolimits_\gamma p^{G\gamma}, \tag{36}$$

so that (32) is identified as

$$p^{G\gamma} = x^{G\gamma}\lambda. \tag{37}$$

This yields the expression for the Cauchy stresses of gas constituents, summed up to the stress of the overall gas phase with

$$\sum\nolimits_\gamma \mathbf{T^{G\gamma}} = -\sum\nolimits_\gamma n^G x^{G\gamma} \lambda \mathbf{I} \qquad = -n^G \lambda \mathbf{I} = \mathbf{T^G}$$

$$\Rightarrow \quad \sum\nolimits_\gamma \mathbf{T^{G\gamma}} = -\sum\nolimits_\gamma n^G p^{G\gamma}\mathbf{I} \qquad = -n^G p^{GR}\mathbf{I} = \mathbf{T^G}. \tag{38}$$

The dissipative part of (80) yields restrictions for the evolution equations for the gas conversion, momentum supply, and the heat flux vector with

$$\hat{\rho}^{GO} = -\delta^{GO}\left(\mu^{GM} - \mu^{GO}\right), \quad \hat{\rho}^{GC} = -\delta^{GC}\left(\mu^{GM} - \mu^{GC}\right)$$

$$\hat{\mathbf{p}}^{G\gamma} = x^{G\gamma}\lambda \operatorname{grad} n^G + \hat{\mathbf{p}}_E^{G\gamma}, \quad \mathbf{q} = -\alpha_{\nabla\theta}\operatorname{grad}\theta, \tag{39}$$

where the terms $\mu^{G\gamma}$ and $\hat{\mathbf{p}}_E^{G\gamma}$ are defined with

$$\mu^{G\gamma} = \psi^{G\gamma} + \frac{x^{G\gamma} p^{G\gamma}}{\rho^{G\gamma x}}, \quad \hat{\mathbf{p}}_E^{G\gamma} = -\delta_{\mathbf{w}_{G\gamma S}}\mathbf{w}_{G\gamma S}, \tag{40}$$

cf. also [19]. Here, $\mu^{G\gamma}$ is defined as the mass specific chemical potential, the so-called Gibbs energy, due to thermodynamically consistence, cf. Appendix 2. The material parameters are restricted by

$$\delta^{GO} \geq 0, \quad \delta^{GC} \geq 0, \quad \delta_{\mathbf{w}_{G\gamma S}} \geq 0, \quad \alpha_{\nabla\theta} \geq 0. \tag{41}$$

The Helmholtz energy functions for the solid phase and gas components are postulated with

$$\psi^{\mathbf{S}} = \frac{1}{\rho_0^{\mathbf{SR}}} \{ \frac{1}{2} \lambda^{\mathbf{S}} (\ln J_{\mathbf{S}})^2 - \mu^{\mathbf{S}} \ln J_{\mathbf{S}} + \mu^{\mathbf{S}} (I_{C_{\mathbf{S}}} - 3)$$

$$- 3\alpha^{\mathbf{S}} k^{\mathbf{S}} (\ln J_{\mathbf{S}}) (\theta - \theta_0) - \rho_0^{\mathbf{SR}} c_V^{\mathbf{S}} (\theta \ln \frac{\theta}{\theta_0} - \theta + \theta_0) \} , \qquad (42)$$

$$\psi^{\mathbf{G}\gamma} = \mu_0^{\mathbf{G}\gamma} + \bar{R} \theta \{ \ln (\frac{\rho^{\mathbf{G}\gamma x}}{\rho_0^{\mathbf{G}\gamma x}}) - 1 \} - c_V^{\mathbf{G}\gamma} \{ \theta \ln(\frac{\theta}{\theta_0}) - \theta + \theta_0 \} .$$

The energy function $\psi^{\mathbf{S}}$ was chosen according to [27]. Therein, $\lambda^{\mathbf{S}}$ and $\mu^{\mathbf{S}}$ denote the macroscopic Lamé constants, $J_{\mathbf{S}} = \det \mathbf{F_S}$ is the determinant of the deformation gradient of the solid phase and $I_{C_{\mathbf{S}}} = \text{tr} \, \mathbf{C_S}$ denotes the first invariant of the right Cauchy–Green tensor $\mathbf{C_S}$. Additionally, θ_0 denotes the reference temperature, $\alpha^{\mathbf{S}}$ the thermal expansion coefficient, $k^{\mathbf{S}} = \lambda^{\mathbf{S}} + 2/3\mu^{\mathbf{S}}$ the bulk modulus, and $c_V^{\mathbf{S}}$ and $c_V^{\mathbf{G}\gamma}$ denote the specific heat capacities of the solid and gas components, respectively. The reference mass specific chemical potential is given with $\mu_0^{\mathbf{G}\gamma}$ and $\bar{R}$ denotes the specific gas constant.

Implementing the Helmholtz energy function into (31) yields for the solid extra stresses

$$\mathbf{T_E^S} = \frac{1}{J_{\mathbf{S}}} \{ 2\mu^{\mathbf{S}} \mathbf{K_S} + \lambda^{\mathbf{S}} (\ln) J_{\mathbf{S}} \mathbf{I} - 3\alpha^{\mathbf{S}} k^{\mathbf{S}} (\theta - \theta_0) \mathbf{I} \} , \qquad (43)$$

where $\mathbf{K_S}$ denotes the Karni–Reiner stress tensor. Evaluating (32) yields with the definition for the chemical potential according to [3] $\mu^{\alpha} = \partial\psi/\partial c^{\alpha}$

$$p^{\mathbf{G}\gamma} = \rho^{\mathbf{G}\gamma x} \mu^{\mathbf{G}\gamma} - \psi^{\mathbf{G}\gamma x} \qquad (44)$$

and with $(42)_2$ the partial pressure with

$$p^{\mathbf{G}\gamma} = \rho^{\mathbf{G}\gamma x} \bar{R} \theta , \qquad (45)$$

which can be identified as the ideal gas law. From that, the overall gas pressure is calculated with

$$p^{\mathbf{GR}} = \sum_\gamma \rho^{\mathbf{G}\gamma x} \bar{R} \theta . \qquad (46)$$

The mixture energy balance equation (30) can be rearranged and evaluated considering the restrictions for the specific entropies as well as the stresses given in (31). Therefore the stress terms have to be rearranged, the mass balances for solid and overall gas (25), (26) (the last one formulated in terms of the gas concentration

balances (27)) have to be inserted as well as the constitutive relation for the interaction terms (39)$_3$. This yields the formulation

$$
\begin{aligned}
& \theta[\rho^{\mathbf{S}}(\eta^{\mathbf{S}})'_{\mathbf{S}} + \textstyle\sum_\gamma \rho^{\mathrm{G}\gamma}(\eta^{\mathrm{G}\gamma})'_{\mathrm{G}\gamma}] + \operatorname{div}\mathbf{q} = \\
& -\textstyle\sum_\gamma \hat{\mathbf{p}}_{\mathrm{E}}^{\mathrm{G}\gamma} \cdot \mathbf{w}_{\mathrm{G}\gamma\mathbf{S}} - \sum_\gamma \hat{\rho}^{\mathrm{G}\gamma}[\psi^{\mathrm{G}\gamma} + \frac{\mathrm{p}^{\mathrm{G}\gamma}}{\rho^{\mathrm{G}\gamma\mathrm{x}}} + \theta\eta^{\mathrm{G}\gamma}] .
\end{aligned}
\tag{47}
$$

Taking a closer look to the mass production term, again the specific Gibbs energy $\Psi^{\mathrm{G}\gamma} = \mu^{\mathrm{G}\gamma}$ can be identified with (cf. (40))

$$
\Psi^{\mathrm{G}\gamma} = \psi^{\mathrm{G}\gamma} + \frac{\mathrm{p}^{\mathrm{G}\gamma}}{\rho^{\mathrm{G}\gamma\mathrm{x}}} ,
\tag{48}
$$

cf. [19], so that the mass production term reads

$$
\textstyle\sum_\gamma \hat{\rho}^{\mathrm{G}\gamma}\left[\Psi^{\mathrm{G}\gamma} + \theta\eta^{\mathrm{G}\gamma}\right] = \sum_\gamma \hat{\rho}^{\mathrm{G}\gamma}\left[\mathrm{h}^{\mathrm{G}\gamma}\right] ,
\tag{49}
$$

where the definition for the specific free enthalpy $\mathrm{h}^{\mathrm{G}\gamma} = \Psi^{\mathrm{G}\gamma} + \theta\eta^{\mathrm{G}\gamma}$ has been used. The free enthalpies are connected with the gas conversion term $\hat{\rho}^{\mathrm{G}\gamma}$, so that it gets clear that the exothermic part of the methane oxidation equation (1) is governed with this part.

The methane oxidation equation is modelled via the stoichiometric coefficients identified as the material parameters δ^{GO} and δ^{GC} given in (39)$_{1,2}$, where the differences of the chemical potentials have to reveal the methane conversion rate with

$$
\hat{\rho}^{\mathrm{GM}} \stackrel{!}{=} (\mu^{\mathrm{GM}} - \mu^{\mathrm{GO}}) \stackrel{!}{=} (\mu^{\mathrm{GM}} - \mu^{\mathrm{GC}}) .
\tag{50}
$$

With that and in accordance to (1), the biological methane oxidation is modelled via

$$
\hat{\rho}^{\mathrm{GO}} = +2\,\hat{\rho}^{\mathrm{GM}} , \quad \hat{\rho}^{\mathrm{GC}} = -1\,\hat{\rho}^{\mathrm{GM}} ,
\tag{51}
$$

where the methane oxidation rate is postulated as

$$
\hat{\rho}^{\mathrm{GM}} = -\hat{\rho}^{\mathrm{GM}}_{\max}\,\hat{\rho}^{\mathrm{GM}}_{\mathrm{GM}}\,\hat{\rho}^{\mathrm{GM}}_{\mathrm{GO}}\,\hat{\rho}^{\mathrm{GM}}_{\theta} .
\tag{52}
$$

Here, $\hat{\rho}^{\mathrm{GM}}_{\max}$ describes the maximum degradation rate, which is temperature dependent represented by the function $\hat{\rho}^{\mathrm{GM}}_{\theta}$ and reduced by the limiting substrate functions for methane $\hat{\rho}^{\mathrm{GM}}_{\mathrm{GM}}$ and oxygen $\hat{\rho}^{\mathrm{GM}}_{\mathrm{GO}}$. The maximum oxidation rate is calculated with

$$
\hat{\rho}^{\mathrm{GM}}_{\max} = \mathrm{V}_{\max}\,\rho^{\mathbf{SR}} ,
\tag{53}
$$

where for V_{max} with the unit [mol/(kg s)] literature reported values depending on the given environmental conditions are taken. For the limiting functions $\hat{\rho}_{GM}^{GM}$ and $\hat{\rho}_{GO}^{GM}$ dual-substrate Michaelis–Menten kinetics are used with

$$\hat{\rho}_{GM}^{GM} = \frac{c^{GM}}{c^{GM} + K_{CH_4}}, \quad \hat{\rho}_{GO}^{GM} = \frac{c^{GO}}{c^{GO} + K_{O_2}} . \tag{54}$$

Here, c^{GM} and c^{GO} are the methane and oxygen concentrations in [vol.]% and K_{CH_4} and K_{O_2} the half saturation constants. The temperature dependence function $\hat{\rho}_\theta^{GM}$ is given with

$$\hat{\rho}_\theta^{GM} = \exp\left[-\kappa(\theta - \theta_{opt})^2\right], \tag{55}$$

revealing a lower oxidation rate with deviating temperatures from the optimum, cf. [21].

With the following postulated ansatz for the material parameter of the extra terms of the interaction forces

$$\delta_{\mathbf{w}_{G\gamma S}} = \frac{(n^{\mathbf{G}})^2 \, c_{mol}^{G\gamma}}{c_{mol}^{G\gamma} \, k_{adv} + d_{diff}} , \tag{56}$$

implemented into the momentum balance of the gas components (29) via (39)$_3$ and (40)$_2$, a formulation for the overall molar gas flux $\mathbf{j}^{G\gamma}$ with reference to the solid velocity $\mathbf{x}'_{\mathbf{S}}$ is derived with

$$n^{\mathbf{G}} c_{mol}^{G\gamma} \mathbf{w}_{G\gamma S} = -c_{mol}^{G\gamma} k_{adv} \, \text{grad} \, p^{G\gamma} - d_{diff} \, \text{grad} \, p^{G\gamma} , \tag{57}$$

cf. (27). Here it becomes clear that the overall gas flux can be additively divided into an advective ($\mathbf{j}_{adv}^{G\gamma} = -c_{mol}^{G\gamma} k_{adv} \, \text{grad} \, p^{G\gamma}$) and a diffusive part ($\mathbf{j}_{diff}^{G\gamma} - d_{diff} \, \text{grad} \, p^{G\gamma}$). The advective flow part, which describes the overall gas flow relative to the solid's movement with $\mathbf{w}_{GS}$, can be described with Darcy's law transferred to porous media with

$$\mathbf{j}_{adv}^{G\gamma}/c_{mol}^{G\gamma} = n^{\mathbf{G}} \mathbf{w}_{GS} = -\frac{K^{\mathbf{S}}}{\eta^{\mathbf{G}}} \left[\text{grad} p^{G\gamma}\right], \tag{58}$$

where the permeability k_{adv} is defined as the intrinsic permeability of the soil K^S [m^2] divided by the dynamic viscosity of the gas mixture $\eta^{\mathbf{G}}$ [Ns/m^2]. The diffusive part which describes the gas component's movement relative to the overall gas flow with $\mathbf{w}_{G\gamma G}$ is modelled in accordance to Fick's law of diffusion with

$$\mathbf{j}_{diff}^{G\gamma} = n^{\mathbf{G}} c_{mol}^{G\gamma} \mathbf{w}_{G\gamma G} = d_{diff} \left[\text{grad} p^{G\gamma}\right]. \tag{59}$$

In combination with (46) and d_{diff} chosen as

$$d_{\text{diff}} = \frac{D_{G\gamma}}{R\,\theta}\,, \tag{60}$$

(59) yields

$$n^{\mathbf{G}} c_{\text{mol}}^{G\gamma} \mathbf{w}_{G\gamma \mathbf{G}} = D_{G\gamma} \left[\text{grad} c_{\text{mol}}^{G\gamma}\right]. \tag{61}$$

5 Governing Equations and Numerical Treatment

Taking into account the assumptions from Sect. 3, the constitutive relations from Sect. 4 as well as the saturation condition and the expressions for the partial densities $\rho^{\boldsymbol{\alpha}} = n^{\boldsymbol{\alpha}} \rho^{\boldsymbol{\alpha}R}$ the remaining unknown quantities are

$$\mathcal{R} = \mathcal{R}(\mathbf{x}, t) = \left\{ \mathbf{u_S}, p^{\mathbf{GR}}, c_{\text{mol}}^{\text{GM}}, c_{\text{mol}}^{\text{GO}}, c_{\text{mol}}^{\text{GC}}, \theta, \right\}, \tag{62}$$

where $\mathbf{u_S}$ denotes the displacement of the solid phase. Moreover, use has been made of the relation

$$n^{\mathbf{S}} = n_{0\mathbf{S}}^{\mathbf{S}} \det \mathbf{F_S}^{-1} = n_{0\mathbf{S}}^{\mathbf{S}} J_{\mathbf{S}}^{-1} \tag{63}$$

with $n_{0\mathbf{S}}^{\mathbf{S}}$ as the reference volume fraction of the solid phase.

Within the framework of a standard Galerkin procedure weak formulations are formulated to determine the independent fields of the unknown quantities $\mathcal{R}$. The balance equation of momentum and mass, both for the mixture, multiplied with the test function $\delta \mathbf{u_S}$ and $\delta p^{\mathbf{GR}}$, respectively, are used to calculate the displacement $\mathbf{u_S}$ and the overall pore pressure $p^{\mathbf{GR}}$, cf. (64) and (65). For the calculation of the molar concentrations the concentration balances multiplied with the test function $\delta c_{\text{mol}}^{G\gamma}$ are used, cf. (66), and the energy balance for the mixture multiplied with $\delta \theta$ is used to determine the overall temperature θ, cf. (67). Thus, we gain the following weak formulations of the governing equations:

- Balance of momentum for the mixture

$$\int\limits_{B_S} (\sum_{\alpha}^{S,G} \mathbf{T}^{\boldsymbol{\alpha}}) \cdot \text{grad}\,\delta \mathbf{u_S}\, dv - \int\limits_{B_S} (\sum_{\alpha}^{S,G} \rho^{\boldsymbol{\alpha}})\, \mathbf{b} \cdot \delta \mathbf{u_S}\, dv = \int\limits_{\partial B_S} \{\mathbf{t} \cdot \delta \mathbf{u_S}\}\, da. \tag{64}$$

- Balance of mass for the overall mixture

$$
\int_{B_S} -\{\frac{1}{c_{mol}^G} \sum_\gamma \mathbf{j}^{G\gamma} \cdot \operatorname{grad} \delta p^{GR}\} \, dv + \int_{B_S} \{\operatorname{tr} \mathbf{D_S} + \frac{n^G}{c_{mol}^G} \sum_\gamma (c_{mol}^{G\gamma})'_{G\gamma}\} \, \delta p^{GR} \, dv
$$
$$
= \int_{\partial B_S} -\{\frac{1}{c_{mol}^G} \sum_\gamma \mathbf{j}^{G\gamma} \cdot \mathbf{n}\} \, \delta p^{GR} \, da. \tag{65}
$$

- Balance of mass for the concentrations for $\gamma = \{M, O, C\}$

$$
\int_{B_S} \{n^G (c_{mol}^{G\gamma})'_S + c_{mol}^{G\gamma}(n^G)'_S\} \, \delta c_{mol}^{G\gamma} \, dv - \int_{B_S} \{\mathbf{j}^{G\gamma} \cdot \operatorname{grad} \delta c_{mol}^{G\gamma}\} \, dv +
$$
$$
\int_{B_S} \{c_{mol}^{G\gamma} n^G \operatorname{tr} \mathbf{D_S} - \hat{\rho}_{mol}^{G\gamma}\} \, \delta c_{mol}^{G\gamma} \, dv = \int_{\partial B_S} \{\mathbf{j}^{G\gamma} \delta c_{mol}^{G\gamma} \cdot \mathbf{n}\} \, da. \tag{66}
$$

- Balance of energy for the mixture

$$
\int_{B_S} \{\theta \rho^S (\eta^S)'_S\} \, \delta\theta \, dv + \int_{B_S} \{\theta \sum_\gamma \rho^{G\gamma}(\eta^{G\gamma})'_{G\gamma}\} \, \delta\theta \, dv
$$
$$
- \int_{B_S} \{\mathbf{q} \cdot \operatorname{grad} \delta\theta\} \, dv + \int_{B_S} \{\hat{\mathbf{p}}_E^{G\gamma} \cdot \mathbf{w}_{G\gamma S}\} \, \delta\theta \, dv + \int_{B_S} \{\sum_\gamma \hat{\rho}^{G\gamma} h^{G\gamma}\} \, \delta\theta \, dv \tag{67}
$$
$$
= \int_{\partial B_S} \{\mathbf{q} \, \delta\theta \cdot \mathbf{n}\} \, da.
$$

For each unknown quantity $\mathcal{R}$ we can either apply Dirichlet or Neumann boundary conditions on ∂B_S, see Fig. 5; in the sequence of above-mentioned balance equations they read:

– displacement $\mathbf{u_S}$ or mechanical force $\mathbf{t}$
– pore pressure p^{GR} or gas flux $n^G \mathbf{w}_{GS}$

Fig. 5 Scheme of Dirichlet ($\mathbf{u_S}$, p^{GR}, $c^{G\gamma}$, θ) and Neumann ($\mathbf{t}$, $n^G \mathbf{w}_{GS}$, $\mathbf{j}^{G\gamma}$, $\mathbf{q}$) boundary conditions
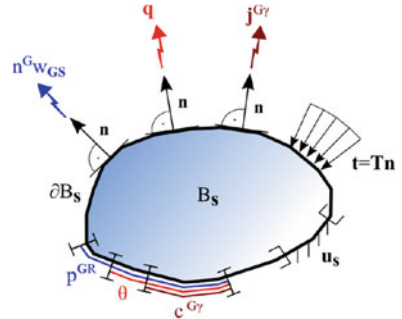
– molar concentration via $c_{mol}^{G\gamma}$ or molar flux $\mathbf{j}^{G\gamma}$
– temperature θ or heat flux $\mathbf{q}$

The weak formulations are implemented into the finite element program FEAP [32] using Taylor–Hood elements for discretization.

6 Experiment and Numerical Simulations

For verification and parameter fitting an experimental setting for a landfill cover system developed in [26] was used. The experimental setup enables the visualization of the so-called methane horizon via thermal imaging. The methane horizon describes a small range within the cover layer, where a steady state of methane oxidation is adjusted and the bacteria are supplied with a continuous flow of methane and oxygen in optimal conditions, see Fig. 6. Since methanotrophic bacteria emit energy in form of heat as a by-product of their metabolism, cf. (1), this effect can be related to bacterial activity and utilized to locate the position of the oxidation horizon in a reaction vessel. Figure 7 shows the technical installation of the experiment, which allows the monitoring of the heat distribution within a soil system.

The reaction vessel consists of a steel frame with dimensions of 200×150 cm, which is closed by two plexiglass plates (each 200×150 cm) on the front and the back with a gap of 12 cm between the plates. The spacing is filled with 0.26 m^3 top soil (water content 9.7% w/w, organic dry substance 2.2%) leading to a height of about 110 cm (Fig. 7-(10)) above a gas distribution layer of 15 cm, cf. Fig. 7-(9). The residual volume above the soil (Fig. 7-(11)) section acts as atmosphere and is flushed by air from a mass flow controller (MFC). The flow of the synthetic landfill gas is regulated and also recorded by a mass flow controller. The mixture of methane and carbon dioxide is humidified and fed into the gas distribution layer via ten separate ports. With that, realistic conditions from the landfill cover layer can be reproduced. A thermographic camera (testo 875-1i, Testo SE & Co. KGaA, Lenzkirch, Germany, 320×240 pixel) was installed in front of the reaction vessel,

Fig. 6 Schematic of oxidation horizon within the cover layer
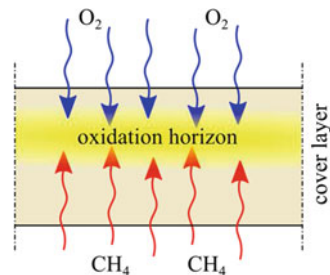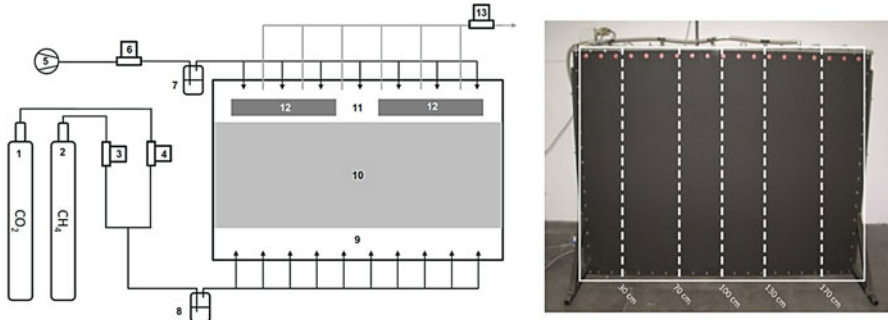
Fig. 7 Experimental setup. Left: schematic figure, (1) carbon dioxide supply, (2) methane supply, (3) MFC for CH_4, (4) MFC for CO_2, (5) compressor, (6) MFC for air, (7+8) humidifier, (9) gas distribution layer, (10) soil section, (11) atmospheric gas phase, (12) heat exchanger, (13) MFM for air, (14) off-gas. Right: Front of the blackened plexiglass plate with marked area for thermal imaging, broken lines indicate sampling profiles
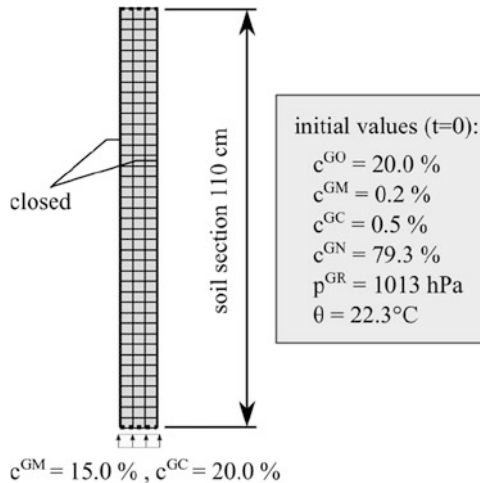
Fig. 8 FE-mesh and Dirichlet boundary-value problem

thus, the front plexiglass plate was blackened in order to achieve a high resolution of the pictures and eliminate reflections.

Although the experiment yields slightly varying distributions for concentration profiles or temperature across the different sampling ports due to natural inhomogeneities of the soil, only one exemplary sampling port was chosen for the numerical simulation. Hence, it was not necessary to consider the whole width of the plate, and just a part of 0.1 m thickness was modelled. Figure 8 reveals the investigated initial boundary-value problem.

The gas distribution layer as well as the atmospheric gas layer (cf. Fig. 7) serve as Dirichlet boundary conditions and are not modelled explicitly. The amounts of methane and carbon dioxide of the gas mixture were measured at the inflow to the soil section during the experiment, so that a constant average value of $c^{GM} = 15.0$ vol.% for methane and $c^{GC} = 20.0$ vol.% for carbon dioxide was applied to reveal the experimental conditions. The horizontal upper and lower boundaries are held permeable, whereas the vertical sides are impermeable for all degrees of freedom. As an exception the lower horizontal boundary is closed for oxygen and heat exchange. The whole model is initiated (time $t = 0$) with atmospheric conditions for pressure and concentrations, and with an initial surrounding temperature of 22.3 °C (taken from experimental data), cf. Fig. 8. These values and further chosen material parameters can be observed in Table 1, where $(...)_0$ indicates the initial value at simulation time $t = 0$.

The experimental reactor vessel was monitored over several days. In the beginning, a tolerably homogeneous temperature distribution over the soil section corresponding to the room temperature of about $\theta = 23$ °C could be observed, see Fig. 9 (left). It turned out that a steady state of the oxidation horizon appeared after approximately 4 days. Figure 9 (right) indicates the bacterial activity at the oxidation horizon with a slight temperature increase at the red zone. The initial higher monitored values over the reactor plate (Fig. 9 (left)) can be explained by slightly varying room temperatures as well as the fact that with the start of methane supply at the beginning of the experiment, the methane oxidation is high across the whole soil section until the initial oxygen is consumed and a steady state has been achieved. Adapting these observations, the overall simulation time was $t = 4$ days. Figure 10 shows the thermal image at the end of simulation time in comparison to the thermal image of the experiment.

The simulation result matches exactly with the thermal image of the reactor plate, which can also be proved with a plot of the temperature against height, cf. Fig. 11. The model values are compared to the average values over the width of the plate taken by the thermographic camera, indicated by the error bars. The experimental data points were taken from the image resolution of the thermal imager, which assigns a temperature to each pixel. One can see that the temperature development within the model lies totally within the scope of the averages. Figure 12 reveals the comparison between the measured values of an experimental sampling profile with the development of calculated values of the model. As already indicated by the heat development, the concentration profiles show also a good correlation, especially hitting the range of the oxidation horizon, where highest bacterial activity is estimated.

Table 1 Initial values and material parameters

Parameter	Symbol	Value	Unit
Volume fraction solid	n_0^S	0.88	–
Volume fraction gas	n_0^G	0.12	–
Concentration CH_4	c_0^{GM}	0.2	[vol.%]
Concentration CO_2	c_0^{GC}	0.5	[vol.%]
Concentration O_2	c_0^{GO}	20.0	[vol.%]
Concentration N_2	c_0^{GN}	79.3	[vol.%]
Density solid	ρ^{SR}	1200	[kg/m^3]
Temperature	θ_0	22.3	[°C]
Pressure	p_0^{GR}	1013.25	[hPa]
Universal gas constant	R	8.3144	[J/(mol K)]
Specific gas constant CH_4	$\bar{R}_M$	518.3	[J/(kg K)]
Specific gas constant CO_2	$\bar{R}_C$	188.9	[J/(kg K)]
Specific gas constant O_2	$\bar{R}_O$	259.8	[J/(kg K)]
Specific gas constant N_2	$\bar{R}_N$	188.9	[J/(kg K)]
Diffusion coefficient CH_4	D_{GM}	6.0E−6	[m^2/s]
Diffusion coefficient CO_2	D_{GC}	1.0E−4	[m^2/s]
Diffusion coefficient O_2	D_{GO}	1.9E−5	[m^2/s]
Diffusion coefficient N_2	D_{GN}	1.3E−5	[m^2/s]
Intrinsic permeability	K^S	10E−14	[m^2]
Dynamic viscosity gas mixture	η^G	13E−6	[Ns/m^2]
Heat dilatation coefficient	α^S	20E−6	[1/K]
Heat conductivity coefficient	$\alpha_{\nabla\theta}$	1.6	[W/(m K)]
Specific heat capacity solid	c_V^S	800	[J/(kg K)]
Specific heat capacity CH_4	c_V^{GM}	2160	[J/(kg K)]
Specific heat capacity CO_2	c_V^{GC}	816	[J/(kg K)]
Specific heat capacity O_2	c_V^{GO}	1000	[J/(kg K)]
Specific heat capacity N_2	c_V^{GN}	930	[J/(kg K)]
Max oxidation rate	V_{max}	7.5E−7	[mol/(kg s)]
Half saturation constant CH_4	K_{CH_4}	0.005	–
Half saturation constant O_2	K_{O_2}	0.001	–
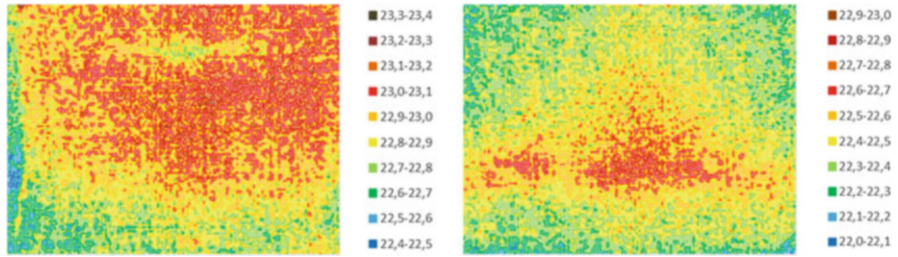
Fig. 9 Thermal image of reactor plate. Left: Contour plot of temperature [°C] at beginning of experiment ($t = 0$). Right: Contour plot of temperature [°C] at day 4 of experiment ($t = 4d$)
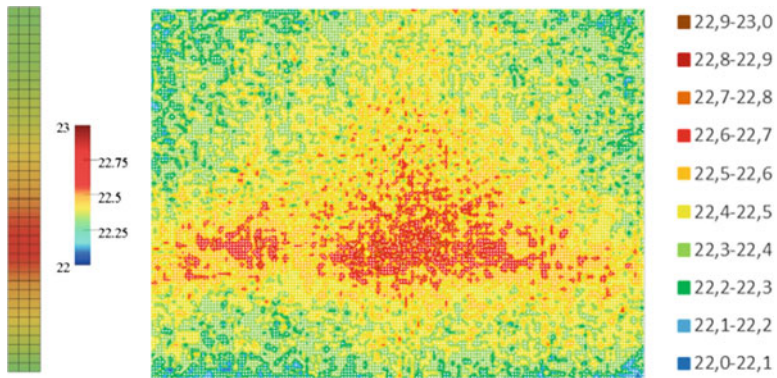
Fig. 10 Comparison between temperature distribution [°C] of simulation (left) and reactor plate (right) after 4 days

7 Conclusions

Besides the measurement and balancing of gas concentrations and conversion rates with batch reactors, which was done in former experiments and successfully simulated with the presented model, cf. [21], the thermal imaging technique is a new helpful tool to visualize the bacterial activity during methane oxidation. This tool is a complementary validation technique to investigate the methane oxidation in cover layers on smaller scales. This was made possible by enhancing the former model by the energy balance equation for the mixture. The presented holistic approach for bio-chemo-thermo coupled conversion processes including finite solid deformation in a continuum mechanical and thermodynamically consistent framework serves as base for future works for simulations on higher scales of the cover layer or generally soil mechanically problems including multi-component gas flows.
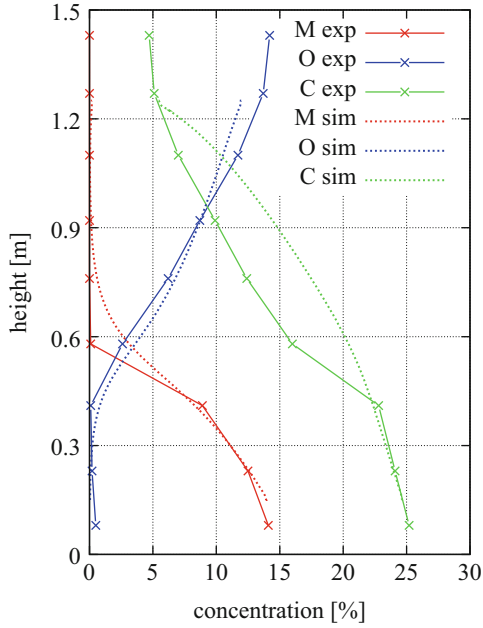
Fig. 11 Concentration profile of simulation (dashed lines) and experiment (continuous lines)

Fig. 12 Temperature profile of simulation (dashed lines) and experiment (measured averages over width of plate, indicated with error bars)
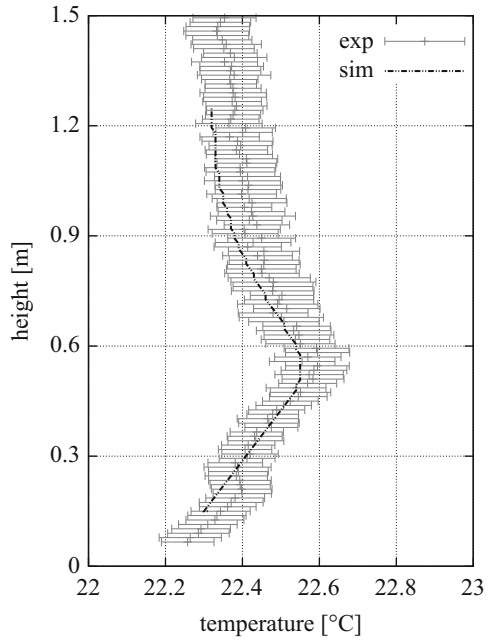
Appendix 1: Kinematics of Porous Media

The homogenized phases $\varphi^{\boldsymbol{\alpha}}$ are composed of particles $X_{\boldsymbol{\alpha}}$. At any time t each spatial point of the current placement is simultaneously occupied by every particle X_S, X_L, X_G of the solid, liquid, and gas phase, whereby each particle proceeds from a different reference position $\mathbf{X}_{\boldsymbol{\alpha}}$ at the time t $= t_0$. Thus, each constituent is assigned to its own independent motion function $\boldsymbol{\chi}_{\boldsymbol{\alpha}}$ with

$$\mathbf{x} = \boldsymbol{\chi}_{\boldsymbol{\alpha}}(\mathbf{X}_{\boldsymbol{\alpha}}, t), \quad \mathbf{X}_{\boldsymbol{\alpha}} = \boldsymbol{\chi}_{\boldsymbol{\alpha}}^{-1}(\mathbf{x}, t),$$

$$\mathbf{x}'_{\boldsymbol{\alpha}} = \frac{\partial \boldsymbol{\chi}_{\boldsymbol{\alpha}}(\mathbf{X}_{\boldsymbol{\alpha}}, t)}{\partial t}, \quad \mathbf{x}''_{\boldsymbol{\alpha}} = \frac{\partial^2 \boldsymbol{\chi}_{\boldsymbol{\alpha}}(\mathbf{X}_{\boldsymbol{\alpha}}, t)}{\partial t^2}. \tag{68}$$

Equation $(68)_1$ is called the Lagrange description of motion, Eq. $(68)_2$ is the inverse map of the motion for a fixed time t, which represents the Euler description. The Euler description develops from the postulation that $\boldsymbol{\chi}_{\boldsymbol{\alpha}}$ is unique and uniquely invertible at any given time t. A mathematically necessary and sufficient condition for the existence of Eq. $(68)_2$ is given, if the Jacobian $J_{\boldsymbol{\alpha}} = \det \mathbf{F}_{\boldsymbol{\alpha}}$ differs from zero with $\mathbf{F}_{\boldsymbol{\alpha}} = \text{Grad}_{\boldsymbol{\alpha}} \boldsymbol{\chi}_{\boldsymbol{\alpha}}$ and its inverse $\mathbf{F}_{\boldsymbol{\alpha}}^{-1} = \text{grad}\,\mathbf{x}_{\boldsymbol{\alpha}}$ as the deformation gradient. "$\text{Grad}_{\boldsymbol{\alpha}}$" denotes the differential operator referring to the reference position $\mathbf{X}_{\boldsymbol{\alpha}}$ of the constituent $\varphi^{\boldsymbol{\alpha}}$, while "grad" refers to the actual position $\mathbf{x}$. During the deformation process, $\mathbf{F}_{\boldsymbol{\alpha}}$ is restricted to $\det \mathbf{F}_{\boldsymbol{\alpha}} > 0$.

The velocity and acceleration vector, cf. $(68)_{3-4}$, are defined with the material time derivatives of the Lagrange description. The material time derivative for scalar fields depending on $\mathbf{x}$ and t with respect to the trajectory of $\varphi^{\boldsymbol{\alpha}}$ is given with $(\ldots)'_{\boldsymbol{\alpha}} = \partial(\ldots) / \partial t + [\text{grad}(\ldots)] \cdot \mathbf{x}'_{\boldsymbol{\alpha}}$.

With $(68)_3$ the material and spatial velocity gradient are defined with

$$(\mathbf{F}_{\boldsymbol{\alpha}})'_{\boldsymbol{\alpha}} = \text{Grad}_{\boldsymbol{\alpha}} \mathbf{x}'_{\boldsymbol{\alpha}}, \quad \mathbf{L}_{\boldsymbol{\alpha}} = (\text{Grad}_{\boldsymbol{\alpha}} \mathbf{x}'_{\boldsymbol{\alpha}}) \mathbf{F}_{\boldsymbol{\alpha}}^{-1} = \text{grad}\,\mathbf{x}'_{\boldsymbol{\alpha}} \tag{69}$$

The tensor $\mathbf{D}_{\boldsymbol{\alpha}} = 1/2\,(\mathbf{L}_{\boldsymbol{\alpha}} + \mathbf{L}_{\boldsymbol{\alpha}}^{\mathsf{T}})$ is defined as the symmetric part of the spatial velocity gradient. An extended explanation of the kinematics of porous media is given in [6] and [9].

Appendix 2: Evaluation of Entropy Inequality

The resultant system of field equations is set up by 29 equations, namely Eqs. (22), (24), (25), (27), (28), (29), (30), as well as the physical constraint $\hat{\mathbf{p}}^S + \sum_{\gamma} \hat{\mathbf{p}}^{G\gamma} = \mathbf{o}$, the partial densities $\rho^S = n^S \rho^{SR}$ and $\rho^G = n^G \rho^{GR}$, respectively. The field equations contain overall 91 scalar field quantities, namely

$$\mathcal{F} = \{\rho^{\mathbf{S}}, \rho^{\mathbf{G}}, \rho^{\mathbf{SR}}, \rho^{\mathbf{GR}}, \mathbf{n}^{\mathbf{S}}, \mathbf{n}^{\mathbf{G}}, \mathbf{c}^{\mathbf{G}}, \mathbf{x}'_{\mathbf{S}}, \mathbf{x}'_{\mathbf{G}\gamma},$$
$$\mathbf{T}^{\mathbf{S}}, \mathbf{T}^{\mathbf{G}\gamma}, \mathbf{b}, \hat{\mathbf{p}}^{\mathbf{S}}, \hat{\mathbf{p}}^{\mathbf{G}\gamma}, \hat{\rho}^{\mathbf{G}\gamma}, \psi^{\mathbf{S}}, \psi^{\mathbf{G}\gamma}, \eta^{\mathbf{S}}, \eta^{\mathbf{G}\gamma}, \mathbf{q}, \theta\}, \tag{70}$$

where the Cauchy stresses $\mathbf{T}^{\mathbf{S}}$ and $\mathbf{T}^{\mathbf{G}\gamma}$ are symmetric. Since the solid phase is assumed to be incompressible and not involved into mass transfer, the real density of the solid is known and stays constant. The gravitational acceleration $\mathbf{b}$ is known as well and nitrogen is not involved into gas exchange, which leads to five known field quantities

$$\mathcal{K} = \{\rho^{\mathbf{SR}}, \mathbf{b}, \hat{\rho}^{\mathbf{GN}}\}. \tag{71}$$

In consequence, 57 field quantities remain for which constitutive relations have to be found. The constitutive quantities are chosen with

$$\mathcal{C} = \{\mathbf{T}^{\mathbf{S}}, \mathbf{T}^{\mathbf{G}\gamma}, \hat{\mathbf{p}}^{\mathbf{G}\gamma}, \hat{\rho}^{\mathbf{GO}}, \hat{\rho}^{\mathbf{GC}}, \psi^{\mathbf{S}}, \psi^{\mathbf{G}\gamma}, \eta^{\mathbf{S}}, \eta^{\mathbf{G}\gamma}, \mathbf{q}\}. \tag{72}$$

In order to provide a thermodynamic consistent description of the material behavior, the entropy inequality for the mixture is evaluated in accordance to [5], which yields restrictions for the constitutive relations. Following the principle of equipresence postulated by [35], the set of constitutive variables (72) can depend on the following process variables

$$\mathcal{P} = \{\mathbf{C}_{\mathbf{S}}, c^{\mathbf{G}\gamma}_{\mathrm{mol}}, \hat{\rho}^{\mathbf{G}\gamma}, \theta, \mathrm{grad}\,\theta, \mathbf{w}_{\mathbf{G}\gamma\mathbf{S}}\}. \tag{73}$$

Here, $\mathbf{C}_{\mathbf{S}} = \mathbf{F}_{\mathbf{S}}^{\mathrm{T}}\mathbf{F}_{\mathbf{S}}$ denotes the right Cauchy–Green deformation tensor. The entropy inequality for the binary model (solid and gas mixture) reads

$$\mathbf{T}^{\mathbf{S}} \cdot \mathbf{D}_{\mathbf{S}} - \rho^{\mathbf{S}}(\psi^{\mathbf{S}})'_{\mathbf{S}} - \rho^{\mathbf{S}}(\theta)'_{\mathbf{S}}\,\eta^{\mathbf{S}} - \hat{\mathbf{p}}^{\mathbf{S}} \cdot \mathbf{x}'_{\mathbf{S}}$$

$$- \sum_{\gamma}[\mathbf{T}^{\mathbf{G}\gamma} \cdot \mathbf{D}_{\mathbf{G}\gamma} - \rho^{\mathbf{G}\gamma}(\psi^{\mathbf{G}\gamma})'_{\mathbf{G}\gamma} - \rho^{\mathbf{G}\gamma}(\theta)'_{\mathbf{G}\gamma}\,\eta^{\mathbf{G}\gamma} - \hat{\mathbf{p}}^{\mathbf{G}\gamma} \cdot \mathbf{x}'_{\mathbf{G}\gamma}] \tag{74}$$

$$- \sum_{\gamma}\hat{\rho}^{\mathbf{G}\gamma}\psi^{\mathbf{G}\gamma} - \frac{1}{\theta}\mathbf{q}\,\mathrm{grad}\,\theta \geq 0$$

It will be enhanced by the constraining saturation condition with the Lagrange multiplicator λ with

$$\lambda\left((\mathbf{n}^{\mathbf{S}})'_{\mathbf{S}} + (\mathbf{n}^{\mathbf{G}})'_{\mathbf{S}}\right). \tag{75}$$

The overall gas balance in terms of molar concentration solved for $(\mathbf{n}^{\mathbf{G}})'_{\mathbf{S}}$ reads

$$(n^{\mathbf{G}})'_{\mathbf{S}} = -\frac{n^{\mathbf{G}}}{c^{\mathbf{G}}_{mol}} \sum_\gamma (c^{G\gamma}_{mol})'_{G\gamma} - n^{\mathbf{G}} \sum_\gamma x^{G\gamma}_{mol} \mathbf{D}_{G\gamma} \cdot \mathbf{I}$$

$$- \operatorname{grad} n^{\mathbf{G}} \sum_\gamma x^{G\gamma}_{mol} \cdot \mathbf{w}_{G\gamma S} + \sum_\gamma \frac{\hat{\rho}^{G\gamma}_{mol}}{c^{\mathbf{G}}_{mol}} \cdot \tag{76}$$

A mass specific Helmholtz free energy $\psi^{G\gamma}$ for the partial gas components is introduced with

$$\rho^{G\gamma} \psi^{G\gamma} = n^{\mathbf{G}} \rho^{G\gamma x} \psi^{G\gamma} = n^{\mathbf{G}} \psi^{G\gamma x}. \tag{77}$$

For simplification we postulate that the Helmholtz free energy functions $\psi^{\boldsymbol{\alpha}}$ hold the following dependencies

$$\psi^{\mathbf{S}} = \psi^{\mathbf{S}}(\mathbf{C_S}, \theta)$$

$$\psi^{G\gamma x} = \psi^{G\gamma x}(\rho^{G\gamma x}, \theta). \tag{78}$$

With the chosen dependencies of the Helmholtz free energy functions on the process variables, the material time derivatives $(\psi^{\boldsymbol{\alpha}})'_{\boldsymbol{\alpha}}$ read

$$\psi^{\mathbf{S}} := \psi^{\mathbf{S}}(\mathbf{C_S}, \theta) \quad \Rightarrow \quad (\psi^{\mathbf{S}})'_{\mathbf{S}} = 2\,\rho^{\mathbf{S}} \mathbf{F_S} \frac{\partial \psi^{\mathbf{S}}}{\partial \mathbf{C_S}} \mathbf{F}^{\mathsf{T}}_{\mathbf{S}} \cdot \mathbf{D_S} + \frac{\partial \psi^{\mathbf{S}}}{\partial \theta}(\theta)'_{\mathbf{S}}$$

$$\psi^{G\gamma x} := \psi^{G\gamma x}(\rho^{G\gamma x}, \theta) \quad \Rightarrow \quad (\psi^{G\gamma x})'_{G\gamma} = \frac{\partial \psi^{G\gamma x}}{\partial \rho^{G\gamma x}}(\rho^{G\gamma x})'_{G\gamma} + \frac{\partial \psi^{G\gamma x}}{\partial \theta}(\theta)'_{G\gamma}, \tag{79}$$

the entropy inequality finally reads (sorted by the process variables and their derivatives):

$$[\mathbf{T^S} + n^{\mathbf{S}}\lambda \mathbf{I} - 2\rho^{\mathbf{S}} \mathbf{F_S} \frac{\partial \psi^{\mathbf{S}}}{\partial \mathbf{C_S}} \mathbf{F}^{\mathsf{T}}_{\mathbf{S}}] \cdot \mathbf{D_S} - \rho^{\mathbf{S}}[\eta^{\mathbf{S}} + \frac{\partial \psi^{\mathbf{S}}}{\partial \theta}](\theta)'_{\mathbf{S}} +$$

$$\sum_\gamma ([\mathbf{T}^{G\gamma} + n^{\mathbf{G}}x^{G\gamma}\lambda \, \mathbf{I}] \cdot \mathbf{D}_{G\gamma} - \rho^{G\gamma}[\eta^{G\gamma} + \frac{1}{\rho^{G\gamma x}}\frac{\partial \psi^{G\gamma x}}{\partial \theta}](\theta)'_{G\gamma} +$$

$$[x^{G\gamma}\lambda \frac{\rho^{G\gamma}}{(\rho^{G\gamma x})^2} + \frac{\rho^{G\gamma}}{(\rho^{G\gamma x})^2}\psi^{G\gamma x} - \frac{\rho^{G\gamma}}{\rho^{G\gamma x}}\frac{\partial \psi^{G\gamma x}}{\partial \rho^{G\gamma x}}](\rho^{G\gamma x})'_{G\gamma} - \tag{80}$$

$$[\hat{\mathbf{p}}^{G\gamma} - \operatorname{grad} n^{\mathbf{G}}x^{G\gamma}\lambda] \cdot \mathbf{w}_{G\gamma S} - \hat{\rho}^{G\gamma}[\psi^{G\gamma} + \frac{x^{G\gamma}\lambda}{\rho^{G\gamma x}}]) - \frac{1}{\theta}\mathbf{q}\operatorname{grad}\theta \geq 0.$$

The evaluation of the restrictions for the constitutive relations is presented in Sect. 4.

References

1. *Climate Change 2013: The Physical Science Basis. Contribution of Working Group I to the Fifth Assessment Report of the Intergovernmental Panel on Climate Change*. Cambridge University Press, Cambridge, United Kingdom and New York, 2013.

2. J. Bluhm. Modelling of saturated thermo-elastic porous solids with different phase temperatures. In W. Ehlers and J. Bluhm, editors, *Porous media: Theory, Experiments and Numerical Applications*, pages 87–118. Springer-Verlag, Berlin - Heidelberg - New York, 2002.

3. R. M. Bowen. Toward a thermodynamics and mechanics of mixtures. *Archives for Rational Mechanics and Analysis*, 24:370–403, 1967.

4. R. M. Bowen. Theory of mixtures. In A. C. Eringen, editor, *Continuum Physics*, volume III, pages 1–127. Academic Press, New York, 1976.

5. B. D. Coleman and W. Noll. The thermodynamics of elastic materials with heat conduction and viscosity. *Archives for Rational Mechanics and Analysis*, 13:167–178, 1963.

6. R. de Boer. *Theory of Porous Media – highlights in the historical development and current state*. Springer-Verlag, Berlin, 2000.

7. A. Ebigbo, R. Helmig, A. B. Cunningham, H. Class, and R. Gerlach. Modelling biofilm growth in the presence of carbon dioxide and water flow in the subsurface. *Advances in Water resources*, 33:762–781, 2010.

8. W. Ehlers. Poröse Medien – ein kontinuumsmechanisches Modell auf der Basis der Mischungstheorie. Technical Report 47, Universität-GH Essen, 1989.

9. W. Ehlers. Foundations of multiphasic and porous materials. In W. Ehlers and J. Bluhm, editors, *Porous Media: Theory, Experiments and Numerical Applications*, pages 3–86. Springer-Verlag, Berlin, 2002.

10. S. Feng, C. W. W. Ng, A. K. Leung, and H. W. Liu. Numerical modelling of methane oxidation efficiency and coupled water-gas-heat reactive transfer in a sloping landfill cover. *Waste Management*, 68:355–368, 2017.

11. F. Golfier, B. D. Wood, L. Orgogozo, and M. Bus. Biofilms in porous media: Development of macroscopic transport equations via volume averaging with closure for local mass equilibrium conditions. *Advances in Water Resources*, 32:463–485, 2009.

12. C. V. Hettiarachchi, P. J. Hettiaratchi, A. K. Mehrotra, and S. Kumar. Field-scale operation of methane bio filtration systems to mitigate point source methane emissions. *Environmental Pollution*, 159 (6):1715–1720, 2011.

13. H. A. Hilger, D. F. Cranford, and M. Barlaz. Methane oxidation and microbial exopolymer production in landfill cover soil. *Soil Biology & Biochemistry*, 23:457–467, 2000.

14. H. A. Hilger, S. K. Liehr, and M. Barlaz. Exopolysaccharide control of methane oxidation in landfill cover soil. *Journal of Environmental Engineering*, 23:457–467, 1999.

15. M. Humer and P. Lechner. Deponiegasentsorgung von Altlasten mit Hilfe von Mikroorganismen. In *sterreichische Wasser- und Abfallwirtschaft*, number Heft 7/8 in 49. Jahrgang, pages 164–171. Springer-Verlag KG, Wien, 1997.

16. S. Molins and K. U. Mayer. Coupling between geochemical reactions and multicomponent gas and solute transport in unsaturated media: A reactive transport modeling study. *Water Resources Research*, 43(W05435), 2007.

17. S. Molins, K. U. Mayer, C. Scheutz, and P. Kjeldsen. Transport and reaction processes affecting the attenuation of landfill gas in cover soils. *Journal of Environmental Quality*, 37:459–468, 2008.

18. C. W. W. Ng, S. Feng, and H. W. Liu. A fully coupled model for water-gas-heat-reactive transport with methane oxidation in landfill covers. *Science of the Total Environment*, 508:307–319, 2015.

19. T. Ricken and J. Bluhm. Modeling of liquid and gas saturated porous solids under freezing and thawing cycles. In T. Schanz and A. Hettler, editors, *Aktuelle Forschung in der Bodenmechanik 2013*, chapter 2, pages 23–42. Springer-Verlag Berlin Heidelberg, 2014.

20. T. Ricken and R. de Boer. Multiphase flow in a capillary porous medium. *Computational Materials Science*, 28:704–713, 2003.

21. T. Ricken, A. Sindern, J. Bluhm, M. Denecke, T. Gehrke, and T. C. Schmidt. Concentration driven phase transitions in multiphase porous media with application to methane oxidation in landfill cover layers. *Journal of Applied Mathematics and Mechanics*, 94(7–8):609–622, 2014.

22. T. Ricken and V. Ustohalova. Modeling of thermal mass transfer in porous media with applications to the organic phase transition in landfills. *Computational Materials Science*, 32:498–508, 2005.

23. T. Ricken, N. Waschinsky, and D. Werner. Simulation of steatosis zonation in liver lobule - a continuummechanical bi-scale, tri-phasic, multicomponent approach. In *Biomedical Technology*, pages 15–33. Springer, 2018.

24. T. Ricken, D. Werner, H. Holzhütter, M. König, and U. D. und O. Dirsch. Modeling function–perfusion behavior in liver lobules including tissue, blood, glucose, lactate and glycogen by use of a coupled two-scale PDE–ODE approach. *Biomechanics and Modeling in Mechanobiology*, 14(3):515–536, 2015.

25. M. Robeck, T. Ricken, and R. Widmann. A finite element simulation of biological conversion processes in landfills. *Waste Management*, 31:663–669, 2011.

26. M. Schulte, M. A. Jochmann, T. Gehrke, A. Thom, T. Ricken, M. Denecke, and T. C. Schmidt. Characterization of methane oxidation in a simulated landfill cover system by comparing molecular and stable isotope mass balances. *International Journal of Environment and Waste Management*, 69:281–288, 2017.

27. J. C. Simo and K. S. Pister. Remarks on rate constitutive equations for finite deformation problems: Computational implications. *Computer Methods in Applied Mechanics and Engineering*, 46 (2):201–215, 1984.

28. A. Sindern, T. Ricken, J. Bluhm, M. Denecke, and T. C. Schmidt. Phase transition in methane oxidation layers - a coupled FE multiphase description. *Proceedings of Applied Mathematics and Mechanics*, 12:371–372, 2012.

29. A. Sindern, T. Ricken, J. Bluhm, R. Widmann, and M. Denecke. Bacterial methane oxidation in landfill cover layers - a coupled FE multiphase description. *Proceedings of Applied Mathematics and Mechanics*, 13:193–194, 2013.

30. A. Sindern, T. Ricken, J. Bluhm, R. Widmann, M. Denecke, and T. Gehrke. A coupled multi-component approach for bacterial methane oxidation in landfill cover layers. *Proceedings of Applied Mathematics and Mechanics*, 14:469–470, 2014.

31. V. B. Stein, J. P. A. Hettiratchi, and G. Achari. Numerical model for biological oxidation and migration of methane in soils. *Practice Periodical ofHazardous, Toxic, and Radioactive Waste Management*, 5 (4):225–234, 2001.

32. R. L. Taylor. *FEAP - A Finite Element Analysis Program*, 2012.

33. K. Terzaghi. *Theoretical Soil Mechanics*. J. Wiley and Sons, inc., 1943.

34. A. Thom, T. Ricken, J. Bluhm, R. Widmann, M. Denecke, and T. Gehrke. Validation of a coupled FE-model for the simulation of methane oxidation via thermal imaging. *Proceedings of Applied Mathematics and Mechanics*, 15:433–434, 2015.

35. C. Truesdell. *Rational Thermodynamics*. Springer-Verlag, Berlin - Heidelberg - New York, 2 edition, 1984.

36. V. Ustohalova, T. Ricken, and R. Widmann. Estimation of landfill emission lifespan using process oriented modeling - decompositions and transport processes. *Waste Management*, 26 (4):442–450, 2006.

37. A. D. Visscher and O. V. Cleemput. Simulation model for gas diffusion and methane oxidation in landfill cover soils. *Waste Management*, 23:581–591, 2003.

38. Q. Xue, Y. Zhao, Z. Li, and L. Liu. Numerical simulation on the cracking and failure law of compacted clay lining in landfill closure cover system. *International Journal for Numerical and Analytical Methods in Geomechanics*, 38:1556–1584, 2014.

Elasticity and Mechanical Behaviour of Granular Materials: Some Insights from Numerical Studies of Simple Systems

Jean-Noël Roux, Mohamed Hassan Khalili, Francesco Froiio, and Chloé Dequeker

Abstract We briefly review the elastic properties of granular materials, as explored in numerical studies of simple model materials by the "discrete element method" (DEM). Elastic or quasielastic responses are obtained as stable contact networks are probed with negligible friction effects. Elastic moduli, at the macroscopic scale, or contact stiffnesses at the contact network scale, have very limited influence on macroscopic constitutive laws ruling quasistatic deformation and inertial flow. The elastic moduli nevertheless provide useful indirect information on internal variables such as coordination and fabric. Singularities in the tensor of elastic moduli are related to the proximity of failure in the microscopic sense (contact network) but not in the macroscopic sense (yield condition). Elastic properties are also useful in the characterization of the directional dependence of incremental stress-strain response, a key ingredient in the identification of instabilities causing localization phenomena.

Keywords Granular materials · Elasticity · Elastoplasticity · Numerical simulation

1 Introduction

Elasticity is often dealt with as an essential ingredient in mechanical models of granular materials [1]. Micromechanical approaches classically involve contact elasticity, combined with friction and viscous dissipation [2]. Macroscopic constitutive laws for granular soils are often assumed in elastoplastic form [3–5], even though the identification of the parameters of such laws might be delicate and the truly elastic range of material behaviour is restricted to very small strains [6].

J.-N. Roux (✉) · M. H. Khalili
Université Paris EST, Laboratoire Navier, Marne-la-Vallée, France
e-mail: jean-noel.roux@ifsttar.fr

F. Froiio · C. Dequeker
Laboratoire de Tribologie et Dynamique des Systèmes, École Centrale de Lyon, Écully, France

Measurements of elastic moduli associated with a linear response to small load or strain increments about well-equilibrated states of grain packs, under controlled confining stress, have quite often been reported in the geomechanics or physics literature, as obtained via static stress-strain relations [7–11], or dynamical means: resonance modes [12–14], or sound propagation [7, 9–11, 14–18]. Those moduli, as probed for typical strain increments of order 10^{-5} or 10^{-6}, differ from the "elastic" ingredients of constitutive laws [4, 6], which are used in practice for considerably larger strains (say, of order 10^{-3} or 10^{-2}).

Numerical simulation studies of model materials, using the "discrete element method" (or DEM), like many experimental studies or modelling attempts, very often investigate either the elastic moduli of equilibrated grain packs under prescribed stresses [19, 20] or the solid material quasistatic rheology [21], thus considering both strain domains separately. Furthermore, numerical studies of elastic properties often focussed on isotropic states, and their sensitivity to the proximity of a "jamming" threshold (transition to a solid-like material resisting shear stress) [22–25], with considerably fewer investigations of anisotropic configurations [26–28]. And, on the other hand, although quite a few DEM studies have successfully explored the moderate to large strain regime associated with particle rearrangements [29–31] with the "Contact Dynamics" method [32, 33], in which grains are dealt with as perfectly rigid and contacts are devoid of elasticity, the theoretical approach known as Granular Solid Hydrodynamics [34, 35] (evoked in [1]) attributes a basic role to an elastic instability in the macroscopic material yield.

It seems thus necessary to better explore and clarify the role of the elastic ingredients of a granular model, and the connections between elastic moduli and constitutive laws or internal material states.

The present paper proposes a contribution to these issues, based on an overview of DEM studies [28, 36–42] of assemblies of spherical beads, with elasticity and friction in their contacts, but devoid of cohesion. The model material and computation methods are described in Sect. 2. The material is subjected to different kinds of loads, and the resulting characteristic behaviours are briefly reviewed in Sect. 3. We then turn to the connections between elastic properties and material state and mechanical properties, first for isotropic and oedometric loading, in which the stresses essentially vary in intensity, in Sect. 4; then for triaxial compression, in which the direction of stresses and the internal state evolve towards failure and plastic flow (Sect. 5). Sect. 6 is a report on some preliminary results in the modelling of non-elastic strains. Some concluding remarks are given in the final part of the chapter, Sect. 7.

2 Model Material and Simulation Procedures

2.1 System and Contact Laws

Spherical beads of diameter a interact via elasticity and friction, with friction coefficient $\mu = 0.3$, supplemented by viscous dissipation in their contacts. Contact elasticity, as in Ref. [36], is modelled with a simplified version of the Hertz-Mindlin law [43]. Specifically, the normal force F_{ij}^N in the contact between beads i and j, the centres of which are located at $\mathbf{r}_i$ and $\mathbf{r}_j$, depends on contact deflection $h_{ij} = a - ||\mathbf{r}_j - \mathbf{r}_i||$, as

$$F_{ij}^N = \frac{\tilde{E}\sqrt{a}}{3} h_{ij}^{3/2}, \tag{1}$$

in which notation $\tilde{E} = E/(1 - \nu^2)$ is introduced, combining the Young modulus E and the Poisson ratio ν of the solid material within the beads. Equation (1) entails that the normal stiffness expressing the response to small variations of deflection $|h_{ij}|$ in the contact varies as

$$K_{ij}^N = \frac{\tilde{E}\sqrt{a}}{2} |h_{ij}|^{1/2} = \frac{3^{1/3}}{2} \tilde{E}^{2/3} a^{1/3} \left(F_{ij}^N \right)^{1/3}. \tag{2}$$

The tangential elastic force $\mathbf{F}_{ij}^T$ [36, 42] is incrementally related to the relative tangential displacement $\delta\mathbf{u}_{ij}^T$ in the contact, by the stiffness coefficient K^T, assumed proportional to K^N:

$$d\mathbf{F}_{ij}^T = K_{ij}^T d\left(\delta\mathbf{u}_{ij}^T\right), \text{ with } K_{ij}^T = \frac{2 - 2\nu}{2 - \nu} K_{ij}^N. \tag{3}$$

Tangential stiffness K^T should be suitably rescaled whenever the normal elastic force decreases, in order to avoid spurious elastic energy creation [36, 44].

The Coulomb condition enforces inequality $||\mathbf{F}_{ij}^T|| \leq \mu F_{ij}^N$. As explained in [36, 45], contact forces also have to follow the general motion of the grain pair (maintaining the objectivity of the model).

While all simulations use the elastic properties of glass, $E = 70\,\mathrm{GPa}$ and $\nu = 0.3$, results, if expressed in dimensionless form, exactly apply to all materials sharing the same dimensionless characteristics μ and ν. A normal viscous force is added to the elastic-frictional one [36, 46], corresponding to a very low coefficient of restitution in binary collisions. This viscous ingredient of contact interaction laws is irrelevant in the simulation of quasistatic processes [2]. Most simulations are carried out in samples of 4000 grains and results are averaged over several realizations. Occasional tests with larger samples revealed no significant size effects.

2.2 Loading Procedures

We consider cuboidal simulation cells and apply periodic boundary conditions in all three directions, following the procedure of Refs. [36, 41, 47]. Cell dimensions L_1, L_2, L_3, parallel to the three axes of coordinates (to which correspond basis unit vectors $\mathbf{e}_1$, $\mathbf{e}_2$, $\mathbf{e}_3$), may vary with prescribed strain rate, or gradually adjust to ensure equilibrium under prescribed stresses. Denoting as σ_1, σ_2, σ_3, the diagonal stresses conjugate to strain components ε_α, $1 \le \alpha \le 3$, associated with changes in dimensions L_α, we show results corresponding to isotropic compression ($\sigma_1 = \sigma_2 = \sigma_3 = P$), to oedometric compression (in which σ_1 and ε_1 increase while L_2, L_3 are maintained fixed—$\varepsilon_2 = \varepsilon_3 = 0$), and triaxial compression (increase of σ_1 and ε_1, while $\sigma_2 = \sigma_3$ are kept constant).

In both strain rate-controlled and stress-controlled simulations, inertial effects as evaluated through the reduced strain rate or *inertial number I* [2] should remain low enough. I is defined in terms of the mass m of a grain and characteristic stress σ as

$$I = \dot{\varepsilon}\sqrt{\frac{m}{a\sigma}}. \tag{4}$$

I values are requested not to exceed some upper bound $I^{\max}$: typically 10^{-3} in the first preparation stage, in which a granular gas is compressed to form the initial solid configuration; down to 10^{-4} or sometimes 10^{-6} in the subsequent quasistatic tests on the solid material. Suitable values are those for which the final results of interest no longer appreciably depend on strain rate.

Stresses are evaluated via the usual formula

$$\sigma_{\alpha\beta} = \frac{1}{V}\left[\sum_{i=1}^{N} m v_i^\alpha v_i^\beta + \sum_{1 \le i < j \le N} F_{ij}^\alpha r_{ij}^\beta\right], \tag{5}$$

with a kinetic term (negligible except in the initial granular gas compression) involving velocities $\mathbf{v}_i$ of all N grains i within sample volume V, and a sum over pairs of interacting grains i, j transmitting force $\mathbf{F}_{ij}$ (from i to j) in their contact, $\mathbf{r}_{ij}$ denoting the "branch vector" pointing from the centre of i to the centre of j. As a result of (5), the average pressure $P = (\sigma_1 + \sigma_2 + \sigma_3)/3$ is simply connected to the average normal force in the contacts as

$$P = \frac{z\Phi\langle F_N\rangle}{\pi a^2}, \tag{6}$$

through the solid fraction Φ and the coordination number z. The dimensionless *stiffness number*, defined as

$$\kappa = \left(\frac{\tilde{E}}{P}\right)^{2/3}, \tag{7}$$

is such that the typical contact deflection h, relative to diameter a, is proportional to κ^{-1} (κ would be defined as K_N/aP with constant contact stiffness K_N, for linear contact elasticity). Using (6), the coefficient can be made explicit:

$$\langle (\frac{h}{a})^{3/2} \rangle^{2/3} = \left(\frac{3\pi}{z\Phi} \right)^{2/3} \kappa^{-1}. \tag{8}$$

2.3 Stiffness Matrices and Tensor of Elastic Moduli

Elastic moduli express the relations between small stress increments $\Delta\underline{\underline{\sigma}}$ and small strains $\underline{\underline{\varepsilon}}$, assuming the contact network, in equilibrium, behaves like a network of elastic springs, with stiffnesses K^N and K^T varying from contact to contact according to relations (2) and (3). This assumes that the effects of the mobilization of friction, which implies a non-elastic contact behaviour, are macroscopically negligible for small strain increments about the investigated equilibrium state, which needs to be checked. Stiffness matrices and their structure are presented and discussed in Refs. [36, 38, 48], and will not be detailed here.

At the macroscopic scale, in the oedometric and triaxial compressions considered here, the granular material is transversely isotropic, i.e., invariant by rotation about the major compression axis (index 1). The moduli are then defined by the following macroscopic relation between stress increments and small strains about an equilibrium prestressed state:

$$\begin{bmatrix} \Delta\sigma_{11} \\ \Delta\sigma_{22} \\ \Delta\sigma_{33} \\ \Delta\sigma_{23} \\ \Delta\sigma_{31} \\ \Delta\sigma_{12} \end{bmatrix} = \begin{bmatrix} C_{11} & C_{12} & C_{12} & 0 & 0 & 0 \\ C_{12} & C_{22} & C_{23} & 0 & 0 & 0 \\ C_{12} & C_{23} & C_{22} & 0 & 0 & 0 \\ 0 & 0 & 0 & 2C_{44} & 0 & 0 \\ 0 & 0 & 0 & 0 & 2C_{55} & 0 \\ 0 & 0 & 0 & 0 & 0 & 2C_{55} \end{bmatrix} \cdot \begin{bmatrix} \varepsilon_{11} \\ \varepsilon_{22} \\ \varepsilon_{33} \\ \varepsilon_{23} \\ \varepsilon_{31} \\ \varepsilon_{12} \end{bmatrix} \tag{9}$$

Equation (9) uses the *Voigt notation*, in which $\Delta\underline{\underline{\sigma}}$ and $\underline{\underline{\varepsilon}}$ are written as 6-dimensional vectors, and the elastic moduli form a second-rank tensor, denoted as $\underline{\underline{C}}$, with corresponding indices, e.g., C_{11} for C_{1111}, or C_{44} for C_{2323}. Isotropy within the transverse plane (2, 3) entails

$$C_{22} - C_{23} = 2C_{44}. \tag{10}$$

In the isotropic case, there are only two independent elastic coefficients, the bulk modulus B and one shear modulus G, and the moduli written in Eq. (9) satisfy $C_{11} = C_{22} = B + 4G/3$, $C_{12} = C_{13} = C_{23} = B - 2G/3$, $C_{44} = C_{55} = G$. In anisotropic systems in which the tensor of elastic moduli has the transversely

isotropic symmetry of (9), a bulk modulus can be defined from the variation of average pressure with an applied, isotropic, volumetric strain, as

$$B = \frac{1}{9} \left(C_{11} + 4C_{12} + 2C_{22} + 2C_{23} \right). \tag{11}$$

3 Stress-Strain Relations and Material State: DEM Observations

This section provides a brief review of some basic features of material behaviour, which are observed and studied by DEM simulations of model systems, outside the elastic regime [37, 39, 40, 42]. Simulations are also used to correlate such macroscopic observations to state variables characterizing the material on the microscopic scale of the grains and the contact network.

3.1 Assembling Grains into Solid Packs

The first solid states are made under low stress on compressing granular gases to equilibrium. By varying either the friction coefficient in the granular compression stage (e.g., setting it to zero) or by mimicking numerically the effects of strong vibrations in dense states, it is possible to produce

(i) very dense, highly coordinated states denoted as A in the isotropic compression study, or DH (dense, high coordination number) in the oedometric compression study;

(ii) very dense, poorly coordinated states, denoted as C (isotropic compression) or DL (dense, low coordination) in the oedometric compression study;

(iii) looser states, referred to as D if isotropically compressed, or LL (loose with low coordination) in the oedometric test study.

The solid fraction Φ in very dense samples (A, C, DH, DL), initially assembled on setting the friction coefficient to zero, is the "random close packing" value $\Phi \simeq 0.64$. The (rattler-corrected) coordination number z^* of well-coordinated samples (A, DH) is near 6, while it decreases to about 4.6 in poorly coordinated ones. The rattlers, grain carrying no force, are very few in highly coordinated systems, but comprise typically 10% of all grains in poorly coordinated ones. Coordination number z becomes $z^* = z/(1 - x_0)$ as rattlers are excluded from the evaluation of the average number of contacts per grain. In addition (iv), intermediate states B were created using a small friction coefficient in the assembling stage, with $\Phi_B \simeq 0.628$ and $z_B \simeq 5.8$—thus looser than C but better coordinated— to further illustrate the independent variations of z and Φ in dense configurations.

The samples that were prepared for oedometric compression were assembled by isotropically or oedometrically compressing the initial granular gas, which duplicates each initial state: DHi/DHo, DLi/DLo, LLi/LLo. The nature of the gas compression does not significantly affect the density and the coordination number, but of course "o" states are anisotropic from the start, while "i" ones gradually become anisotropic in the oedometric compression process.

Finally, we also exploit a set of loose initial isotropic configurations, simply denoted as "L", with $\Phi = 0.571 \pm 0.005$ and $z^* \simeq 4.7$, as obtained from a compression cycle applied to initially wet beads, with a model of capillary cohesion—the liquid menisci being removed in the final state [49].

3.2 Changing Stress Intensity: Isotropic and Oedometric Compressions

We first discuss the elastic properties of systems subjected to large variations of stress intensities, without or with comparatively little change in stress directions.

Density and Coordination

States A, B, C, D are isotropically compressed up to large values of confining pressure P (100 MPa). The grains are assumed not to undergo any damage, despite the very large stress levels involved in their contacts [37]. States DH, DL and LL are similarly subjected to oedometric compressions, with σ_1 reaching 30 MPa. Such compression processes impose an increase of the solid fraction and of contact deflections, and consequently strongly depend on contact elasticity, which sets the scale of strains, determined by κ^{-1}. As κ (defined with P in (7) for isotropic compression, with σ_1 for oedometric compression) decreases from order 10^4–10^5 down to $\kappa \sim 100$ during compression, Φ typically increases by 2 to 5×10^{-2}. Meanwhile, coordination number z increases and rattler fraction x_0 decreases, as shown in Fig. 1, for the different systems subjected to oedometric compression. Note however that the coordination number, if initially high (as for DHo and DHi), does not increase monotonically with axial stress in oedometric compression.

Force Distribution and Friction Mobilization

The distribution of normal force values, regarded as characteristic of granular disorder, has been quite extensively studied in equilibrated granular assemblies [50–53]. It usually exhibits an exponential decrease of the probability density for large force values, and its width tends to vary with coordination number, the wider the smaller the contact density. Upon increasing the pressure in compressive loading,
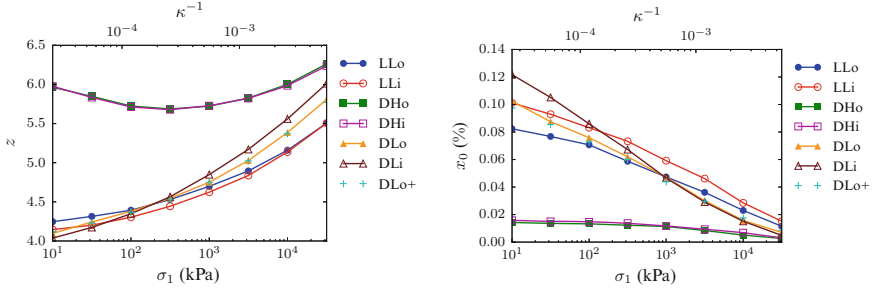
Fig. 1 Coordination number z (left graph) and rattler fraction x_0 (right graph) versus axial stress σ_1, or κ^{-1}, in oedometric compression of the different initial states ("DLo+" data pertain to DLo-type sample with 13,500 grains instead of 4000, showing size independence)

the coordination number increases and the force distribution becomes correlatively narrower [37, 54]. In the context of the estimation of stiffnesses and elastic moduli, force distributions are usefully characterized by their reduced moments, defined as

$$Z(\alpha) = \frac{\langle F_N^\alpha \rangle}{\langle F_N \rangle^\alpha}. \tag{12}$$

Thus the average contact stiffness, from Eq. (2), is related to $Z(1/3)$, which varies between 0.92 and 0.96 in the set of investigated bead packs. The width of the large force wing of the distribution may be assessed, e.g., from the values of $Z(2)$, which vary between 1.45 and 1.65.

A related quantity (close to $Z(5/3)$) is useful to evaluate elastic energies from contact forces. If r_{TN} is the ratio $\frac{||\mathbf{F_T}||}{F_N}$ in any contact, and α_T denotes the stiffness ratio K_T/K_N (see Eqs. (2) and (3)), then we define

$$\tilde{Z}(5/3) = \frac{\langle F_N^{5/3}(1 + \frac{r_{TN}^2}{\alpha_T}) \rangle}{\langle F_N \rangle^{5/3}}. \tag{13}$$

Values of $\tilde{Z}(5/3)$ are observed to vary between 1.1 and 1.4.

Friction mobilization is systematically larger in contacts carrying small normal forces [36, 37], and, globally, larger in scarcely coordinated systems. In oedometric compression, it is (surprisingly) larger in contacts with normal direction transverse to the major compression axis [42].

Anisotropy

Anisotropy is introduced in the assembling stage in systems DHo, DLo, LLo, for which the granular gas is assembled in solid form by oedometric compression. It

is gained in the course of compression for initially isotropic systems DHi, DLi, LLi or A to D. The simplest characteristics of anisotropy are the coefficients of the distribution of unit normal vector orientations and the angular distribution of normal force intensities. Defining angle θ between direction 1 and normal unit vector $\mathbf{n}$, with $0 \leq \theta \leq \pi$, the orientation distribution (or *fabric*) anisotropy is conveniently expressed by the probability density function (p. d. f.) of $\cos\theta = n_1$ over interval $-1 \leq n_1 \leq 1$, $p(n_1)$. By construction, it is an even function ($\mathbf{n}$ and $-\mathbf{n}$ are equivalent), constant with value $1/2$ in an isotropic system. $p(n_1)$ might be expanded in the series of Legendre polynomials, with only terms of even order. Truncating the series after the term of order 4, one has

$$p(n_1) = 1 + A_2 \left(3n_1^2 - 1\right) + A_4 \left(35n_1^4 - 30n_1^2 + 3\right), \tag{14}$$

in which coefficients are related to moments of the distribution: thus coefficient, A_2, given by

$$A_2 = \frac{15}{4} \left(\langle n_1^2 \rangle - \frac{1}{3}\right) = \frac{15}{4} \int_{-1}^{1} p(n_1) n_1^2 dn_1 - \frac{5}{4}, \tag{15}$$

is directly related to the difference between the second moment and its isotropic value, for which we introduce the notation

$$\tilde{c}_2 = \langle n_1^2 \rangle - \frac{1}{3}. \tag{16}$$

Figure 2 shows that the distribution of contact orientations (normalized, using $P(|n_1|) = 2p(n_1)$, such that the integral from 0 to 1 equals unity) is well fitted with relation (14), with coefficient A_4 given by

$$A_4 = \frac{9}{64} \left(35\langle n_1^4 \rangle - 30\langle n_1^2 \rangle + 3\right). \tag{17}$$

Figure 3 shows the evolution of $\tilde{c}_2$ in oedometric compression. We denote as $\mathcal{F}(\mathbf{n})$ the average normal force amplitude for contacts with normal direction $\mathbf{n}$, normalized by the global average $\langle F^N \rangle$, such that its integral over the unit sphere, Σ, weighed by the orientation distribution $p(\mathbf{n})$, satisfies

$$\int_{\Sigma} p(\mathbf{n})\mathcal{F}(\mathbf{n})d^2\mathbf{n} = 1. \tag{18}$$

Similarly to $p(\mathbf{n})$, $\mathcal{F}$, a function of $|n_1|$ may be expanded in a series of Legendre polynomials. We define

$$\tilde{f}_2 = \frac{1}{4\pi} \int_{\Sigma} \mathcal{F}(|n_1|) n_1^2 d^2\mathbf{n} - \frac{1}{3}, \tag{19}$$
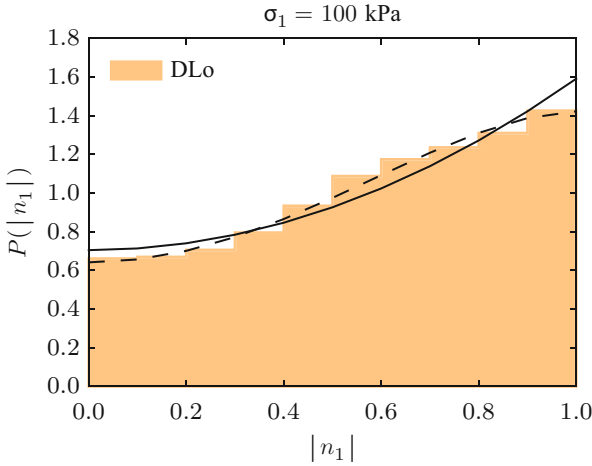
Fig. 2 Anisotropy of contact orientations: histogram of $|n_1|$ values in system DLo at $\sigma_1 = 100$ kPa, and its representation with expansion (14), truncated after order 2 (solid line) or order 4 (dashed line)
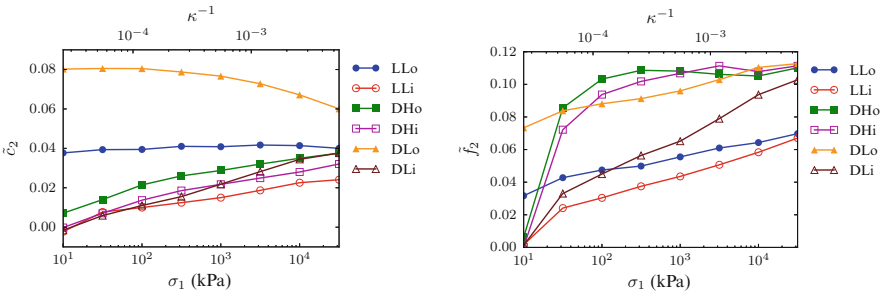
Fig. 3 Fabric anisotropy parameter $\tilde{c}_2$ and force anisotropy parameter $\tilde{f}_2$ versus axial stress σ_1 or κ^{-1} in oedometric compression of the different initial states

which vanishes in isotropic systems (Fig. 4).

Stress anisotropy in oedometric compression is characterized by the ratio of lateral to axial stresses $K_0 = \sigma_2/\sigma_1 = \sigma_3/\sigma_1$, traditionally referred to as the coefficient of earth pressure at rest [55, 56]. Stress components relate, in good approximation, to $\tilde{c}_2$ and $\tilde{f}_2$ [31, 41, 42, 57]. Ignoring the (very small) contribution of tangential forces to principal stresses in oedometric compression, one obtains

$$K_0 = \frac{2 - 3(\tilde{c}_2 + \tilde{f}_2)}{2 + 3(\tilde{c}_2 + \tilde{f}_2)}. \tag{20}$$
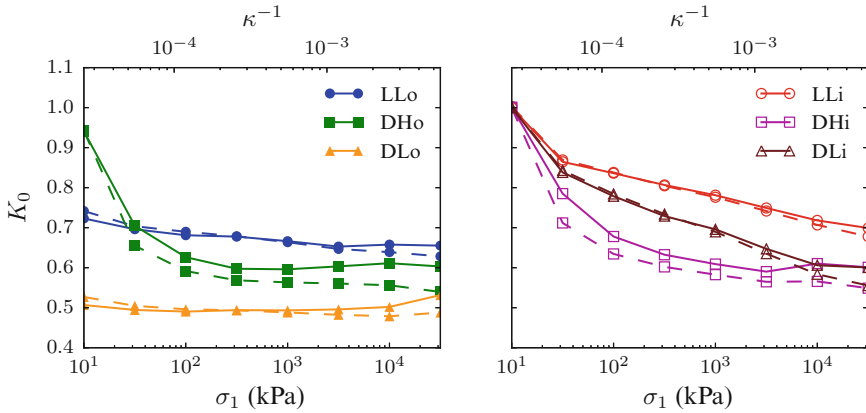
Fig. 4 Dots joined by solid lines: K_0 versus axial stress or κ^{-1} in oedometric compression. Dots joined by dashed lines: K_0 approximated by Eq. (20)
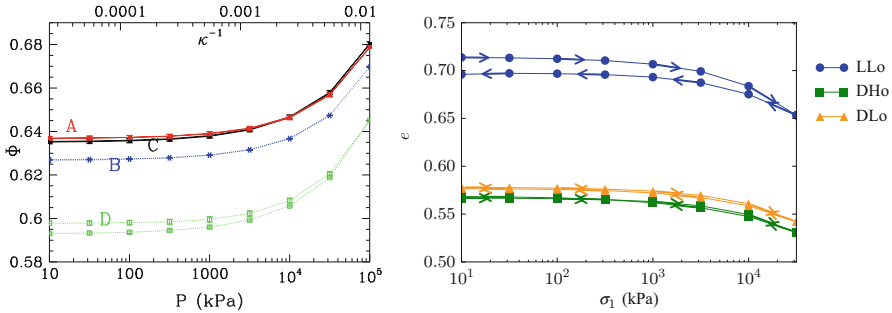
Fig. 5 Left: variations of solid fraction Φ in isotropic compression cycle for states A, B, C and D. Right: variations of void ratio e (see Eq. (21)) in oedometric compression cycle for states LLo, DLo and DHo

Unloading and Irreversibility

The increase in density under isotropic compression is, in appearance, very nearly reversed and cancelled upon reducing the pressure back to its initial value, as shown in Fig. 5. Remarkably, the small initial difference in solid fraction between states A and C (the latter being very slightly less dense) survives a loading cycle in which the pressure varies by 4 orders of magnitude. Only the looser state D exhibits a notable density change. Similar observations are made in oedometric compression, in which case, to conform to soil mechanics tradition, the *void ratio*, i.e.,

$$e = \frac{1 - \Phi}{\Phi},\tag{21}$$
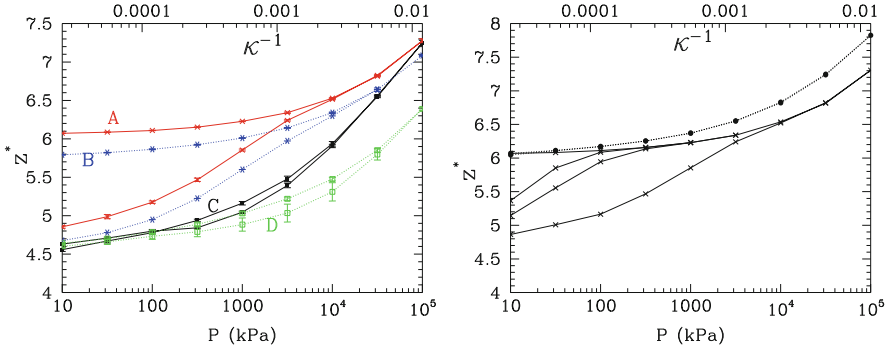
Fig. 6 Left: variations of rattler-corrected coordination number z^* in isotropic compression cycle for states A to D. Right: effects on z^* of smaller pressure cycles in A systems, with load reversals at 316.2 kPa, 3.162 MPa and 31.62 MPa, instead of 100 MPa
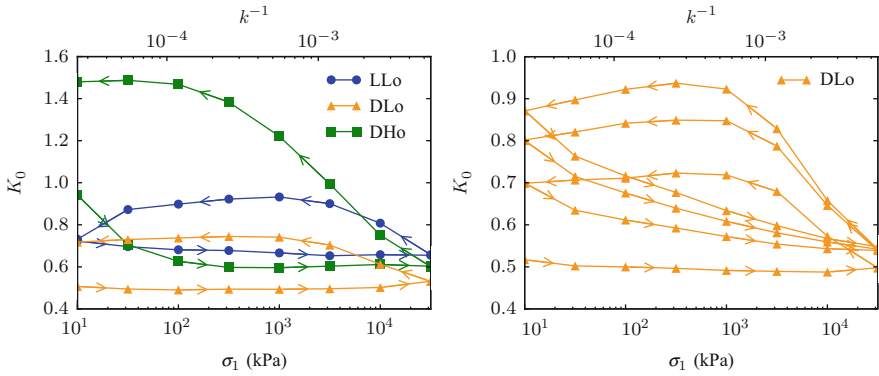
Fig. 7 Left: variations of stress ratio K_0 in oedometric compression cycle for states LLo, DLo and DHo. Right: effect of 3 repeated cycles on K_0 in state DLo

is plotted versus axial stress σ_1 on a logarithmic scale in Fig. 5 (right). As in the isotropic case, the small differences in initial densities are retrieved after a compression cycle in which stresses vary by more than 3 orders of magnitude, and a change in density is only notable in the loosest initial state (LLo).

Coordination numbers, on the other hand, do change over such a cycle, especially in the initially highly coordinated systems, in which the number of contacts is considerably decreased. This is shown in the isotropic compression case in Fig. 6.

Similar observations are made in oedometrically compressed systems, with coordination numbers, if initially large, as in systems DHi and DHo, reduced to smaller values the larger the loading cycle in terms of axial stress σ_1. Furthermore, this lack of reversibility is also extremely conspicuous for stress ratio K_0, the evolution of which on the unloading branch of the cycle, as shown in Fig. 7, is quite different from the one on the loading branch. The effect of the oedometric

loading cycle, in systems with small initial stress anisotropy (such as DHo, as well as initially isotropic systems DHi, DLi, LLi) is such that the stresses become larger in horizontal directions than along the compression axis, with $K_0 > 1$, up to about 1.5. This lack of reversibility rules out an elastic response in compression. In view of the subsequent behaviour under repeated load cycles (see right graph in Fig. 7), the unloading part of the cycle is also irreversible and anelastic. This conclusion is apparently at odds with the elastic-plastic compression laws often adopted in soil mechanics treatises, according to which the compression, both in isotropic and oedometric cases, should be plastic (irreversible) for growing stress levels but reversible and "elastic" on the unloading branch of the cycle, and as long as the maximum loading level the maximum has known in the past (the maximum pressure in isotropic compression), termed "preconsolidation stress", is not exceeded. We attribute this discrepancy to the frequent grain breakage or contact damage experienced by irregular sand grains under growing pressure, which is ignored in the numerical model. Such phenomena naturally explain the strong dissymmetry between loading and unloading, and are very likely to entail larger irreversibilities than the ones observed in DEM with elastic-frictional grains without damage in the contacts.

Another remarkable feature of the simulated isotropic or oedometric compression tests investigated in the model systems discussed here is the enduring memory of the initial assembling procedure kept in the internal states of the different systems despite the large increase of the applied stresses. The different initial configurations do not approach the same state under large pressure or axial stress.

3.3   Changing Stress Direction: Triaxial Compression

Axisymmetric triaxial compression (Fig. 8) is the most classical mechanical test probing the shear strength of a granular material in controlled stress conditions [6]. In the most frequent experimental configuration, as schematized in Fig. 8, it consists in subjecting a cylindrical specimen, maintained under constant lateral pressure $\sigma_2 = \sigma_3 = P_0$, to a vertical stress σ_1 gradually growing from initial value P_0. The principal stress values thus evolve from the initial isotropic state $\sigma_1 = \sigma_2 = \sigma_3 = P_0$ to growing values of deviator stress $q = \sigma_1 - \sigma_3 = \sigma_1 - \sigma_2$, maintaining the same symmetry of revolution as in the oedometric test. Results of the triaxial compression test are traditionally expressed as the dependence of *deviator stress* $q = \sigma_1 - \sigma_3$ and of the *volumetric strain* $\varepsilon_v = \varepsilon_1 + \varepsilon_2 + \varepsilon_3$ on the axial strain, $\varepsilon_a = \varepsilon_1$. (For large strains, keeping the simple definition of ε_1, ε_2, ε_3 as relative length reductions along the principal axes, open should use the definition $\varepsilon_v = 1 - (1 - \varepsilon_1)(1 - \varepsilon_2)(1 - \varepsilon_3)$). The growth of $-\varepsilon_v$, expressing material dilation, with ε_a is the dilatancy of the granular material under deviatoric (shear) strain.
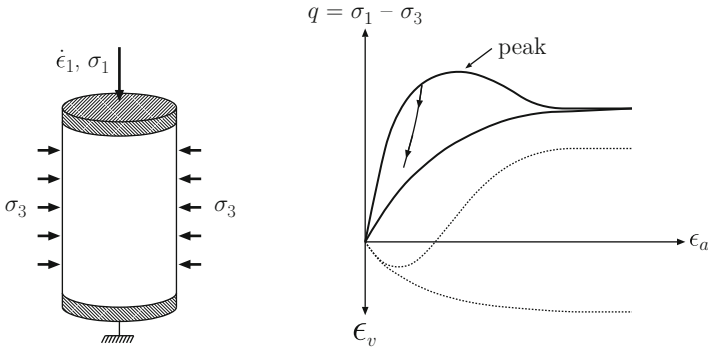
Fig. 8 Left: schematic view of triaxial compression test. Right: aspect of deviatoric stress q (solid line) and volumetric strain ε_v (thin dotted line) versus axial strain $\varepsilon_a = \varepsilon_1$ for initially dense (upper curves for both q and $-\varepsilon_v$) and loose (lower curves) states

Approach to the Critical State for Large Strains

A fundamental property of quasistatic granular mechanics is the existence of *critical states*, attractor states approached by the material subjected to monotonically growing strain, irrespective of the initial state. Thus under growing axial strain ε_a in triaxial compression, the material achieves a certain deviator stress level, as well as values of density and internal structure parameters, independent of its initial preparation. As sketched in the second graph of Fig. 8, initially dense samples first slightly contract, and then dilate. The deviator stress, in those systems, first grows, then passes through a maximum (the "peak" deviator stress) and then decreases to a plateau. In initially loose systems, both q and solid fraction Φ monotonically increase to the same asymptotic values as in the dense case.

Lots of DEM studies were devoted to the investigation of the critical state and characteristic internal state parameters approaching the corresponding critical values [58–62]. Typical results [39] are shown in Figs. 9 and 10. Figure 9 shows the evolution of deviator stress and solid fraction, both quantities approaching their asymptotic critical values for $\varepsilon_a \geq 0.25$, irrespective of their initial structure. The approach of internal variables to specific critical values is visualized in Fig. 10. Note that the same value $\tilde{c}_2 = \langle n_1^2 \rangle - 1/3 \simeq 0.07$ for large strains is obtained in both graphs, and thus for all three initial states A, D and L.

4 Elastic Properties in Isotropic or Oedometric Compression

We now turn to the investigation of elastic response in the case of the compression tests of Sect. 3.2, either isotropic or oedometric, in which stresses mostly change in intensity, over several decades.
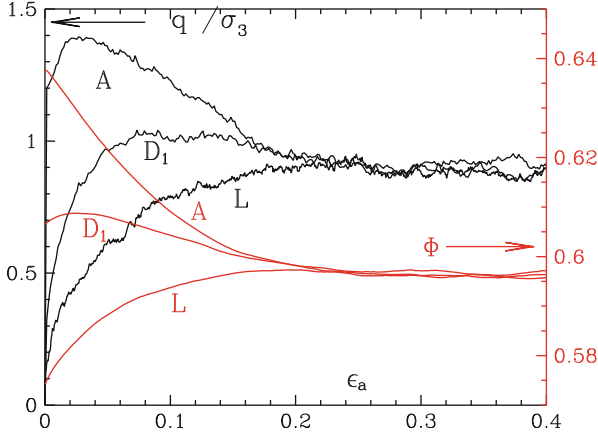
Fig. 9 Deviator stress q and solid fraction Φ versus axial strain ε_a in simulated triaxial tests ($P_0 = 100$ kPa or $\kappa \simeq 8000$) carried out with initial states A, D and L
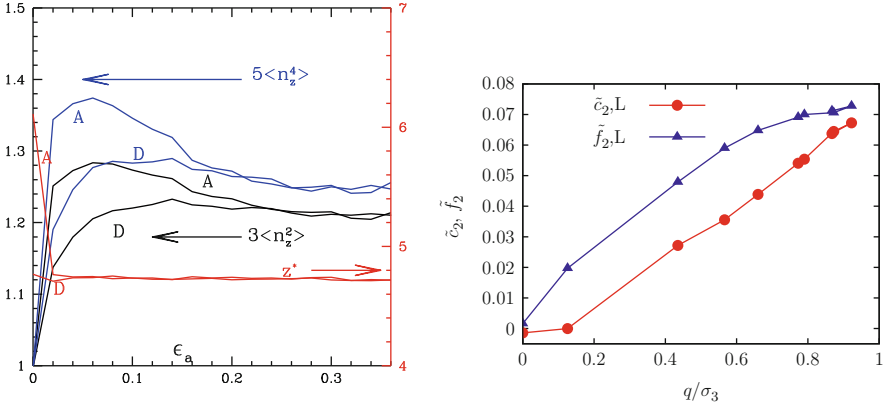
Fig. 10 Left: evolution of coordination number z^* and fabric parameters (here $n_z = n_1$) in dense and medium dense systems A and D in triaxial compression test, versus ε_a. Right: increase of anisotropy parameters $\tilde{c}_2$ and $\tilde{f}_2$ (see Eqs. (16) and (19)) in loose system L, versus normalized deviator q/σ_3

4.1 Moduli in Isotropic Compression

Under growing isotropic or oedometric load, contact stiffnesses (see Eqs. (2) and (6)) scale as $(z\Phi)^{-1/3}P^{1/3}$, while the density of contacts is proportional to $z\Phi$, whence an expected scaling for elastic moduli C:

$$C \sim (z\Phi)^{2/3}P^{1/3}. \tag{22}$$
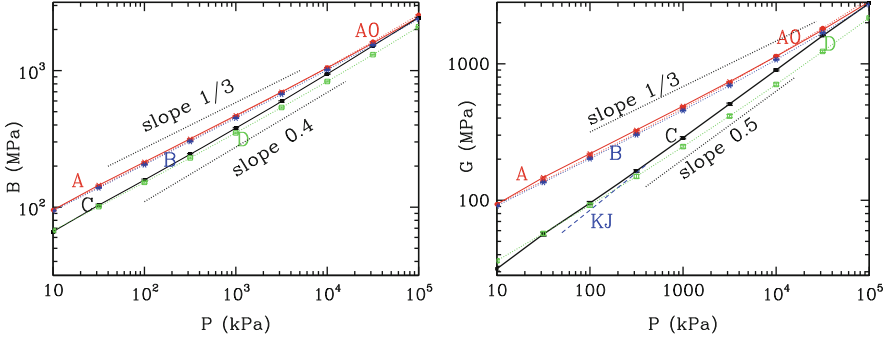
Fig. 11 Bulk (left) and shear (right) moduli versus confining pressure on doubly logarithmic scale in isotropic compression of states A, B, C, D. Line marked "KJ": fit through experimental data of Ref. [9]
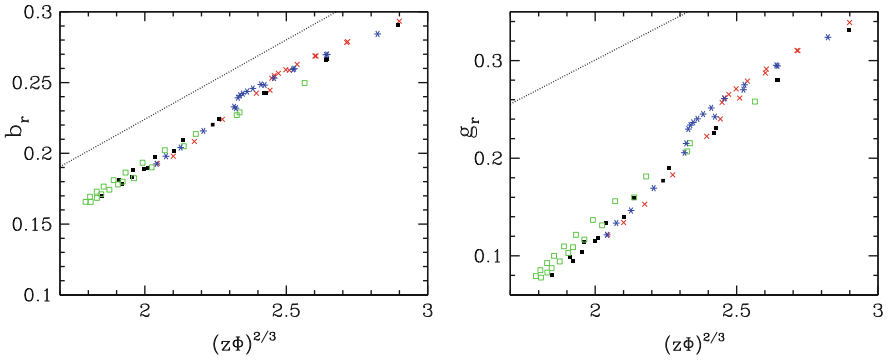
Fig. 12 Left: reduced bulk modulus $b_r = B/(\tilde{E}^{2/3}P^{1/3})$, for systems A to D in compression cycle, versus $(z\Phi)^{2/3}$. Right: same graph for reduced shear modulus $g_r = G/(\tilde{E}^{2/3}P^{1/3})$. Dotted lines show Voigt predictions

Figure 11 shows the evolution of bulk and shear moduli, computed for a set of intermediate equilibrium states, versus confining pressure in isotropically compressed systems A to D (among which intermediate system B is less dense than C, with $\Phi_B \simeq 0.625$, but more coordinated, $z_B^* \simeq 5.8$). It is immediately apparent that moduli primarily depend on coordination number, as moduli in poorly coordinated systems C and D, despite their different densities, nearly coincide, and significantly differ from those in well-coordinated systems A and B. To some extent, this is explained by the predicted scaling with $(z\Phi)^{2/3}$, since coordination number z (from 4 to 6 at low pressure) differs more than solid fraction Φ (from 0.6 to 0.64 at low pressure) between the different preparation procedures. This scaling is however imperfectly satisfied, as shown in Fig. 12. While the bulk modulus approximately abides by the behaviour expected from (22), the shear modulus increases significantly faster with z.

4.2   Estimating Elastic Moduli

Voigt Estimates   By analogy with elasticity of heterogeneous continuous media, we refer as *Voigt estimates* to the approximate values of elastic moduli obtained from the assumption of homogeneous strains, which in the case of a discrete granular assembly amounts to assuming that grain centres move like the points of a homogeneous elastic medium. As in the continuous case, it can be shown [38] that the resulting estimated bulk and shear moduli are upper bounds to the true values. In the isotropic case, one obtains (superscript V denotes Voigt estimates, and $Z(1/3)$ is defined in Eq. (12)):

$$B^{\mathrm{V}} = \frac{Z(1/3)}{2} \left(\frac{z\Phi\tilde{E}}{3\pi} \right)^{2/3} P^{1/3}$$

$$G^{\mathrm{V}} = \frac{6 + 9\alpha_T}{10} B^{\mathrm{Voigt}}. \tag{23}$$

The Voigt estimates for the five moduli defined in Eq. (9) are obtained analogously. Let us introduce notations $f_N = F_N/\langle F_N \rangle$ for the normal contact force divided by its average, $\alpha_T = K^T/K^N = (2 - 2\nu)/(2 - \nu)$ (see Eq. (3)) for the ratio of tangential to normal contact stiffnesses, and C_0, for the following factor (involving contact density and typical contact stiffness):

$$C_0 = \frac{3^{4/3}}{2\pi^{2/3}} (z\Phi)^{2/3} \tilde{E}^{2/3} P^{1/3}. \tag{24}$$

Then, defining the following averages for any coordinates α, β of unit normal vector **n**,

$$\mathcal{A}_\alpha = \langle f_N^{1/3} n_\alpha^2 \rangle; \quad \mathcal{B}_{\alpha\beta} = \langle f_N^{1/3} n_\alpha^2 n_\beta^2 \rangle, \tag{25}$$

Voigt estimates of elastic moduli read (no summation implied over repeated indices)

$$C_{\alpha\alpha}^{\mathrm{V}} = C_0 \left[(1 - \alpha_T)\mathcal{B}_{\alpha\alpha} + \alpha_T \mathcal{A}_\alpha \right] \quad (1 \le \alpha \le 3) \tag{26}$$

$$C_{\alpha\beta}^{\mathrm{V}} = C_0 (1 - \alpha_T)\mathcal{B}_{\alpha\beta} \quad (1 \le \alpha < \beta \le 3) \tag{27}$$

$$C_{44}^{\mathrm{V}} = C_0 \left[(1 - \alpha_T)\mathcal{B}_{23} + \frac{1}{2}\alpha_T \mathcal{A}_3. \right] \tag{28}$$

Optimal Voigt estimates of moduli involve [38, 63, 64] a common spin to all particles, which vanishes if the strain tensor has common eigendirections with the

fabric tensor $\underline{\mathbf{F}}$, defined as $F_{\alpha\beta} = \langle n_\alpha n_\beta \rangle$. In the present case of transverse isotropic media this only affects shear modulus C_{55}, resulting in formula

$$C_{55}^{V} = C_0 \left[(1 - \alpha_T)\mathcal{B}_{12} + \alpha_T \frac{\mathcal{A}_1 \mathcal{A}_2}{\mathcal{A}_1 + \mathcal{A}_2} \right]. \tag{29}$$

Relations (23) and (24) abide by the expected scaling (Eq. (22)). As to quantitatively estimating the values of moduli, Fig. 12 shows that, although B is only slightly overestimated in isotropic systems, Voigt predictions of shear moduli can be much larger than actual values for poorly coordinated systems. Turning to anisotropic, oedometrically compressed systems, similar observations can be made: the bulk modulus, as expressed in (11), is not sensitive to the varying degree of anisotropy between the different states, and only distinguishes highly coordinated (DH) from poorly coordinated (DL and LL) states, as shown in Fig. 13. As in the isotropic case, the Voigt estimate B^V only exceeds the true value of B by less than 15%. On the other hand, as shown in the second plot of Fig. 13, the shear moduli are grossly overestimated by the Voigt approximation, the more the lower the coordination number, ratio G^V/G reaching 3.5 in the worst case, state DLo under low axial stress.

Reuss Estimates Just like in elasticity of heterogeneous continua, it is possible in principle to write down upper bounds to elastic compliances using trial values of contact force increments balancing applied stress increments. Such trial forces are, however, not known in general, except in the special case of stress increments proportional to the preexisting stresses. One may then, as described in Ref. [38], exploit the knowledge of the distribution of forces to write an estimate of one specific elastic compliance, expressing the response to a change in stress intensity for the same stress direction. Assuming transverse isotropy as in the oedometric or triaxial compression tests, elements of the 3×3 upper left block of the compliance
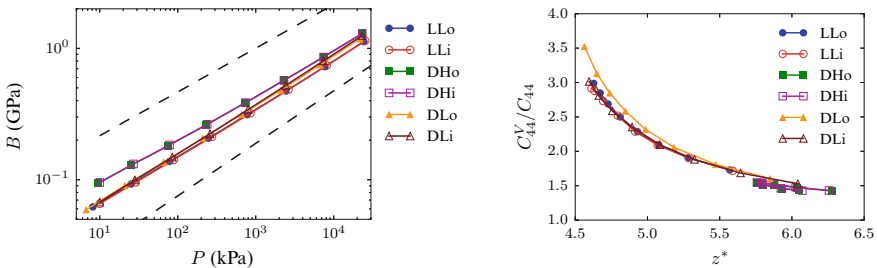
Fig. 13 Left: bulk modulus, as defined in Eq. (11), under oedometric compression cycle, versus average pressure in different systems subjected to oedometric compression. Dashed line slopes: 1/3 (top), 0.4 (bottom). Right: ratio C_{44}^V/C_{44} versus rattler-corrected coordination number z^* in oedometric compression

matrix (the inverse to the matrix written in Eq. (9)) are usually defined in terms of Young moduli E_1, E_2 and Poisson ratios ν_{12}, ν_{23} as

$$
\underline{\underline{\tilde{\mathbf{M}}}} = \begin{bmatrix} \dfrac{1}{E_1} & \dfrac{-\nu_{12}}{E_1} & \dfrac{-\nu_{12}}{E_1} \\ \dfrac{-\nu_{12}}{E_1} & \dfrac{1}{E_2} & \dfrac{-\nu_{23}}{E_2} \\ \dfrac{-\nu_{12}}{E_1} & \dfrac{-\nu_{23}}{E_2} & \dfrac{1}{E_2} \end{bmatrix}. \tag{30}
$$

Specifically, in the transversely symmetric case, denoting as K_0 the stress ratio as in Sect. 3.2, a Reuss estimate might be written for the following compliance:

$$
S_P = \frac{1 - 4\nu_{12} K_0}{E_1} + \frac{2(1 - \nu_{23}) K_0^2}{E_2}, \tag{31}
$$

as [38, 41]

$$
S_P^R = 2 \left(\frac{3\pi}{z\Phi} \right)^{2/3} \frac{\tilde{Z}(5/3)}{\tilde{E}^{2/3} P^{1/3}}. \tag{32}
$$

In the isotropic case $1/S_P^R$ provides a lower bound to B, which only differs from B^{V}, as written in (23), by factors of order 1 related to the shape of the force distribution. This explains the success of the Voigt approximation for the bulk modulus in isotropic systems. In transversely isotropic ones, modulus B also turns out correctly estimated (within 15%) in our results [28]: it appears to be nearly equal to the bulk modulus of an isotropic system with the same coordination number. The error on S_P as predicted by the Reuss estimate is also of order 10% (16% in the worst case in [28]). Meanwhile, errors in Voigt-estimated shear moduli (see Figs. 12 and 13) are quite large, especially in poorly coordinated systems. Poisson ratios are also very poorly predicted [28, 38].

More Sophisticated Approaches La Ragione and Jenkins [65], in the isotropic case, designed an improved prediction scheme for elastic moduli, based on a self-consistent approach to the fluctuations (ignored in the Voigt approach) of local grain displacements about the average affine field, on the scale of a pair of contacting grains. The resulting formulae are quite complex and have not been generalized to anisotropic systems. They were observed to improve the prediction of shear moduli to some extent, although still not accurately in systems with low coordination number. The role of fluctuations was explored by numerical means [20, 66], with investigations of the scale over which a similar self-consistent scheme should become accurate [20].

The Singular Limit of Vanishing Force Indeterminacy The anomalously low values of elastic moduli in poorly coordinated granular systems, as observed in

numerical studies, have been related to the singular values of eigenfrequencies of stiffness matrices [22, 67]. Both phenomena are controlled by the approach of a state of vanishing force indeterminacy (or degree of hyperstaticity). Such a situation occurs in packings of frictionless objects in the rigid limit ($\kappa \rightarrow \infty$) [68], as often studied in numerical simulations of spherical bead assemblies [22, 36, 69, 70]. It was predicted in [24] that the singular moduli (the shear modulus in the isotropic case) should vary proportionally to the degree of force indeterminacy as this limit is approached. With frictionless beads, the degree of force indeterminacy H is directly related to coordination number z^*, as

$$\text{H} = \frac{1}{2}n(1 - x_0)(z^* - 6), \tag{33}$$

in a system of n particles with rattler proportion x_0 [68]. In the presence of friction, one should in principle [36, 38] define a slightly corrected value of z^*, denoted as z^{**}:

$$z^{**} = z^* + \frac{2x_2}{3(1 - x_0)}, \tag{34}$$

where x_2 is the proportion of 2-coordinated beads. The degree of force indeterminacy is then given by

$$\text{H} = \frac{3}{2}n(1 - x_0)(z^{**} - 4). \tag{35}$$

x_2 values raise to about 2.5% in configurations C and D discussed here, for which z^* on the order of 4.5 under low pressure still implies a notable force indeterminacy. H = 0, in frictional systems, may be approached in simulations carried out in the (unrealistic) limit of very large friction coefficient ($\mu \rightarrow \infty$) [25, 36].

The prediction $G \propto \text{H}/n$ is checked in Fig. 14, using a reduced shear modulus g_a obtained by dividing G by density and average contact stiffness. The vanishing of shear modulus proportionally to the force indeterminacy is very well satisfied in the frictionless case. With frictional beads, such a behaviour is retrieved in the infinite friction case (state Z on the figure), and approached in some poorly coordinated systems with a realistic value of μ. The linear fits through the data predict that the shear modulus should vanish for $z^* = 6$ for frictionless beads and $z^{**} = 4$ for frictional ones, and thus, from relations (33) and (35), for H = 0. The self-consistent approach of La Ragione and Jenkins [65] does not capture this tendency. The results on modulus C_{44} in oedometrically compressed systems shown in Fig. 13 exhibit a similar vanishing tendency for the smallest values of z^* (evidenced by the growth of ratio C_{44}^{V}/C_{44}).

Studies of frictionless systems under low pressure (in the rigid limit of large κ) [41, 71] reveal that, in general, all moduli tend to vanish with the degree of force
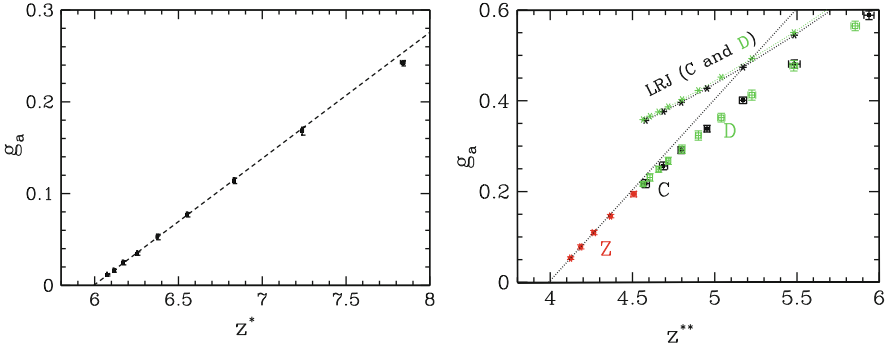
Fig. 14 Reduced shear moduli g_a versus corrected coordination number, in systems in isotropic compression. Left: frictionless case. Right: frictional case, with poorly coordinated states C and D, and state Z, assembled with infinite friction coefficient. z^{**} defined from z^* as in Eq. (34). Data points marked "LRJ": prediction of the La Ragione-Jenkins scheme [65]. Dotted lines: linear fits
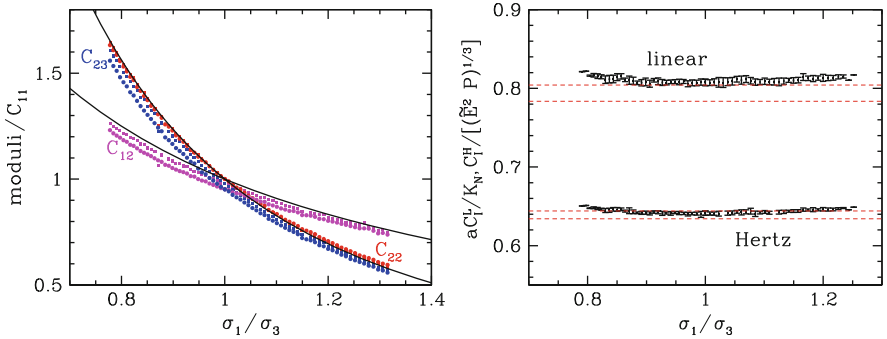
Fig. 15 Elastic moduli of nearly rigid frictionless bead packs under triaxial compression ($\sigma_1 \geq \sigma_2 = \sigma_3$) or extension ($\sigma_1 \leq \sigma_2 = \sigma_3$). Left: ratio of moduli to C_{11}, for Hertzian (square dots) or linear (round dots) contact elasticity. Continuous lines: behaviour predicted in Eqs. (36). Right: dominant eigenvalue C_I (data points) of tensor of elastic moduli, compared to Reuss prediction (between dashed lines) with Hertzian (C_I^H) or linear (C_I^L) contact elasticity

indeterminacy, except the one ($1/S_P$) associated with a proportional increase of all stress components, for which the Reuss estimate becomes exact [41] (see Fig. 15).

4.3 Anisotropy

The dominant feature in the variations of elastic moduli within the set of material states obtained through different preparation methods and subsequently subjected to oedometric compression is the role of coordination number—this is similar, as explained above, to the behaviour of isotropic systems. We now turn to specific

properties of transversely isotropic system, and briefly discuss the sensitivity of elastic moduli to fabric and force anisotropy parameters.

In the extreme case of nearly isostatic frictionless bead assemblies in the rigid limit [41], the one non-singular eigenvalue of the tensor of elastic moduli, playing the role of bulk modulus B in the isotropic case, is $1/S_P$, all the others becoming negligible in comparison. This implies the following relations between moduli:

$$
\begin{aligned}
\frac{C_{22}}{C_{11}} &\simeq \left(\frac{\sigma_{33}}{\sigma_{11}}\right)^2 \simeq \frac{C_{23}}{C_{11}} \\
\frac{C_{12}}{C_{11}} &\simeq \frac{\sigma_{33}}{\sigma_{11}},
\end{aligned}
\tag{36}
$$

a behaviour clearly satisfied by the data shown in Fig. 15. Remarkably, these relations, characteristic of a nearly singular tensor of moduli, with all eigenvalues vanishing except one, still hold on replacing the Hertzian contact elasticity by a linear unilateral law.

In the general case, assemblies of frictional beads under axisymmetric compression (oedometric or triaxial) depart from the singular limit of vanishing force indeterminacy, and their moduli, even though some are anomalously small (see Fig. 13, right graph), are sensitive both to fabric anisotropy and, because from (2) and (3), stiffnesses increase with forces, also to force anisotropy. The latter effect should be smaller in systems with small force indeterminacy H, and it vanishes for H = 0, as the force values are then determined by the sole contact network geometry. Figure 16 shows the variations of the ratio of longitudinal moduli in oedometrically assembled systems. The Voigt prediction is inaccurate for these moduli, but it may provide a fair prediction of ratio C_{11}/C_{22} for moderately
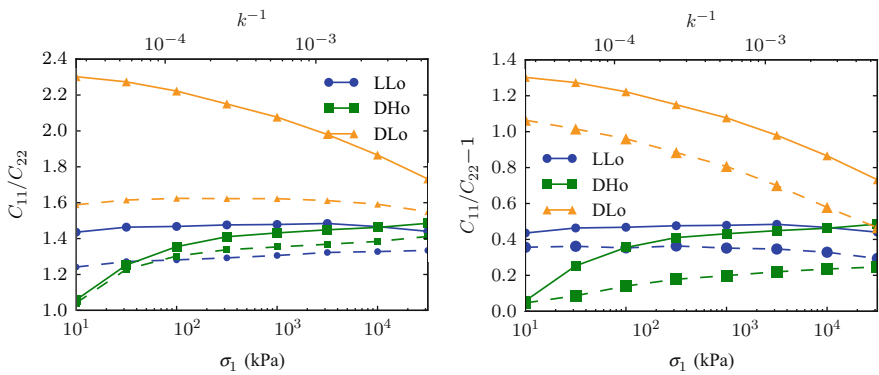
Fig. 16 Ratio, C_{11}/C_{22}, of longitudinal moduli in axial and lateral directions in oedometrically compressed transversely isotropic systems, versus axial stress (or κ^{-1}) in oedometric compression for different initial states. Dashed lines show Voigt prediction in left graph, results for linear contact elasticity in right graph
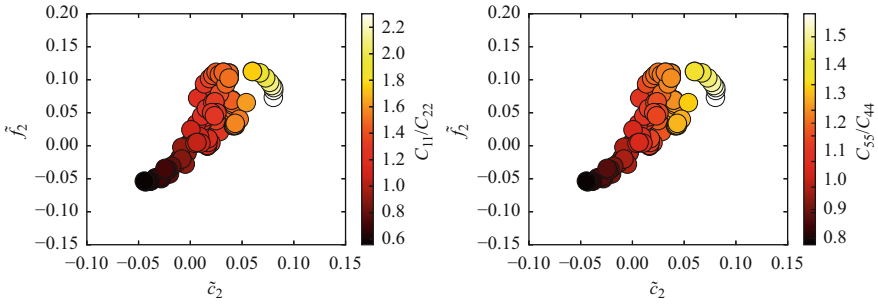
Fig. 17 Ratios of moduli characterizing elastic anisotropy: C_{11}/C_{22} (left) and C_{55}/C_{44} (right), with values encoded as colour intensity in $\tilde{c}_2$, $\tilde{f}_2$ plane

anisotropic, well-coordinated systems (DHo). However, it underestimates relative difference $C_{11}/C_{22} - 1$ by as much as 50% for large anisotropies (DLo) and/or small coordination numbers (DLo and LLo). On computing the moduli with linear contact elasticity, one keeps the effect of fabric anisotropy, but suppresses the one of force anisotropy. The second graph of Fig. 16 shows that the effect of force anisotropy, as expected, decreases for smaller force indeterminacies (in poorly coordinated systems). Then the anisotropy of the moduli appears to be primarily due to fabric anisotropy. This stronger effect of fabric, as opposed to force anisotropy, is also apparent on plots of elastic anisotropy, as characterized by the ratios of longitudinal moduli and of shear moduli, encoded as colour intensity, shown in Fig. 17, versus both anisotropy parameters $\tilde{c}_2$ and $\tilde{f}_2$. While it is not obvious in general to distinguish the effects of anisotropic fabric ($\tilde{c}_2$) from those of anisotropic forces ($\tilde{f}_2$), given that both vary in a correlated way, it does appear that the rightmost regions of the graphs contain lighter dots on going from top left towards the bottom right direction, implying a larger effect of fabric in the most anisotropic cases. Given that the Voigt approximation scheme, as shown in Fig. 16, proves again insufficient, we do not have any quantitative means to relate the force network anisotropy to the anisotropy of the tensor of elastic moduli. The results reported here nevertheless indicate qualitative trends and attainable orders of magnitude for elastic anisotropy among a series of states varying in density, coordination and initial fabric.

4.4 Anelasticity and Irreversibility: Elastic Range

We now compare the stresses (σ_1 and $\sigma_2 = K_0\sigma_1$)) versus strain ($\varepsilon_a = \varepsilon_1$) curves to the elastic response about an equilibrium state along the oedometric curve. It should be recalled that moduli are measured from stiffness matrices of contact networks, built on assimilating all contacts to elastic elements (involving normal and tangential stiffness constants, depending on the instantaneous value of the contact force). To obtain non-singular, well behaved matrices the system has to be carefully

Fig. 18 Ratio of elastic moduli C_{12}/C_{22} versus stress ratio K_0 in oedometric compression (arrows indicating growing stress) for differently assembled samples
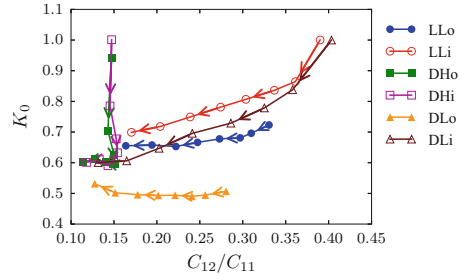
equilibrated, and it turns out, in practice, to suppress full friction mobilization in the contacts: the Coulomb inequality, in all contacts, is satisfied in the strict form, and no situation of incipient sliding is to be found anywhere in the contact network. If the equilibration is carried out under constant applied stress from an intermediate configuration reached along a strain rate-controlled compression path, it involves then an additional creep strain interval (typically of order 10^{-5} in the conditions of the simulations). Because of the role of friction in oedometric compression [42] the evolution is not elastic. In particular, as clearly shown in Fig. 18, the stress ratio K_0 systematically differs from the moduli ratio C_{12}/C_{11}. A nearly constant value of C_{12}/C_{11}, as in well-coordinated systems, over 3 decades of stress should imply a constant K_0 if the compression were elastic. A nearly constant K_0, as for LLo and DLo, should imply a constant C_{12}/C_{11}. This is contradicted by the results of Fig. 18.

The small elastic response after equilibration is similar to the one observed in experiments on sands [11, 72] after some creep strain (obtained by waiting a few hours). Even though the experimental creep, likely due to microcreep on the grain surfaces, as discussed, e.g., in Refs. [73, 74] and the numerical one (corresponding to the approach to equilibrium of a system subjected to much higher strain rates than in the laboratory) are of different physical origins, they entail similar effects: the system subsequently responds quasielastically, and the initial anelastic stress-strain curves are retrieved beyond a small strain domain. This is illustrated in Fig. 19.

The quasielastic domain, as identified in tests like the one of the first graph in Fig. 19, from the interval of strain ε for which the stress increment $\Delta\sigma$ differs from the elastic prediction $C\varepsilon$ by less than 5%, is observed to extend in the 10^{-6} or 10^{-5} range for the available data set, approximately growing with axial stress as $\sigma_1^{2/3}$. This power law corresponds to a constant relative stress increment $\Delta\sigma_1/\sigma_1$ for the quasielastic domain, assuming the modulus to grow as $\sigma_1^{1/3}$. This trend is apparent in Fig. 20. While oedometric unloading is sometimes regarded as elastic, it is observed here to be associated with irreversible evolutions, and the stresses, upon unloading, also depart from the elastic prediction after a strain interval larger than in the forward loading direction, but still of order 10^{-5} or 10^{-4}.
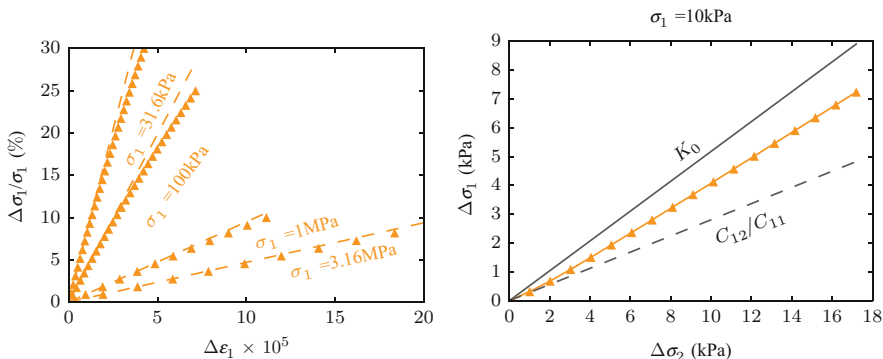
Fig. 19 Left: quasielastic range near equilibrated state along compression path of a sample of type DLo, for different values of axial stress σ_1. Straight lines have slopes C_{11}. Dots show stress-strain curves on resuming oedometric compression. Right: evolution of stresses from intermediate equilibrium. Slope of σ_2 versus σ_1 gradually evolves from C_{12}/C_{22} to K_0
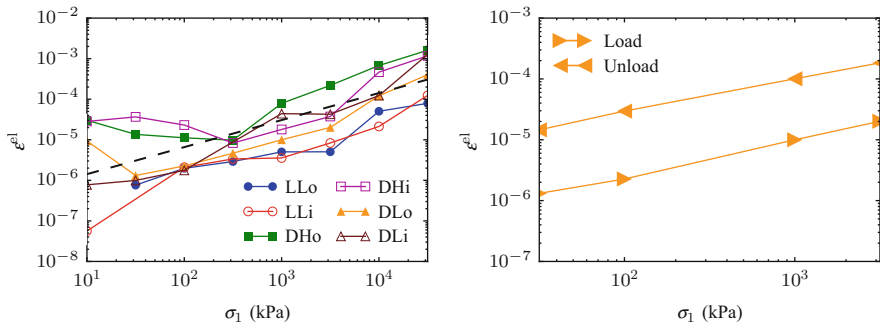
Fig. 20 Left: quasielastic range near equilibrated state along compression path of samples of different types, versus axial stress σ_1. Straight line has slope 2/3. Right: elastic domain in loading and unloading in states DLo

5 Elastic Properties in Triaxial Compression

In many respects, the evolution of a granular material under triaxial compression, as briefly described in Sect. 3.3, strongly differs from its evolution under the isotropic or oedometric compressions of Sects. 3.2 and 4. The direction of the stresses is changing, as opposed to their intensity. As the deviator level gradually increases, macroscopic failure is approached, as the fabric and force distribution in the rearranging contact network will prove unable to support the stresses. Such a failure is gradual as the critical state is approached from an initially loose configuration. It might be more sudden and catastrophic in initially dense systems, which should be unstable in deviator stress-controlled compression as the peak value is reached (other instabilities, associated with shear banding localisation, tend

to occur before the peak [75–77]). Do elastic properties detect incipient material failure (as speculated, e.g., in [34])? From the observations reported in the previous sections on the nature of elastic response and the conditions in which elastic moduli are measured, it transpires that the answer to this question should be negative. While elastic moduli are attached to one particular contact network, material failure is associated with the impossibility of rearranging the contact network in order to support larger deviatoric stresses.

In this section, we quickly review some results on the elastic moduli and their connections to internal state variables (Sect. 5.1), showing similar results as in Sect. 4. Then we discuss the role of contact stiffness and contact deflections in macroscopic strains (Sect. 5.2), and discuss the elastic or quasielastic range in Sect. 5.3.

5.1 Moduli and Internal State Parameters

Comparing Figs. 10 and 3, it is noteworthy that parameters $\tilde{c}_2$ and $\tilde{f}_2$, characterizing fabric and force anisotropy, reach similar values in triaxial compression of loose systems evolving to the critical state and in some samples under oedometric compression. Both L systems in triaxial compression and poorly coordinated ones (types DL and LL) in the early stages of oedometric compression also share similar coordination numbers (z^* between 4.5 and 4.8). Quite unsurprisingly, similar observations are also made on moduli in triaxial compression and under oedometric loading, as shown in Fig. 21. The ratio of longitudinal moduli in the major principal direction and in the transverse direction, C_{11}/C_{22}, grows along with anisotropy parameters, reaching 2 as anisotropy is maximized (compare with Fig. 16). The ratio C_{44}^V/C_{44} of the Voigt estimate of the shear modulus in the transverse plane to its exact value varies between 2 and 3, showing that C_{44} is anomalously low, as previously observed in all systems with low coordination. In general, all Voigt
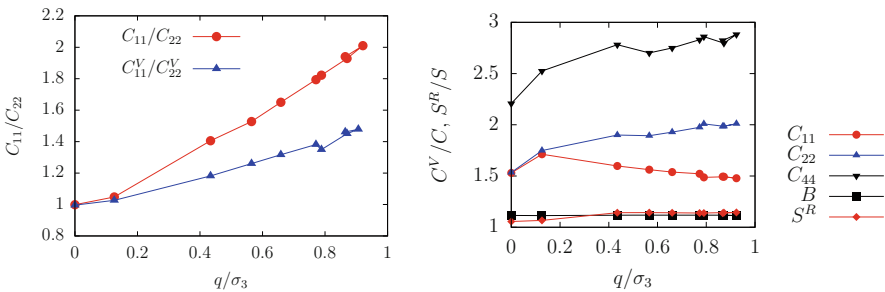
Fig. 21 Left: ratio of longitudinal moduli versus normalized deviator q/σ_3 in triaxial compression of loose systems (L), along with Voigt prediction. Right: ratios of Voigt predictions to measured moduli, and ratio S_P^R/S_P, versus q/σ_3

estimates perform poorly, except the bulk modulus as defined in (11). The Reuss estimate of compliance S_P, as defined in (31), is also quite correct. And, just like in the oedometric compression case, Voigt estimates also fail to predict ratios like C_{11}/C_{22} accurately. A similarly elastic anisotropy is observed in dense systems (such as A and C, see Sect. 3.1), for which ratio C_{11}/C_{22} grows from 1 to 2.5 in the pre-peak range (i.e., for $\varepsilon_a \leq 0.02$, see Fig. 9).

5.2 Elasticity and Stress-Strain Curves

An important difference between isotropic or oedometric compression (Sect. 3.2), on the one hand, and triaxial compression (Sect. 3.3), on the other hand, is the possibility to observe the evolution towards the characteristic behaviour of granular assemblies under shear or triaxial compression with rigid grains, as in simulations carried out with the *Contact Dynamics* method [31, 59]. It is indeed widely accepted [2] that elastic deflections in contacts are irrelevant on the scale of the strains (or order 10^{-2} or above) corresponding to the attainment of the peak stress in the dense case or, *a fortiori*, to the approach to the critical state. Yet, at the very beginning of the triaxial test, within the quasielastic range, strains are directly related to contact deflections, resulting from material strain in the intergranular contact regions at small scale. How the initial regime with strains associated with contact deflections is replaced by the strains associated with rearrangements, which no longer depend on contact stiffnesses, is worth investigating [78–81]. The difference between very dense initial states (type A of Sects. 3.1 and 4) with coordination number near 6 under small pressure, on the one hand, and equally dense systems with low coordination (type C) is particularly striking in the pre-peak strain range, and relates to their different sensitivity to dimensionless stiffness number κ. Figure 22 shows that the deviator stress and volumetric strain variations with axial strain in A-type samples, assembled with a large coordination number, strongly depend on stiffness level κ (or on confining stress P for given material elasticity). In the elastic range, strains under given P should vary approximately as $P^{2/3}$, due to the scaling of stiffnesses as $P^{1/3}$. Upon dividing strains by $(P/P_0)^{2/3}$, one should then renormalize the strains so that, if they are on the scale of elastic strains, then the curve coincides with the ones obtained under reference confining pressure P_0. Once carried out in the second plot of Fig. 22 (choosing $P_0 = 100$ kPa) this rescaling operation leads to a successful collapse of the different curves onto a single one, in a small initial strain range, within which ratio q/σ_3 raises nearly up to 1. Outside this initial interval (note the fast initial increase of the deviator), the scaling is no longer satisfied.

On the other hand, in C-type systems, as shown in Fig. 23, on the scale of the axial strain corresponding to the deviator peak, the deviator stress and volumetric strain curves do not appear to depend strongly on stiffness level κ-except in some initial range, hardly visible in the main plots Fig. 23, including the elastic range shown in the insets. This regime should correspond to the very fast increase of q
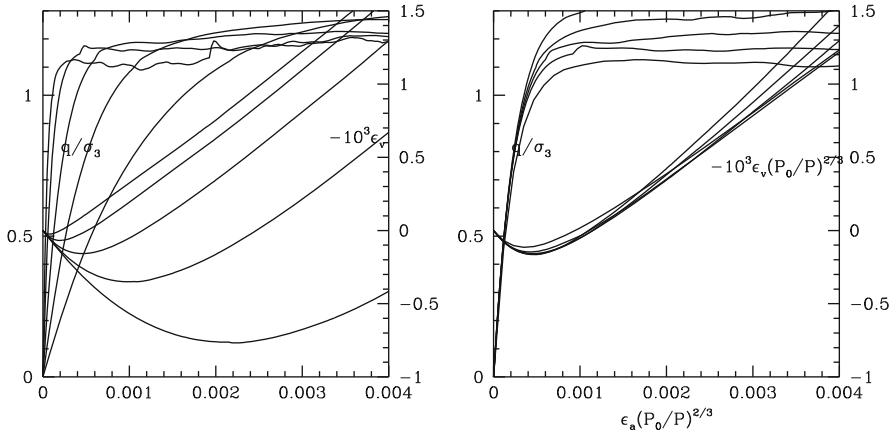
Fig. 22 Normalized deviator q/σ_3 and volumetric strain $-\varepsilon_v$ versus axial strain ε_a in triaxial compression of A-type system with different values of initial isotropic pressure $P = \sigma_3$, from 10 kPa ($\kappa \simeq 39{,}000$) to 1 MPa ($\kappa \simeq 1800$). Left: natural strains; right: rescaled strains, using $P_0 = 100$ kPa
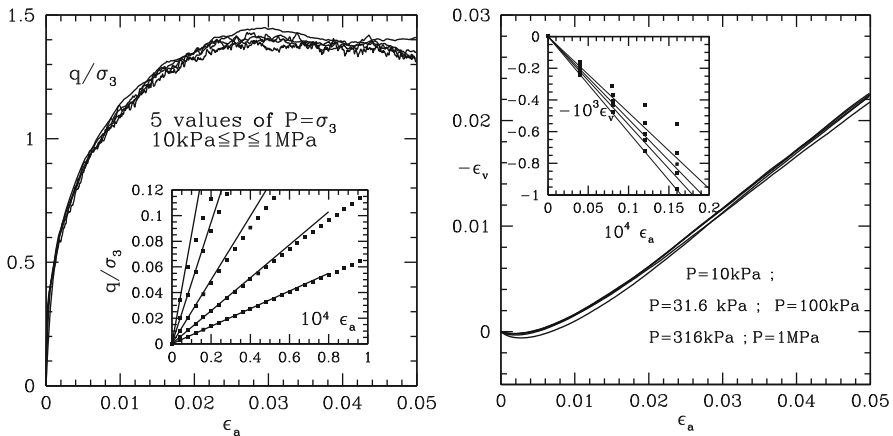
Fig. 23 Normalized deviator q/σ_3 (left) and volumetric strain $-\varepsilon_v$ versus axial strain ε_a (right) in triaxial compression of C-type system with different values of initial isotropic pressure $P = \sigma_3$. Insets show very small strain range, with straight line slopes equal to elastic prediction

(the part of the curve confused with the axis). The very different approach to the peak deviator between A and C systems, with a much faster initial increase in case A (for which the stiffness scales with the elastic stiffness), should be noted. For $\sigma_3 = 100$ kPa, $q/\sigma_3 = 1$ is reached near $\varepsilon_a = 4.10^{-4}$ or A, near 8.10^{-3} for C. However, the value of the peak deviator is near $q = 1.38 \times \sigma_3$ in both systems (see Fig. 9 for A). While the strain curves are strongly different in the first part of the

pre-peak range, both systems A and C, which have the same initial density, exhibit the same peak strength.

In Refs. [48, 80, 81] the strains due to varying contact deflections, characterizing the response of A-type systems (in which the initial coordination number is very high) as shown in Fig. 22, for $q/\sigma_3 \leq 1$, are termed "type I strains". Strains stemming mainly from network breakage and rearrangement, occurring for higher deviators in A samples, and dominating the response of poorly coordinated C samples, as shown in Fig. 23, at least for $q/\sigma_3 \geq 0.2$, are referred to as "type II strains". Type I strains, although their scale is determined by the elasticity of the contact network, are not elastic, because of Coulomb friction. In a type I strain regime, as long as the contact network does not break, a purely static simulation method may be adopted instead of standard dynamical DEM. The contact network is dealt with as a set of connected elastic springs and plastic sliders. Such static methods [48, 78] are based on elastoplastic stiffness matrices, similarly to finite element computations in elastoplastic problems of continuum mechanics, and dispense with all dynamical ingredients of DEM computations, i.e., inertia and viscous forces. Interesting examples and discussions of the applicability of such approaches are to be found in papers by McNamara and coworkers [82–84]. If the initial coordination number can be inferred from the values of elastic moduli, then measurements of the initial, very small strain, quasielastic response could provide useful information—extension of some type I strain regime—on the stress-strain curves in the pre-peak strain interval.

5.3 Irreversibility and Anelasticity: Elastic Range

The irreversibility of the deviator stress variation in triaxial tests is a well-known phenomenon, and its occurrence within the initial regime of type I strains is illustrated in Fig. 24, showing that the unloading branches do not retrace the loading curve back. The deviator stress on unloading will decrease to zero without cancelling the accumulated axial strain, and the residual part of ε_a increases in proportion with the amplitude of the deviator cycle. In Fig. 24, the results of a DEM computation of the triaxial compression test without creation of new contacts are also presented, showing its coincidence with the complete calculation in an initial type I strain regime, observed as long as the initial contact network is able to support the growing deviator stress. Note the different stress and strain scales on the two graphs, highlighting the different behaviours according to coordination number (let us recall that both initial states are isotropic, with the same density). Regime I (i.e., with type I strains) extends to about $\varepsilon_a = 3.10^{-4}$ and $q/\sigma_3 = 0.9$ in case A and to nearly $\varepsilon_a = 10^{-4}$ and $q/\sigma_3 = 0.15$ in case C. It should also be noted that the slope of the unloading curves coincides with the initial elastic modulus, showing that friction mobilization, the physical origin of anelasticity and softening in the forward loading direction, is suppressed in the initial stage of unloading (the change of direction in volumetric strain curves on reversing the loading direction, more
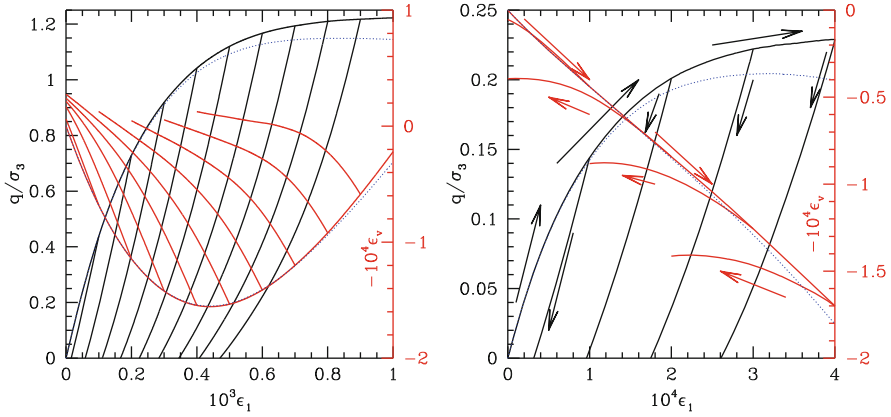
Fig. 24 Behaviour of dense systems upon load reversal (reversing of the sign of $\dot{\varepsilon}_a$) at different stages within initial regime of type I strain in triaxial compression at constant lateral stress 100 kPa. Left: high coordination number (A). Right: low coordination number (C). Thin dotted lines: response on ignoring the creation of new contacts

obviously in the first graph, also tends to return to the initial quasielastic slope). The elastic or quasielastic range was investigated in [38] for the isotropic state at the beginning of such triaxial test, with results analogous to those of Figs. 20 and 19 (corresponding to oedometric compression): elastic ranges are of order 10^{-6} or 10^{-5}, tend to grow like $\sigma_3^{2/3}$, and correspond to relative deviator increases $\Delta q/\sigma_3$ of the order of a few times 10^{-2}.

One may also evaluate elastic properties along the triaxial loading curve, first equilibrating the configuration under constant stresses, thereby causing small creep motion and strain intervals, as shown in Fig. 25. The second graph in Fig. 25 shows that, after equilibrating intermediate states along the triaxial loading curve, the obtained contact networks respond quasielastically to very small stress or strain increments in the forward loading direction, with an initial stiffness, upon resuming the DEM-simulated triaxial compression, equal in good approximation to the one evaluated in static computations using the contact elastic stiffness matrix. The response in unloading (not shown here) exhibits a larger quasielastic interval.

5.4 Some Conclusions and Remarks

The correlations one may find between elastic moduli and internal variables in configurations along the triaxial loading curve prove, as expected, quite similar to the ones observed in oedometric compression (Sect. 4). As the material state evolves towards the critical state, the coordination number quickly evolves (Fig. 10) to a small value ($z^* \sim 4.5 - 4.7$ for $\sigma_3 = 100$ kPa, or $\kappa \simeq 8400$, not too far from the rigid limit). This is similar, for the same range of average pressure, to
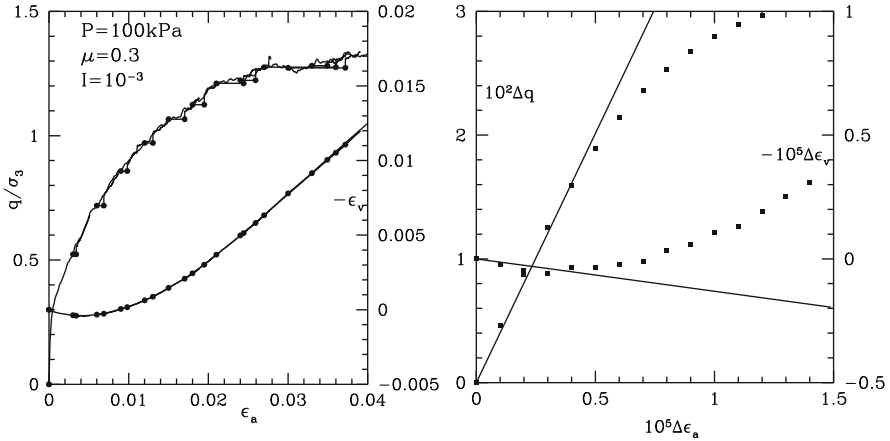
Fig. 25 Left: equilibration after small creep strain interval (beginning and end marked by round dots), followed by resumed strain rate-controlled loading. Right: deviator and volumetric strain curves, on small scale, upon resuming loading from equilibrated configurations. Straight lines: elastic response

z^* values observed in states C, D, L, DL and LL, under isotropic or oedometric compression, initially assembled as poorly coordinated. Elastic moduli exhibit the specific properties observed in isotropic or oedometric loading: anomalously small shear moduli, poor performance of Voigt approximation (see Figs. 12, 13, and 21). Meanwhile, the force network anisotropy increases, reaching levels similar to the ones observed in oedometric compression (see Figs. 3 and 10) whence a similar anisotropy in the tensor of elastic moduli in triaxial as in oedometric compression (see Figs. 16 and 21). The elastic moduli of the states reached along the triaxial loading curve, as anticipated, do not show any sign of the material incipient yield.

One major difference between isotropic or oedometric compressions, up to very large stresses, on the one hand, and triaxial compression, up to large strains and to the critical state, on the other hand, is that the magnitude of strains, in the second case, is such that the material gets strongly restructured. Elastic behaviour could be expected in isotropic or oedometric compression, and the stress-strain relations may seem reversible in such cases (Fig. 5). However, the evolution of internal variables (see Fig. 6 for coordination numbers) and the behaviour of stress ratio K_0 (Fig. 7) clearly show that the response to such compression tests is inherently irreversible and anelastic. On the other hand, one may expect the stress and strain curves in a triaxial compression test to be completely insensitive to contact elasticity, as the behaviour is dominated by the contact network rearrangements. This proves correct for type II strains, but a regime characterized by type I strains, the scale of which is set by the stiffness number κ. Such a regime is present in the beginning of a triaxial compression from isotropically prepared initial packings, and tends to reappear upon unloading, even in rearrangement regimes for which type II strains dominate the material behaviour in forward loading [78].

The existence of a small quasielastic regime in well-equilibrated numerical configuration, once the material sample has acquired a stable contact network and remaining vibrations have been damped out, appears to be a constant feature, occurring even in configurations along the triaxial loading path close to the yield limit. Even though the creep or shakedown stage observed before the quasielastic behaviour is recorded has different causes in simulations and in laboratory experiments, the phenomenon is similar. In this small range (sometimes called "elastic bubble") about a well-stabilized equilibrium state, one observes an elastic response, with a tensor of elastic moduli, endowed with all classical symmetries, expressing the linear dependence of stress increments on strain increments; approximate for finite increments, those stress-strain relations become very nearly exact in the limit of small amplitudes. The slope of stress-strain curves, however, differs, as shown in Fig. 25, before and after creep and full equilibration. Before creep, as the material is being deformed at controlled $\dot{\varepsilon}_a$, due to contact sliding and/or continuous network rearrangements, the stress-strain evolution is considerably softer than the one observed right after equilibrium, upon resuming triaxial loading, when a stabler contact network in which friction is not completely mobilized is being probed. Investigating the full response to incremental stress probes is one way to clarify such issues, as attempted in the 2D studies reported in the next section.

6 Some Investigations of Incremental Elastoplasticity

We report in this section on the investigations [85] of the effect of stress probes incrementally applied to equilibrated granular materials, carried out in two-dimensional (2D) disk samples, along the biaxial test loading trajectory. Similar studies have been carried out by several groups [86, 87], with the objective, in particular, of testing instability criteria based on incremental constitutive laws [75]. The study recalled here [85] was carried out with attention to the influence of initial coordination number (as in the previous sections for 3D simulations), and stiffness level. The biaxial test is similar to the triaxial test of Sect. 3.3, except that there is only one transverse direction (labelled here with index 1) to the axial direction (index 2), which is the major principal stress direction. The typical results of such tests on samples of 5600 polydisperse disks (with a uniform distribution of radii between $R_{\min}$ and $R_{\max} = 13 R_{\min}/7$) are shown in Fig. 26. Those biaxial tests are carried out starting with isotropic systems under pressure P, under constant lateral stress $\sigma_1 = P$. The curves of Fig. 26, showing the variations of normalized deviator stress $q/P = (\sigma_2 - \sigma_1)/P$ and "volumetric" strain $\varepsilon_v = 1 - (1 - \varepsilon_1)(1 - \varepsilon_2)$ pertain to a dense, poorly coordinated sample analogous to 3D systems labelled C in the previous sections. Along such curves, *investigation points* are chosen, corresponding to different values of principal stress ratio $\zeta = \sigma_2/\sigma_1$. In those points, after equilibrating the system with good accuracy under the current values of σ_1, σ_2, stress increments of growing amplitudes along different directions in plane σ_1, σ_2 are applied, as indicated in Fig. 27 (16 different directions, 12 values
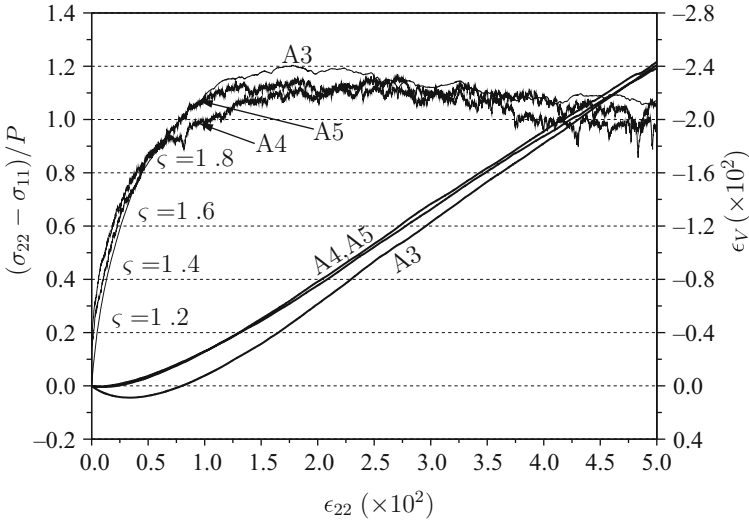
Fig. 26 Biaxial test on dense sample with low coordination number, for different stiffness number κ: 10^5, 10^4 and 10^3. Written values of ζ correspond to chosen investigation points
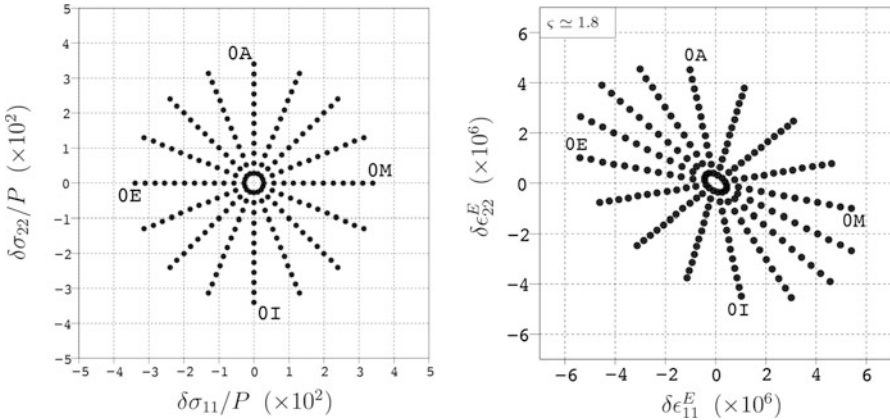
Fig. 27 Applied stress increments (left), example of resulting elastic strain increments (right)

of the amplitude in this case), and the system carefully equilibrated after each new increment. Adopting vector notations for stress and strain (three-dimensional, symmetric tensors in 2D), the aim of such studies is the identification of direction-dependent compliance tensors $\underline{\underline{\mathbf{M}}}$ such that the relation between increments $\delta\boldsymbol{\sigma}$ and $\delta\boldsymbol{\varepsilon}$ takes the form

$$\delta\boldsymbol{\varepsilon} = \underline{\underline{\mathbf{M}}}\left(\frac{\delta\boldsymbol{\sigma}}{||\delta\boldsymbol{\sigma}||}\right) \cdot \delta\boldsymbol{\sigma}. \tag{37}$$
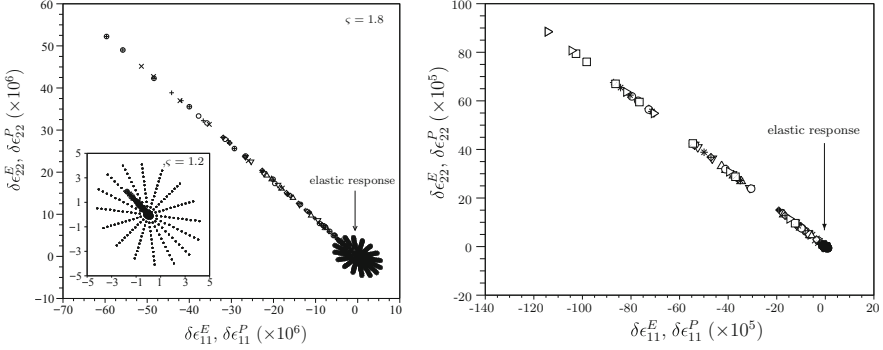
Fig. 28 Decomposition of strain increments into elastic and plastic parts. Left: stress probes in type I strain regime with $\zeta = 1.8$ (main plot) or $\zeta = 1.2$ (inset). Right: stress probes in type II strain regime ($\zeta = 1.8$)

Using the elastic compliance matrix, $\underline{\underline{\mathbf{M}}}^E$, associated with the contact network ($\underline{\underline{\mathbf{M}}}^E$ does not depend on the direction $\frac{\delta\boldsymbol{\sigma}}{||\delta\boldsymbol{\sigma}||}$ of $\delta\boldsymbol{\sigma}$ in stress space) one may extract the elastic part $\delta\boldsymbol{\varepsilon}^E = \underline{\underline{\mathbf{M}}}^E \cdot \delta\boldsymbol{\sigma}$ of the strain increment response. $\delta\boldsymbol{\varepsilon}^E$ is shown in Fig. 27 for one particular investigation point. The elastic compliance tensor $\underline{\underline{\mathbf{M}}}^E$ is computed similarly to the 3D calculations of the previous sections, based on the stiffness matrix of the contact network. The transformation of isotropically oriented $\delta\boldsymbol{\sigma}$ values into an ellipse of $\delta\boldsymbol{\varepsilon}$ values reflects the anisotropy of tensor $\underline{\underline{\mathbf{M}}}^E$. The plastic (or anelastic) part of the strain increment is defined as $\delta\boldsymbol{\varepsilon}^P = \delta\boldsymbol{\varepsilon} - \delta\boldsymbol{\varepsilon}^E$. On subtracting $\delta\boldsymbol{\varepsilon}^E$ from the total strain increment, a plastic component $\delta\boldsymbol{\varepsilon}^P$ is defined, which, as apparent in Fig. 28, stays in a well-defined *flow direction* for all stress increments $\delta\boldsymbol{\sigma}$ within the σ_1, σ_2 plane. According to the probed investigation point, the relative importance of elastic and plastic strains varies considerably. The total strain increment for a given deviator increase should become larger and larger as the deviator curve softens. Consequently, as the elastic moduli remain of the same order and the elastic strain does not increase, the strain gradually becomes mostly plastic. In the case of type II strains (right graph in Fig. 28), the scale of global strains is set by network rearrangements and the elastic term $\delta\boldsymbol{\varepsilon}^E$ becomes negligible.

An incremental law in the form of Eq. (37) should also imply the identification of a plastic criterion, and of a plastic modulus E^P, such that the magnitude of the plastic strain increment is proportional to the stress increment projected along the outward normal $\boldsymbol{\xi}$ in stress space. The choice of $\boldsymbol{\xi}$ is the one leading to a linear relation between $[\boldsymbol{\xi} \cdot \delta\boldsymbol{\sigma}]_+$ (the positive part of $\boldsymbol{\xi} \cdot \delta\boldsymbol{\sigma}$, equal to itself if positive, to zero otherwise) and $||\delta\boldsymbol{\varepsilon}^P||$,

$$||\delta\boldsymbol{\varepsilon}^P|| = \frac{1}{E^P} [\boldsymbol{\xi} \cdot \delta\boldsymbol{\sigma}]_+, \tag{38}$$
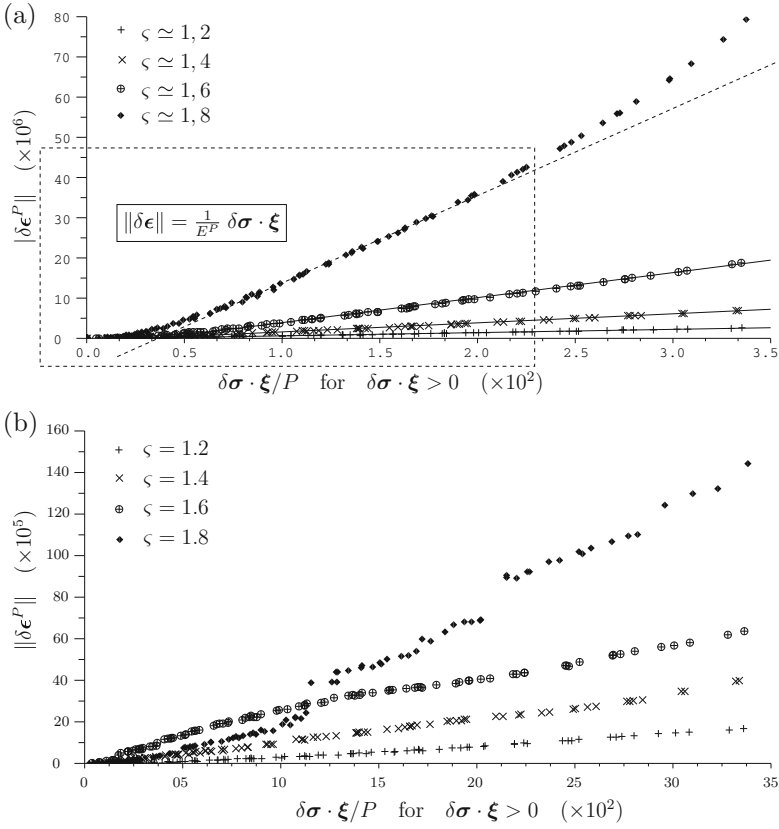
Fig. 29 $||\delta\boldsymbol{\varepsilon}^P||$ versus $[\boldsymbol{\xi} \cdot \delta\boldsymbol{\sigma}]_+$, for different stress ratios ζ and $\kappa = 10^4$. (**a**): type I strains. (**b**): type II strains

as represented in Fig. 29. In good approximation, it is observed that direction $\boldsymbol{\xi}$ is orthogonal to the vector of coordinates σ_1, σ_2 in stress space, oriented in the direction of growing principal stress ratio σ_2/σ_1. The directional linearity (or positive homogeneity of order (1) expressed by Eqs. (37) and (38) is obtained in practice with an appropriate choice of increment sizes. With too large increments the linearity is lost as the stress-strain curve departs from its tangent. With very small increments, greater computational accuracy could be required. Note also that one may observe the "elastic bubble" phenomenon mentioned in Sect. 5.4: a small interval $[\boldsymbol{\xi} \cdot \delta\boldsymbol{\sigma}]_+^E$ of $[\boldsymbol{\xi} \cdot \delta\boldsymbol{\sigma}]_+$ entails no plastic strain. This is apparent, in particular, in the data of Fig. 29a pertaining to stress ratio $\zeta = 1.8$. Thus the linear law written in (38) applies to some difference $[\boldsymbol{\xi} \cdot \delta\boldsymbol{\sigma}]_+ - [\boldsymbol{\xi} \cdot \delta\boldsymbol{\sigma}]_+^E$.

In the case of strains of type II, caused by instabilities and rearrangements of the network, the hardening modulus has to be identified from the slope of a staircase-shaped curve, as shown in Fig. 29b, corresponding to the discontinuous appearance of the second plot of Fig. 28.

These results should be generalized to three-dimensional stress space in 2D, before dealing with 3D systems. Preliminary results show then that the applications of increments of shear stress σ_{12} always cause plastic strains, and that the incremental law (37) relates stress and strain increments both spanning a two-dimensional space [85].

7 A Few Remarks and Perspectives

As announced, and commented in Sect. 5.4, the measurement of elastic moduli, although indicative of some properties of the contact network (coordination number, fabric, and, to a lesser extent, anisotropy of forces), does not provide information about incipient failure modes. This information, on the other hand, is contained in the incremental anelastic response, which may apparently be described, to some extent, with the ingredients of elastoplastic models: flow rule, criterion, plastic hardening modulus (although some results, not reported in Sect. 6, imply that several plasticity mechanisms are required). Singularities in the elastic response occur in poorly connected contact networks with very small force indeterminacy. Systems with vanishing degree of force indeterminacy are observed with frictionless grains, but are not usually obtained in the presence of friction. The absence of observed elastic singularity in assemblies of frictional grains is related to the conditions for observing elastic properties, which usually imply a stable network and negligible effects of friction forces in contacts. The exploration of the incremental behaviour of granular materials outside a quasielastic range is difficult. Experimentally, it is impossible to repeat the test with the same sample as the material state is bound to evolve irreversibly. One thus needs to prepare, e.g., as many samples in the same state as there are directions of stress increments to probe, a cumbersome and technically challenging task. Numerically, although it is feasible to apply different probes to the same system, one has to characterize a behaviour from the noisy response of systems of relatively small size, especially on dealing with strains "of type II", caused by network failure and rearrangements. Careful and statistically representative tests still need to be carried out to understand frictional failure of contact networks, and how such accumulated events, in which the networks get repeatedly broken and repaired, give rise to well-defined stress-strain relations, involving fabric and friction mobilization evolutions.

References

1. B. Andreotti, Y. Forterre, and O. Pouliquen. *Granular Media: Between Fluid and Solid.* Cambridge University Press, Cambridge, UK, 2013.
2. J.-N. Roux and F. Chevoir. Dimensional Analysis and Control Parameters. In Radjaï and Dubois [88], chapter 8, pages 199–232.

3. P. Vermeer. A five constant model unifying well established concepts. In *International Workshop on Constitutive Behaviour of Soils*, pages 175–197, Grenoble, 1982. Balkema.

4. D. M. Wood. *Soil Behaviour and Critical State Soil Mechanics*. Cambridge University Press, 1990.

5. P. A. Vermeer. Non-associated plasticity for soils, concrete and rock. In H. J. Herrmann, J.-P. Hovi, and S. Luding, editors, *Physics of Dry Granular Media*, pages 163–196, Dordrecht, 1998. Balkema.

6. J.K. Mitchell and K. Soga. *Fundamentals of Soil Behavior*. Wiley, 2005.

7. S Shibuya, F. Tatsuoka, S. Teachavorasinskun, X.-J. Kong, F. Abe, Y.-S. Kim, and C.-S. Park. Elastic deformation properties of geomaterials. *Soils and Foundations*, 32:26–46, 1992.

8. P.-Y. Hicher. Elastic properties of soils. *ASCE Journal of Geotechnical Engineering*, 122:641–648, 1996.

9. R. Kuwano and R. J. Jardine. On the applicability of cross-anisotropic elasticity to granular materials at very small strains. *Géotechnique*, 52:727–749, 2002.

10. H. Geoffroy, H. di Benedetto, A. Duttine, and C. Sauzéat. Dynamic and cyclic loadings on sands: results and modelling for general stress-strain conditions. In di Benedetto et al. [89], pages 353–363.

11. A. Ezaoui and H. di Benedetto. Experimental measurements of the global anisotropic elastic behaviour of dry Hostun sand during triaxial tests, and effect of sample preparation. *Géotechnique*, 59(7):621–635, 2009.

12. Y.-C. Chen, I. Ishibashi, and J. T. Jenkins. Dynamic shear modulus and fabric: part i, depositional and induced anisotropy. *Géotechnique*, 38(1):23–32, 1988.

13. Y.-C. Chen, I. Ishibashi, and J. T. Jenkins. Dynamic shear modulus and fabric: part ii, stress reversal. *Géotechnique*, 38(1):33–37, 1988.

14. Thomas G. Thomann and Roman D. Hryciw. Laboratory measurement of small strain shear modulus under K_0 conditions. *ASTM Geotechnical Testing Journal*, 13(2):97–105, 1990.

15. X. Jia, C. Caroli, and B. Velický. Ultrasound propagation in externally stressed granular media. *Phys. Rev. Lett.*, 82:1863–1866, 1999.

16. X. Jia and P. Mills. Sound propagation in dense granular materials. In Y. Kishino, editor, *Powders and Grains 2001*, pages 105–112, Lisse, 2001. Swets & Zeitlinger.

17. I. Agnolin, J.-N. Roux, P. Maassad, X. Jia, and P. Mills. Sound wave velocities in dry and lubricated granular packings: numerical simulations and experiments. In R. García Rojo, H. J. Herrmann, and S. McNamara, editors, *Powders and Grains 2005*, pages 313–317, Leiden, 2005. Balkema.

18. Y. Khidas and X. Jia. Anisotropic nonlinear elasticity in a spherical bead pack: influence of the fabric anisotropy. *Phys. Rev. E*, 81:021303, 2010.

19. H. A. Makse, N. Gland, D. L. Johnson, and L. Schwartz. Granular packings: Nonlinear elasticity, sound propagation, and collective relaxation dynamics. *Phys. Rev. E*, 70:061302, 2004.

20. N. P. Kruyt. Micromechanical study of elastic moduli of three-dimensional granular assemblies. *International Journal of Solids and Structures*, 51:2336–2344, 2014.

21. A. S. J. Suiker and N. A. Fleck. Frictional collapse of granular assemblies. *ASME Journal of Applied Mechanics*, 71:350–358, 2004.

22. C. O'Hern, L. E. Silbert, A. J. Liu, and S. R. Nagel. Jamming at zero temperature and zero applied stress: The epitome of disorder. *Phys. Rev. E*, 68(1):011306, 2003.

23. H. P. Zhang and H. A. Makse. Jamming transition in emulsions and granular materials. *Phys. Rev. E*, 72:011301, 2005.

24. M. Wyart. On the rigidity of amorphous solids. *Annales de Physique Fr.*, 30:1–96, 2006.

25. Ellák Somfai, Martin van Hecke, Wouter G. Ellenbroek, Kostya Shundyak, and Wim van Saarloos. Critical and noncritical jamming of frictional grains. *Phys. Rev. E*, 75(2):020301, 2007.

26. L. La Ragione and V. Magnanimo. Contact anisotropy and coordination number for a granular assembly: A comparison of distinct-element-method simulations and theory. *Phys. Rev. E*, page 031304, 2012.

27. L. La Ragione and V. Magnanimo. Evolution of the effective moduli of an anisotropic, dense, granular material. *Granular Matter*, 14:749–757, 2012.
28. M. H. Khalili, J.-N. Roux, J.-M. Pereira, S. Brisard, and M. Bornert. Numerical simulation of one-dimensional compression of granular materials: II. Elastic moduli, stresses and microstructure. *Phys. Rev. E*, 95:032908, 2017.
29. F. Radjaï, H. Troadec, and S. Roux. Basic features of granular plasticity. In S. J. Antony, W. Hoyle, and Y. Ding, editors, *Granular Materials: Fundamentals and Applications*, pages 157–183, Cambridge, 2004. Royal Society of Chemistry.
30. F. Radjaï, J.-Y. Delenne, E. Azéma, and S. Roux. Fabric evolution and accessible geometrical states in granular materials. *Granular Matter*, 14:259–264, 2012.
31. E. Azéma, F. Radjaï, and F. Dubois. Packings of irregular polyhedral particles: Strength, structure, and effects of angularity. *Phys. Rev. E*, 87:062223, 2013.
32. M. Jean. The non-smooth contact dynamics method. *Computational Methods in Applied Engineering*, pages 235–257, 1999.
33. F. Radjaï and V. Richefeu. Contact dynamics as a nonsmooth discrete element method. *Mechanics of Materials*, 41:715–728, 2009.
34. Y. Jiang and M. Liu. Granular solid hydrodynamics. *Granular Matter*, 11:139–156, 2009.
35. YM Jiang and M. Liu. Granular Solid Hydrodynamics (GSH): a broad-ranged macroscopic theory of granular media. *Acta Mechanica*, 225:2363–2384, 2014.
36. I. Agnolin and J.-N Roux. Internal states of model isotropic granular packings. I. Assembling process, geometry, and contact networks. *Phys. Rev. E*, 76(6):061302, 2007.
37. I. Agnolin and J.-N Roux. Internal states of model isotropic granular packings. II. Compression and pressure cycles. *Phys. Rev. E*, 76(6):061303, 2007.
38. I. Agnolin and J.-N. Roux. Internal states of model isotropic granular packings. III. Elastic properties. *Phys. Rev. E*, 76(6):061304, 2007.
39. J.-N. Roux. DEM simulations of triaxial tests on dense bead assemblies. Unpublished.
40. C. Dequeker and J.-N. Roux. DEM simulations of triaxial tests of loose bead assemblies. Unpublished results.
41. P.-E. Peyneau and J.-N. Roux. Solidlike behavior and anisotropy in rigid frictionless bead assemblies. *Phys. Rev. E*, 78:041307, 2008.
42. M. H. Khalili, J.-N. Roux, J.-M. Pereira, S. Brisard, and M. Bornert. A numerical study of one-dimensional compression of granular materials: I. Stress-strain behavior, microstructure and irreversibility. *Phys. Rev. E*, 95(032907), 2017.
43. K. L. Johnson. *Contact Mechanics*. Cambridge University Press, 1985.
44. D. Elata and J. G. Berryman. Contact force-displacement laws and the mechanical behavior of random packs of identical spheres. *Mechanics of Materials*, 24:229–240, 1996.
45. M. R. Kuhn and C. S. Chang. Stability, Bifurcation and Softening in Discrete Systems: A Conceptual Approach for Granular Materials. *International Journal of Solids and Structures*, 43:6026–6051, 2006.
46. P.-E. Peyneau and J.-N. Roux. Frictionless bead packs have macroscopic friction, but no dilatancy. *Phys. Rev. E*, 78:011307, 2008.
47. F. Radjaï and C. Voivret. Periodic Boundary Conditions. In Radjaï and Dubois [88], chapter 7, pages 181–198.
48. J.-N. Roux and G. Combe. Quasi-Static Methods. In Radjaï and Dubois [88], chapter 3, pages 67–101.
49. V.-D. Than, S. Khamseh, A. M. Tang, J.-M. Pereira, F. Chevoir, and J.-N. Roux. Basic Mechanical Properties of Wet Granular Materials: A DEM Study. *ASCE Journal of Engineering Mechanics*, 2016.
50. D. M. Mueth, H. M. Jaeger, and S. R. Nagel. Force distribution in a granular medium. *Phys. Rev. E*, 57:3164–3169, 1998.
51. F. Radjaï, S. Roux, and J.-J Moreau. Contact forces in a granular packing. *Chaos*, 9(3):544–550, 1999.

52. D. L. Blair, N. W. Mueggenburg, A. H. Marshall, H.M. Jaeger, and S. R. Nagel. Force distribution in three-dimensional granular assemblies: Effects of packing order and interparticle friction. *Phys. Rev. E*, 63:041304, 2001.

53. F. Radjai. Modeling force transmission in granular materials. *Comptes Rendus Physique*, 16(1):3–9, 2015.

54. H. A. Makse, D. L. Johnson, and L. M. Schwartz. Packing of compressible granular materials. *Phys. Rev. Lett.*, 84(18):4160–4163, 2000.

55. Y. Okuchi and F. Tatsuoka. Some factors affecting K_0 values of sand measured in triaxial cell. *Soils and Foundations*, 24(3):52–68, 1984.

56. Junhwan Lee, Sup Yun Tae, Dongyeol Lee, and Junghwoon Lee. Assessment of K_0 correlation to strength for granular materials. *Soils and Foundations*, 53(4):584–595, 2013.

57. L. Rothenburg and R.J. Bathurst. Analytical study of induced anisotropy in idealized granular materials. *Géotechnique*, 39:601–614, 1989.

58. C. Thornton. Numerical simulations of deviatoric shear deformation of granular media. *Géotechnique*, 50:43–53, 2000.

59. F. Radjaï and S. Roux. Contact dynamics study of 2d granular media : critical states and relevant internal variables. In H. Hinrichsen and D. E. Wolf, editors, *The Physics of Granular Media*, pages 165–187, Berlin, 2004. Wiley-VCH.

60. L. Rothenburg and N. P. Kruyt. Critical state and evolution of coordination number in simulated granular materials. *International Journal of Solids and Structures*, 41(2):5763–5774, 2004.

61. N. P. Kruyt and L. Rothenburg. Shear strength, dilatancy, energy and dissipation in quasistatic deformation of granular materials. *Journal of Statistical Mechanics: Theory and Experiment*, page P07021, 2006.

62. C. Thornton and L. Zhang. On the evolution of stress and microstructure during general 3D deviatoric straining of granular media. *Géotechnique*, 60(5):333–341, 2010.

63. J. T. Jenkins and L. La Ragione. Particle spin in anisotropic granular materials. *International Journal of Solids and Structures*, 38:1063–1069, 2001.

64. C. Gay and R. A. da Silveira. Anisotropic elastic theory of preloaded granular media. *Europhysics Letters*, 68:51–57, 2004.

65. L. La Ragione and J. T. Jenkins. The initial response of an idealized granular material. *Proceedings of the Royal Society A*, 63(2079):735–758, 2007.

66. I. Agnolin and J.-N. Roux. On the elastic moduli of three-dimensional assemblies of spheres: Characterization and modeling of fluctuations in the particle displacement and rotation. *International Journal of Solids and Structures*, 45(3–4):1101–1123, 2008.

67. E. Somfai, J.-N. Roux, J. H. Snoeijer, M. van Hecke, and W. van Saarloos. Elastic wave propagation in confined granular systems. *Phys. Rev. E*, 72:021301, 2005.

68. J.-N. Roux. Geometric origin of mechanical properties of granular materials. *Phys. Rev. E*, 61:6802–6836, 2000.

69. L. E. Silbert, D. Ertaş, G. S. Grest, T. C. Halsey, and D. Levine. Geometry of frictionless and frictional sphere packings. *Phys. Rev. E*, 65(3):031304, 2002.

70. A. Donev, S. Torquato, and F. H. Stillinger. Pair correlation function characteristics of nearly jammed disordered and ordered hard-sphere solids. *Phys. Rev. E*, 71(1):011105, 2005.

71. M. Baity-Jesi, C.P. Goodrich, A.J. Liu, and J.P. Nagel, S. R. Sethna. Emergent SO(3) Symmetry of the Frictionless Shear Jamming Transition. *Journal of Statistical Physics*, 167:735–748, 2017.

72. A. Duttine, H. Di Benedetto, D. Pham Van Bang, and A. Ezaoui. Anisotropic small strain elastic properties of sands and mixture of sand-clay measured by dynamic and static methods. *Soils and Foundations*, 47(3):457–472, 2007.

73. E. T. Bowman and K. Soga. Creep, ageing and microstructural change in dense granular materials. *Soils and Foundations*, 43:107–117, 2003.

74. Y. Gao, Y.-H. Wang, and J.C.P. Xu. Mechanisms of Aging-Induced Modulus Changes in Sand under Isotropic and Anisotropic Loading. *ASCE J. Geotech. Geoenviron. Eng*, 139:470–482, 2013.

75. I. Vardoulakis and J. Sulem. *Bifurcation Analysis in Geomechanics*. Blackie Academic and Professional, 1995.
76. J. Desrues, R. Chambon, M. Mokni, and F. Mazerolle. Void ratio evolution inside shear bands in triaxial sand specimens studied by computed tomography. *Géotechnique*, 46:529–546, 1996.
77. S. Fazekas, J. Török, and J. Kertész. Critical packing in granular shear bands. *Phys. Rev. E*, 2007.
78. J.-N. Roux and G. Combe. Quasistatic rheology and the origins of strain. *C. R. Physique*, 3:131–140, 2002.
79. G. Combe and J.-N. Roux. Discrete numerical simulations, quasistatic deformation and the origins of strain in granular materials. In di Benedetto et al. [89], pages 1071–1078.
80. J.-N. Roux and G. Combe. How granular materials deform in quasistatic conditions. In Goddard et al. [90], pages 260–270.
81. J.-N. Roux. Pre-peak deformation of model granular materials: A DEM study. In K. Soga, K. Kumar, G. Biscontin, and M. Kuo, editors, *Geomechanics from micro to macro*, pages 49–54. CRC-Press-Taylor & Francis, 2015.
82. S. McNamara, R. García Rojo, and H. J. Herrmann. Indeterminacy and the onset of motion in a simple granular packing. *Phys. Rev. E*, 72:021304, 2005.
83. S. McNamara and H. J. Herrmann. Quasirigidity: some uniqueness issues. *Phys. Rev. E*, 74:061303, 2006.
84. P. R. Welker and S. C. McNamara. What triggers failure in frictional granular assemblies? *Phys. Rev. E*, 79:061305, 2009.
85. F. Froiio and J.-N. Roux. Incremental response of a model granular material by stress probing with DEM simulations. In Goddard et al. [90], pages 260–270.
86. F. Alonso-Marroquin and H. J. Herrmann. Calculation of the incremental stress-strain relation of a polygonal packing. *Phys. Rev. E (2002) 66:021301*, 66:021301, 2005.
87. C Tamagnini, F. Calvetti, and G. Viggiani. An assessment of plasticity theories for modelling the incrementally non-linear behavior of granular soils. *ASCE Journal of Engineering Mechanics*, 52:265–291, 2005.
88. F. Radjaï and F. Dubois, editors. *Discrete-element modeling of granular materials*. Wiley, 2011.
89. H. di Benedetto, T. Doanh, H. Geoffroy, and C. Sauzéat, editors. *Deformation characteristics of geomaterials*, Lisse, 2003. Swets and Zeitlinger.
90. J. D. Goddard, J. T. Jenkins, and P. Giovine, editors. *IUTAM-ISIMM symposium on mathematical modeling and physical instances of granular flow*, volume 1227 of *AIP conference proceedings*. AIP, 2010.

Multiscale Phenomena in Continuum Mechanics: Mesoscopic Justification of Rational Extended Thermodynamics of Gases with Internal Structure

Tommaso Ruggeri

Abstract In many physical systems one encounters situations where phenomena occur at different scales. An example is the modeling of a rarefied gas at varying Knudsen number (Kn). Large Kn corresponds to a case where the Boltzmann equation is the most appropriate model while, for small Kn, one can obtain the Euler or Navier–Stokes–Fourier system. At intermediate regime, using the mathematical methods of Rational Extended Thermodynamics (RET), one can obtain the closure of hyperbolic moment system associated with the Boltzmann equation for monatomic gas. This methodology can be extended to polyatomic gas by considering a distribution function depending on an extra variable that takes into account the internal motion of polyatomic molecule (rotation and vibration). In this survey paper we consider first the state-of-the-art of RET and at the end we give a summary on the recent results about more refined version of RET of polyatomic gas in which molecular rotational and vibrational relaxation processes are treated individually.

1 Thermodynamics of Irreversible Processes

A continuous medium is a continuous distribution of material points which occupy a region of the Euclidean space Ω with boundary Σ. The typical unknown fields depending on space $\mathbf{x} \equiv (x_i)$ $(i = 1, 2, 3)$ and time t are the mass density ρ, the velocity $\mathbf{v} \equiv (v_i)$, the temperature T, the specific internal energy ε, the heat flux $\mathbf{q} \equiv (q_i)$, and the stress tensor $\mathbf{t} \equiv (t_{ij})$ that in the case of a fluid can be decomposed into the equilibrium and non-equilibrium parts:

$$t_{ij} = -p\,\delta_{ij} + \sigma_{ij} = -(p + \Pi)\,\delta_{ij} + \sigma_{<ij>}, \tag{1}$$

T. Ruggeri (✉)
Department of Mathematics and Alma Mater Research Center on Applied Mathematics AM²,
University of Bologna, Bologna, Italy
e-mail: tommaso.ruggeri@unibo.it; http://www.dm.unibo.it/~ruggeri

where p is the equilibrium pressure, δ_{ij} is the Kronecker symbol, and $\sigma \equiv (\sigma_{ij})$ is the viscous stress tensor that is decomposed furthermore into isotropic and deviatoric parts: Π is called the dynamical pressure and $\sigma_{<ij>}$ is the deviatoric (traceless) shear viscosity tensor.

These fields obey two kinds of equations: the *universal balance laws* (valid for all materials) which are typically: Conservation of mass; Balance law of momentum; Balance laws of energy; and the so-called *constitutive equations* that are necessary to close the system and to characterize the constitutive properties of the material in question.

For example in the case of one-component fluid we have:

$$\frac{\partial \rho}{\partial t} + \frac{\partial \rho v_i}{\partial x_i} = 0,$$

$$\frac{\partial \rho v_j}{\partial t} + \frac{\partial}{\partial x_i}(\rho v_i v_j - t_{ij}) = \rho b_j, \tag{2}$$

$$\frac{\partial E}{\partial t} + \frac{\partial}{\partial x_i}(E v_i + q_i - t_{ij} v_j) = \rho b_j v_j + r,$$

where $E = \rho v^2/2 + \rho \varepsilon$ is the total energy that is the sum of the kinetic energy density and the internal energy density, $\mathbf{b} \equiv (b_i)$ and r are, respectively, the external body force and the heat supply. If $\mathbf{b}$ and r vanish, the balance laws become conservation laws.

As is well known the previous system (2) in the absence of external sources can be rewritten, for classical solutions, in the form:

$$\dot{\rho} + \rho \frac{\partial v_j}{\partial x_j} = 0,$$

$$\rho \dot{v}_i - \frac{\partial t_{ij}}{\partial x_j} = 0, \tag{3}$$

$$\rho \dot{\varepsilon} - t_{ij} \frac{\partial v_i}{\partial x_j} + \frac{\partial q_i}{\partial x_i} = 0,$$

where a dot on a quantity denotes the material time derivative operator:

$$\frac{\partial}{\partial t} + v_i \frac{\partial}{\partial x_i}.$$

The specific internal energy ε and the pressure p are considered to be functions of ρ and T that are prescribed by the thermal and caloric equations of state of equilibrium thermodynamics

$$p \equiv p(\rho, T), \qquad \varepsilon \equiv \varepsilon(\rho, T). \tag{4}$$

In order to close the system (3), we need the constitutive relations of σ_{ij} and q_i in terms of the independent fields ρ, v_i, and T. In TIP, such relations are derived in a heuristic manner from the entropy balance equation that is based on the Gibbs equation of the concept of *local equilibrium*.

First of all we need to recall the important contribution by the mathematician Constantin Carathéodory with his fundamental work on the *axiomatic approach of thermodynamics*. He postulated the so-called *principle of inaccessibility* that states [1] (see also [2, 3]): *"In the neighborhood of any equilibrium state of a system (of any number of thermodynamic coordinates), there exist states that are inaccessible by reversible adiabatic processes"*.

Starting with this axiom and using some properties of Pfaffian forms Carathéodory showed how to derive the absolute temperature as integral factor and he justify rigorously the famous Gibbs equation in thermostatics:

$$T\,ds = d\varepsilon - \frac{p}{\rho^2}\,d\rho, \tag{5}$$

where s is the specific entropy density.

In non-equilibrium according to the procedure TIP the concept of local equilibrium is introduced and the Gibbs relation (5) is assumed to be valid. From (5) we have

$$\dot{s} = \frac{1}{T}\left(\dot{\varepsilon} - \frac{p}{\rho^2}\dot{\rho}\right). \tag{6}$$

Elimination of $\dot{\varepsilon}$ and $\dot{\rho}$ in (6) by using (3) gives

$$\rho\dot{s} + \frac{\partial}{\partial x_i}\left(\frac{q_i}{T}\right) = \frac{1}{T}\sigma_{\langle ij\rangle}\frac{\partial v_{\langle i}}{\partial x_{j\rangle}} - \frac{1}{T}\Pi\frac{\partial v_i}{\partial x_i} - \frac{1}{T^2}q_i\frac{\partial T}{\partial x_i},$$

or equivalently:

$$\frac{\partial \rho s}{\partial t} + \frac{\partial}{\partial x_i}\left(\rho s v_i + \frac{q_i}{T}\right) = \frac{1}{T}\sigma_{\langle ij\rangle}\frac{\partial v_{\langle i}}{\partial x_{j\rangle}} - \frac{1}{T}\Pi\frac{\partial v_i}{\partial x_i} - \frac{1}{T^2}q_i\frac{\partial T}{\partial x_i},$$

which can be seen as a balance equation of the entropy with the following interpretation:

$$\text{intrinsic entropy flux :} \quad \Phi_i = \frac{q_i}{T},$$

$$\text{entropy production:} \quad \Sigma = \frac{1}{T}\sigma_{\langle ij\rangle}\frac{\partial v_{\langle i}}{\partial x_{j\rangle}} - \frac{1}{T}\Pi\frac{\partial v_i}{\partial x_i} - \frac{1}{T^2}q_i\frac{\partial T}{\partial x_i}.$$

The entropy production is a sum of products of:

	Dissipative fluxes	Thermodynamic forces
shear stress	$\sigma_{\langle ij \rangle}$	deviatoric velocity gradient $\quad \dfrac{1}{T}\dfrac{\partial v_{<i}}{\partial x_{j>}},$
dynamic pressure	Π	divergence of velocity $\quad -\dfrac{1}{T}\dfrac{\partial v_i}{\partial x_i},$
heat flux	q_i	temperature gradient $\quad -\dfrac{1}{T^2}\dfrac{\partial T}{\partial x_i}.$

From the second law of thermodynamics, the entropy production must be non-negative. Assuming linear relations between the dissipative fluxes and the thermodynamic forces, we have the constitutive equations (phenomenological equations) of the type:

$$\sigma_{\langle ij \rangle} = 2\mu \frac{\partial v_{<i}}{\partial x_{j>}} \qquad \mu \geq 0,$$

$$\Pi = -\nu \frac{\partial v_i}{\partial x_i} \qquad \nu \geq 0, \qquad (7)$$

$$q_i = -\kappa \frac{\partial T}{\partial x_i} \qquad \kappa \geq 0.$$

These are known as the constitutive laws of Navier-Stokes and Fourier with μ and ν being the shear and bulk viscosities and κ the thermal conductivity. All of these coefficients may be functions of ρ and T.

Along with the thermal and caloric equations of state, the equations (7) are adopted as the constitutive equations of the thermodynamical of irreversible processes (TIP), and the differential system (3) is closed, i.e., 5 equations for 5 unknowns [4]. The system formed by the balance laws (2) and the constitutive laws (4), (7) is called briefly *Navier–Stokes–Fourier system* and if isothermal *Navier-Stokes system*.

1.1 Equations of Heat and Heat Paradox

In the simplified case of a rigid heat conductor the system of balance equations (3) reduces to that of energy:

$$\rho \dot{\varepsilon} + \frac{\partial q_j}{\partial x_j} = 0, \qquad (8)$$

which, combined with the Fourier equation (7)$_3$ and the caloric equation $\varepsilon \equiv \varepsilon(T)$, provides the classic heat equation, a prototype of a parabolic equation:

$$\frac{\partial T}{\partial t} = \mathcal{D}\Delta T, \qquad \left(\mathcal{D} = \frac{\kappa}{\rho c_V}, \quad c_V = \frac{d\varepsilon}{dT} \right) \tag{9}$$

that, in the simple case of constant $\mathcal{D}$, has the following solution of the Cauchy problem:

$$T(\mathbf{x}, t) = \frac{1}{(4\pi\mathcal{D}t)^{3/2}} \int\limits_{-\infty}^{\infty} T(\mathbf{y}, 0) e^{-\frac{(\mathbf{y}-\mathbf{x})^2}{4\mathcal{D}t}} \, d\mathbf{y}. \tag{10}$$

We notice that $T(\mathbf{x}, t)$ is nonzero for any $\mathbf{x}$ if $t > 0$ even though the initial value $T(\mathbf{x}, 0)$ is nonzero only in a bounded domain. This phenomenon has been sometimes called a paradox, because the temperature perturbations propagate with infinitely large speed. From a mathematical point of view, this is due to the parabolic character of the basic equation (9).

The assertion of infinite speed is, of course, beyond the validity range of TIP. We cannot describe properly such a rapid change by TIP because TIP is based on the local equilibrium assumption. On the other hand, it is well known that Eqs. (9) and (10) have been utilized quite successfully in various practical situations. Indeed, if we take carefully its validity range into account, and if we do not care about its unphysical predictions, we would have useful results from a practical point of view.

There is, however, a situation where the infinite speed should be avoided strictly. It is a relativistic thermodynamic case where propagation speed of a wave should be less or equal to the light speed. How can we construct a new thermodynamic theory that predicts only finite speed of waves by generalizing TIP? Carlo Cattaneo addressed this paradox, and proposed in 1948 a modified Fourier equation which is known as Cattaneo equation [5]:

$$\tau \dot{q}_i + q_i = -\chi \frac{\partial T}{\partial x_i}. \tag{11}$$

Combining (8) with (11) we obtain instead of the classical heat equation an hyperbolic equation called the *telegraph equation*:

$$\tau \frac{\partial^2 T}{\partial t^2} + \frac{\partial T}{\partial t} = \mathcal{D}\Delta T.$$

The importance of hyperbolic equations has its experimental evidence in the so-called second sound, which is a perturbation wave of temperature observed firstly in liquid helium at low temperatures [6] and subsequently in crystals [7]. However Cattaneo equation has several weak points: it can predict negative value

of the temperature and the entropy principle is not satisfied for processes far from equilibrium (see [8] and references therein on this subject).

On the other hand, Cattaneo equation has an empirical genesis and is oversimplified. To find a theoretical justification for hyperbolic systems for heat propagation need the approach of extended thermodynamics as we shall see in Sect. 3.

2 Successive Approach

After the pioneering work of Cattaneo the most fundamental improvements on this subject were done:

– 1949—Grad [9] constructed by kinetic methods the so-called 13 moments fields theory that give a system of hyperbolic type for monatomic rarefied gases.
– 1966—Müller [10] determined, via a continuum approach, a hyperbolic system for a generic gas abandoning the local equilibrium assumption and modifying the Gibbs equations using as extended fields the heat flux and the viscous stress tensor. This was the first version and the begin of *Extended Thermodynamics theory*. This point of view has been adopted by several authors and is the starting point of Extended Irreversible Thermodynamics (EIT), which has gained popularity through the book of Jou et al. [11].
– 1983—Following some criticism of Ruggeri in [12] a revision of ET was proposed by Liu and Müller [13] in a classic context, and by Liu, Müller and Ruggeri in a relativistic framework [14]. This new approach was named *Rational Extended Thermodynamics* (RET) and the main results obtained at that time were summarized in the two editions of the book by Müller and Ruggeri [15, 16].
– 2012—The previous RET theory, being strictly connected with the kinetic theory, suffers from nearly the same limitations as the Boltzmann equation. Indeed, the theory is valid only for rarefied monatomic gases, where the specific internal energy ε and the pressure p are connected by the relation $2\rho\varepsilon = 3p$, and the dynamic pressure Π vanishes identically. In the case of polyatomic gases, on the other hand, the rotational and vibrational degrees of freedom of a molecule, which are not present in monatomic gases, come into play. After several tentative theories, a satisfactory *14-field* ET theory for rarefied polyatomic ones was recently developed by Arima et al. [17]. The recent book of Ruggeri and Sugiyama summarizes this new extension of RET [8].

This list reflects the personal opinion of the present author but of course it is not exhaustive because it is well known that several different approaches on non-equilibrium thermodynamics are present in the literature. A first tentative of comparison between different theories was done in [18].

3 Rational Extended Thermodynamics of Rarefied Monatomic Gas

The kinetic theory describes a state of a rarefied gas through the phase density $f(\mathbf{x}, t, \mathbf{c})$, where $f(\mathbf{x}, t, \mathbf{c})d\mathbf{c}$ is the number density of atoms at point $\mathbf{x}$ and time t that have velocities between $\mathbf{c}$ and $\mathbf{c} + d\mathbf{c}$. The phase density obeys the Boltzmann equation that in the case of absence of external forces reads:

$$\frac{\partial f}{\partial t} + c_i \frac{\partial f}{\partial x_i} = Q, \tag{12}$$

where Q represents the collisional term. Most macroscopic thermodynamic quantities are identified as moments of the phase density

$$F_{k_1 k_2 \cdots k_j} = \int_{\mathbb{R}^3} m f c_{k_1} c_{k_2} \cdots c_{k_j} d\mathbf{c},$$

where m is the mass of a molecule. Due to the Boltzmann equation (12), the moments satisfy an infinite hierarchy of balance laws in which the flux in one equation becomes the density in the next one:

$$\partial_t F + \partial_i F_i = 0$$

$$\swarrow$$

$$\partial_t F_{k_1} + \partial_i F_{ik_1} = 0$$

$$\swarrow$$

$$\partial_t F_{k_1 k_2} + \partial_i F_{ik_1 k_2} = P_{<k_1 k_2>}$$

$$\swarrow \tag{13}$$

$$\partial_t F_{k_1 k_2 k_3} + \partial_i F_{ik_1 k_2 k_3} = P_{k_1 k_2 k_3}$$

$$\vdots$$

$$\partial_t F_{k_1 k_2 \ldots k_n} + \partial_i F_{ik_1 k_2 \ldots k_n} = P_{k_1 k_2 \ldots k_n},$$

$$\vdots$$

where

$$\partial_t = \frac{\partial}{\partial t}, \qquad \partial_i = \frac{\partial}{\partial x_i}$$

and $< \cdots >$ indicates the deviatoric part of a tensor, $(i, k_1, k_2, \cdots = 1, 2, 3)$.

Taking into account that $P_{kk} = 0$, the first five equations are conservation laws and coincide with the mass, momentum, and energy conservation, respectively, while the remaining ones are balance laws.

Remark ET with this hierarchy structure is valid only for *monatomic gases*. In fact due to the previous structure we have from $(13)_2$ that the momentum flux:

$$F_{ik} = \rho v_i v_k - t_{ik},$$

while the trace of $(13)_3$ is the conservation of energy with:

$$F_{ll} = 2\rho\varepsilon + \rho v^2$$

then taking into account (1) we have

$$3p = 2\rho\varepsilon, \qquad \Pi = 0. \tag{14}$$

The first of (14) gives

$$\gamma = \frac{c_p}{c_V} = \frac{5}{3},$$

i.e. monatomic gas; while the second of (14) implies that in monatomic gas the dynamical pressure is identical zero.

When we cut the hierarchy at the density with tensor of rank n, we have the problem of closure because the last flux and the production terms are not in the list of the densities. The first idea of Rational Extended Thermodynamics [16] was, by assumptions to adopt, as differential system, the one with the structure of moments (13) but forgetting that the fields are moments of a distribution function. Then the truncated system at tensorial index n is considered as a phenomenological system of continuum mechanics. As usual in continuum mechanics we consider the quantities (last flux and the production terms) that are not in the list of densities as constitutive functions:

$$F_{k_1 k_2 \ldots k_n k_{n+1}} \equiv F_{k_1 k_2 \ldots k_n k_{n+1}} \left(F, F_{k_1}, F_{k_1 k_2}, \ldots F_{k_1 k_2 \ldots k_n} \right)$$

$$P_{k_1 k_2 \ldots k_j} \equiv P_{k_1 k_2 \ldots k_j} \left(F, F_{k_1}, F_{k_1 k_2}, \ldots F_{k_1 k_2 \ldots k_n} \right), \qquad (2 \leq j \leq n).$$

According to the continuum theory, the restrictions on the constitutive equations come only from *universal principles*, i.e.: *Entropy principle*, *Objectivity Principle*,

and *Causality and Stability* (convexity of the entropy). The most interesting physical cases were the 13 fields theory [13]:

$$\partial_t F + \partial_i F_i = 0$$
$$\partial_t F_{k_1} + \partial_i F_{ik_1} = 0$$
$$\partial_t F_{k_1 k_2} + \partial_i F_{ik_1 k_2} = P_{<k_1 k_2>}$$
$$\partial_t F_{k_1 jj} + \partial_i F_{ik_1 jj} = P_{k_1 jj}.$$

The surprising result is that the closure adopted by the Rational Extended Thermodynamics via phenomenological approach gives the same differential system obtained by Grad using the well known 13 moments perturbation method of the Maxwellian in terms of Hermite polynomials [16].

4 Closure via the Maximum Entropy Principle and Molecular RET of Monatomic Gases

If the number of moments increases, it is too difficult to adopt the pure continuum approach for a system with such a large number of field variables. Therefore it is necessary to recall that the field variables are the moments of a distribution function truncated at some order. And then the closure of the balance equations of the moments, which is known as the *Maximum Entropy Principle* (MEP), should be introduced. This approach was called by Müller and Ruggeri *Molecular Extended Thermodynamics* [15]. The principle of maximum entropy has its root in statistical mechanics. It is developed by Jaynes [19] in the context of the theory of information basing on the Shannon entropy. Nowadays the importance of MEP is recognized fully due to the numerous applications in many fields, for example, in the field of computer graphics.

MEP states that the probability distribution that represents the current state of knowledge in the best way is the one with the largest entropy.

Another way of stating this is as follows: *Take precisely stated prior data or testable information about a probability distribution function. Then consider the set of all trial probability distributions that would encode the prior data. Of those, one with maximal information entropy is the proper distribution, according to this principle.*

Concerning the applicability of MEP in non-equilibrium thermodynamics, this was originally by the observation made by Kogan [20] that Grad's distribution function maximizes the entropy. The MEP closure was proposed in RET for the first time by Dreyer in 1987 [21]. In this way the closure of 13-moment theory can be obtained in three different ways: RET, Grad, and MEP. A remarkable point is that all closures are equivalent to each other!

In 1993 the MEP procedure was then generalized by Müller and Ruggeri to the case of any number of moments in the first edition of their book [15] proving that the system is symmetric hyperbolic if the Lagrange multipliers are chosen as field variables. The complete equivalence between the entropy principle closure and the MEP ones in molecular extended thermodynamics was finally proved by Boillat and Ruggeri in 1997 [22] who proved that the Lagrange multipliers coincide with the so-called *main field* that symmetrize any hyperbolic system compatible with a convex entropy law [23, 24].

The RET has been successful because several experiments are in agreement with the theory (sound waves in high frequencies, light scattering, shock waves) [16]. Nevertheless it has two limitations:

1. The theory is valid only for monatomic rarefied gas.
2. The theory is substantially valid only near equilibrium.

5   Polyatomic Gases

In 2012 Arima et al. [17] deduced a 14-fields phenomenological theory for polyatomic rarefied gas using the universal principles of RET postulating a double hierarchy of equations. We do not discuss here this macroscopic theory. The interested reader may consult the original paper [17] or the book [8]. Instead we want to recall the molecular approach in the present case of polyatomic gas. The first question is that "does a macroscopic system have a kinetic counterpart?" The idea first developed by Borgnakke and Larsen [25] and successively reconsidered in more mathematical aspects by Bourgat et al. [26] to have a kinetic theory of polyatomic gas is to assume that the distribution function $f(t, \mathbf{x}, \mathbf{c}, I)$ defined on extended domain $[0, \infty) \times \mathbb{R}^3 \times \mathbb{R}^3 \times [0, \infty)$ depends on an additional continuous variable I representing the energy of the internal mode. Its rate of change is determined by the Boltzmann equation which has the same form as for monatomic gas (12), but collision integral $Q(f)$ takes into account the influence of internal degrees of freedom through collisional cross section.

5.1   Equilibrium Distribution Function for Polyatomic Gases

In the present approach the collision invariants form a vector with five components:

$$\boldsymbol{\psi}(\mathbf{c}, I) = \left(m, mc_i, \frac{1}{2}mc^2 + I \right)^T,$$

which lead to hydrodynamic variables in the form:

$$
\begin{pmatrix} \rho \\ \rho v_i \\ \frac{1}{2}\rho v^2 + \rho\varepsilon \end{pmatrix} = \int_{\mathbb{R}^3} \int_0^\infty \boldsymbol{\psi}(\mathbf{c}, I) f(t, \mathbf{x}, \mathbf{c}, I)\varphi(I)\, dI\, d\mathbf{c}. \tag{15}
$$

Here $\varphi(I)\,dI$ represents the number of internal modes between I and $I+dI$. Entropy is defined by the following relation:

$$
h = \rho s = -k_B \int_{\mathbb{R}^3} \int_0^\infty f \log f\varphi(I)\, dI\, d\mathbf{c}, \tag{16}
$$

where k_B i the Boltzmann constant. We shall introduce the peculiar velocity $\mathbf{C} \equiv (C_i)$:

$$
\mathbf{C} = \mathbf{c} - \mathbf{v}, \qquad C^2 = C_i C_i
$$

and rewrite the Eq. (15) in terms of it. Then

$$
\begin{pmatrix} \rho \\ 0_i \\ 2\rho\varepsilon \end{pmatrix} = \int_{\mathbb{R}^3} \int_0^\infty m \begin{pmatrix} 1 \\ C_i \\ C^2 + 2I/m \end{pmatrix} f(t, \mathbf{x}, \mathbf{C}, I)\varphi(I)\, dI\, d\mathbf{C}.
$$

Note that the internal energy density can be divided into the translational part $\rho\varepsilon_K$ and the part related to the internal degrees of freedom $\rho\varepsilon_I$:

$$
\rho\varepsilon_K = \int_{\mathbb{R}^3} \int_0^\infty \frac{1}{2}mC^2 f(t, \mathbf{x}, \mathbf{C}, I)\varphi(I)\, dI\, d\mathbf{C},
$$

$$
\rho\varepsilon_I = \int_{\mathbb{R}^3} \int_0^\infty I f(t, \mathbf{x}, \mathbf{C}, I)\varphi(I)\, dI\, d\mathbf{C}. \tag{17}
$$

The former can be related to the kinetic temperature in the following way:

$$
\varepsilon_K = \frac{3}{2}\frac{k}{m}T, \tag{18}
$$

whereas the latter is the energy contribution of internal degrees of freedom to the internal energy, which is determined by

$$
\varepsilon_I = \varepsilon - \varepsilon_K. \tag{19}
$$

Pavic et al. [27][1] firstly considered the five moments of Euler fluids and they proved using MEP that the distribution function in equilibrium that maximizes the entropy has the form:

$$f_E = \frac{\rho}{m\,A(T)} \left(\frac{m}{2\pi k_B T}\right)^{3/2} \exp\left\{-\frac{1}{k_B T}\left(\frac{1}{2}mC^2 + I\right)\right\}, \tag{20}$$

where

$$A(T) = \int_0^\infty \exp\left(-\frac{I}{k_B T}\right)\varphi(I)dI. \tag{21}$$

This is a generalization of the Maxwellian distribution function to the case of polyatomic gas and was obtained first with different arguments in [26].

Non-polytropic Gas In the case of ideal non-polytropic gases the specific heat $c_v = d\varepsilon(T)/dT$ is, in general, a non-linear function of the temperature and the caloric and thermal equations of state read:

$$\varepsilon \equiv \varepsilon(T), \qquad p = \frac{k_B}{m}\rho T = \frac{2}{3}\rho\varepsilon_K.$$

As c_v can be measured by experiments as a function of the temperature T we can obtain the specific internal energy ε as

$$\varepsilon(T) = \frac{k_B}{m}\int_{T_0}^T \hat{c}_v(T')\,dT', \tag{22}$$

where $\hat{c}_v = (m/k_B)c_v$ is the dimensionless specific heat and T_0 is an inessential reference temperature.

From (17), inserting the equilibrium distribution (20) and taking into account (21), we obtain the internal energy at equilibrium due to the internal motion:

$$\varepsilon_I(T) = \frac{k_B}{m}T^2\frac{d\log A(T)}{dT}, \tag{23}$$

with ε_K given by (18).

Therefore if we know the caloric equation of state (22) we know from (19) the expression of ε_I and from (23) we can obtain $A(T)$:

$$A(T) = A_0 \exp\left(\frac{m}{k_B}\int_{T_0}^T \frac{\varepsilon_I(T')}{T'^2}dT'\right),$$

---

[1]In this paper there are some misprints and therefore interested reader can check also Chapter 6 of the book [8].

where A_0 and T_0 are inessential constants. As it was observed in [28] and in [29], the function A is, according to (21), the Laplace transform of φ:

$$A(s) = \mathcal{L}[\varphi(I)](s) = \int_0^\infty e^{-sI}\varphi(I)dI, \qquad s = \frac{1}{k_B T},$$

and then we can obtain the weighting function φ as the inverse Laplace transform of A:

$$\varphi(I) = \mathcal{L}^{-1}[A(s)].$$

Polytropic Gas In the polytropic case c_v is constant and the internal energy is linear in the temperature:

$$\varepsilon(T) = \frac{D}{2}\frac{k_B}{m}T,$$

where D is the number of degrees of freedom of a molecule. This is a particular case of the previous non-polytropic case and we obtain the following weighting function:

$$\varphi(I) = I^\alpha, \quad \text{with} \quad \alpha = \frac{D-5}{2} > -1$$

and

$$A(T) = (k_B T)^{1+\alpha}\Gamma(1+\alpha),$$

where Γ is the gamma function.

Observe that model for a monatomic gas ($D = 3$) cannot be recovered from the one with continuous internal energy, since the value of parameter α in monatomic case violates the overall restriction $\alpha > -1$ but can be considered only as singular limit for $\alpha \to -1$.

5.2 The Closure of 14-Field Model of Polyatomic Gas

Pavić, Ruggeri and Simić after they considered the case of 14 moments in the case of polytropic gas [27] considering the same binary hierarchy proposed in the macroscopic approach [30]:

$$\partial_t F + \partial_k F_k = 0,$$

$$\partial_t F_i + \partial_k F_{ik} = 0,$$

$$\partial_t F_{ij} + \partial_k F_{ijk} = P_{ij}, \qquad \partial_t G_{ll} + \partial_k G_{llk} = 0,$$

$$\partial_t G_{lli} + \partial_k G_{llik} = Q_{lli},$$

where F is the mass density, F_i is the momentum density, G_{ii} is the energy density, F_{ij} is the momentum flux, and G_{lli} is the energy flux. And F_{ijk} and G_{llik} are the fluxes of F_{ij} and G_{lli}, respectively, and P_{ij} and Q_{lli} are the productions with respect to F_{ij} and G_{lli}, respectively. In the present case they take into account that the fields are moments of the generalized distribution function in this way:

$$
\begin{pmatrix} F \\ F_{i_1} \\ F_{i_1 i_2} \\ F_{i_1 i_2 i_3} \end{pmatrix} = \int_{\mathbb{R}^3} \int_0^\infty m \begin{pmatrix} 1 \\ c_{i_1} \\ c_{i_1} c_{i_2} \\ c_{i_1} c_{i_2} c_{i_3} \end{pmatrix} f(t, \mathbf{x}, \mathbf{c}, I)\, \varphi(I)\, dI\, d\mathbf{c},
$$

$$
\begin{pmatrix} G_{ll} \\ G_{llk_1} \\ G_{llk_1 k_2} \end{pmatrix} = \int_{\mathbb{R}^3} \int_0^\infty m \begin{pmatrix} c^2 + 2\frac{I}{m} \\ \left(c^2 + 2\frac{I}{m}\right) c_{k_1} \\ \left(c^2 + 2\frac{I}{m}\right) c_{k_1} c_{k_2} \end{pmatrix} f(t, \mathbf{x}, \mathbf{c}, I)\, \varphi(I)\, dI\, d\mathbf{c}.
$$

For the entropy defined by (16), the following variational problem, expressing the maximum entropy principle, can be formulated: determine the velocity distribution function $f(t, \mathbf{x}, \mathbf{c}, I)$ such that $h \to$ max., being subjected to the constraints of prescribed 14 moments. The solution near an equilibrium state is that the distribution function, which maximizes the entropy with weighting function $\varphi(I) = I^\alpha$, has the form:

$$
f = f_E \left\{ 1 - \frac{\rho}{p^2} q_i C_i + \frac{\rho}{p^2} \left[-\sigma_{\langle ij \rangle} + \left(\frac{5}{2} + \alpha \right) (1 + \alpha)^{-1} \Pi \delta_{ij} \right] C_i C_j \right.
$$

$$
\left. - \frac{3}{2(1 + \alpha)} \frac{\rho}{p^2} \Pi \left(\frac{1}{2} C^2 + \frac{I}{m} \right) + \left(\frac{7}{2} + \alpha \right)^{-1} \frac{\rho^2}{p^3} q_i \left(\frac{1}{2} C^2 + \frac{I}{m} \right) C_i \right\},
$$

$$(24)$$

where f_E is the equilibrium distribution (20). The non-equilibrium distribution (24) reduces to the velocity distribution obtained by Mallinger for gases composed of diatomic molecules ($\alpha = 0$). Again as in the monatomic case also in polyatomic gas for any $\alpha > -1$, the closure gives exactly the same equations obtained previously by using the macroscopic approach [17]:

$$
\dot{\rho} + \rho \frac{\partial v_k}{\partial x_k} = 0,
$$

$$
\rho \dot{v}_i + \frac{\partial p}{\partial x_i} + \frac{\partial \Pi}{\partial x_i} - \frac{\partial \sigma_{\langle ij \rangle}}{\partial x_j} = 0,
$$

$$
\dot{T} + \frac{2}{D \frac{k_B}{m} \rho} (p + \Pi) \frac{\partial v_k}{\partial x_k} - \frac{2}{D \frac{k_B}{m} \rho} \frac{\partial v_i}{\partial x_k} \sigma_{\langle ik \rangle} + \frac{2}{D \frac{k_B}{m} \rho} \frac{\partial q_k}{\partial x_k} = 0,
$$

$$\dot{\sigma}_{\langle ij\rangle} + \sigma_{\langle ij\rangle}\frac{\partial v_k}{\partial x_k} - 2\Pi\frac{\partial v_{\langle i}}{\partial x_{j\rangle}} + 2\frac{\partial v_{\langle i}}{\partial x_k}\sigma_{\langle j\rangle k\rangle} - \frac{4}{D+2}\frac{\partial q_{\langle i}}{\partial x_{j\rangle}} - 2p\frac{\partial v_{\langle i}}{\partial x_{j\rangle}} = -\frac{1}{\tau_S}\sigma_{\langle ij\rangle},$$

$$\dot{\Pi} + \frac{5D-6}{3D}\Pi\frac{\partial v_k}{\partial x_k} - \frac{2(D-3)}{3D}\frac{\partial v_{\langle i}}{\partial x_{k\rangle}}\sigma_{\langle ik\rangle} + \frac{4(D-3)}{3D(D+2)}\frac{\partial q_k}{\partial x_k} + \frac{2(D-3)}{3D}p\frac{\partial v_k}{\partial x_k} = -\frac{1}{\tau_\Pi}\Pi,$$

$$\dot{q}_i + \frac{D+4}{D+2}q_i\frac{\partial v_k}{\partial x_k} + \frac{2}{D+2}q_k\frac{\partial v_k}{\partial x_i} + \frac{D+4}{D+2}q_k\frac{\partial v_i}{\partial x_k}$$

$$+\frac{k_B}{m}T\frac{\partial \Pi}{\partial x_i} - \frac{k_B}{m}T\frac{\partial \sigma_{\langle ik\rangle}}{\partial x_k} + \Pi\left[-\frac{\frac{k_B}{m}T}{\rho}\frac{\partial \rho}{\partial x_i} + \frac{D+2}{2}\frac{k_B}{m}\frac{\partial T}{\partial x_i} - \frac{1}{\rho}\frac{\partial \Pi}{\partial x_i} + \frac{1}{\rho}\frac{\partial \sigma_{\langle ik\rangle}}{\partial x_k}\right]$$

$$-\sigma_{\langle ik\rangle}\left[-\frac{\frac{k_B}{m}T}{\rho}\frac{\partial \rho}{\partial x_k} + \frac{D+2}{2}\frac{k_B}{m}\frac{\partial T}{\partial x_k} - \frac{1}{\rho}\frac{\partial \Pi}{\partial x_k} + \frac{1}{\rho}\frac{\partial \sigma_{\langle pk\rangle}}{\partial x_p}\right]$$

$$+\frac{D+2}{2}\left(\frac{k_B}{m}\right)^2\rho T\frac{\partial T}{\partial x_i} = -\frac{1}{\tau_q}q_i, \tag{25}$$

where τ_S, τ_Π, and τ_q are the relaxation times. The Navier–Stokes Fourier theory is contained in the present theory as a limit of small relaxation times (the Maxwellian iteration [31]) as shown in [17].

The monatomic gas limit $D \to 3$ is a singular limit. It is possible to prove that the 14 equations (25) and the solutions of the system converge to the 13 equations and solutions of monatomic gas with $\Pi = 0$, respectively, provided that the initial data are chosen in such a way that the data are compatible with a monatomic gas, i.e., $\Pi(\mathbf{x}, 0) = 0$ [32].

6   The General Hierarchy of Moment Equations for Polyatomic Gases

In non-equilibrium motivated by the idea of phenomenological ET, we shall generalize the moment equations for polyatomic gases by constructing two independent hierarchies. One will be much alike classical "*momentum*" hierarchy of monatomic gases (*F*-hierarchy); the other one, "*energy*" hierarchy, commences with the moment related to the energy collision invariant and proceeds with standard increase of the order through multiplication by velocities (*G*-hierarchy). They read [27, 33]:

$$\partial_t F + \partial_i F_i = 0,$$

$$\partial_t F_{k_1} + \partial_i F_{ik_1} = 0,$$

$$\partial_t F_{k_1 k_2} + \partial_i F_{i k_1 k_2} = P_{k_1 k_2}, \qquad\qquad \partial_t G_{kk} + \partial_i G_{ikk} = 0,$$

$$\vdots \qquad\qquad\qquad\qquad\qquad \partial_t G_{kk j_1} + \partial_i G_{kk i j_1} = Q_{kk j_1},$$

$$\vdots \qquad\qquad\qquad\qquad\qquad\qquad \vdots$$

$$\partial_t F_{k_1 k_2 \ldots k_N} + \partial_i F_{i k_1 k_2 \ldots k_N} = P_{k_1 k_2 \ldots k_N}, \qquad \vdots$$

$$\partial_t G_{kk j_1 j_2 \ldots j_M} + \partial_i G_{kk i j_1 j_2 \ldots j_M}$$

$$= Q_{kk j_1 j_2 \ldots j_M}.$$

The particular case are ($N = 1$, $M = 0$) and ($N = 2$, $M = 1$), which correspond to the Euler system and the 14-field system, respectively. The interested reader can see the results in this general case in [8, 33, 34].

7   RET with Different Molecular Relaxations Processes

It is evident, however, that the ET theory of polyatomic gases with the binary hierarchy has the limitation of its applicability, although the theory has been successfully utilized to analyze various non-equilibrium phenomena. In fact, we have many experimental data showing that the relaxation times of the rotational mode and of the vibrational mode are quite different to each other. In such a case, more than one molecular relaxation processes should be taken into account to make the ET theory more precise. In order to describe the relaxation processes of rotational and vibrational modes separately, Arima, Ruggeri and Sugiyama, first in the case of 7 fields [35] and then in the general case of 15 fields [36], proposed to decompose the energy of internal modes I as the sum of the energy of rotational mode I^R and the energy of vibrational mode I^V:

$$I = I^R + I^V.$$

Generalizing the Borgnakke–Larsen idea, we assume the same form of the Boltzmann equation with a velocity distribution function that depends on these additional parameters, i.e., $f \equiv f\left(\mathbf{x}, \mathbf{c}, t, I^R, I^V\right)$. And we also take into account the effect of the parameters I^R and I^V on the collision term $Q(f)$.

Let us introduce three kinds of moments F, H^R, and H^V as follows:

$$F_{i_1 \ldots i_j} = \int_{R^3} \int_0^\infty \int_0^\infty m c_{i_1} \cdots c_{i_j} f\, \varphi\left(I^R\right) \psi\left(I^V\right) dI^R dI^V d\mathbf{c},$$

$$H^R_{ll i_1 \ldots i_k} = \int_{R^3} \int_0^\infty \int_0^\infty 2 I^R c_{i_1} \cdots c_{i_k} f\, \varphi\left(I^R\right) \psi\left(I^V\right) dI^R dI^V d\mathbf{c},$$

$$H^V_{ll i_1 \ldots i_l} = \int_{R^3} \int_0^\infty \int_0^\infty 2 I^V c_{i_1} \cdots c_{i_l} f\, \varphi\left(I^R\right) \psi\left(I^V\right) dI^R dI^V d\mathbf{c},$$

where $j, k, l = 1, 2, \cdots$. From the Boltzmann equation (12), we obtain three hierarchies (a triple hierarchy) of balance equations, i.e., F, H^R, and H^V-hierarchies in the following form:

$$\partial_t F + \partial_i F_i = 0,$$

$$\partial_t F_{i_1} + \partial_i F_{ii_1} = 0,$$

$$\partial_t F_{i_1 i_2} + \partial_i F_{ii_1 i_2} = P^K_{i_1 i_2}, \qquad \partial_t H^R_{ll} + \partial_i H^R_{lli} = P^R_{ll}, \qquad \partial_t H^V_{ll} + \partial_i H^V_{lli} = P^V_{ll}, \tag{26}$$

$$\partial_t F_{i_1 i_2 i_3} + \partial_i F_{ii_1 i_2 i_3} = P^K_{i_1 i_2 i_3}, \quad \partial_t H^R_{lli_1} + \partial_i H^R_{llii_1} = P^R_{lli_1}, \quad \partial_t H^V_{lli_1} + \partial_i H^V_{llii_1} = P^V_{lli_1},$$

$$\vdots \qquad\qquad\qquad\qquad \vdots \qquad\qquad\qquad\qquad \vdots$$

where the production terms are related to the collision term as follows:

$$P^K_{i_1 \ldots i_j} = \int_{R^3} \int_0^\infty \int_0^\infty m c_{i_1} \cdots c_{i_j} Q(f) \varphi \left(I^R \right) \psi \left(I^V \right) dI^R dI^V d\mathbf{c},$$

$$P^R_{lli_1 \ldots i_k} = \int_{R^3} \int_0^\infty \int_0^\infty 2 I^R c_{i_1} \cdots c_{i_k} Q(f) \varphi \left(I^R \right) \psi \left(I^V \right) dI^R dI^V d\mathbf{c},$$

$$P^V_{lli_1 \ldots i_l} = \int_{R^3} \int_0^\infty \int_0^\infty 2 I^V c_{i_1} \cdots c_{i_l} Q(f) \varphi \left(I^R \right) \psi \left(I^V \right) dI^R dI^V d\mathbf{c}.$$

We notice that the first and second equations of the F-hierarchy represent the conservation laws of mass and momentum, while the sum of the balance equations of F_{ll}, H^R_{ll}, and H^R_{ll} represents the conservation law of energy with

$$Q_{ll} = P^K_{ll} + P^R_{ll} + P^V_{ll} = 0.$$

In each of the three hierarchies, the flux in one equation appears as the density in the next equation. Here $\varphi \left(I^R \right)$ and $\psi \left(I^V \right)$ are the state densities corresponding to I^R and I^V, i.e., $\varphi \left(I^R \right) dI^R$ ($\psi \left(I^V \right) dI^V$) represents the number of internal rotational (vibrational) state between I^R and $I^R + dI^R$ (I^V and $I^V + dI^V$).

7.1 Entropy Law

The entropy density $h = \rho s$, the entropy flux h_i, and the entropy production Σ are defined by

$$h = -k_B \int_{R^3} \int_0^\infty \int_0^\infty f \log f \, \varphi \left(I^R \right) \psi \left(I^V \right) dI^R dI^V d\mathbf{c},$$

$$h_i = -k_B \int_{R^3} \int_0^\infty \int_0^\infty c_i f \log f \, \varphi \left(I^R \right) \psi \left(I^V \right) dI^R dI^V d\mathbf{c}, \qquad (27)$$

$$\Sigma = -k_B \int_{R^3} \int_0^\infty \int_0^\infty Q(f) \log f \, \varphi \left(I^R \right) \psi \left(I^V \right) dI^R dI^V d\mathbf{c}.$$

Then we have the entropy law: $\partial_t h + \partial_i h_i = \Sigma$.

7.2 Equilibrium Distribution Function

We derive the equilibrium distribution function f_E by means of MEP. We remark that the collision invariants of the present model are m, mc_i, and $mc^2 + 2I^R + 2I^V$. These quantities correspond to the hydrodynamics variables, i.e., the mass density $F(= \rho)$, the momentum density $F_i(= \rho v_i)$, and twice the energy density $G_{ll}(= 2\rho\varepsilon + \rho v^2)$:

$$G_{ll} = \int_{R^3} \int_0^\infty \int_0^\infty \left(mc^2 + 2I^R + 2I^V \right) f \, \varphi \left(I^R \right) \psi \left(I^V \right) dI^R dI^V d\mathbf{c}. \qquad (28)$$

It is easy to see, from (28), that the specific internal energy ε is composed of the kinetic, rotational, and vibrational parts, ε^K, ε^R, and ε^V, i.e.,

$$\varepsilon = \varepsilon^K + \varepsilon^R + \varepsilon^V.$$

The equilibrium distribution function f_E, which maximizes the entropy density $(27)_1$ under the constraints that the first five moments are prescribed, is given by

$$f_E = f_E^{(K)} f_E^{(R)} f_E^{(V)} \qquad (29)$$

with

$$f_E^{(K)} = \frac{\rho}{m} \left(\frac{m}{2\pi k_B T} \right)^{3/2} \exp\left(-\frac{mC^2}{2k_B T} \right),$$

$$f_E^{(R)} = \frac{1}{A^R(T)} \exp\left(-\frac{I^R}{k_B T} \right), \qquad f_E^{(V)} = \frac{1}{A^V(T)} \exp\left(-\frac{I^V}{k_B T} \right),$$

where $A^R(T)$ and $A^V(T)$ are normalization factors (partition functions):

$$A^R(T) = \int_0^\infty \varphi\left(I^R\right) e^{-\beta_E I^R} dI^R, \qquad A^V(T) = \int_0^\infty \psi\left(I^V\right) e^{-\beta_E I^V} dI^V.$$

$$(30)$$

Here $\beta_E = 1/(k_B T)$ and T is the equilibrium temperature. For the proof see [29, 35, 37].

Using the equilibrium distribution function f_E, we obtain the caloric and thermal equations of state. The caloric equation of state is given by

$$\varepsilon = \varepsilon_E(T) = \varepsilon_E^K(T) + \varepsilon_E^R(T) + \varepsilon_E^V(T),$$

and we have

$$\varepsilon_E^K(T) \equiv \frac{3}{2}\frac{k_B}{m}T, \quad \varepsilon_E^R(T) \equiv \frac{k_B}{m}T^2\frac{d\log A^R(T)}{dT}, \quad \varepsilon_E^V(T) \equiv \frac{k_B}{m}T^2\frac{d\log A^V(T)}{dT}.$$

$$(31)$$

If the partition functions A^R and A^V are given, for example, by a statistical-mechanical analysis, we obtain the equilibrium energies of rotational and vibrational modes from (31). Vice versa, if we know the caloric equations of state $\varepsilon_E^K(T)$ and $\varepsilon_E^R(T)$, we can obtain, by integration of (31)$_{2,3}$, the partition functions. We remark that the knowledge of the partition functions permits us to obtain, from (30), the measures $\varphi\left(I^R\right)$ and $\psi\left(I^V\right)$ via the inverse Laplace transform. The thermal equation of state is given by

$$p = p^K(\rho, T) \equiv \frac{k_B}{m}\rho T = \frac{2}{3}\rho\varepsilon_E^K(T).$$

The specific entropy density in equilibrium $s_E = h_E/\rho$ is given by

$$s_E(\rho, T) = s_E^K(\rho, T) + s_E^R(T) + s_E^V(T),$$

where

$$s_E^K(\rho, T) \equiv -\frac{k_B}{\rho}\int_{R^3}\int_0^\infty\int_0^\infty f_E \log f_E^{(K)} \varphi\left(I^R\right)\psi\left(I^V\right) dI^R dI^V d\mathbf{c},$$

$$= \frac{k_B}{m}\log\left(\frac{T^{3/2}}{\rho}\right) + \frac{\varepsilon_E^K(T)}{T} - \frac{k_B}{m}\log\left[\frac{1}{m}\left(\frac{m}{2\pi k_B}\right)^{3/2}\right],$$

$$s_E^R(T) \equiv -\frac{k_B}{\rho} \int_{R^3} \int_0^\infty \int_0^\infty f_E \log f_E^{(R)} \, \varphi\left(I^R\right) \psi\left(I^V\right) dI^R dI^V d\mathbf{c},$$

$$= \frac{k_B}{m} \log A^R(T) + \frac{\varepsilon_E^R(T)}{T},$$

$$s_E^V(T) \equiv -\frac{k_B}{\rho} \int_{R^3} \int_0^\infty \int_0^\infty f_E \log f_E^{(V)} \, \varphi\left(I^R\right) \psi\left(I^V\right) dI^R dI^V d\mathbf{c},$$

$$= \frac{k_B}{m} \log A^V(T) + \frac{\varepsilon_E^V(T)}{T}.$$

7.3 Molecular ET Theory with 7 Independent Fields (ET$_7$)

The simplest RET theory with the triple hierarchy is the theory with 7 fields (ET$_7$); mass density, velocity, internal energy of translational mode, internal energy of rotational mode, and internal energy of vibrational mode [35]. The system of balance equations is the system of (26) but truncated at the second-order tensor:

$$\frac{\partial F}{\partial t} + \frac{\partial F_i}{\partial x_i} = 0,$$

$$\frac{\partial F_j}{\partial t} + \frac{\partial F_{ij}}{\partial x_i} = 0,$$

$$\frac{\partial F_{ll}}{\partial t} + \frac{\partial F_{lli}}{\partial x_i} = P_{ll}^K, \qquad \frac{\partial H_{ll}^R}{\partial t} + \frac{\partial H_{lli}^R}{\partial x_i} = P_{ll}^R, \qquad \frac{\partial H_{ll}^V}{\partial t} + \frac{\partial H_{lli}^V}{\partial x_i} = P_{ll}^V.$$

The closure in this simple case is very interesting because as in the previous ET$_6$ [29, 37] can be done in full non-linear way and therefore is not necessary to assume that the processes are near an equilibrium state [35]. On the basis of this theory, it was revealed that the internal energies of the three modes can be characterized by the three non-equilibrium temperatures and the non-equilibrium entropy is expressed in terms of these non-equilibrium temperatures. It was also shown that the dispersion relation derived by ET$_7$ is in excellent agreement with the experimental data of CO_2, Cl_2, and Br_2 gases [35].

7.4 Molecular ET Theory with 15 Independent Fields (ET$_{15}$)

Because the ET$_7$ theory describes the relaxation processes of molecular rotational and vibrational modes satisfactorily, but it ignores the effect of shear stress and heat

flux, a more realistic theory including all these dissipative fluxes was established in [36]. In this case the starting moments are:

$$\frac{\partial F}{\partial t} + \frac{\partial F_i}{\partial x_i} = 0,$$

$$\frac{\partial F_j}{\partial t} + \frac{\partial F_{ij}}{\partial x_i} = 0,$$

$$\frac{\partial F_{ij}}{\partial t} + \frac{\partial F_{ijk}}{\partial x_k} = P_{ij}^K, \qquad \frac{\partial H_{ll}^R}{\partial t} + \frac{\partial H_{lli}^R}{\partial x_i} = P_{ll}^R, \qquad \frac{\partial H_{ll}^V}{\partial t} + \frac{\partial H_{lli}^V}{\partial x_i} = P_{ll}^V,$$

$$\frac{\partial G_{lli}}{\partial t} + \frac{\partial G_{llik}}{\partial x_k} = Q_{lli},$$

$$(32)$$

where $(F_{ijk}, H_{lli}^R, H_{lli}^V, G_{llik})$ and $(P_{ij}^K, P_{ll}^R, P_{ll}^V, Q_{lli})$ are, respectively, the fluxes and productions of the densities $(F_{ij}, H_{ll}^R, H_{ll}^V, G_{lli})$. It is worth emphasizing again that the ET$_{14}$ theory adopts $F, F_i, F_{ij}, G_{ll}(= F_{ll} + H_{ll}^R + H_{ll}^V)$ and G_{lli} as independent fields and the internal modes of a molecule are treated as a unit. On the other hand, ET$_{15}$ describes the rotational and vibrational modes individually. The densities of the system (32) are related to the following conventional field variables:

$$\rho \equiv \int_{R^3} \int_0^\infty \int_0^\infty mf\, \varphi\left(I^R\right) \psi\left(I^V\right) dI^R dI^V d\mathbf{c},$$

$$v_i \equiv \frac{1}{\rho} \int_{R^3} \int_0^\infty \int_0^\infty mc_i f\, \varphi\left(I^R\right) \psi\left(I^V\right) dI^R dI^V d\mathbf{c},$$

$$\varepsilon^K \equiv \frac{1}{2\rho} \int_{R^3} \int_0^\infty \int_0^\infty mC^2 f\, \varphi\left(I^R\right) \psi\left(I^V\right) dI^R dI^V d\mathbf{c},$$

$$\varepsilon^R \equiv \frac{1}{\rho} \int_{R^3} \int_0^\infty \int_0^\infty mI^R f\, \varphi\left(I^R\right) \psi\left(I^V\right) dI^R dI^V d\mathbf{c}, \qquad (33)$$

$$\varepsilon^V \equiv \frac{1}{\rho} \int_{R^3} \int_0^\infty \int_0^\infty mI^V f\, \varphi\left(I^R\right) \psi\left(I^V\right) dI^R dI^V d\mathbf{c},$$

$$\sigma_{\langle ij \rangle} \equiv - \int_{R^3} \int_0^\infty \int_0^\infty mC_{\langle i}C_{j\rangle} f\, \varphi\left(I^R\right) \psi\left(I^V\right) dI^R dI^V d\mathbf{c},$$

$$q_i \equiv \frac{1}{2} \int_{R^3} \int_0^\infty \int_0^\infty (mC^2 + 2I^R + 2I^V)C_i f\, \varphi\left(I^R\right) \psi\left(I^V\right) dI^R dI^V d\mathbf{c}.$$

We define three new variables θ^K, θ^R, and θ^V associated with the specific energies ε^K, ε^R, and ε^V in (33)$_{3,4,5}$ through the caloric equations of state given in (31) [35]:

$$\varepsilon^K = \varepsilon_E^K(\theta^K), \qquad \varepsilon^R = \varepsilon_E^R(\theta^R), \qquad \varepsilon^V = \varepsilon_E^V(\theta^V).$$

Because of the monotonicity of $\varepsilon_E^{K,R,V}$, these are one-to-one relations between the new variables $\theta^{K,R,V}$ and the specific energies $\varepsilon^{K,R,V}$. From (29), the temperature T is determined in an implicit way by the relation:

$$\varepsilon_E(T) = \varepsilon_E^K(\theta^K) + \varepsilon_E^R(\theta^R) + \varepsilon_E^V(\theta^V).$$

The trace part of the momentum flux is related to the pressure p and the dynamic pressure Π in continuum mechanics as follows:

$$F_{ll} = 3(p + \Pi) + \rho v^2.$$

The dynamic pressure is expressed as [37, 38]:

$$\Pi = p^K(\rho, \theta^K) - p^K(\rho, T) = \frac{2}{3}\rho\left(\varepsilon_E^K(\theta^K) - \varepsilon_E^K(T)\right). \tag{34}$$

It is convenient to introduce the following variables, i.e., energy deviations of the three modes from the state with the common temperature T [35, 38–40]:

$$\Delta^K = \varepsilon_E^K(\theta^K) - \varepsilon_E^K(T), \quad \Delta^R = \varepsilon_E^R(\theta^R) - \varepsilon_E^R(T), \quad \Delta^V = \varepsilon_E^V(\theta^V) - \varepsilon_E^V(T).$$

Then, from (34), the dynamic pressure Π is expressed as

$$\Pi = \frac{2}{3}\rho\Delta^K.$$

Proceeding with the usual technique of MEP we obtain for processes near the equilibrium the following closed differential system written with the usual physical symbols:

$$\frac{\partial\rho}{\partial t} + \frac{\partial}{\partial x_i}(\rho v_i) = 0,$$

$$\frac{\partial\rho v_j}{\partial t} + \frac{\partial}{\partial x_i}\left\{[p(\rho,T) + \Pi]\delta_{ij} - \sigma_{\langle ij\rangle} + \rho v_i v_j\right\} = 0,$$

$$\frac{\partial}{\partial t}\left\{2\rho\varepsilon_E(T) + \rho v^2\right\} + \frac{\partial}{\partial x_i}\left\{2q_i + 2\left[\rho\varepsilon(T) + p(\rho,T) + \Pi\right]v_i - 2\sigma_{\langle li\rangle}v_l + \rho v^2 v_i\right\} = 0,$$

$$\frac{\partial}{\partial t}\left\{2\rho\left[\varepsilon_E{}^R(T) + \Delta^R\right]\right\} + \frac{\partial}{\partial x_i}\left\{2\rho\left[\varepsilon_E{}^R(T) + \Delta^R\right]v_i + \frac{2c_v^R(T)}{\frac{k_B}{m} + c_v(T)}q_i\right\} = \hat{P}_{ll}^R,$$

$$\frac{\partial}{\partial t}\left\{2\rho\left[\varepsilon_E{}^V(T) + \Delta^V\right]\right\} + \frac{\partial}{\partial x_i}\left\{2\rho\left[\varepsilon_E{}^V(T) + \Delta^V\right]v_i + \frac{2c_v^V(T)}{\frac{k_B}{m} + c_v(T)}q_i\right\} = \hat{P}_{ll}^V,$$

$$\frac{\partial}{\partial t}\left(-\sigma_{\langle ij\rangle}+\rho v_{\langle i}v_{j\rangle}\right)+\frac{\partial}{\partial x_k}\left\{\frac{2\frac{k_B}{m}}{\frac{k_B}{m}+c_v(T)}q_{\langle i}\delta_{j\rangle k}+2[p(\rho,T)+\Pi]v_{\langle i}\delta_{j\rangle k}\right.$$

$$\left.-\sigma_{\langle ij\rangle}v_k-2\sigma_{\langle k\langle i\rangle}v_{j\rangle}+\rho v_{\langle i}v_{j\rangle}v_k\right\}=\hat{P}^K_{\langle ij\rangle},$$

$$\frac{\partial}{\partial t}\left\{2q_i+2\left[\rho\varepsilon_E(T)+p(\rho,T)+\Pi\right]v_i-2\sigma_{\langle li\rangle}v_l+\rho v^2 v_i\right\}+$$

$$+\frac{\partial}{\partial x_k}\left\{2\left[p(\rho,T)\left(\varepsilon_E(T)+\frac{p(\rho,T)}{\rho}\right)+\Pi\left(\varepsilon_E(T)+2\frac{p(\rho,T)}{\rho}\right)\right]\delta_{ik}\right.$$

$$-2\left[\varepsilon_E(T)+2\frac{p(\rho,T)}{\rho}\right]\sigma_{\langle ik\rangle}+\frac{2\frac{k_B}{m}}{\frac{k_B}{m}+c_v(T)}q_l v_l\delta_{ik}$$

$$+2\left[1+\frac{\frac{k_B}{m}}{\frac{k_B}{m}+c_v(T)}\right](q_i v_k+q_k v_i)+[p(\rho,T)+\Pi]v^2\delta_{ik}$$

$$+2\left[\rho\varepsilon_E(T)+2p(\rho,T)+2\Pi\right]v_i v_k-v^2\sigma_{\langle ik\rangle}-2v_l v_i\delta_{\langle lk\rangle}-2v_l v_k\sigma_{\langle il\rangle}+\rho v^2 v_i v_k\right\}$$

$$=2v_l\hat{P}^K_{il}+\hat{Q}_{lli}.$$

7.5 Three Relaxation Times

In polyatomic gases, we may introduce three characteristic times corresponding to three relaxation processes caused by the molecular collision:

1. Relaxation time τ_K: This characterizes the relaxation process within the translational mode (mode K) of molecules. The process shows the tendency to approach an equilibrium state of the mode K.

2. Relaxation time $\tau_{\mathfrak{bc}}$: There are energy exchanges among the three modes: mode K, rotational mode (mode R), and vibrational mode (mode V). The relaxation process occurs in such a way that two of the three modes (say $(\mathfrak{bc})$ = (KR), (KV), (RV)) approach, after the relaxation time $\tau_{\mathfrak{bc}}$, an equilibrium state characterized by a common temperature $\theta^{\mathfrak{bc}}$.

3. Relaxation time τ of the last stage: after the relaxation process between $\mathfrak{b}$ and $\mathfrak{c}$, all modes, K, R, and V, eventually approach a local equilibrium state characterized by f_E with a common temperature T.

7.6 Generalized BGK Collision Term

The generalized BGK collision term for $(\mathfrak{bc})$-process $((\mathfrak{bc}) = (KR), (KV), (RV))$ is proposed as follows:

$$Q^{\mathfrak{bc}}(f) = -\frac{1}{\tau_K}(f - f_{K:E}) - \frac{1}{\tau_{\mathfrak{bc}}}(f - f_{\mathfrak{bc}:E}) - \frac{1}{\tau}(f - f_E),$$

where the distribution functions $f_{K:E}$ and $f_{\mathfrak{bc}:E}$ are given as follows:

$$f_{K:E} = \frac{\rho^{RV}(I^R, I^V)}{m}\left(\frac{m}{2\pi k_B \theta^K}\right)^{3/2} \exp\left(-\frac{mC^2}{2k_B \theta^K}\right),$$

$$f_{KR:E} = \frac{\rho^V(I^V)}{mA^R(\theta^{KR})}\left(\frac{m}{2\pi k_B \theta^{KR}}\right)^{3/2} \exp\left\{-\frac{1}{k_B \theta^{KR}}\left(\frac{mC^2}{2} + I^R\right)\right\},$$

$$f_{KV:E} = \frac{\rho^R(I^R)}{mA^V(\theta^{KV})}\left(\frac{m}{2\pi k_B \theta^{KV}}\right)^{3/2} \exp\left\{-\frac{1}{k_B \theta^{KV}}\left(\frac{mC^2}{2} + I^V\right)\right\},$$

$$f_{RV:E} = \frac{\rho}{mA^R(\theta^{RV})A^V(\theta^{RV})}\left(\frac{m}{2\pi k_B \theta^K}\right)^{3/2} \exp\left(-\frac{mC^2}{2k_B \theta^K} - \frac{I^R + I^V}{k_B \theta^{RV}}\right),$$

with

$$\rho^{RV}(I^R, I^V) = \int_{\mathbb{R}^3} mf d\mathbf{c},$$

$$\rho^V(I^V) = \int_{\mathbb{R}^3}\int_0^\infty mf\,\varphi\left(I^R\right) dI^R d\mathbf{c}, \quad \rho^V(I^V) = \int_{\mathbb{R}^3}\int_0^\infty mf\,\varphi\left(I^R\right) dI^R d\mathbf{c}.$$

Several works are now in progress with the new ET_{15} theory in particular comparison of dispersion relation between theoretical prediction and experimental data, and the analysis of shock waves.

References

1. Charathédory, C.: Untersuchungen über die Grundlagen der Thermodynamik, Math. Ann. 67 355–386 (1909).
2. Pogliani, L., Berberan-Santos M.N.: Constantin Carathéodory and the axiomatic thermodynamics. Journal of Mathematical Chemistry Vol. 28, N. 1–3, (2000).
3. Boyling, J.B.: Carathéodory's Principle and the Existence of Global Integrating Factors, Commun. math. Phys. 10, , 52–68, (1968).

4. de Groot, S. R., Mazur, P.: *Non-Equilibrium Thermodynamics*; Dover: New York, (1984).
5. Cattaneo C.: Sulla conduzione del calore, Atti Sem. Mat. Fis. Univ. Modena 3, 83–101 (1948).
6. Landau, L.: Theory of the Superfluidity of Helium II, J. Physique U.S.S.R. 5, 71–90 (1941).
7. Peshkov, V.: Second Sound in Helium II, J. Physique U.S.S.R. 8, 381–383 (1944).
8. Ruggeri, T., Sugiyama, M.: Rational Extended Thermodynamics beyond the Monatomic Gas, Springer, Cham Heidelberg New York Dordrecht London (2015).
9. Grad, H.: On the kinetic theory of rarefied gases, Comm. Pure Appl. Math., 2 331–407 (1949).
10. Müller, I.: On the frame dependence of stress and heat flux, Arch. Rat. Mech. Anal. 45, 241–250 (1972).
11. Jou, D., Casas-Vázquez, J., Lebon, G.: Extended Irreversible Thermodynamics. 4th edn., Springer: Berlin, (2010).
12. Ruggeri, T.: Struttura dei sistemi alle derivate parziali compatibili con un principio di entropia e termodinamica estesa, Supplemento Boll. UMI. del GNFM Fisica - Matematica (Volume dedicato al Prof. L. Caprioli nel suo 70 compleanno) 4, 261–279 (1985).
13. Liu, I-S., Müller, I.: Extended thermodynamics of classical and degenerate ideal gases, Arch. Rat. Mech. Anal. 83, 285-332 (1983).
14. Liu, I-S., Müller, I., Ruggeri, T.: Relativistic thermodynamics of Gases, Annals of Physics, 169, 191–219 (1986).
15. Müller, I., Ruggeri, T.: Extended Thermodynamics, Springer Tracts in Natural Philosophy 37 (I edition), Springer-Verlag, New York (1993).
16. Müller, I., Ruggeri, T.: Rational Extended Thermodynamics, Springer Tracts in Natural Philosophy 37 (II edition), Springer-Verlag, New York (1998).
17. Arima, T., Taniguchi, S., Ruggeri, T., Sugiyama, M.: Extended thermodynamics of dense gases, Cont. Mech. Thermodyn. 24, 271–292 (2012).
18. Cimmelli, V. A., Jou, D., Ruggeri, T., Ván, P.: Entropy principle and recent results in non-equilibrium theories. Entropy, 16, 1756–1807 (2014).
19. Jaynes, E. T.: Information Theory and Statistical Mechanics, Phys. Rev., 106, 620-630 (1957). Jaynes, E. T.: Information Theory and Statistical Mechanics II, Phys. Rev., 108, 171- 190 (1957).
20. Kogan M.N.: Rarefied Gas Dynamics, Plenum Press, New York (1969).
21. Dreyer, W.: Maximization of the entropy in non-equilibrium, J. Phys. A: Math. Gen. 20, 6505-6517 (1987).
22. Boillat, G., Ruggeri, T.: Moment equations in the kinetic theory of gases and wave velocities, Continuum Mech. Thermodyn. 9, 205-212 (1997).
23. Boillat, G.: Sur l'existence et la recherche d'équations de conservation supplémentaires pour les systémes hyperboliques, C. R. Acad. Sci. Paris A, 278, 909-912 (1974).
24. Ruggeri, T., Strumia, A.: Main field and convex covariant density for quasi-linear hyperbolic systems. Relativistic fluid dynamics, Ann. Inst. H. Poincaré, Section A, 34, 65-84 (1981).
25. Borgnakke, C., Larsen, P. S.: Statistical Collision Model for Monte Carlo Simulation of Polyatomic Gas Mixture, J. Comput. Phys. 18, 405-420 (1975).
26. Bourgat, J.-F., Desvillettes, L., Le Tallec, P., Perthame, B.: Microreversible collisions for polyatomic gases, Eur. J. Mech. B/Fluids, 13, 237-254(1994).
27. Pavić, M., Ruggeri, T., Simić, S.: Maximum entropy principle for rarefied polyatomic gases, Physica A, 392, 1302- 1317 (2013).
28. Arima, T., Ruggeri, T., Sugiyama, M., Taniguchi, S.: Recent results on nonlinear extended thermodynamics of real gases with six fields Part I: general theory, Ric. Mat., 65, 263–277 (2016).
29. Bisi, M., Ruggeri,T., Spiga, G.: Dynamical pressure in a polyatomic gas: Interplay between kinetic theory and extended thermodynamic, Kinetic and Related Models, 11 (1), 71–95, (2018).
30. Arima, T., Ruggeri, T., Sugiyama, M., Taniguchi, S.: Monatomic Rarefied Gas as a Singular Limit of Polyatomic Gas in Extended Thermodynamics, Phys. Lett. A, 377, 2136–2140 (2013).
31. Ikenberry, E.; Truesdell, C.: On the pressure and the flux of energy in a gas according to Maxwell's kinetic theory. J. Rational Mech. Anal. 5, 1–54 (1956).

32. T. Arima, S. Taniguchi, T. Ruggeri, M. Sugiyama, Monatomic rarefied gas as a singular limit of polyatomic gas in extended thermodynamics, Phys. Lett. A 377, 2136 (2013).
33. Arima, T., Mentrelli, A., Ruggeri, T.: Molecular Extended Thermodynamics of Rarefied Polyatomic Gases and Wave Velocities for Increasing Number of Moments, Annals of Physics 345, 111–140 (2014).
34. Arima, T., Ruggeri, T., Sugiyama, M., Taniguchi, S.: Monatomic gas as a singular limit of polyatomic gas in molecular extended thermodynamics with many moments, Annals of Physics 372, 83-109 (2016).
35. Arima, T.; Ruggeri, T.; Sugiyama, M.: Rational extended thermodynamics of a rarefied polyatomic gas with molecular relaxation processes. Phys. Rev. E, 96, 042143 (2017).
36. Arima, T.; Ruggeri, T.; Sugiyama, M.: Extended Thermodynamics of Rarefied Polyatomic Gases: 15-Field Theory Incorporating Relaxation Processes of Molecular Rotation and Vibration. Entropy, 20, 301 (2018).
37. Ruggeri, T.: Non-linear maximum entropy principle for a polyatomic gas subject to the dynamic pressure. Bull. Inst. Math. Acad. Sin., 11, 1–22 (2016).
38. Arima, T.; Ruggeri, T.; Sugiyama, M.: Duality principle from rarefied to dense gas and extended thermodynamics with six fields. Phys. Rev. Fluids, 2, 013401 (2017).
39. Arima, T.; Sugiyama, M.: Extended thermodynamics of dense polyatomic gases: modeling of molecular energy exchange. Ricerche mat. 68, 91–101 (2019). https://doi.org/10.1007/s11587-018-0386-8.
40. Arima, T. Six-field extended thermodynamics models representing molecular energy exchange in a dense polyatomic gas. J. Phys.: Conf. Ser. 1035, 012002 (2018).

A Multi-Scale Continuum View on Granular Flows

Paolo Maria Mariano

Abstract We review some results related to a nonstandard view on the role of fluctuations in granular flows. The analysis underlines how we can move the boundary between what we intend to be mechanics and what we consider to be thermodynamics, depending on the details we involve in the description of body morphology and related motion.

Keywords Granular matter · Multi-field theories · Dynamics · Grand canonical view · Granular temperature

1 Introduction

Granular materials are sparse media with a grain diameter greater than one micron. In a sense, according to P. G. de Gennes, they can be considered "a new type of condensed matter, as fundamental as a liquid or a solid and showing in fact two states: one fluid-like, one solid-like. But there is as yet no consensus on the description of these two states" [14, p. 1]. Their behavior ranges from fluid-like-type—with no thermal fluctuations as a consequence of grain size—to solid-like-type, the latter pertaining to jammed states with possible nonsymmetric traction-compression response, above all in dry states and at points where confinement exerted by surrounding grains has (let us say) weak character. However, if we leave a part of such a circumstance and we think just of a grain cluster in a jammed state within a certain volume, we realize that grains there can be packed in different configurations. Consequently, a statistical view is an almost necessary intermediate step toward a continuum description of the pertinent mechanics based on a grain-scale knowledge of the material structure. To this aim, we need a sufficiently wide volume to look at so that it contains a number of grains appropriate for computing

P. M. Mariano (✉)
Department of Civil and Environmental Engineering, University of Florence, Firenze, Italy
e-mail: paolomaria.mariano@unifi.it; paolo.mariano@unifi.it

significant statistics. To analyze this case, S. F. Edwards and R. B. S. Oakeshott [16] adopted a microcanonical view and consider equi-probable all mechanically stable configurations occupying the same volume, which plays the role of energy in traditional microcanonical analyses in statistical mechanics. Such an assumption fails when we look at (fast) granular flow because the same control volume in space loses or gains and exchanges energy with the environment, owing to collisions across the boundary. In other words, we have to consider the control volume as a grand canonical ensemble. However, that is not all. In addition to evaluating averages, a further question is how to consider fluctuations. A common measure of fluctuations is the pertinent Reynolds stress tensor, which plays an energetic role and can be considered—and at times it is so—as a granular temperature of tensor character. We can refine the view on fluctuations as proposed in 2003 by G. Capriz [4], a way enhanced in subsequent works [3, 5–9, 21]. In such a view, we decompose fluctuations into an accessory component and a remaining part. Then, we imagine involving the accessory component of fluctuations in the representation of granular flow mechanics at continuum scale [10, 11], by associating true interactions with such a component. They enter a nonstandard tensor moment of momentum balance, which allows us to consider the continuum description of granular flow within the general model-building framework of complex material mechanics, enriched by a low-spatial-scale energy balance associated with the Reynolds stress tensor determined by the spurious fluctuations. This nonstandard view on fluctuations allows us to analyze naturally common anisotropies, such as those we see with the naked eye in falling hail. The view is multi-scale in essence, as it is based on a hierarchical description of the spatial control volume. We review below the skeletal structure of the pertinent theory, merely with the aim of introducing the reader to an approach, which can sew the seed for further fruitful research.

2   Control Volumes as Grand Canonical Ensembles

At any instant τ, we indicate by $\mathcal{B}_\tau$ a (bounded) fit region $\mathcal{B}_\tau$ in the point space $\mathcal{E}$, endowed with Euclidean structure, and taken to be three-dimensional. We attribute to every point $x \in \mathcal{B}_\tau$ properties pertaining to a cluster of grains pictured as mass points, each with mass μ, occupying at the instant τ a control volume $\mathfrak{e}$, a cube of edge δ. We call $\mathfrak{e}$ a *loculus* for the sake of brevity, avoiding a less readable (at least to us) acronym. We write $\mathfrak{e}(x)$ to recall the relationship between $\mathfrak{e}$ and x, among all possible loculi with the same shape, but possibly a different content of molecules, at the instant τ. The length δ must be large enough to allow the loculus to contain a sufficiently populous cluster of grains, a subset of those occupying $x \in \mathcal{B}_\tau$, to allow

significant statistical estimates beyond averages. We assume that the cluster in each loculus, and at each instant τ, may exchange mass with the environment, assuming in this sense the character of a *grand canonical ensemble*.

We may imagine to place each loculus into a copy of the Euclidean space $\mathcal{E}$. In this way, the context the model inhabits is the Cartesian product of Euclidean spaces $\mathcal{E} \times \mathcal{E}_x$, where the subscript x indicates that $\mathcal{E}_x$ contains $\mathfrak{e}(x)$. In other words, we may consider as ambient a fiber bundle with basis $\mathcal{E}$ and typical fiber a copy of $\mathcal{E}$ at every x. In this way, we point out that we consider distinguished and non-overlapping loculi. The geometrical picture formalizes the naive idea of taking two scales in $\mathcal{E}$, one larger than δ, the other smaller. In this view, the loculi constitute a squared tessellation not viewed by a coarse observer—the scale at which we choose x—but recognized at a closer look when an observer able to record a resolution below δ can individualize points within $\mathfrak{e}(x)$, distinguished from x. Although we may find it convenient to exploit the Cartesian product $\mathcal{E} \times \mathcal{E}_x$, embedding the loculus in $\mathcal{E}_x$, events occur only in the physical space. An observer evaluates both scenes at the same time: $\mathcal{E}$ and $\mathcal{E}_x$. When we impose the independence of the observer on some quantity, the rotation tensor entering the requirement is unique on both $\mathcal{E}$ and $\mathcal{E}_x$.

We identify $x \in \mathcal{B}_\tau$ with the mass center of $\mathfrak{e}(x)$. A vector y, issued from x, indicates a generic place in $\mathfrak{e}(x)$, through which a grain with velocity w may transit. A distribution $\Theta(\tau, x; y, w)$ indicates the number of molecules per unit volume, $\Theta \, \mathrm{d}w$, with $\mathrm{d}w$ the vector measure in $\mathcal{V}$, having velocities within the infinitesimal ball $(w + \mathrm{d}w)$ around w. We consider $\Theta(\tau, x; y, w)$ to be regular enough to ensure the significance of the analyses developed below, which involve quantities defined through it.

We define the **number density** θ at y by

$$\theta(\tau, x; y) := \int_{\mathcal{V}} \Theta(\tau, x; y, w) \, \mathrm{d}w,$$

and the **local average velocity** w_* at y by

$$w_*(\tau, x; y) := \theta^{-1} \int_{\mathcal{V}} w\Theta(\tau, x; y, w) \, \mathrm{d}w.$$

The **numerosity** $\omega(\tau, x)$ of all molecules in $\mathfrak{e}(x)$ at time τ is given by

$$\omega(\tau, x) := \int_{\mathfrak{e}(x)} \theta(\tau, x; y) \, \mathrm{d}y.$$

By using ω, we define the **homogenized mass density** $\rho(\tau, x)$ by

$$\rho(\tau, x) := \mu\delta^{-3}\omega(\tau, x).$$

The loculus scale (filtered) **averaged velocity** v is also defined by

$$v(\tau, x) := \delta^{-3} \int_{\mathfrak{e}} \theta w_*(\tau, x; y) \, dy.$$

By assuming for v *differentiability in space*, we also write L for ∇v.

We decompose w_* into the sum of three addenda, namely

$$w_*(\tau, x; y) = v(\tau, x) + B(\tau, x)y + c(\tau, x; y) \tag{1}$$

with B a second-rank tensor depending on τ and x only, c a *remaining fluctuation*, a vector depending on y besides τ and x. The decomposition (1) distinguishes three scales of analysis: the *macroscopic* (or gross) view $v(\tau, x)$, the *mesoscopic* rate $B(\tau, x)$, and the *microscopic* fluctuations c. In fact, besides the average velocity, we consider an affine motion *within* $\mathfrak{e}(x)$, measured at the instant τ, and a *remaining fluctuation* c.

For any orthonormal frame of reference in $\mathfrak{e}(x)$, with origin coinciding with x at the instant τ, we find

$$\int_{\mathfrak{e}(x)} \theta B y \, dy = B \int_{\mathfrak{e}(x)} \theta y \, dy = 0. \tag{2}$$

Consequently, since the average of w_* over the loculus is v, we also get

$$\int_{\mathfrak{e}(x)} \theta c \, dy = 0. \tag{3}$$

We define two second-rank tensors, Y and K, by

$$Y(\tau, x) := \omega^{-1} \int_{\mathfrak{e}(x)} \theta y \otimes y \, dy,$$

and

$$K(\tau, x) := \omega^{-1} \int_{\mathfrak{e}(x)} \theta y \otimes (w_* - v) \, dy.$$

Y is the instantaneous **inertia binor** of the grain cluster in $\mathfrak{e}(x)$. K is the instantaneous **tensor moment of momentum per unit mass**, again for all grains in $\mathfrak{e}(x)$. We choose B, in the decomposition of w_* to be such that

$$K = Y B^T, \tag{4}$$

i.e.,

$$B := K^T Y^{-T} = K^T Y^{-1},$$

a relation accounting for the symmetry and invertibility of Y. The superscript T indicates standard transposition.

The choice (4) imposes

$$\int_{\mathfrak{e}(x)} \theta y \otimes c \, dy = 0 \tag{5}$$

because

$$K = \omega^{-1} \int_{\mathfrak{e}(x)} \theta y \otimes (w_* - v) \, dy$$

$$= \omega^{-1} \int_{\mathfrak{e}(x)} \theta y \otimes y B^T \, dy + \omega^{-1} \int_{\mathfrak{e}(x)} \theta y \otimes c \, dy$$

$$= Y B^T + \omega^{-1} \int_{\mathfrak{e}(x)} \theta y \otimes c \, dy.$$

Definition (4) implies Eq. (5). Vice versa, Eq. (5), taken as a basic assumption about the nature of remaining fluctuations, implies the relation (4).

With the remaining fluctuation velocity c we construct the **Reynolds stress tensor**

$$H(\tau, x) := \omega^{-1} \int_{\mathfrak{e}(x)} \theta c \otimes c \, dy.$$

Its time variation, dragged by B, measures kinetic fluctuations within each loculus.

We may imagine a reference (although fictitious) fixed-in-time arrangement of molecules within the generic loculus and the pertinent Y, indicated by Y_* and linked to Y by a linear mapping G, which can be interpreted as a micro-deformation gradient, such that $Y = GY_*G^T$. Among possible definitions of G (allowed by the arbitrariness in choosing Y_*), we select G as a linear mapping linked to B by the relation

$$\dot{G} + \frac{\sigma}{2}G = BG \tag{6}$$

(see also [9]). Incidentally, when $\sigma = 0$, i.e., when $\text{tr}L = \text{tr}B$, at the scale of the loculus, the reduced equation $\dot{G} = BG$ plays the role of the standard relation $\dot{F} = LF$, with F the macroscopic deformation gradient not defined in the previous lines. With the choices above, we compute

$$\dot{Y} = \dot{G}Y_*G^T + GY_*\dot{G}^T = BY + YB^T - \sigma Y. \tag{7}$$

3 Time Rates

Consider the dynamical system

$$\frac{d\hat{x}}{dt} = v(\tau, x),$$

such that $\hat{x}(\bar{\tau}, x) = x$, and presume that we can integrate it backward in the interval $[\tau_0, \bar{\tau}]$. We write x_0 for $\hat{x}(\tau_0, x)$. For $\hat{x}$, a diffeomorphism, we introduce a placement gradient $F(\bar{\tau}, x_0) = F(\bar{\tau}, \hat{x}(\tau_0, x))$, referred to the flow $\hat{x}^{-1}$ and defined by

$$F := D_{x_0} x,$$

where $x = \hat{x}^{-1}(\bar{\tau}, x_0)$, so that

$$\dot{F} = LF,$$

with

$$\dot{F} = \frac{\partial F}{\partial \tau} + \frac{\partial F}{\partial x_0} \frac{\partial \hat{x}(\tau_0, x)}{\partial x} v,$$

We assume that F preserves the orientation, i.e., its determinant is positive. Euler's lemma implies

$$\frac{\overline{\det F}}{\det F} = \mathrm{tr} L.$$

We also assume to be able to integrate backward in $[\tau_0, \bar{\tau}]$ the velocity By, finding with the same retrogression procedure another placement gradient $\tilde{G}$ such that

$$\dot{\tilde{G}} = B\tilde{G}.$$

As for F, we assume here that $\tilde{G}$ preserves orientation, so that, once again by Euler's formula,

$$\frac{\overline{\det \tilde{G}}}{\det \tilde{G}} = \mathrm{tr} B.$$

Notice that $\tilde{G}$ differs from G defined above. In fact, G refers to a constant Y_*, whereas the pull-back of Y through $\tilde{G}$, i.e., $Y_p := \tilde{G}^{-1} Y \tilde{G}^{-T}$, is not necessarily constant in time. The linear operators F and G do not necessarily coincide. By

referring the two backward integrations determining them to the same interval of time, we define the second-rank tensor

$$\tilde{\tilde{X}} := F\tilde{G}^{-1}$$

as an indicator of the discrepancy between the rearrangement of matter viewed on the different scales of observation involved in the two backward integrations. In the definition of $\tilde{\tilde{X}}$, $\tilde{G}^{-1}$ maps a vector referring to the current arrangement of molecules in the loculus to the cluster at time τ_0. Then, F pushes forward such a vector into the cluster at time $\bar{\tau}$. By direct computation, we get

$$\frac{\overline{\det\tilde{\tilde{X}}}}{\det\tilde{\tilde{X}}} = \frac{\overline{\det F}}{\det F} + \frac{\overline{\det\tilde{G}^{-1}}}{\det\tilde{G}^{-1}},$$

and also

$$\begin{aligned}
\overline{\det\tilde{G}^{-1}} &= \frac{d(\det\tilde{G}^{-1})}{d\tilde{G}^{-1}} \cdot \overline{\tilde{G}^{-1}} = (\det\tilde{G}^{-1})\tilde{G}^T \cdot \frac{d\tilde{G}^{-1}}{d\tilde{G}}[\dot{\tilde{G}}] \\
&= -(\det\tilde{G}^{-1})\tilde{G}^T \cdot \tilde{G}^{-1}\dot{\tilde{G}}\tilde{G}^{-1} = -(\det\tilde{G}^{-1})\tilde{G}^T\tilde{G}^{-T} \cdot B\tilde{G}\tilde{G}^{-1} \\
&= -(\det\tilde{G}^{-1})I \cdot B = -(\det\tilde{G}^{-1})\mathrm{tr}B,
\end{aligned}$$

so that

$$\frac{\overline{\det\tilde{\tilde{X}}}}{\det\tilde{\tilde{X}}} = \mathrm{tr}L - \mathrm{tr}B =: \sigma.$$

The difference σ is a measure of the relative rate of change in volume across the scales determined by the loculus (i.e., *within* the loculus and *inter* neighboring loculi).

Then, we think of a time derivative following the (mesoscopic) locally affine motion with rate By, weighted by the rate of change in volume along the relative flow between the two backward integrations. For A, arbitrarily one of the second-rank tensors Y, K, and H, we indicate by a superposed circle, namely $\mathring{A}$, such a derivative. We define $\mathring{A}$ by

$$\mathring{A} := \frac{1}{\det\tilde{\tilde{X}}}\tilde{G}\overline{(\det\tilde{\tilde{X}})\tilde{G}^{-1}A\tilde{G}^{-T}}\tilde{G}^T,$$

so that

$$\frac{1}{\det\tilde{X}}\tilde{G}\overline{(\det\tilde{X})\tilde{G}^{-1}A\tilde{G}^{-T}\dot{\tilde{G}}^{T}} = \tilde{G}\overline{\tilde{G}^{-1}A\tilde{G}^{-T}}\tilde{G}^{T} + \dot{A} + A\overline{\tilde{G}^{-T}\dot{\tilde{G}}^{T}} + \sigma A$$

$$= \dot{A} - BA - AB^{T} + \sigma A,$$

because, as shown above,

$$\overline{\dot{\tilde{G}^{-1}}} = -\tilde{G}^{-1}B.$$

In the previous expressions,

$$\dot{A} := \frac{\partial A}{\partial \tau} + (\nabla A)v,$$

so that, when $\sigma = 0$, $\overset{\circ}{A}$ reduces to the Oldroyd derivative $\overset{\circ}{A} = \dot{A} - BA - AB^{T}$, with A considered a second-rank tensor with both contravariant components.

The linear operator G has one component in the fictitious reference place, a component on which B does not act because both components of B refer to the loculus at instant τ. Consequently, we define $\overset{\circ}{G}$ by

$$\overset{\circ}{G} := \frac{1}{\sqrt{\det\tilde{X}}}\tilde{G}\overline{(\sqrt{\det\tilde{X}})\tilde{G}^{-1}G},$$

and we have

$$\overset{\circ}{G} = \dot{G} - BG + \frac{\sigma}{2}G.$$

We also define $\overset{\circ}{v}$ to be

$$\overset{\circ}{v} := \frac{1}{\sqrt{\det\tilde{X}}}\overline{(\sqrt{\det\tilde{X}})v},$$

which is

$$\overset{\circ}{v} = \dot{v} + \frac{\sigma}{2}v.$$

In the definition of $\overset{\circ}{v}$, the affine rate B does not appear because v is the velocity of the mass center x of $\mathfrak{e}(x)$, whereas B is the affine rate of grains in the loculus

relative to v. The circumstance implies that if we substitute to A the dyad $v \otimes v$ and compute $\overline{v \overset{\circ}{\otimes} v}$, we get

$$\overline{v \overset{\circ}{\otimes} v} = \overset{\circ}{v} \otimes v + v \otimes \overset{\circ}{v} = \overline{v \overset{\cdot}{\otimes} v} + \sigma v \otimes v = \dot{v} \otimes v + v \otimes \dot{v} + (\frac{\sigma}{2}v) \otimes v + v \otimes (\frac{\sigma}{2}v),$$

i.e., once again, $\overset{\circ}{v} = \dot{v} + \frac{\sigma}{2}v$.

4 Balance of Mass

The mass density $\rho(\tau, x)$ already defined above is a global quantity for $\mathfrak{e}(x)$. Its time variation depends on the change of mass within the loculus. Since $\mathrm{tr}B$ indicates the rate of change in volume of the grain cluster in $\mathfrak{e}(x)$, owing to the affine velocity By, we write

$$\dot{\rho} = -\rho \mathrm{tr}B,$$

where the algebraic sign minus refers to the inflow of mass. This choice implies assuming that the fluctuation c determines a volume-preserving flow.

By adding and subtracting $\rho \mathrm{tr}L$, we get

$$\dot{\rho} + \rho \mathrm{tr}L - \rho \mathrm{tr}L + \rho \mathrm{tr}B = 0,$$

i.e.,

$$\frac{\partial \rho}{\partial \tau} + \mathrm{div}(\rho v) - \sigma \rho = 0.$$

Such a balance corresponds to equating to zero the rate of ρ computed following the flow determined by the backward integration of By, i.e.,

$$\overset{\circ}{\rho} := \frac{1}{\det \tilde{G}} \overline{(\det \tilde{G})\rho}^{\cdot} = 0.$$

5 Observers and Their Changes

Take in the physical space two frames of reference, say $\mathcal{O}$ and $\mathcal{O}'$, differing from one another by a rigid body motion. Write v for the average velocity recorded by $\mathcal{O}$, and v' for that measured by $\mathcal{O}'$. When we pull back the velocity v' into the frame $\mathcal{O}$, the resulting image of v' is the vector given by the standard relation

$$v^\diamond = v + \hat{\mathsf{c}} + \hat{\mathsf{W}}(x - x_0), \tag{8}$$

with x_0 an arbitrary point in space, $\hat{\mathsf{c}}$ a (relative) translational velocity and $\hat{\mathsf{W}}$ a second-rank skew-symmetric tensor indicating the (relative) rotational speed between the two observer considered at instant τ.

Also, consider two frames within the loculus, differing from one another by the *same* rigid body motion considered outside of the loculus. By indicating by $B^\diamond$ the counterpart of $v^\diamond$, we adopt a rule of changes in observers given by

$$B^\diamond = B + \hat{\mathsf{W}}. \tag{9}$$

c is independent of the movement of observers, being a relative velocity, inside the loculus.

6 External Power and Invariance

Two fields describe from a macroscopic view the kinematic mechanisms in the scheme proposed here: the velocity v and the tensor time rate B. Since H has the dimension of an energy, we include it into an inertial argument called upon in the next section.

The symbol $\mathfrak{b}_\tau$ indicates below any inner subset of $\mathcal{B}_\tau$ with non-null volume, which is a fit region, as $\mathcal{B}_\tau$ itself is. We call $\mathfrak{b}_\tau$ a *part*.

For any $\mathfrak{b}_\tau$, we define the *power of the external actions* over it as a functional including bulk and contact actions determined by the kinematic mechanisms described by v and B. We indicate such a power by $\mathcal{P}^{ext}_{\mathfrak{b}_\tau}(v, B)$ and define it by

$$\mathcal{P}^{ext}_{\mathfrak{b}_\tau}(v, B) := \int_{\mathfrak{b}_\tau} (\rho b^\ddagger \cdot v + \rho O^\ddagger \cdot B)\, \mathrm{d}x + \int_{\partial \mathfrak{b}_\tau} (\mathsf{t}_\partial \cdot v + \hat{\mathsf{M}}_\partial \cdot B)\, \mathrm{d}\mathcal{H}^2(x), \tag{10}$$

where $\mathrm{d}\mathcal{H}^2(x)$ is the surface measure over $\partial \mathfrak{b}_\tau$.

We subordinate $\mathcal{P}^{ext}_{\mathfrak{b}_\tau}(v, B)$ to an invariance axiom.

Axiom 1 (Invariance of the External Power) $\mathcal{P}^{ext}_{\mathfrak{b}_\tau}(v, B)$ *is invariant under the rigid body type class of changes in observers described by* (8) *and* (9), *i.e.,*

$$\mathcal{P}^{ext}_{\mathfrak{b}_\tau}(v^\diamond, B^\diamond) = \mathcal{P}^{ext}_{\mathfrak{b}_\tau}(v, B)$$

for any choice of $\hat{\mathsf{c}}$ *and* $\hat{\mathsf{W}}$, *and the part* $\mathfrak{b}_\tau$.

A theorem follows.

Theorem 1 *If we assume as a foundational axiom that* $\mathcal{P}^{ext}_{\mathfrak{b}_\tau}(v, B)$ *is invariant under the rigid body type class of changes in observers described by* (8) *and* (9),

i.e.,

$$\mathcal{P}^{ext,m}_{\mathfrak{b}_\tau}(v^\diamond, B^\diamond) = \mathcal{P}^{ext}_{\mathfrak{b}_\tau}(v, B)$$

for any choice of $\hat{\mathsf{c}}$ and $\hat{\mathsf{W}}$, and the part $\mathfrak{b}_\tau$, the following propositions hold true:

- *If $\sup_{x \in \mathcal{B}_\tau} |\rho b^\ddagger| < +\infty$ and $\mathfrak{t}_\partial$ is continuous in space, $\mathfrak{t}_\partial$ itself depends on $\partial\mathfrak{b}_\tau$ only through the normal n to $\partial\mathfrak{b}_\tau$ at all points in which it is well-defined, i.e.,*

$$\mathfrak{t}_\partial = \mathfrak{t} := \tilde{\mathfrak{t}}(\tau, x, n); \tag{11}$$

and satisfies the action–reaction principle

$$\tilde{\mathfrak{t}}(\tau, x, n) = -\tilde{\mathfrak{t}}(\tau, x, -n) \tag{12}$$

and is linear in the normal n, i.e.,

$$\tilde{\mathfrak{t}}(\tau, x, n) = T(\tau, x)n \tag{13}$$

- *If the bulk action $\rho b^\ddagger$ is continuous in space and the second-rank tensor stress field T is $C^1(\mathcal{B}_\tau) \cap C(\bar{\mathcal{B}}_\tau)$, the following pointwise balance holds:*

$$\rho b^\ddagger + \mathrm{div}T = 0. \tag{14}$$

- *Under the boundedness of bulk actions assumed above, if $\sup_{x \in \mathcal{B}_\tau} |\rho \mathbf{e} O^\ddagger| < +\infty$ and M_∂ is continuous in space, $\hat{\mathsf{M}}_\partial$ itself depends on $\partial\mathfrak{b}_\tau$ only by the normal n to $\partial\mathfrak{b}_\tau$ at all points in which it is well-defined, i.e.,*

$$\hat{\mathsf{M}}_\partial = \hat{\mathsf{M}} := \tilde{\mathsf{M}}(\tau, x, n); \tag{15}$$

also $\hat{\mathsf{M}}$ satisfies the nonstandard *action–reaction principle*

$$\mathrm{skw}(\tilde{\mathsf{M}}(\tau, x, n) - \tilde{\mathsf{M}}(\tau, x, -n)) = 0, \tag{16}$$

and is linear in the normal n, i.e., there is a third-rank tensor $\mathbf{m}$ such that

$$\tilde{\mathsf{M}}(\tau, x, n) = \mathbf{m}(\tau, x)n. \tag{17}$$

- *In addition, if $\rho \mathbf{e} O^\ddagger$ is continuous in space and the third-rank tensor stress field $\mathbf{m}$ is $C^1(\mathcal{B}_\tau) \cap C(\bar{\mathcal{B}}_\tau)$, there exists a second-rank tensor field A, depending on space and time, such that*

$$\mathrm{skw}T = \mathrm{skw}A. \tag{18}$$

and

$$\rho_m O^{\ddagger} - A + \text{div}\mathbf{m} = 0. \tag{19}$$

Proof Since $\hat{\mathsf{W}}$ is skew symmetric, we can replace it with $\mathbf{e}q$, where $q \in \mathbb{R}^3$ and $\mathbf{e}$ is Ricci's alternating symbol, as already declared above. The invariance axiom implies

$$\mathcal{P}_{\mathfrak{b}_\tau}^{ext,m}(\hat{\mathsf{c}} + \hat{\mathsf{W}}(x - x_0), \mathbf{e}q) = 0,$$

i.e.,

$$\hat{\mathsf{c}} \cdot \left(\int_{\mathfrak{b}_\tau} \rho b^{\ddagger} \, dx + \int_{\partial \mathfrak{b}_\tau} \mathsf{t}_\partial \, d\mathcal{H}^2(x) \right) + q \cdot \left(\int_{\mathfrak{b}_\tau} \mathbf{e}((x - x_0) \otimes \rho b^{\ddagger} + \rho O^{\ddagger}) \, dx \right.$$

$$\left. + \int_{\partial \mathfrak{b}_\tau} \mathbf{e}((x - x_0) \otimes \mathsf{t}_\partial + \hat{\mathsf{M}}_\partial) \, d\mathcal{H}^2(x) \right) = 0.$$

The arbitrariness of $\hat{\mathsf{c}}$ and q implies the integral balance of standard forces, namely

$$\int_{\mathfrak{b}_\tau} \rho b^{\ddagger} \, dx + \int_{\partial \mathfrak{b}_\tau} \mathsf{t}_\partial \, d\mathcal{H}^2(x) = 0, \tag{20}$$

and a nonstandard balance of couples expressed in tensor form:

$$\int_{\mathfrak{b}_\tau} \mathbf{e}((x - x_0) \otimes \rho b^{\ddagger} + \rho O^{\ddagger}) \, dx$$

$$+ \int_{\partial \mathfrak{b}_\tau} \mathbf{e}((x - x_0) \otimes \mathsf{t}_\partial + \hat{\mathsf{M}}_\partial) \, d\mathcal{H}^2(x) \, dx = 0. \tag{21}$$

For any part $\mathfrak{b}_\tau$, the boundedness of $b_m^{\ddagger}$ implies the inequality

$$\left| \int_{\partial \mathfrak{b}_\tau} \mathsf{t}_\partial \, d\mathcal{H}^2(x) \right| \leq K \, \text{vol}(\mathfrak{b}_\tau), \tag{22}$$

with K a constant bounding $|\rho b^{\ddagger}|$. Hamel–Noll's argument (see [24]) allows us to prove that t_∂ depends on $\partial \mathfrak{b}_\tau$ only through its normal n at all points where n is well-defined, i.e., relation (11). Also, by selecting a part $\mathfrak{b}_\tau$ to be a parallelepiped constructed over a square, oriented by the normal n, with side length $\lambda < 1$, staking the square itself by a thickness λ^2, the assumed continuity of $\tilde{\mathsf{t}}(\tau, \cdot, n)$ implies as $\lambda \to 0$ the action–reaction principle (12). On the basis of these results, the standard tetrahedron argument, referring to a generic basis $\{e_i\}$, $i = 1, 2, 3$, allows us to write

$$\tilde{\mathsf{t}}(\tau, x, n) = \sum_{i=1}^{3} (\tilde{\mathsf{t}}(\tau, x, n) \otimes e_i)n,$$

i.e., t is a linear function of n, the proportional factor being the second-rank tensor

$$T = \sum_{i=1}^{3} \tilde{\mathfrak{t}}(\tau, x, e_i) \otimes e_i.$$

This is standard Cauchy's theorem [24], which also holds in less stringent regularity assumptions, variously discussed in the literature (see, for example, [13]).

By setting

$$\mathsf{r} := \mathbf{e}((x - x_0) \otimes \rho b^{\ddagger} + \rho_m O^{\ddagger})$$

and

$$\mathsf{h} := \mathbf{e}((x - x_0) \otimes \mathfrak{t}_{\partial} + \hat{\mathsf{M}}_{\partial}),$$

the previous integral balance (21) becomes

$$\int_{\mathfrak{b}_{\tau}} \mathsf{r} \, dx + \int_{\partial \mathfrak{b}_{\tau}} \mathsf{h} \, d\mathcal{H}^2(x) = 0.$$

Since $\mathcal{B}_{\tau}$ is bounded and x_0 is arbitrary, we can select x_0 such that the boundedness of $|\rho b^{\ddagger}|$ over $\mathcal{B}_{\tau}$ implies that of $|(x - x_0) \otimes \rho b^{\ddagger}|$. Consequently, owing to the assumed boundedness of $|\rho \mathbf{e} O^{\ddagger}|$, we get the inequality

$$\left| \int_{\partial \mathfrak{b}_{\tau}} \mathsf{h} \, d\mathcal{H}^2(x) \right| \leq \bar{K} \, \mathrm{vol}(\mathfrak{b}_{\tau}),$$

with $\bar{K}$ an appropriate constant. We can re-use the standard arguments above to get first that h depends on $\partial \mathfrak{b}_{\tau}$ only through n at all points where n is well-defined; consequently, $\hat{\mathsf{M}}_{\partial}$ itself depends just on the normal n, which is relation (15). Moreover, we get

$$\mathsf{h}(\tau, x, n) = -\mathsf{h}(\tau, x, -n),$$

i.e., Eq. (16), owing to the validity of the relation (12), and we find the existence of a second-rank tensor $\mathcal{T}(\tau, x)$ such that

$$\mathsf{h}(\tau, x, n) = \mathcal{T}(\tau, x)n,$$

i.e.,

$$\mathbf{e}\hat{\mathsf{M}}(\tau, x, n) = \mathcal{T}(\tau, x)n - \mathbf{e}(x - x_0) \otimes Tn,$$

a relation stating the linearity of $\hat{\mathsf{M}}$ with respect to n, i.e., relation (17).

If $\mathbf{m}(\tau, \cdot)$ is continuous and continuously differentiable in space, the integral balance (21) becomes

$$\int_{\mathfrak{b}_\tau} \mathbf{e}((x - x_0) \otimes (\rho b^\ddagger + \mathrm{div}T) - T + \rho O^\ddagger + \mathrm{div}\mathbf{m})\,\mathrm{d}x = 0.$$

Consequently, the pointwise balance of forces (14) and the assumed continuity of the integrand in the previous integral imply

$$\mathbf{e}T = \mathbf{e}(\rho O^\ddagger + \mathrm{div}\mathbf{m})$$

By multiplying from the left by Ricci's alternating symbol $\mathbf{e}$, and taking into account that for every second-rank tensor U we compute $\mathbf{e}\mathbf{e}U = 2\mathrm{skew}U$, we may say that a tensor field taking values $A \in \mathbb{R}^3 \otimes \mathbb{R}^3$ exists and is such that the relations (18) and (19) hold.

7   A Tensor Inertial Balance

A standard assumption prescribes the additive decomposition of bulk actions $b^\ddagger$ into inertial and non-inertial components, indicated respectively by b^{in} and b, i.e.,

$$b^\ddagger = b + b^{in},$$

Here, we accept an analogous assumption for $O^\ddagger$, prescribing

$$O^\ddagger = O + O^{in}.$$

Then, a question is the identification of inertial terms. With this aim, we consider a **reduced tensor kinetic energy**

$$\mathcal{W}_* = \frac{1}{2\omega} \int_{\mathfrak{e}(x)} \theta w_\star \otimes w_\star \,\mathrm{d}y.$$

The word *reduced* recalls that we define $\mathcal{W}_*$ by using the local average w_* instead of the true grain velocity w. By using the decomposition (1), we compute

$$w_\star \otimes w_\star = v \otimes v + By \otimes yB^T + c \otimes c$$
$$+ 2\mathrm{sym}(v \otimes By) + 2\mathrm{sym}(v \otimes c) + 2\mathrm{sym}(By \otimes c).$$

Integration over the loculus implies

$$\int_{\mathfrak{e}(x)} \theta v \otimes v \, \mathrm{d}y = v \otimes v \int_{\mathfrak{e}(x)} \theta \, \mathrm{d}y = v \otimes v,$$

$$\int_{\mathfrak{e}(x)} \theta By \otimes By \, \mathrm{d}y = B \int_{\mathfrak{e}(x)} \theta y \otimes y \, \mathrm{d}y B^Y = BYB^T,$$

$$\int_{\mathfrak{e}(x)} \theta 2\mathrm{sym}(v \otimes By) \, \mathrm{d}y = 2\mathrm{sym}\left(v \otimes \left(\int_{\mathfrak{e}(x)} \theta y \, \mathrm{d}y \right) B^T \right) = 0,$$

thanks to the identity (2),

$$\int_{\mathfrak{e}(x)} \theta 2\mathrm{sym}(v \otimes c) \, \mathrm{d}y = 2\mathrm{sym}\left(v \otimes \int_{\mathfrak{e}(x)} \theta c \, \mathrm{d}y \right) = 0,$$

and

$$\int_{\mathfrak{e}(x)} \theta 2\mathrm{sym}(By \otimes c) \, \mathrm{d}y = 2\mathrm{sym}\left(B \int_{\mathfrak{e}(x)} \theta y \otimes c \, \mathrm{d}y \right) = 0,$$

owing to Eqs. (3) and (5) respectively. Thus, $\mathcal{W}_*$ can be written as

$$\mathcal{W}_* = \frac{1}{2}(v \otimes v + BYB^T + H).$$

Its extended Oldroyd derivative with respect to B is given by

$$\overset{\circ}{\mathcal{W}}_* = \mathrm{sym}(v \otimes \overset{\circ}{v}) + \mathrm{sym}(B\overset{\circ}{K}) + \frac{1}{2}\dot{H} - \mathrm{sym}(BH) + \frac{1}{2}\sigma H, \qquad (23)$$

because $\overset{\circ}{H} = \dot{H} - 2\mathrm{sym}(BH) + \sigma H$, since H is symmetric.

We *postulate* a **tensor inertial balance**:

$$\int_{\mathfrak{b}_\tau} \rho \overset{\circ}{\mathcal{W}}_* \, \mathrm{d}x + \int_{\mathfrak{b}_\tau} \rho\mathrm{sym}(v \otimes b^{in} + BO^{in}) \, \mathrm{d}x$$
$$- \frac{1}{2} \int_{\mathfrak{b}_\tau} (\rho J - Z) \, \mathrm{d}x - \frac{1}{2} \int_{\partial \mathfrak{b}_\tau} \hat{\mathsf{J}}_\partial \, \mathrm{d}\mathcal{H}^2(x) = 0, \qquad (24)$$

presuming that it holds true for every choice of the rate fields v and B compactly supported over $\mathcal{B}_\tau$. The symmetry of $\mathcal{W}_*$ suggests involving the symmetric component of the tensor power density $v \otimes b^{in} + BO^{in}$. We add bulk sources per unit volume, ρJ and Z, the former due to the direct action of the environment, the latter associated with events inside the loculus, and fluxes $\hat{\mathsf{J}}_\partial$, all compensating for the

time variation of H, i.e., the fluctuations of the tensor kinetic energy. By substituting in the inertial balance (24) the expression (23), we get

$$\int_{\mathfrak{b}_\tau} (\rho\mathrm{sym}(v \otimes (\mathring{v} + b^{in})) + \rho\mathrm{sym}(B(\mathring{K} - H + O^{in}))) \ \mathrm{d}x$$

$$+ \frac{1}{2}\left(\int_{\mathfrak{b}_\tau} (\rho(\dot{H} + \sigma H) - \rho J + Z) \ \mathrm{d}x - \int_{\partial\mathfrak{b}_\tau} \hat{\mathsf{J}}_\partial \ \mathrm{d}\mathcal{H}^2(x) \right) = 0.$$

$$(25)$$

Further assumptions apply:

(1) The flux $\hat{\mathsf{J}}_\partial$ depends on the boundary $\partial\mathfrak{b}_\tau$, for any $\mathfrak{b}_\tau$, besides space and time.
(2) Bulk actions determined by the fluctuations inside the loculus are bounded, i.e.,

$$\sup_{x\in\mathcal{B}_\tau} |\rho(\dot{H} + \sigma H) - (\rho J - Z)| < +\infty.$$

(3) As a function of x, $\hat{\mathsf{J}}_\partial$ is continuous.

The first assumption implies from Eq. (25) the identities

$$\rho b^{in} = -\rho\dot{v}$$

and

$$\rho O^{in} = -\rho\mathring{K} + \rho H.$$

Consequently, the balance (25) reduces to

$$\int_{\mathfrak{b}_\tau} \rho(\dot{H} + \sigma H) \ \mathrm{d}x - \int_{\mathfrak{b}_\tau} (\rho J - Z) \ \mathrm{d}x - \int_{\partial\mathfrak{b}_\tau} \hat{\mathsf{J}}_\partial \ \mathrm{d}\mathcal{H}^2(x) = 0.$$

The boundedness of the bulk integrands and the continuity of $\hat{\mathsf{J}}_\partial$ through the boundary imply first that $\hat{\mathsf{J}}_\partial$ depends on $\partial\mathfrak{b}_\tau$ just to the normal n at all points where it is well-defined, namely $\hat{\mathsf{J}}_\partial = \hat{\mathsf{J}} = \tilde{\mathsf{J}}(\tau, x, n)$ and is such that

$$\tilde{\mathsf{J}}(\tau, x, n) = -\tilde{\mathsf{J}}(\tau, x, -n),$$

as a consequence of the same standard arguments exploited in Theorem 1. A further consequence is the linearity of $\hat{\mathsf{J}}$ with respect to n, i.e.,

$$\hat{\mathsf{J}} := \tilde{\mathsf{J}}(\tau, x, n) = \tilde{\mathbf{j}}(\tau, x)n,$$

with $\mathbf{j} = \tilde{\mathbf{j}}(\tau, x)$ the value of a third-rank tensor field. Then, when $\rho \dot{H} - (\rho J - Z)$ is continuous in space and $\tilde{\mathbf{j}}(\tau, \cdot)$ is $C^1(\mathcal{B}_\tau) \cap C(\bar{\mathcal{B}}_\tau)$, the arbitrariness of $\mathfrak{b}_\tau$ and use of the Gauss theorem imply

$$\rho(\dot{H} + \sigma H) = \rho J - Z + \operatorname{div} \mathbf{j}.$$

8 Actions in the Homogenized Sparse Phase in Terms of the Discrete Ones

Looking at the discrete grain cluster, we may distinguish two possible actions on each grain: drag exerted by the environment and grain-to-grain interactions. Also, we consider collective actions between neighboring loculi, exerted at the mesoscopic loculus scale, and due to the relative flow of pertinent grain clusters.

8.1 Actions Exerted on a Single Grain by the Environment

Let vector ℓ be the value of a function

$$\ell := \tilde{\ell}(\tau, x; y, w),$$

assumed to be sufficiently smooth to be involved in the following developments. It represents the **external (environmental) force** on a particle crossing y in $\mathsf{e}(x)$ with velocity w. The average of ℓ over the space of velocities is given by

$$\ell_* := \tilde{\ell}_*(\tau, x; y) := \theta^{-1} \int_{\mathfrak{e}(x)} \Theta (\tau, x; y, w) \, \tilde{\ell}(\tau, x; y, w) \, \mathrm{d}w.$$

According to reference [11], we assume first that **the tensor power density $w_* \otimes \ell_*(\tau, x; y)$ equals external sources and fluxes appearing in the tensor balance of kinetic energy for any choice of the velocity fields involved**, i.e.,

$$\delta^{-3} \mu \omega(\tau, x) \int_{\mathfrak{e}(x)} \theta w_* \otimes \ell_* \, \mathrm{d}y = v \otimes \rho b + \rho B O + \frac{1}{2}(\rho J + \operatorname{div} \mathbf{j}). \qquad (26)$$

Since, by the decomposition of w_*, we have

$$w_* \otimes \ell_* = v \otimes \ell_* + By \otimes \ell_* + c \otimes \ell_*,$$

The arbitrariness of v and B implies

$$\rho b = \delta^{-3} \mu \omega(\tau, x) \int_{\mathfrak{e}(x)} \theta \tilde{\ell}_*(\tau, x; y) \, \mathrm{d}y,$$

$$\rho O = \delta^{-3} \mu \omega(\tau, x) \int_{\mathfrak{e}(x)} \theta y \otimes \tilde{\ell}_*(\tau, x; y) \, \mathrm{d}y,$$

$$\rho J + \mathrm{div} \, \mathbf{j} = 2\delta^{-3} \mu \omega(\tau, x) \int_{\mathfrak{e}(x)} \theta c \otimes \tilde{\ell}_*(\tau, x; y) \, \mathrm{d}y.$$

8.2 Grain-to-Grain Interactions

We consider here **only pairwise interactions**. We indicate by f the **force** at instant τ, within the loculus $\mathsf{e}(x)(x)$, between a molecule at y and one at y', characterized by velocities w and w' respectively. Such a force is given by a sufficiently smooth function $\tilde{\mathsf{f}}$ such that

$$\mathsf{f} := \tilde{\mathsf{f}}(\tau, x; y, w, y', w').$$

We assume

$$\tilde{\mathsf{f}}(\tau, x; y, w, y, w) = 0$$

to exclude **particle self-interactions**. Objectivity may restrict further the dependence of $\tilde{\mathsf{f}}$ on its entries. In reality, grains are extended in space, whereas here we describe them as mass points. To account indirectly for the grain radius, and the possibility of having interactions at a *short* distance, we include in the averages presented below an **influence function**, f, compactly supported, which we write both as $f(y, y')$ and $f(x, x')$, considering *the same structure* for the influence function, assumed as smooth as necessary, at both scales involved. Its choice is a constitutive ingredient and has to be determined in every specific application. The introduction of f share analogies with the resistance kernel used by Goddard in [15]. Also, if we imagine in two-dimensional space a jammed cluster of grains, $f(x, x')$ reduces to Edwards' quadron indicator function [2]. However, analogies apart, we assume that at every x, the support of f is such that for any other x' in it, the following relations hold true:

$$v(\tau, x') - v(\tau, x) = L(x' - x)$$

and

$$B(\tau, x')y - B(\tau, x)y = (\mathbf{b}y)(x' - x),$$

where $\mathbf{b} := \nabla B$. The two relations above are a **version of the Cauchy–Born rule re-interpreted in a two-scale sense and written in terms of velocities**.

By averaging over velocities, we get

$$\bar{\mathsf{f}}(\tau, x; y, y') := \theta^{-2} \int_{\mathcal{V}} \Theta(\tau, x; y, w) \int_{\mathcal{V}} \Theta(\tau, x; y', w')\mathsf{f}(\tau, x; y, w, y', w') \, dw' \, dw,$$

and we may define

$$\mathsf{f}_*(\tau, x; y) := \delta^{-3} \int_{\mathfrak{e}(x)} \theta f(y, y')\bar{\mathsf{f}}(\tau, x; y, y') \, dy'.$$

$\mathsf{f}_*(\tau, x; y)$ is the force on y, within $\mathfrak{e}(x)$ at the instant τ, exerted by the particles in a small neighborhood defined by $f(y, y')$. For $\mathsf{f}_*(\tau, x; y)$, written just as f_* for short-hand notation, we compute

$$\delta^{-3} \int_{\mathfrak{e}(x)} \theta w_* \otimes \mathsf{f}_* \, dy = v \otimes \bar{\mathsf{t}}(\tau, x) + \delta^{-3} B \int_{\mathfrak{e}(x)} \theta y \otimes \mathsf{f}_* \, dy + \delta^{-3} \int_{\mathfrak{e}(x)} \theta c \otimes \mathsf{f}_* \, dy,$$

where we use $\bar{\mathsf{t}}(\tau, x)$ to indicate the integral

$$\bar{\mathsf{t}}(\tau, x) := \delta^{-3} \int_{\mathfrak{e}(x)} \theta \mathsf{f}_*(\tau, x; y) \, dy.$$

Two vectors, namely t and k, account for inter-loculus interactions, those of weakly nonlocal nature. They are values of sufficiently smooth functions

$$\mathsf{t} := \tilde{\mathsf{t}}(\tau, x, x')$$

with $\tilde{\mathsf{t}}(\tau, x, x') = \hat{\mathsf{t}}(\tau, x, x', v_m(\tau, x), v'_m(\tau, x'))$, such that $\tilde{\mathsf{t}}(\tau, x, x) = \bar{\mathsf{t}}(\tau, x)$, and

$$\mathsf{k} := \tilde{\mathsf{k}}(\tau, x, x'; y),$$

with $\tilde{\mathsf{k}}(\tau, x, x; y) = 0$ by assumption.

With $\text{supp}_x f(x, x')$ the support of $f(x, \cdot)$ around x, we define $P^{int}_{dis[x]}(\tau, x)$ and $P^{int}_{dis[B]}(\tau, x)$ as partial tensor discrete internal powers, associated with v_m and B, by

$$P^{int}_{dis[x]}(\tau, x) := |\text{supp}_x f(x, x')|^{-1} L \int_{\mathcal{B}} f(x, x')(x' - x) \otimes \tilde{\mathsf{t}}(\tau, x, x') \, dx',$$

and

$$P_{dis[B]}^{int}(\tau, x) := |\mathrm{supp}_x f(x, x')|^{-1} \nabla B \int_{\mathcal{B}} f(x, x') \int_{\mathfrak{e}(x)} (x' - x) \otimes y \otimes \tilde{k}(\tau, x, x'; y) \, dy dx'.$$

By summing them and adding the tensor power $\delta^{-3} \int_{\mathfrak{e}(x)} \theta w_* \otimes f_* \, dy$, we define the overall **discrete internal interaction tensor power** $P_{dis,m}^{int}$ by

$$P_{dis,m}^{int}(\tau, x) := P_{dis[x]}^{int}(\tau, x) + P_{dis[B]}^{int}(\tau, x) + \delta^{-3} B \int_{\mathfrak{e}(x)} \theta y \otimes f_* \, dy + \delta^{-3} \int_{\mathfrak{e}(x)} \theta c \otimes f_* \, dy.$$

As **homogenization axiom**, we impose the identity between discrete power and the full internal one in the continuum description:

$$P_{dis,m}^{int} = LT^T + BA + \mathbf{b}\mathbf{m}^T + \frac{1}{2}Z,$$

presuming that **it holds for any independent choice** of L, B, and ∇B. Arbitrariness of the rate fields implies the following identifications:

$$T(\tau, x) = |\mathrm{supp}_x f(x, x')|^{-1} \int_{\mathcal{B}} f(x, x') \tilde{t}(\tau, x, x') \otimes (x' - x) \, dx',$$

$$\mathbf{m}(\tau, x) = |\mathrm{supp}_x f(x, x')|^{-1} \int_{\mathcal{B}} f(x, x') \int_{\mathfrak{e}(x)} \tilde{k}(\tau, x, x'; y) \otimes y \otimes (x' - x) \, dy dx',$$

$$A(\tau, x) = \delta^{-3} \int_{\mathfrak{e}(x)} \theta y \otimes f_*(\tau, x; y) \, dy,$$

$$Z(\tau, x) = 2\delta^{-3} \int_{\mathfrak{e}(x)} \theta c \otimes f_*(\tau, x; y) \, dy.$$

They clarify the nature and the role of the interactions measure appearing in the (homogenized) continuum description of the sparse phase.

8.3 A Prominent Special Case: Inhomogeneous Stokesian Suspensions

Consider Stokesian suspensions, i.e., fluid–particle mixtures with negligible particle-scale inertia and Brownian motion. if we look at the sole sparse phase, in these suspensions the fluctuation velocity c is negligible; so are the loculus-scale Reynolds stress tensor H and the self-action Z, which depend on c. The evolution equation for H, a balance of low-scale energy, does indeed reduce to $\rho J + \mathrm{div}\, \mathbf{j} = 0$.

Assume also that **j** vanishes for the absence of external fluxes directly activating fluctuations, which are—as already assumed—negligible. Eventually, we have $\rho_m J = 0$.

In deriving the representation of actions at continuum scale in terms of those on grains (particles), the inter-loculus force $\tilde{k}(\tau, x, x'; y)$ is a fluctuation with respect to $\tilde{t}(\tau, x, x')$. Let us consider it negligible, as fluctuations are in the present special case. Consequently, we may also take $\mathbf{m}(\tau, x) = 0$.

Finally, since by the definition quoted at the beginning of this section particle-scale inertia is also negligible, the balance of tensor moment of momentum at the same scale reduces to

$$\rho O = A. \tag{27}$$

As a constitutive structure, assume that the self-action A is proportional to G, a second-rank **fabric tensor** defined by

$$\mathsf{G} := \frac{1}{2} \int_{\mathfrak{e}(x)} \theta(\tau, x; y) \int_{\mathfrak{e}(x)} \theta(\tau, x; y')(y - y') \otimes (y - y')\mathrm{d}y\mathrm{d}y'.$$

When the external action ℓ_* on each grain depends on the strain history, we can in principle reduce the balance (27) to Goddard's equation *postulated* in reference [15, eq. 31]. Rather than being only a constitutive assumption, as declared in [15], that equation is the mixing of a pure balance of loculus-scale actions *and* a constitutive choice.

As a further constitutive example, assume that the self-action A is purely dissipative in the sense that $A \cdot \hat{\mathsf{G}} \leq 0$ with $\hat{\mathsf{G}} := \dot{\mathsf{G}} - \mathsf{G}\nabla v + (\nabla v)\mathsf{G}$, the inequality holding for any choice of $\hat{\mathsf{G}}$. The arbitrariness of $\hat{\mathsf{G}}$ implies from the inequality that A is proportional to $\hat{\mathsf{G}}$ itself. Consequently, appropriate choices for ℓ_*, may give to ρO a form reducing Eq. (27) to Phan-Thien's evolution equation [23] for the same fabric tensor above.

9   Granular Temperatures

When grains have a diameter larger than one micron, thermal fluctuations are negligible. However, in granular flows fluctuations beyond the average velocity can be appreciable. So, we can imagine a notion of **granular temperature** as a (scalar or tensor) measure of the velocity fluctuations. We may find proposals in which the fluctuation velocity $w - v$ enters the dyad $(w - v) \otimes (w - v)$, considered as a tensor-type **granular temperature**. In this view, mechanics refers just to the average velocity v, whereas, in the proposal discussed above, mechanics includes both v and By, so the representation is more refined with respect to $w - v$. In this sense, H can play such a role per se. If so, the kinetic energy balance discussed above plays the

role of a first principle of thermodynamics and the local evolution equation for H is a reduced version of that first principle in which the right-hand-side terms are outer and inner sources of (granular) heat, namely J and Z respectively, and of (granular) heat flux **j**. At variance, we can consider H as a dynamic variable, with the right-hand-side terms considered to be measures of interaction fluctuations, compatible with the analysis developed above. In any case, in the picture of kinematics chosen here, we have **residual fluctuations** $\bar{c} := w - w_*$, which could be non-negligible in the presence of velocity field high variability in space. A question is whether effects associated with $\bar{c}$ have to be considered mechanical or whether they have a thermodynamic character. Such a question falls within a fundamental problem, i.e., the nature and "place" of the boundary between mechanics and thermodynamics. The answer suggested by Miroslav Grmela and Gianfranco Capriz, independently, has—in a sense—a philosophical character: we decide a *level* of detail in the representation of motion (even taking the word "motion" in a generalized sense), and this is to us *mechanics*; what remains of this representation falls within what we call *thermodynamics*.

A pertinent notion of granular temperature seems to be appropriate. Thus, we can explore different possible definitions of (scalar and tensor) granular temperatures associated with $\bar{c}$. They have been introduced and discussed in references [9–11]. In this section, we summarize the pertinent results.

9.1 Scalar Temperature

For Ω an open subset of $\mathcal{V}$ and $\mathcal{D}(\Omega)$ the space of C^∞ maps into a linear space, compactly supported over Ω, we define a distribution $\mathcal{T}$ to be a linear form on $\mathcal{D}(\Omega)$ such that $\lim_i \mathcal{T}(\varphi_i) = \varphi$, for any sequence $\{\varphi_i\}$ converging toward φ in $\mathcal{D}(\Omega)$. As $\mathcal{T}$ belongs to the dual space of $\mathcal{D}(\Omega)$, namely $\mathcal{D}^*(\Omega)$, we use the common notation $\langle \mathcal{T}, \varphi \rangle$ for the value $\mathcal{T}(\varphi)$. Moreover, if the map $\mathcal{T}$ can be integrated on every compact subset of Ω, in short, $\mathcal{T} \in L^1_{loc}(\Omega)$, $\mathcal{T}$ defines a distribution through the formula

$$\langle \mathcal{T}, \varphi \rangle = \int_\Omega \mathcal{T}(u) \cdot \varphi(u) \, \mathrm{d}u,$$

with $\mathcal{T}(u)$ belonging to the dual space of $\varphi(u)$ (see [12]).

Consequently, we can look at Θ in operational terms, as it is a distribution density. Then, we write

$$\Theta(u) = \hat{\mathsf{t}} \cdot u,$$

and presume that the covector $\hat{\mathsf{t}}$ (here identified with a vector for we are referring to orthonormal frames of references), evaluated on the generic vector u, depends on τ, x, y, and

$$\bar{c} = w - w_*.$$

For the sake of convenience, let us reduce to the case in which Θ is **isotropic** with respect to $\bar{c}$. In this case, we get

$$\hat{\mathsf{t}} := \bar{\alpha}\left(\tau, x; y, \xi'\right)\bar{c},$$

with $\bar{\alpha}$ a scalar-valued function, assumed to have a sufficiently smooth dependence on its entries, among which we include by assumption the **residual fluctuation molecular kinetic energy**

$$\xi' := \frac{1}{2}|\bar{c}|^2$$

per unit mass of the molecules, instead of $\bar{c}$.

With these notations, the **residual fluctuation kinetic energy κ per unit mass of all molecules** in e, is given by

$$\kappa = \omega^{-1}\int_0^{+\infty}\left(\int_{\mathsf{e}}\bar{\alpha}\,\mathrm{d}y\right)\xi'\mathrm{d}\xi'.$$

By defining $\xi = \kappa^{-1}\xi'$, and

$$\alpha = \kappa\omega^{-1}\int_{\mathsf{e}}\bar{\alpha}\,\mathrm{d}y,$$

we find $\Theta(u) = \omega\kappa^{-1}\alpha\bar{c}\cdot u$ for every $u \in \mathcal{V}$, with the constraints

$$\int_0^{+\infty}\alpha\left(\tau, x; \xi\right)\mathrm{d}\xi = 1, \qquad \int_0^{+\infty}\xi\alpha\left(\tau, x; \xi\right)\mathrm{d}\xi = 1. \tag{28}$$

Function $\alpha(\cdot)$ is the frequency of occurrence in a ball of radius $\mathrm{d}y$ centered at $y \in \mathsf{e}(x)$ of molecules with remaining fluctuation kinetic energy ξ per unit molecular mass. Thus, α is a descriptor of remaining fluctuations *within* the loculus and we can consider it to be governed by an independent rule, as

$$D_\tau\hat{\alpha} = \mathcal{F}\left(\hat{\alpha}\right),$$

where $\hat{\alpha}(\tau, x; \xi) := \kappa\alpha(\tau, x; \xi)$. The right-hand-side term is a functional to be specified, and $D_\tau\hat{\alpha}$ is the total time variation. In particular, thinking of the Maxwell distribution, we reduce such an evolution equation as

$$\frac{\partial \hat{\alpha}}{\partial \tau} + \frac{\partial \hat{\alpha}}{\partial x} \cdot v = \frac{1}{\tau_*} \left(\beta + \frac{\partial \bar{\psi}}{\partial \xi} + \operatorname{div} p \right), \tag{29}$$

where τ_* is a constant with the dimension of time, the scalar β a source, p a vector associated with a flux, and $\frac{\partial \bar{\psi}}{\partial \xi}$ the derivative of a potential with respect to ξ. Explicit expressions of β, $\bar{\psi}$, and p have to be specified by constitutive rules. With the nonzero right-hand-side term, a constant is not a solution of the previous equation.

To look at a special case furnishing a closed-form solution, let us assume the existence of a chemical potential $\hat{\mu}(\xi, \hat{\alpha})$ such that

$$\psi = \frac{d\hat{\mu}}{d\xi} = \frac{\partial \hat{\mu}}{\partial \xi} + \frac{\partial \hat{\mu}}{\partial \hat{\alpha}} \frac{\partial \hat{\alpha}}{\partial \xi}, \quad p = \frac{\partial \hat{\mu}}{\partial \hat{\alpha}} \nabla \hat{\alpha}.$$

For it, take the expression suggested in reference [10], namely

$$\hat{\mu} = \hat{\mu}_0 \ln \hat{\alpha} + \xi,$$

with $\hat{\mu}_0$ a nondimensional constant. We compute

$$\psi = 1 + \frac{\hat{\mu}_0}{\hat{\alpha}} \frac{\partial \hat{\alpha}}{\partial \xi}, \quad p = \frac{\hat{\mu}_0}{\hat{\alpha}} \nabla \hat{\alpha},$$

so that we get

$$\frac{\partial \hat{\alpha}}{\partial \tau} + \frac{\partial \hat{\alpha}}{\partial x} \cdot v = \frac{1}{\tau_*} \left(\beta + \frac{\hat{\mu}_0}{\hat{\alpha}} \frac{\partial^2 \hat{\alpha}}{\partial \xi^2} - \frac{\hat{\mu}_0}{\hat{\alpha}^2} \left(\frac{\partial \hat{\alpha}}{\partial \xi} \right)^2 + \frac{\hat{\mu}_0}{\hat{\alpha}} \Delta \hat{\alpha} - \frac{\hat{\mu}_0}{\hat{\alpha}^2} \left(\nabla \hat{\alpha} \right)^2 \right), \tag{30}$$

an equation of the Fokker–Planck type. When $\hat{\alpha}$ is independent of time and place, β and p vanish. Also, Eq. (29) imposes that ψ is independent of ξ. Hence, $\hat{\alpha}$ satisfies the condition

$$\frac{\partial \hat{\mu}}{\partial \xi} + \frac{\partial \hat{\mu}}{\partial \hat{\alpha}} \frac{\partial \hat{\alpha}}{\partial \xi} = \psi_0,$$

with ψ_0 a constant, so that

$$\hat{\mu}\left(\xi, \hat{\alpha}(\xi)\right) = \psi_0 \xi + \psi_1.$$

When $\hat{\mu}\left(\xi, \hat{\alpha}(\xi)\right) = \hat{\mu}_1(\xi) + \hat{\mu}_2(\hat{\alpha})$, with $\hat{\mu}_2(\hat{\alpha})$ a strictly monotonic function, we get

$$\hat{\alpha}(\xi) = \hat{\mu}_2^{-1}[\psi_0 \xi + \psi_1 - \hat{\mu}_1(\xi)].$$

Also, when $\hat{\mu}_1(\xi) = \xi$ and $\hat{\mu}_2(\hat{\alpha}) = \hat{\mu}_0 \ln \hat{\alpha}$, we compute

$$\hat{\alpha}(\xi) = \exp\left(\frac{(\psi_0 - 1)\xi + \psi_1}{\hat{\mu}_0}\right) = \hat{\alpha}_0 \exp\left(\frac{(\psi_0 - 1)}{\hat{\mu}_0}\xi\right),$$

with $\hat{\alpha}_0 = \exp(\frac{\psi_1}{\hat{\mu}_0})$, so that

$$\frac{d\hat{\alpha}}{d\xi} = \frac{(\psi_0 - 1)}{\hat{\mu}_0}\hat{\alpha}.$$

With the previous special choice, made merely to compute a physically reasonable explicit example, $\hat{\alpha}$ is either null or exponential in ξ. If $[\xi_0, \xi_1]$ is the support of $\hat{\alpha}$, we eventually get

$$\hat{\alpha}(\xi_0) = \frac{(1 - \xi_1)(1 - \psi_0) - \hat{\mu}_0}{\hat{\mu}_0(\xi_1 - \xi_0)} = (\xi_1 - \xi_0)^{-1}\left[(1 - \xi_1)\frac{(1 - \psi_0)}{\hat{\mu}_0} - 1\right],$$

and

$$\hat{\alpha}(\xi_1) = \frac{(1 - \xi_0)(1 - \psi_0) - \hat{\mu}_0}{\hat{\mu}_0(\xi_1 - \xi_0)} = (\xi_1 - \xi_0)^{-1}\left[(1 - \xi_0)\frac{(1 - \psi_0)}{\hat{\mu}_0} - 1\right]$$

(for further details, see reference [10]).

In the portion of its range where $\ln \hat{\alpha}$ is defined, we can consider as a (granular) **temperature** the scalar ϑ defined by

$$\vartheta = -\frac{\rho\delta^3}{\omega k_B}\left(\frac{\partial \ln \hat{\alpha}}{\partial \xi}\right)^{-1},$$

with k_B the Boltzmann constant.

An alternative choice is the scalar ϑ_* defined by

$$\vartheta_* = \frac{1}{\omega_*}\left(\frac{\ln \alpha(\xi_0) - \ln \alpha(\xi_1)}{\xi_1 - \xi_0}\right)^{-1},$$

where

$$\omega_* = \frac{\omega k_B}{\rho\delta^3},$$

which we can admit when $\hat{\alpha}$ is monotonous and supported over the interval $[\xi_0, \xi_1]$.

Preference is dictated by consequences we get once constitutive structures for the right-hand-side term of Eq. (29) have been made and a solution reached. Previous analysis sketches only the variety of choices we can make in defining a scalar granular temperature as a measure of energy fluctuations in a flow of a sparse phase.

9.2 Temperature Tensor

In jammed states, we may induce thermal-like agitations by applying repeatedly tapping or sharing protocols [1]. They decay when we remove the excitation. We may use such a protocol to define statistically a notion of temperature even for jammed states. We have already mentioned Edwards a Oakeshott's microcanonical assumption: all jammed states occupying the same volume are equi-probable. When we consider the possibility of applying shaking protocols, we have to enlarge the view from a microcanonical to a canonical ensemble.

Consider a container, with volume V, endowed with N_V jammed grains. The (extended in space) i-th grain has z_i contacts, each assumed to be exerted at a single point where, on the boundary, a grain j touches it. A vector r_{ij}, issued by the grain center of mass, indicates each contact point where the two grains exchange a force $\bar{\mathsf{f}}_{ij}$, so that the total stress $\hat{T}$ in V is given by $\hat{T}^T := V^{-1} \sum_i^{N_V} \sum_j^{z_i} r_{ij} \otimes \bar{\mathsf{f}}_{ij}$. It is exerted on the container walls and is balanced. According to Edwards and Oakeshott, the probability P_ς that a subsystem of volume $\bar{V} < V$ be in a given state ς is $P_\varsigma = \exp(-\frac{\bar{V}}{\chi(V)})$. The scalar factor $\chi(V)$, dubbed the so-called **compactivity**, is the inverse of a temperature, which is a scalar associated in a sense with the loss of information induced by microcanonical assumption. The total stress, however, can be used to factorize the possible state (essentially configuration) space into sectors $\mathcal{M}_{\hat{T}}$, each containing all possible (balanced) jammed states with total stress $\hat{T}$. Transient shaking protocols allow us to transit from a sector to another through a generally non-ergodic dynamics. With $\beta_\varsigma^{dyn}(\bar{T}, V, N_V)$ the frequency at which a state can be accessed by the induced dynamics, the number $X(\bar{T}, V, N_V) := \sum_{\varsigma \in \mathcal{M}_{\hat{T}}} \beta_\varsigma^{dyn}(\bar{T}, V, N_V)$ defines the **density of states in the state space** [19]. According to Boltzmann, the logarithm of X defines an **entropy** associated with (and a shaking protocol induced on) the state space. In this setting, the second-rank tensor $\Xi := \frac{\partial \ln X(\bar{T}, V, N_V)}{\partial \bar{T}}$ plays the role of a **temperature** [20], its scalar version being $\mathrm{tr}\Xi$.

When we look at flows, we do not need to introduce fluctuations by shaking protocols; they emerge naturally along the motion of a granular cluster. In common instances (see pertinent remarks in [17, 25]), the average of $(w - v) \otimes (w - v)$ over the loculus can be taken as a measure of fluctuations, i.e., it can play the role of a temperature, although with tensor character. However, in the view discussed here, we associate a portion of fluctuations to true mechanical interactions. Consequently, at least their accessory component associated with the rate B, as defined above, has to be left a part. The low-spatial-scale Reynolds stress tensor H remains. Its evolution equation can be considered as an additional balance of low-spatial-scale energy. However, if we consider it as a putative tensor temperature, other fluctuations remain: $\bar{c} := w - w_*$. Once again, we could consider the dyad $\bar{c} \otimes \bar{c}$ as a local tensor temperature density. However, we could do something more, which allows us to underline the grand canonical character of the loculus. With this aim,

we take $\frac{1}{2}\bar{c} \otimes \bar{c}$, assigning to it the role of **residual fluctuation tensor kinetic energy per unit mass**. Then, we consider distribution densities of the type

$$\Theta(\tau, x; y, \bar{c} \otimes \bar{c}) = \lambda(\tau, x; y) \exp(-\Lambda \cdot (\bar{c} \otimes \bar{c})),$$

where Λ is a second-rank symmetric tensor and λ an appropriate real-valued function. Then,

$$\Gamma_\omega(\tau, x; \Lambda) := \frac{1}{2\delta^3} \mu \int_{\mathbf{e}(x)} \lambda(\tau, x; y) \exp(-\Lambda \cdot (\bar{c} \otimes \bar{c}))(\bar{c} \otimes \bar{c}) \, \mathrm{d}y$$

is the **averaged residual fluctuation tensor kinetic energy**. To ensure the thermodynamic stability of the loculus, there should exist a differentiable entropy function $\eta_\omega(\tau, x; \Gamma_\omega)$ (see [22]) such that

$$\Lambda = \frac{\partial \eta_\omega}{\partial \Gamma_\omega}.$$

If Λ is nonsingular ($\det \Lambda \neq 0$), its inverse $\Upsilon := \Lambda^{-1}$ is a **temperature tensor** per se.

Write π_ω for a (real-valued) probability density that ω be the grain content in the loculus. By definition, the normalization condition

$$\int_0^{+\infty} \pi_\omega \, \mathrm{d}\omega = 1 \tag{31}$$

holds true. A pertinent (scalar) **entropy** is

$$\eta(\Lambda, \pi) := \int_0^{+\infty} \pi_\omega \eta_\omega(\Gamma_\omega(\Lambda)) \, \mathrm{d}\omega - \int_0^{+\infty} \pi_\omega \ln \pi_\omega \, \mathrm{d}\omega,$$

where the last integral is Shannon's entropy accounting for the loss of information associated with π_ω, with the grain content variation in the loculus.

To determine π_ω, we first define the Lagrangian

$$\int_0^{+\infty} \mathcal{L}(\pi_\omega) \, \mathrm{d}\omega := \eta(\Lambda, \pi) - \Lambda \cdot \Gamma(\Lambda, \pi) + \Lambda \cdot M\bar{\omega} - (\gamma - 1) \int_0^{+\infty} \pi_\omega \, \mathrm{d}\omega,$$

where $\gamma - 1$ is the Lagrangian multiplier through which we impose the constraint (31) and M is a second-rank tensor, here playing the role of **chemical potential**. The condition $\frac{\mathrm{d}\mathcal{L}}{\mathrm{d}\pi_\omega} = 0$ defines stationary points, where

$$\eta_\omega(\Gamma_\omega(\Lambda)) - \ln \pi_\omega - \Lambda \cdot \Gamma_\omega(\Lambda) + \Lambda \cdot M\omega - \gamma = 0.$$

The normalization condition (31) implies

$$\gamma = \ln \int_0^{+\infty} \exp(\eta_\omega(\Gamma_\omega(\Lambda)) - \Lambda \cdot \Gamma_\omega(\Lambda)) \exp(\Lambda \cdot M\omega) \, d\omega$$

and

$$\pi_\omega = \frac{1}{\mathcal{Z}} \exp(\eta_\omega(\Gamma_\omega(\Lambda)) - \Lambda \cdot \Gamma_\omega(\Lambda)) \exp(\Lambda \cdot M\omega),$$

where $\mathcal{Z} := \exp(\gamma)$.

By writing $\exp(\tilde{a}(s))$ for the argument defining γ, we may obviously write

$$\gamma = \ln \int_0^{+\infty} \exp(\tilde{a}(s)) \, ds = \lim_{r \to \infty} \ln \int_0^r \exp(\tilde{a}(s)) \, ds.$$

The loculus boundedness and the finite extension in space of grains allow us to consider the functions of ω defined above, as compactly supported over the non-negative real line, precisely, defined over $[0, k]$, where k is the number of molecules pertaining to the highest packing of a jammed state in the loculus. When $\tilde{a}(s)$ is bounded, the integral converges and we get

$$\ln \int_0^r \exp(\tilde{a}(s)) \, ds \le \ln(r \sup_{[0,r]} \exp(\tilde{a}(s))),$$

so that, *for large r*,

$$\frac{\ln \int_0^r \exp(\tilde{a}(s)) \, ds}{\ln r} \le 1 + \frac{\ln(\sup_{[0,r]} \exp(\tilde{a}(s)))}{\ln r},$$

i.e., γ *behaves asymptotically as* $\ln \omega$.

A pertinent **tensor grand canonical potential** then emerges and is defined by

$$\Psi(\Lambda, M) = -\Upsilon \ln \mathcal{Z}.$$

10   Further Remarks

As we have seen, we can define different notions of temperature, each capturing some aspects of fluctuations left out from the definition (and consequent representation) of interactions governing the motion. Preference depends on what kind of physical aspects we aim to represent in a model. Once the choice has been made, a related problem is to determine the pertinent evolution equation. And it is not a trivial problem.

The whole structure presented here implicitly underlines a conceptual aspect: the boundary between what we consider mechanics and what we set in the structures describing heat fluctuates depending on the level of detail we adopt in describing the motion (for further remarks and analyses of this concept, see [18])

References

1. Becker V., Kassner K. (2015), Protocol-independent granular temperature supported by numerical simulations, *Phys. Rev. E. Stat. Nonlin. Soft Matter Phys.*, **92**, art. 052201 (1–15).
2. Blumenfeld R., Edwards S. F. (2009), On granular stress statistics: compactivity, angoricity, and some open issues, *J. Phys. Chem.*, **113**, 3981–3987.
3. Brocato M., Capriz G. (2011), Clockwork, ephemeral and hybrid continua, *Phys. Mesomech.*, **14**, 124–144.
4. Capriz G. (2003), Elementary preamble to a theory of granular gases, *Rend. Mat. Univ. Padova*, **110**, 179–198.
5. Capriz G. (2006), Pseudofluids, in *Material substructures in complex bodies: from atomic level to continuum*, G. Capriz and P. M. Mariano Eds, Elsevier, pp. 238–261.
6. Capriz G. (2008), On ephemeral continua, *Phys. Mesomech.*, **11**, 285–298.
7. Capriz G., Giovine P. (2016), Hypocontinua, in *Continuum Media with Microstructure 2*, B. Albers and M. Kuczma Eds, Springer Verlag, Berlin, pp. 23–43.
8. Capriz G., Giovine P. (2017), Classes of ephemeral continua, *Math. Meth. Appl. Sci.*, **43**, 1175–1196.
9. Capriz G., Mariano P. M. (2014), Objective fluxes in a multiscale continuum description of sparse medium dynamics, *Phys. A*, **415**, 354–365.
10. Capriz G., Mariano P. M. (2018), Multi-scale kinetic description of granular clusters: invariance, balance, and temperature, *Cont. Mech. Thermodyn.*, **30**, 1323–1342.
11. Capriz G., Mariano P. M. (2019), Interactions in a multi-scale representation of sparse media: from mechanics to thermodynamics, *J. Elast.*, **135**, 91–115.
12. Chipot M. M. (2000), *Elements of nonlinear analysis*, Birkhäuser Verlag, Basel, 2000.
13. Dafermos C. M. (2016), *Hyperbolic conservation laws in continuum physics*, Springer Verlag, Berlin.
14. de Gennes P. G. (1999), Granular matter: a tentative view, *Rev. Mod. Phys.*, **71**, S374-S382.
15. Goddard J. D. (2008), A weakly nonlocal anisotropic fluid model for inhomogeneous Stokesian suspensions, *Phys. Fluids*, **20**, paper n. 040601-(1-16).
16. Edwards S. F., Oakeshott R. B. S. (1989), Theory of powders, *Phys. A*, **157**, 1080–1090.
17. Goldhirsch I. (2008), Introduction to granular temperature, *Powder Tech.*, **182**, 130–136.
18. Grmela M. (2017), Externally driven macroscopic systems: dynamics versus thermodynamics, *J. Stat. Phys.*, **166**, 282–316.
19. Henkes S., Chakraborty B. (2009), Statistical mechanics framework for static granular matter, *Phys. Rev. E. Stat. Nonlin. Soft Matter Phys.*, **79**, 061301-1/19.
20. Henkes S., O'Hern C. S., Chakraborty B. (2007), Entropy and temperature of a static granular assembly: an *ab initio* approach, *Phys. Rev. Lett.*, **99**, 038002-1/4.

21. Mariano P. M. (2020), Flows of suspended grains: mixing a sparse phase with simple and complex continua, *Int. J. Solids Struct.*, **187**, 141–161.
22. Naudts J., van der Straeten E. (2004), The grand canonical ensemble in generalized thermo-statistics, *J. Stat. Mech. Theor. Exp.*, P12002.
23. Phan-Thien N. (1995), Constitutive equation for concentrated suspensions in Newtonian liquids, *J. Rheol.*, **39**, 679–695.
24. Truesdell C. A. (1977), *A first course in rational continuum mechanics*, Academic Press, New York.
25. Truesdell C. A., Muncaster R. G. (1980), Fundamentals of Maxwell's kinetic theory of a simple monatomic gas. Treated as a branch of rational mechanics. *Academic Press*, New York-London.